

Supporting Information for:

Macrocyclic Control of Electron Transfer to High Valent Uranium in Heterobimetallic Complexes

*Amit Kumar,^{a,d,#} Riddhi R. Golwankar,^{a,#} Mikaela M. F. Pynch,^{b,e} Fynn L. Cooper,^a
Grant A. Arehart,^a Korey P. Carter,^b Allen G. Oliver,^c Victor W. Day,^a Tori Z. Forbes,^{b,*} and
James D. Blakemore^{a,*}*

^a Department of Chemistry, University of Kansas,
1567 Irving Hill Road, Lawrence, Kansas 66045, United States

^b Department of Chemistry, University of Iowa,
Iowa City, Iowa 52242, United States

^c Department of Chemistry and Biochemistry, University of Notre Dame,
Notre Dame, Indiana 46556, United States

^d Current address: Heraeus Precious Metals,
15524 Carmenita Road, Santa Fe Springs, California 90670, United States

^e Current address: Department of Chemistry, University of California, Berkeley,
Berkeley, California 94720, United States

These authors contributed equally to this work.

* To whom correspondence should be addressed:
blakemore@ku.edu (J.D.B.) and tori-forbes@uiowa.edu (T.Z.F.)

Contents

Experimental Section	S9
<i>General Considerations</i>	S9
<i>Electrochemical Methods</i>	S9
<i>Vibrational Analysis</i>	S10
<i>Synthesis and characterization</i>	S11
NMR Spectra	S15
Figure S1. ¹ H NMR spectrum of isolated BaPenta	S15
Figure S2. ¹⁹ F { ¹ H} NMR spectrum of isolated BaPenta	S15
Figure S3. ¹ H NMR spectrum of isolated L⁵UO₂	S16
Figure S4. ¹ H NMR spectrum of <i>in situ</i> generated L⁵UO₂Cs	S16
Figure S5. ¹⁹ F { ¹ H} NMR spectrum of <i>in situ</i> generated L⁵UO₂Cs	S17

Figure S6. ^1H NMR spectrum of <i>in situ</i> generated $\text{L}^5\text{UO}_2\text{Rb}$	S17
Figure S7. $^{19}\text{F}\{^1\text{H}\}$ NMR spectrum of <i>in situ</i> generated $\text{L}^5\text{UO}_2\text{Rb}$	S18
Figure S8. ^1H NMR spectrum of <i>in situ</i> generated $\text{L}^5\text{UO}_2\text{K}$	S18
Figure S9. $^{19}\text{F}\{^1\text{H}\}$ NMR spectrum of <i>in situ</i> generated $\text{L}^5\text{UO}_2\text{K}$	S19
Figure S10. ^1H NMR spectrum of <i>in situ</i> generated $\text{L}^5\text{UO}_2\text{Na}$	S19
Figure S11. $^{19}\text{F}\{^1\text{H}\}$ NMR spectrum of <i>in situ</i> generated $\text{L}^5\text{UO}_2\text{Na}$	S20
Figure S12. ^1H NMR spectrum of <i>in situ</i> generated $\text{L}^5\text{UO}_2\text{Li}$	S20
Figure S13. $^{19}\text{F}\{^1\text{H}\}$ NMR spectrum of <i>in situ</i> generated $\text{L}^5\text{UO}_2\text{Li}$	S21
Figure S14. ^1H NMR spectrum of <i>in situ</i> generated $\text{L}^5\text{UO}_2\text{Ca}$	S21
Figure S15. $^{19}\text{F}\{^1\text{H}\}$ NMR spectrum of <i>in situ</i> generated $\text{L}^5\text{UO}_2\text{Ca}$	S22
Figure S16. Stacked ^1H NMR spectra showing the aromatic and imine region of the L^5UO_2 and $\text{L}^5\text{UO}_2\text{M}$ complexes	S22
Figure S17. Stacked ^1H NMR spectra showing the aliphatic region of the L^5UO_2 and $\text{L}^5\text{UO}_2\text{M}$ complexes	S23
Figure S18. Stacked $^{19}\text{F}\{^1\text{H}\}$ NMR spectra of the L^5UO_2 and $\text{L}^5\text{UO}_2\text{M}$ complexes.	S23
Figure S19. ^1H NMR spectrum of isolated L^6UO_2	S24
Figure S20. ^1H NMR spectrum of <i>in situ</i> generated $\text{L}^6\text{UO}_2\text{Cs}$	S24
Figure S21. $^{19}\text{F}\{^1\text{H}\}$ NMR spectrum of <i>in situ</i> generated $\text{L}^6\text{UO}_2\text{Cs}$	S25
Figure S22. ^1H NMR spectrum of <i>in situ</i> generated $\text{L}^6\text{UO}_2\text{Rb}$	S25
Figure S23. $^{19}\text{F}\{^1\text{H}\}$ NMR spectrum of <i>in situ</i> generated $\text{L}^6\text{UO}_2\text{Rb}$	S26
Figure S24. ^1H NMR spectrum of <i>in situ</i> generated $\text{L}^6\text{UO}_2\text{K}$	S26
Figure S25. $^{19}\text{F}\{^1\text{H}\}$ NMR spectrum of <i>in situ</i> generated $\text{L}^6\text{UO}_2\text{K}$	S27
Figure S26. ^1H NMR spectrum of <i>in situ</i> generated $\text{L}^6\text{UO}_2\text{Na}$	S27
Figure S27. $^{19}\text{F}\{^1\text{H}\}$ NMR spectrum of <i>in situ</i> generated $\text{L}^6\text{UO}_2\text{Na}$	S28
Figure S28. ^1H NMR spectrum of <i>in situ</i> generated $\text{L}^6\text{UO}_2\text{Li}$	S28
Figure S29. $^{19}\text{F}\{^1\text{H}\}$ NMR spectrum of <i>in situ</i> generated $\text{L}^6\text{UO}_2\text{Li}$	S29
Figure S30. ^1H NMR spectrum of isolated $\text{L}^6\text{UO}_2\text{Sr}$	S29
Figure S31. $^{19}\text{F}\{^1\text{H}\}$ NMR spectrum of isolated $\text{L}^6\text{UO}_2\text{Sr}$	S30
Figure S32. ^1H NMR spectrum of <i>in situ</i> generated $\text{L}^6\text{UO}_2\text{Ca}$	S30
Figure S33. $^{19}\text{F}\{^1\text{H}\}$ NMR spectrum of <i>in situ</i> generated $\text{L}^6\text{UO}_2\text{Ca}$	S31
Figure S34. ^1H NMR spectrum of isolated $\text{L}^6\text{UO}_2\text{La}$	S31
Figure S35. $^{19}\text{F}\{^1\text{H}\}$ NMR spectrum of isolated $\text{L}^6\text{UO}_2\text{La}$	S32
Figure S36. Stacked ^1H NMR spectra showing the aromatic and imine region of the L^6UO_2 and $\text{L}^6\text{UO}_2\text{M}$ complexes	S32
Figure S37. Stacked ^1H NMR spectra showing the aliphatic region of the L^6UO_2 and $\text{L}^6\text{UO}_2\text{M}$ complexes	S33
Figure S38. Stacked $^{19}\text{F}\{^1\text{H}\}$ NMR spectra of the L^5UO_2 and $\text{L}^5\text{UO}_2\text{M}$ complexes	S33
 Solid-state Raman Spectroscopy	
Table S1. Solid-state Raman assignments for $\text{L}^5\text{UO}_2\text{M}$ series	S34

Table S2. Solid-state Raman Assignments for L^6UO_2M series	S35
Figure S39. Solid-state Raman spectrum for L^5UO_2	S36
Figure S40. Solid-state Raman spectrum for L^5UO_2Rb	S37
Figure S41. Solid-state Raman spectrum for L^5UO_2K	S38
Figure S42. Solid-state Raman spectrum for L^5UO_2Na	S39
Figure S43. Solid-state Raman spectrum for L^5UO_2Li	S40
Figure S44. Solid-state Raman spectrum for L^5UO_2Sr	S41
Figure S45. Solid-state Raman spectrum for L^6 Ligand	S42
Figure S46. Solid-state Raman spectrum L^6UO_2	S43
Figure S47. Solid-state Raman spectrum for L^6UO_2Rb	S44
Figure S48. Solid-state Raman spectrum for L^6UO_2K	S45
Figure S49. Solid-state Raman spectrum for L^6UO_2Na	S46
Figure S50. Solid-state Raman spectrum for L^6UO_2Li	S47
Figure S51. Solid-state Raman spectrum for L^6UO_2Sr	S48
Figure S52. Solid-state Raman spectrum for L^6UO_2Ca	S49
Figure S53. Solid-state Raman spectrum for L^6UO_2La	S50
Figure S54. Dependence of the U=O symmetric stretching frequency from solid-state Raman spectroscopy of the L^6UO_2M complexes on pK_a of $[M(H_2O)_m]^{n+}$	S51
Solution Raman Spectroscopy	S52
Table S3. Solution-state Raman Assignments for L^6UO_2M series	S52
Figure S55. Fitted solution Raman spectrum for L^6UO_2 in MeCN	S53
Figure S56. Fitted solution Raman spectrum for L^6UO_2Rb in MeCN	S54
Figure S57. Fitted solution Raman spectrum for L^6UO_2K in MeCN	S55
Figure S58. Fitted solution Raman spectrum for L^6UO_2Na in MeCN	S56
Figure S59. Fitted solution Raman spectrum for L^6UO_2Li in MeCN	S57
Figure S60. Fitted solution Raman spectrum for L^6UO_2Sr in MeCN	S58
Figure S61. Fitted solution Raman spectrum for L^6UO_2Ca in MeCN	S59
Figure S62. Fitted solution Raman spectrum for L^6UO_2La in MeCN	S60
Figure S63. Dependence of the U=O symmetric stretching frequency from solution Raman spectroscopy of the L^6UO_2M complexes on pK_a of $[M(H_2O)_m]^{n+}$	S61
Figure S64. Variable concentration solution Raman spectra for L^6UO_2Li in MeCN	S62
Figure S65. Variable concentration fitted solution Raman spectra for L^6UO_2Li in MeCN	S63
Table S4. Fitting parameters for variable concentration solution Raman spectra of L^6UO_2Li in MeCN	S63
Solid-state Infrared Spectroscopy	S64
Figure S66. Fitted mid-IR spectrum for L^6UO_2	S64
Figure S67. Fitted mid-IR spectrum for L^6UO_2Rb	S65

Figure S68. Fitted mid-IR spectrum for L^6UO_2Na	S66
Figure S69. Fitted mid-IR spectrum for L^6UO_2Li	S67
Figure S70. Fitted mid-IR spectrum for L^6UO_2Ca	S68
Figure S71. Fitted mid-IR spectrum for L^6UO_2Sr	S69
Figure S72. Fitted mid-IR spectrum for L^6UO_2La	S70
Solid-state Far Infrared Spectroscopy	S71
Figure S73. Fitted far-IR spectrum for L^6UO_2	S71
Figure S74. Fitted far-IR spectrum for L^6UO_2Sr	S72
Figure S75. Fitted far-IR spectrum for L^6UO_2Rb	S73
Figure S76. Fitted far-IR spectrum for L^6UO_2K	S74
Figure S77. Fitted far-IR spectrum for L^6UO_2Na	S75
Figure S78. Fitted far-IR spectrum for L^6UO_2Li	S76
Figure S79. Fitted far-IR spectrum for L^6UO_2Ca	S77
Electrochemistry	S78
Figure S80. Scan rate dependence data for L^5UO_2	S78
Figure S81. Scan rate dependence data for L^5UO_2Cs	S79
Figure S82. Scan rate dependence data for L^5UO_2Rb	S80
Figure S83. Scan rate dependence data for L^5UO_2K	S81
Figure S84. Scan rate dependence data for L^5UO_2Na	S82
Figure S85. Scan rate dependence data for L^5UO_2Li	S83
Figure S86. Scan rate dependence data for L^5UO_2Ca	S84
Figure S87. Scan rate dependence data for L^6UO_2	S85
Figure S88. Scan rate dependence data for L^6UO_2Cs	S86
Figure S89. Scan rate dependence data for L^6UO_2Rb	S87
Figure S90. Scan rate dependence data for L^6UO_2K	S88
Figure S91. Scan rate dependence data for L^6UO_2Na	S89
Figure S92. Scan rate dependence data for L^6UO_2Li	S90
Figure S93. Scan rate dependence data for L^6UO_2Ca	S91
Figure S94. Plot of $E_{1/2}$ vs. pK_a of $[M(H_2O)_m]^{n+}$ for L^5UO_2M and L^6UO_2M complexes including L^5UO_2Ca and L^6UO_2Ca	S92
Figure S95. Plot of $E_{p,c}$ vs. pK_a of $[M(H_2O)_m]^{n+}$ for L^5UO_2M and L^6UO_2M complexes	S93
Figure S96. Plot of $E_{p,c}$ vs. pK_a of $[M(H_2O)_m]^{n+}$ for L^5UO_2M and L^6UO_2M complexes including L^5UO_2Ca and L^6UO_2Ca	S94
Electrochemical Titrations	S95
Figure S97. Titration of L^6UO_2 with KOTf	S95
Table S5. Metrics for titration of L^6UO_2 with KOTf	S96
Figure S98. Multi-scan cyclic voltammogram of L^6UO_2 with 1 and 10 equiv. of KOTf	S97

Figure S99. Cyclic voltammogram of L^6UO_2 with 10 equiv. of KOTf and KOTf	S97
Figure S100. Titration of L^6UO_2 with NaOTf	S98
Table S6. Metrics for titration of L^6UO_2 with NaOTf	S99
Figure S101. Multi-scan cyclic voltammogram of L^6UO_2 with 1 and 10 equiv. of NaOTf	S100
Figure S102. Cyclic voltammogram of L^6UO_2 with 10 equiv. of NaOTf and NaOTf	S100
Figure S103. Titration of L^6UO_2 with LiOTf (single scan)	S101
Table S7. Metrics for titration of L^6UO_2 with LiOTf (single scan)	S102
Figure S104. Titration of L^6UO_2 with LiOTf	S103
Table S8. Metrics for titration of L^6UO_2 with LiOTf	S104
Figure S105. Multi-scan cyclic voltammogram of L^6UO_2 with 1 and 10 equiv. of LiOTf	S105
Figure S106. Cyclic voltammogram of L^6UO_2 with 10 equiv. of LiOTf and LiOTf	S105
Figure S107. Titration of L^6UO_2 with $Ca(OTf)_2$ (single scan)	S106
Table S9. Metrics for titration of L^6UO_2 with $Ca(OTf)_2$ (single scan)	S107
Figure S108. Titration of L^6UO_2 with $Ca(OTf)_2$	S108
Table S10. Metrics for titration of L^6UO_2 with $Ca(OTf)_2$	S109
Figure S109. Multi-scan cyclic voltammogram of L^6UO_2 with 1 and 10 equiv. of $Ca(OTf)_2$	S110
Figure S110. Cyclic voltammogram of L^6UO_2 with 10 equiv. of $Ca(OTf)_2$ and $Ca(OTf)_2$	S110
Figure S111. Plot of concentration of $M(OTf)_n$ vs. $\Delta E_{1/2}$ for L^6UO_2M	S111
Figure S112. Cyclic voltammograms of L^6UO_2 with 10 equiv. of select $M(OTf)_n$	S112
Figure S113. Cyclic voltammograms of L^6UO_2 with 10 equiv. of all $M(OTf)_n$	S113
NMR Titrations	S114
Figure S114. Titration of L^5UO_2 with CsOTf showing the full region	S114
Figure S115. Titration of L^5UO_2 with CsOTf showing the imine & aromatic region	S114
Figure S116. Titration of L^5UO_2 with CsOTf showing the aliphatic region	S115
Figure S117. Titration of L^5UO_2 with CsOTf showing the -N- CH_3 peak	S115
Figure S118. Titration of L^5UO_2 with RbOTf showing the full region	S116
Figure S119. Titration of L^5UO_2 with RbOTf showing the imine & aromatic region	S116
Figure S120. Titration of L^5UO_2 with RbOTf showing the aliphatic region	S117
Figure S121. Titration of L^5UO_2 with RbOTf showing the -N- CH_3 peak	S117
Figure S122. Titration of L^5UO_2 with KOTf showing the full region	S118
Figure S123. Titration of L^5UO_2 with KOTf showing the imine & aromatic region	S118
Figure S124. Titration of L^5UO_2 with KOTf showing the aliphatic region	S119
Figure S125. Titration of L^5UO_2 with KOTf showing the -N- CH_3 peak	S119
Figure S126. Titration of L^5UO_2 with NaOTf showing the full region	S120
Figure S127. Titration of L^5UO_2 with NaOTf showing the imine & aromatic region	S120

Figure S128. Titration of L^5UO_2 with NaOTf showing the aliphatic region	S121
Figure S129. Titration of L^5UO_2 with NaOTf showing the -N- CH_3 peak	S121
Figure S130. Titration of L^5UO_2 with LiOTf showing the full region	S122
Figure S131. Titration of L^5UO_2 with LiOTf showing the imine & aromatic region	S122
Figure S132. Titration of L^5UO_2 with LiOTf showing the aliphatic region	S123
Figure S133. Titration of L^5UO_2 with LiOTf showing the -N- CH_3 peak	S123
Figure S134. Titration of L^5UO_2 with $Ca(OTf)_2$ showing the full region	S124
Figure S135. Titration of L^5UO_2 with $Ca(OTf)_2$ showing the imine & aromatic region	S124
Figure S136. Titration of L^5UO_2 with $Ca(OTf)_2$ showing the aliphatic region	S125
Figure S137. Titration of L^5UO_2 with $Ca(OTf)_2$ showing the -N- CH_3 peak	S125
Figure S138. Titration of L^6UO_2 with CsOTf showing the full region	S126
Figure S139. Titration of L^6UO_2 with CsOTf showing the imine & aromatic region	S126
Figure S140. Titration of L^6UO_2 with CsOTf showing the aliphatic region	S127
Figure S141. Titration of L^6UO_2 with CsOTf showing the -N- CH_3 peak	S127
Figure S142. Titration of L^6UO_2 with RbOTf showing the full region	S128
Figure S143. Titration of L^6UO_2 with RbOTf showing the imine & aromatic region	S128
Figure S144. Titration of L^6UO_2 with RbOTf showing the aliphatic region	S129
Figure S145. Titration of L^6UO_2 with RbOTf showing the -N- CH_3 peak	S129
Figure S146. Titration of L^6UO_2 with KOTf showing the full region	S130
Figure S147. Titration of L^6UO_2 with KOTf showing the imine & aromatic region	S130
Figure S148. Titration of L^6UO_2 with KOTf showing the aliphatic region	S131
Figure S149. Titration of L^6UO_2 with KOTf showing the -N- CH_3 peak	S131
Figure S150. Titration of L^6UO_2 with NaOTf showing the full region	S132
Figure S151. Titration of L^6UO_2 with NaOTf showing the imine & aromatic region	S132
Figure S152. Titration of L^6UO_2 with NaOTf showing the aliphatic region	S133
Figure S153. Titration of L^6UO_2 with NaOTf showing the -N- CH_3 peak	S133
Figure S154. Titration of L^6UO_2 with LiOTf showing the full region	S134
Figure S155. Titration of L^6UO_2 with LiOTf showing the imine & aromatic region	S134
Figure S156. Titration of L^6UO_2 with LiOTf showing the aliphatic region	S135
Figure S157. Titration of L^6UO_2 with LiOTf showing the -N- CH_3 peak	S135
Figure S158. Titration of L^6UO_2 with $Ca(OTf)_2$ showing the full region	S136
Figure S159. Titration of L^6UO_2 with $Ca(OTf)_2$ showing the imine & aromatic region	S136
Figure S160. Titration of L^6UO_2 with $Ca(OTf)_2$ showing the aliphatic region	S137
Figure S161. Titration of L^6UO_2 with $Ca(OTf)_2$ showing the -N- CH_3 peak	S137
Figure S162. Titration studies of monovalent metal ions with L^5UO_2 and L^6UO_2	S138
Figure S163. Stacked 1H NMR spectra of L^6UO_2 over five hours	S139
Table S11. Chemical shift of -N- CH_3 group at varied time intervals	S139

Evaluation of the heterogeneous electron transfer rate, k^0	S140
---	-------------

X-Ray Crystallography	S141
<i>Refinement Details</i>	S141
Special Refinement Details for BaPenta (q55j)	S143
Figure S164. Solid-state structure of the first dimeric unit of BaPenta	S143
Figure S165. Solid-state structure of the second dimeric unit of BaPenta	S144
Figure S166. Full solid-state asymmetric unit for BaPenta	S145
Figure S167. Solid-state structure of BaHexa	S146
Figure S168. Solid-state structure comparison for BaPenta and BaHexa	S147
Table S12. Comparison of selected structural parameters in Ba complexes	S148
Special Refinement Details for L⁵UO₂ (q75k)	S149
Figure S169. Solid-state structure of L⁵UO₂	S149
Figure S170. Solid-state structure of L⁵UO₂ , showing amine backbone disorder	S151
Figure S171. Views of the solid-state structure of L⁵UO₂ showing co-crystallized CH ₃ CN	S151
Figure S172. Full solid-state asymmetric unit for L⁵UO₂	S152
Table S13. Comparison of selected structural parameters of L⁵UO₂ with the previously published structure	S154
Figure S173. Solid-state structure comparison for L⁵UO₂ and L⁶UO₂	S155
Table S14. Comparison of selected structural parameters in monometallic UO ₂ ²⁺ complexes	S156
Special Refinement Details for L⁵UO₂Na (q50k)	S157
Figure S177. Solid-state structure of L⁵UO₂Na	S158
Figure S178. Full solid-state asymmetric unit for L⁵UO₂Na	S158
Special Refinement Details for L⁵UO₂Na' (v16f)	S159
Figure S174. Solid-state structure of L⁵UO₂ Na'	S159
Figure S175. Solid-state structure of L⁵UO₂ Na' , showing amine backbone disorder	S160
Figure S176. Full solid-state asymmetric unit for L⁵UO₂ Na'	S161
Special Refinement Details for L⁵UO₂Na-DCE (q49k)	S162
Figure S179. Solid-state structure of L⁵UO₂Na-DCE	S162
Figure S180. Solid-state structure of L⁵UO₂Na-DCE showing amine backbone disorder	S163
Figure S181. Full solid-state asymmetric unit for L⁵UO₂Na-DCE	S164
Special Refinement Details for L⁵UO₂Na-MeCN (q56k)	S165
Figure S182. Solid-state structure of L⁵UO₂Na-MeCN	S165
Figure S183. Full solid-state asymmetric unit for L⁵UO₂Na-MeCN	S166
Figure S184. Superimposed view of the structures of L⁵UO₂Na and L⁵UO₂Na-DCE	S167
Figure S185. Superimposed view of the structures of L⁵UO₂Na and L⁵UO₂Na-MeCN	S168
Table S15. Comparison of selected structural parameters in [UO ₂ ,Na] complexes	S169
Special Refinement Details for L⁵UO₂Li (ak2133c)	S170
Figure S186. Solid-state structure of L⁵UO₂Li	S171
Figure S187. Solid-state structure of L⁵UO₂Li showing amine backbone disorder	S172
Figure S188. Full solid-state asymmetric unit for L⁵UO₂Li	S173
Special Refinement Details for L⁶UO₂Li (ak2152c)	S174

Figure S189. Solid-state structure of L^6UO_2Li at 50% probability level	S174
Figure S190. Solid-state structure of L^6UO_2Li at 20% probability level	S175
Figure S191. Solid-state structure of L^6UO_2Li dimer generated by symmetry	S176
Figure S192. Full solid-state asymmetric unit for L^6UO_2Li	S177
Special Refinement Details for L^5UO_2Ca (ak2153g)	S178
Figure S193. Solid-state structure of L^5UO_2Ca	S178
Figure S194. Full solid-state asymmetric unit for L^5UO_2Ca	S179
Special Refinement Details for L^5UO_2Ca' (ak2153n-No33)	S180
Figure S195. Solid-state structure of L^5UO_2Ca'	S181
Figure S196. Solid-state structure of the full asymmetric unit of L^5UO_2Ca'	S182
Figure S197. Solid-state asymmetric unit for L^5UO_2Ca'	S183
Figure S198. Solid-state structure of the full molecule for L^5UO_2Ca' showing end-to-end view to highlight the symmetric nature of the molecule	S184
Figure S199. Superimposed view of the structures of L^5UO_2Ca and L^5UO_2Ca'	S185
Table S16. Comparison of selected structural parameters in $[UO_2,Ca]$ complexes	S186
Table S17. Comparison of $U-O_{oxo}$ bond lengths	S187
Table S18. Crystal and Refinement Data for BaPenta and L^5UO_2	S188
Table S19. Crystal and Refinement Data for L^5UO_2Na and L^5UO_2Na'	S189
Table S20. Crystal and Refinement Data for $L^5UO_2Na-DCE$ & $L^5UO_2Na-MeCN$	S190
Table S21. Crystal and Refinement Data for L^5UO_2Li and L^6UO_2Li	S191
Table S22. Crystal and Refinement Data for L^5UO_2Ca and L^5UO_2Ca'	S192
References	S193

Experimental Section

General Considerations

All manipulations were carried out in dry N₂-filled gloveboxes (Vacuum Atmospheres Co., Hawthorne, CA) or under N₂ atmosphere using standard Schlenk techniques unless otherwise noted. All solvents were of commercial grade and dried over activated alumina using a PPT Glass Contour (Nashua, NH) solvent purification system prior to use, and were stored over molecular sieves. All chemicals were from major commercial suppliers and used as received or after extensive drying. Deuterated NMR solvents were purchased from Cambridge Isotope Laboratories (Tewksbury, MA, USA). ¹H and ¹⁹F NMR spectra were collected on a 400 MHz Bruker spectrometer (Bruker, Billerica, MA, USA) and referenced to the residual protio-solvent signal¹ in the case of ¹H. ¹⁹F NMR spectra were referenced and reported relative to CCl₃F as external standards following the recommended scale based on ratios of absolute frequencies (Ξ).^{2,3} Chemical shifts (δ) are reported in units of ppm and coupling constants (J) are reported in Hz. All experiments were conducted at room temperature (298 K).

Regarding special safety precautions needed for this work, depleted uranium is a weak alpha-particle emitter; all manipulations of U-containing materials should be carried out in a laboratory equipped with appropriate radiation safety protocols.

Electrochemical Methods

Electrochemical experiments were carried out in a N₂-filled glovebox in dry, degassed CH₃CN. 0.10 M tetra(*n*-butylammonium) hexafluorophosphate ([ⁿBu₄N]⁺[PF₆]⁻; Sigma-Aldrich, electrochemical grade) served as the solvent and supporting electrolyte. Measurements were carried out with a Gamry Reference 600+ Potentiostat/Galvanostat (Gamry Instruments, Warminster, PA, USA), using a standard three-electrode configuration. The working electrode was the basal plane of highly oriented pyrolytic graphite (HOPG) (GraphiteStore.com, Buffalo Grove, Ill.; surface area: 0.09 cm²), the counter electrode was a platinum wire (Kurt J. Lesker, Jefferson Hills, PA; 99.99%, 0.5 mm diameter), and a silver wire immersed in electrolyte served as a pseudo reference electrode (CH Instruments). The reference was separated from the working solution by a Vycor frit (Bioanalytical Systems, Inc., West Lafayette, IN, USA). Ferrocene (Sigma Aldrich, St. Louis, MO, USA; twice-sublimed) was added to the electrolyte solution prior to the beginning of each experiment; the midpoint potential of the ferrocenium/ferrocene couple (denoted as Fc⁺⁰) served as an external standard for comparison of the recorded potentials. Concentrations of analytes for cyclic voltammetry were typically 1 mM unless otherwise noted. Experiments were conducted by first scanning cathodically, then anodically on the return sweep.

Vibrational Analysis

Raman spectra of single crystals were collected on a Renishaw inVia Raman microscope with a Raman microscope enclosure, equipped with a 785 nm laser and a 1200 mm grating. The maximum operating power is 200 mW (laser power at 100%). WiRE 3.4 served as the operating software utilized to collect all raw data and spectra. Each sample was placed under a confocal microscope, and the surface was focused on at 50x magnification. Incremental scans were used to evaluate the optimal laser power and integration time for each sample, where signal to noise was considered and the integrity of the material. Each spectrum was collected with an accumulation of three scans and a pinhole aperture resulting in a laser width of three micrometers. Infrared (IR) spectra of single crystals were collected on a Bruker VERTEX 70v instrument using a platinum ATR microscope objective and the OPUS 8.5 software package. The resolution was 0.4 cm^{-1} in the mid-IR region ($4000 - 400\text{ cm}^{-1}$) and 1 cm^{-1} in the FIR region ($400 - 100\text{ cm}^{-1}$). Background scans were collected ahead of measurements on each sample and IR data were collected using half the number of scans used for background scanning.

Spectral analysis (baseline, peak fitting, and determination of the full-width half-max) for Raman and IR data for spectral windows of $1100 - 550\text{ cm}^{-1}$ (Raman), $1000 - 700\text{ cm}^{-1}$ (mid-IR), and $350 - 150\text{ cm}^{-1}$ (far-IR) were done in OriginPro version 2021b (9.8.5.204). Peak fittings were done using Lorentzian or Gaussian functions and refined until a convergence of 1×10^{-6} was reached.

Synthesis and Characterization

Complexes **BaHexa** and **L⁶UO₂** were prepared according to literature procedures, while complexes **BaPenta** and **L⁵UO₂** were prepared following literature procedures used for the preparation of **BaHexa** and **L⁶UO₂**, respectively.⁴ Spectroscopic characterizations of **BaPenta** and **L⁵UO₂** by NMR (Figures S1-S3) confirmed preparation of the desired compounds. Crystals suitable for X-ray diffraction were obtained by vapor diffusion of diethyl ether into a CH₃CN solution of **L⁵UO₂** and by vapor diffusion of diethyl ether into a CH₃OH solution of **BaPenta**. Crystals for **L⁵UO₂** could also be grown using by vapor diffusion of diethyl ether into a CH₂Cl₂ solution of the complex; this solvent system was used for bulk recrystallization in order to prepare a sample for elemental analysis. **BaPenta**, when dissolved in CD₃CN, contains complex peaks in the ¹H NMR suggesting different conformers of the complex in CD₃CN. This is also evident from the sandwiching nature of the **BaPenta** (*vide infra*) in solid-state.

BaPenta. ¹H NMR (400 MHz, CD₃CN) δ 13.59 (bs, 3H), 8.28 (d, J = 13.3 Hz, 2H), 8.16 (d, J = 12.9 Hz, 1H), 6.97 – 6.73 (m, 6H), 6.44 (t, J = 7.9 Hz, 2H), 6.36 (t, J = 7.9 Hz, 1H), 4.22 (t, J = 4.7 Hz, 6H), 4.12 – 3.90 (m, 7H), 3.88 – 3.72 (m, 7H), 3.63 (dd, J = 6.4, 5.3 Hz, 2H), 2.79 – 2.66 (m, 6H), 2.47 (d, J = 11.7 Hz, 2H), 2.32 (s, 3H), 2.15 (s, 1H). ¹⁹F{¹H} NMR (376 MHz, CD₃CN): δ –80.10.

L⁵UO₂. ¹H NMR (500 MHz, CD₃CN) δ 9.50 (dd, ⁴ $J_{H,H}$ = 2.1 Hz, ⁴ $J_{H,H}$ = 1.1 Hz, 2H), 7.19 (dd, ³ $J_{H,H}$ = 7.8 Hz, ⁴ $J_{H,H}$ = 1.6 Hz, 2H), 7.15 (dd, ³ $J_{H,H}$ = 7.9 Hz, ⁴ $J_{H,H}$ = 1.6 Hz, 2H), 6.66 (t, ³ $J_{H,H}$ = 7.8 Hz, 2H), 5.13 – 5.01 (m, 2H), 4.59 – 4.51 (m, 2H), 4.22 – 4.17 (m, 4H), 4.09 – 4.04 (m, 4H), 3.90 (td, ³ $J_{H,H}$ = 13.2, ⁴ $J_{H,H}$ = 4.6 Hz, 2H), 3.62 – 3.56 (m, 2H), 3.23 (s, 3H). Anal. Calcd for C₂₃H₂₇N₃O₇U (**L⁵UO₂**): C 39.72, H 3.91, N 6.04; Found: C 38.31, H 3.47, N 5.57. Calcd for C₂₃H₂₇N₃O₇U + 0.5 CH₂Cl₂: C 38.25, H 3.82, N 5.69. This analysis is consistent with the observation of CH₂Cl₂ in the ¹H NMR spectrum (Figure S3) for **L⁵UO₂**, which was incorporated during crystallization of the compound. Cyclic Voltammetry (0.1 M [ⁿBu₄N]⁺[PF₆][–] in CH₃CN): $E_{1/2}$ = –1.57 V vs. Fc⁺⁰.

We also confirmed the formulation of the previously reported **L⁶UO₂** by elemental analysis (EA) to provide additional evidence for the purity and composition of the synthesized complexes.

Anal. Calcd for C₂₅H₃₁N₃O₈U (**L⁶UO₂**): C 40.60, H 4.23, N 5.68; Found: C 40.63, H 3.96, N 5.38.

In situ NMR scale preparation of L⁵UO₂M complexes. In a J-young NMR tube under an inert atmosphere, a solution of **L⁵UO₂** in CD₃CN was added to 1 equiv. of corresponding metal salt solution in CD₃CN. The contents in the tube were mixed by vigorously shaking the tube, and the solution was left to equilibrate for 5 min before recording the ¹H and ¹⁹F{¹H} NMR (Figures S4-S18). Crystals suitable for X-ray diffraction were obtained by vapor diffusion of diethyl ether into a CH₃CN solution of the **L⁵UO₂M** (M = K, Na, Li) complexes.

L⁵UO₂Cs. ¹H NMR (500 MHz, CD₃CN): δ 9.52 (dd, ⁴ $J_{H,H}$ = 2.1 Hz, ⁴ $J_{H,H}$ = 1.0 Hz, 2H), 7.23 (dd, ³ $J_{H,H}$ = 7.9 Hz, ⁴ $J_{H,H}$ = 1.6 Hz, 2H), 7.20 (dd, ³ $J_{H,H}$ = 7.9 Hz, ⁴ $J_{H,H}$ = 1.6 Hz, 2H), 6.72 (t, ³ $J_{H,H}$ =

7.9 Hz, 2H), 5.14 – 5.03 (m, 2H), 4.62 – 4.52 (m, 2H), 4.23 – 4.15 (m, 4H), 4.04 – 3.96 (m, 4H), 3.89 (td, $^3J_{\text{H,H}} = 13.2$ Hz, $^4J_{\text{H,H}} = 4.5$ Hz, 2H), 3.68 – 3.60 (m, 2H), 3.26 (s, 3H). $^{19}\text{F}\{^1\text{H}\}$ NMR (471 MHz, CD_3CN): $\delta -80.22$. Cyclic Voltammetry (0.1 M $[\text{nBu}_4\text{N}]^+[\text{PF}_6]^-$ in CH_3CN): $E_{1/2} = -1.40$ V vs. $\text{Fc}^{+/0}$.

$\text{L}^5\text{UO}_2\text{Rb}$. ^1H NMR (500 MHz, CD_3CN): δ 9.52 (dd, $^4J_{\text{H,H}} = 2.1$ Hz, $^4J_{\text{H,H}} = 1.1$ Hz, 2H), 7.28 (dd, $^3J_{\text{H,H}} = 7.9$ Hz, $^4J_{\text{H,H}} = 1.5$ Hz, 2H), 7.22 (dd, $^3J_{\text{H,H}} = 7.9$ Hz, $^4J_{\text{H,H}} = 1.6$ Hz, 2H), 6.74 (t, $^3J_{\text{H,H}} = 7.9$ Hz, 2H), 5.16 – 5.05 (m, 2H), 4.62 – 4.53 (m, 2H), 4.31 – 4.19 (m, 4H), 4.08 – 4.01 (m, 4H), 3.90 (td, $^3J_{\text{H,H}} = 13.2$ Hz, $^4J_{\text{H,H}} = 4.5$ Hz, 2H), 3.70 – 3.61 (m, 2H), 3.27 (s, 3H). $^{19}\text{F}\{^1\text{H}\}$ NMR (471 MHz, CD_3CN): $\delta -80.22$. Cyclic Voltammetry (0.1 M $[\text{nBu}_4\text{N}]^+[\text{PF}_6]^-$ in CH_3CN): $E_{1/2} = -1.40$ V vs. $\text{Fc}^{+/0}$.

$\text{L}^5\text{UO}_2\text{K}$. ^1H NMR (500 MHz, CD_3CN) δ 9.52 (dd, $^4J_{\text{H,H}} = 2.1$ Hz, $^4J_{\text{H,H}} = 1.1$ Hz, 2H), 7.31 (dd, $^3J_{\text{H,H}} = 7.9$, $^4J_{\text{H,H}} = 1.6$ Hz, 2H), 7.23 (dd, $^3J_{\text{H,H}} = 7.9$, $^4J_{\text{H,H}} = 1.6$ Hz, 2H), 6.76 (t, $^3J_{\text{H,H}} = 7.9$ Hz, 2H), 5.17 – 5.05 (m, 2H), 4.64 – 4.54 (m, 2H), 4.36 – 4.24 (m, 4H), 4.12 – 4.02 (m, 4H), 3.91 (td, $^3J_{\text{H,H}} = 13.2$ Hz, $^4J_{\text{H,H}} = 4.6$ Hz, 2H), 3.70 – 3.62 (m, 2H), 3.28 (s, 3H). $^{19}\text{F}\{^1\text{H}\}$ NMR (471 MHz, CD_3CN): $\delta -80.22$. Cyclic Voltammetry (0.1 M $[\text{nBu}_4\text{N}]^+[\text{PF}_6]^-$ in CH_3CN): $E_{1/2} = -1.37$ V vs. $\text{Fc}^{+/0}$.

$\text{L}^5\text{UO}_2\text{Na}$. ^1H NMR (500 MHz, CD_3CN) δ 9.52 (dd, $^4J_{\text{H,H}} = 2.1$ Hz, $^4J_{\text{H,H}} = 1.1$ Hz, 2H), 7.36 (dd, $^3J_{\text{H,H}} = 7.9$ Hz, $^4J_{\text{H,H}} = 1.6$ Hz, 2H), 7.28 (dd, $^3J_{\text{H,H}} = 7.9$ Hz, $^4J_{\text{H,H}} = 1.5$ Hz, 2H), 6.82 (t, $^3J_{\text{H,H}} = 7.9$ Hz, 2H), 5.21 – 5.10 (m, 2H), 4.66 – 4.57 (m, 2H), 4.39 – 4.34 (m, 4H), 4.15 – 4.10 (m, 4H), 3.96 (td, $^3J_{\text{H,H}} = 13.3$ Hz, $^4J_{\text{H,H}} = 4.5$ Hz, 2H), 3.75 – 3.69 (m, 2H), 3.34 (s, 3H). $^{19}\text{F}\{^1\text{H}\}$ NMR (471 MHz, CD_3CN): $\delta -80.21$. Cyclic Voltammetry (0.1 M $[\text{nBu}_4\text{N}]^+[\text{PF}_6]^-$ in CH_3CN): $E_{1/2} = -1.27$ V vs. $\text{Fc}^{+/0}$.

$\text{L}^5\text{UO}_2\text{Li}$. ^1H NMR (500 MHz, CD_3CN) δ 9.50 (dd, $^4J_{\text{H,H}} = 2.0$ Hz, $^4J_{\text{H,H}} = 1.0$ Hz, 2H), 7.34 (dd, $^3J_{\text{H,H}} = 7.9$ Hz, $^4J_{\text{H,H}} = 1.6$ Hz, 2H), 7.27 (dd, $^3J_{\text{H,H}} = 8.0$ Hz, $^4J_{\text{H,H}} = 1.5$ Hz, 2H), 6.82 (t, $^3J_{\text{H,H}} = 7.9$ Hz, 2H), 5.21 – 5.10 (m, 2H), 4.66 – 4.58 (m, 2H), 4.40 – 4.31 (m, 4H), 4.17 – 4.05 (m, 4H), 3.96 (td, $^3J_{\text{H,H}} = 13.2$ Hz, $^4J_{\text{H,H}} = 4.5$ Hz, 2H), 3.77 – 3.69 (m, 2H), 3.35 (s, 3H). $^{19}\text{F}\{^1\text{H}\}$ NMR (471 MHz, CD_3CN): $\delta -80.19$. Cyclic Voltammetry (0.1 M $[\text{nBu}_4\text{N}]^+[\text{PF}_6]^-$ in CH_3CN): $E_{1/2} = -1.25$ V vs. $\text{Fc}^{+/0}$.

$\text{L}^5\text{UO}_2\text{Ca}$. ^1H NMR (500 MHz, CD_3CN) δ 9.56 (s, 2H), 7.52 (d, $^3J_{\text{H,H}} = 8.0$ Hz, 2H), 7.42 (d, $^3J_{\text{H,H}} = 7.9$ Hz, 2H), 6.97 (t, $^3J_{\text{H,H}} = 8.0$ Hz, 2H), 5.23 – 5.13 (m, 2H), 4.77 – 4.68 (m, 2H), 4.61 – 4.49 (m, 4H), 4.30 – 4.18 (m, 4H), 4.01 (td, $^3J_{\text{H,H}} = 13.2$ Hz, $^4J_{\text{H,H}} = 4.7$ Hz, 2H), 3.78 (dd, $^3J_{\text{H,H}} = 12.8$ Hz, $^4J_{\text{H,H}} = 4.0$ Hz, 2H), 3.38 (s, 3H). $^{19}\text{F}\{^1\text{H}\}$ NMR (471 MHz, CD_3CN): $\delta -80.18$. Cyclic Voltammetry (0.1 M $[\text{nBu}_4\text{N}]^+[\text{PF}_6]^-$ in CH_3CN): $E_{1/2} = -0.83$ V vs. $\text{Fc}^{+/0}$.

***In situ* NMR scale preparation of $\text{L}^6\text{UO}_2\text{M}$ complexes.** In a J-young NMR tube under an inert atmosphere, a solution of L^6UO_2 in CD_3CN was added to 1 equiv. of corresponding metal salt solution in CD_3CN . The contents in the tube were mixed by vigorously shaking the tube, and the solution was left to equilibrate for 5 min before recording the ^1H and $^{19}\text{F}\{^1\text{H}\}$ NMR (Figures S20-

S29, S32-S33, and S36-S38). All the L^6UO_2M complexes, when dissolved in CD_3CN , contain two conformers in a 3:1 ratio, as determined by the integration of peaks in the 1H NMR. L^6UO_2Sr and L^6UO_2La for spectroscopic studies were synthesized using the respective triflate salts, using previously reported procedures (Figures S30-S31 and S34-S35).⁴

L^6UO_2Cs . 1H NMR (500 MHz, CD_3CN) δ 9.56 (t, $J = 1.5$ Hz, 2H), 9.42 – 9.32 (s, 0.7H), 7.33 (dd, $J = 8.0, 1.6$ Hz, 2H), 7.24 (dd, $J = 7.9, 1.6$ Hz, 2H), 7.18 (dt, $J = 7.9, 1.8$ Hz, 0.7H), 6.97 (d, $J = 7.6$ Hz, 0.5H), 6.76 (t, $J = 7.9$ Hz, 2H), 6.64 (td, $J = 7.8, 4.1$ Hz, 0.7H), 5.08 – 4.88 (m, 3H), 4.64 – 4.30 (m, 7H), 4.07 – 3.46 (m, 18H), 3.21 (s, 3H), 3.16 (s, 1H). $^{19}F\{^1H\}$ NMR (471 MHz, CD_3CN): δ –80.21. Cyclic Voltammetry (0.1 M $[^nBu_4N]^+[PF_6]^-$ in CH_3CN): $E_{1/2} = -1.38$ V vs. $Fc^{+/0}$.

L^6UO_2Rb . 1H NMR (500 MHz, CD_3CN) δ 9.56 (t, $J = 1.5$ Hz, 2H), 9.42 – 9.32 (m, 0.66H), 7.33 (dd, $J = 8.0, 1.6$ Hz, 2H), 7.27 – 7.15 (m, 3.5H), 6.96 (d, $J = 7.6$ Hz, 1H), 6.76 (t, $J = 7.9$ Hz, 2H), 6.64 (td, $J = 7.8, 4.1$ Hz, 1H), 5.09 – 4.87 (m, 3H), 4.64 – 4.53 (m, 2H), 4.51 – 4.30 (m, 5H), 4.07 – 3.46 (m, 18H), 3.21 (s, 4H). $^{19}F\{^1H\}$ NMR (471 MHz, CD_3CN): δ –80.21. Cyclic Voltammetry (0.1 M $[^nBu_4N]^+[PF_6]^-$ in CH_3CN): $E_{1/2} = -1.37$ V vs. $Fc^{+/0}$.

L^6UO_2K . 1H NMR (500 MHz, CD_3CN) δ 9.56 (t, $J = 1.5$ Hz, 2H), 9.47 – 9.43 (m, 0.7H), 7.35 (dd, $J = 8.0, 1.6$ Hz, 2H), 7.28 – 7.15 (m, 3.5H), 6.78 (t, $J = 7.9$ Hz, 2H), 6.62 (t, $J = 7.8$ Hz, 0.7H), 5.07 – 4.93 (m, 3H), 4.65 – 4.48 (m, 3H), 4.46 – 4.29 (m, 6H), 4.03 – 3.54 (m, 18H), 3.02 (s, 3H), 3.19 – 3.12 (m, 1H). $^{19}F\{^1H\}$ NMR (471 MHz, CD_3CN): δ –80.21. Cyclic Voltammetry (0.1 M $[^nBu_4N]^+[PF_6]^-$ in CH_3CN): $E_{1/2} = -1.36$ V vs. $Fc^{+/0}$.

L^6UO_2Na . 1H NMR (500 MHz, CD_3CN) δ 9.53 (t, $J = 1.5$ Hz, 2H), 9.50 (s, 0.7H), 7.40 (dd, $J = 7.9, 1.6$ Hz, 2H), 7.32 – 7.20 (m, 3.5H), 6.80 (t, $J = 7.9$ Hz, 2H), 6.72 (t, $J = 7.9$ Hz, 0.7H), 5.12 – 4.98 (m, 3H), 4.67 – 4.52 (m, 3H), 4.48 – 4.34 (m, 6H), 3.99 – 3.59 (m, 18H), 3.27 (s, 3H), 3.24 – 3.21 (m, 1H). $^{19}F\{^1H\}$ NMR (471 MHz, CD_3CN): δ –80.20. Cyclic Voltammetry (0.1 M $[^nBu_4N]^+[PF_6]^-$ in CH_3CN): $E_{1/2} = -1.35$ V vs. $Fc^{+/0}$.

L^6UO_2Li . 1H NMR (500 MHz, CD_3CN) δ 9.51 (dd, $J = 2.0, 1.0$ Hz, 2H), 9.47 (s, 0.7H), 7.43 (dd, $J = 7.9, 1.6$ Hz, 2H), 7.33 (dd, $J = 7.9, 1.6$ Hz, 3H), 7.26 (dd, $J = 7.9, 1.6$ Hz, 0.7H), 6.81 (t, $J = 7.9$ Hz, 2H), 6.73 (t, $J = 7.8$ Hz, 0.7H), 5.21 – 5.02 (m, 3H), 4.67 – 4.45 (m, 8H), 4.02 – 3.63 (m, 17H), 3.33 (s, 3H), 3.29 – 3.22 (m, 1H). $^{19}F\{^1H\}$ NMR (471 MHz, CD_3CN): δ –80.23. Cyclic Voltammetry (0.1 M $[^nBu_4N]^+[PF_6]^-$ in CH_3CN): $E_{1/2} = -1.23$ V vs. $Fc^{+/0}$.

L^6UO_2Sr . 1H NMR (500 MHz, CD_3CN) δ 9.59 (s, 2H), 7.47 (d, $J = 8.0$ Hz, 2H), 7.38 (d, $J = 7.8$ Hz, 2H), 6.94 (t, $J = 7.9$ Hz, 2H), 5.04 (ddd, $J = 16.4, 13.7, 4.3$ Hz, 2H), 4.68 (dd, $J = 15.3, 5.0$ Hz, 2H), 4.50 (t, $J = 4.6$ Hz, 4H), 4.15 (q, $J = 3.7$ Hz, 4H), 4.01 (s, 4H), 3.97 (dt, $J = 13.0, 6.4$ Hz, 2H), 3.81 – 3.74 (m, 2H), 3.30 (s, 3H). $^{19}F\{^1H\}$ NMR (471 MHz, CD_3CN): δ –80.15.

L^6UO_2Ca . 1H NMR (500 MHz, CD_3CN) δ 9.56 (s, 2H), 9.48 (s, 0.6H), 7.47 (dd, $J = 8.0, 1.6$ Hz, 2H), 7.39 (dd, $J = 7.8, 1.5$ Hz, 2H), 7.35 – 7.25 (m, 1H), 6.95 (t, $J = 7.9$ Hz, 2H), 6.79 (t, $J = 7.9$ Hz, 0.5H), 5.14 – 4.98 (m, 3H), 4.69 (dd, $J = 15.5, 4.9$ Hz, 2H), 4.63 – 4.46 (m, 6H), 4.20 – 3.95 (m, 13H), 3.89 – 3.76 (m, 3H), 3.66 (d, $J = 12.9$ Hz, 0.7H), 3.34 (s, 3H), 3.17 (s,

1H). $^{19}\text{F}\{^1\text{H}\}$ NMR (471 MHz, CD_3CN): δ -80.16. Cyclic Voltammetry (0.1 M [$^n\text{Bu}_4\text{N}^+$][PF_6^-] in CH_3CN): $E_{1/2} = -0.88$ V vs. $\text{Fc}^{+/0}$.

L⁶UO₂La. ^1H NMR (500 MHz, CD_3CN) δ 9.64 (s, 2H), 7.54 (d, $J = 8.2$ Hz, 2H), 7.49 (d, $J = 7.7$ Hz, 2H), 7.09 (t, $J = 8.0$ Hz, 2H), 5.11 – 5.01 (m, 2H), 4.76 (dd, $J = 15.3, 5.1$ Hz, 2H), 4.71 (d, $J = 5.2$ Hz, 4H), 4.41 (t, $J = 4.9$ Hz, 4H), 4.32 (s, 4H), 4.01 (dt, $J = 12.9, 6.5$ Hz, 2H), 3.92 – 3.86 (m, 2H), 3.35 (s, 3H). $^{19}\text{F}\{^1\text{H}\}$ NMR (471 MHz, CD_3CN): δ -80.07.

NMR Spectra

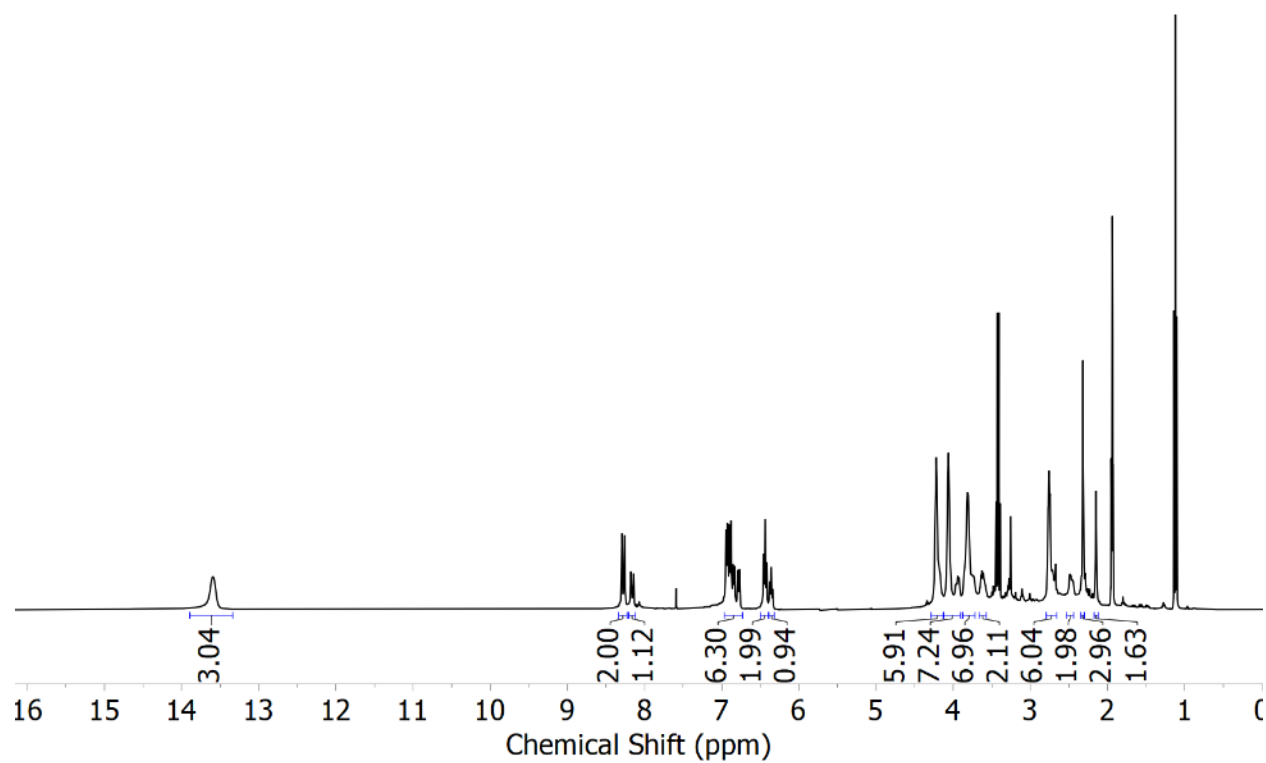


Figure S1. ^1H NMR spectrum (400 MHz, CD_3CN) of **BaPenta**.

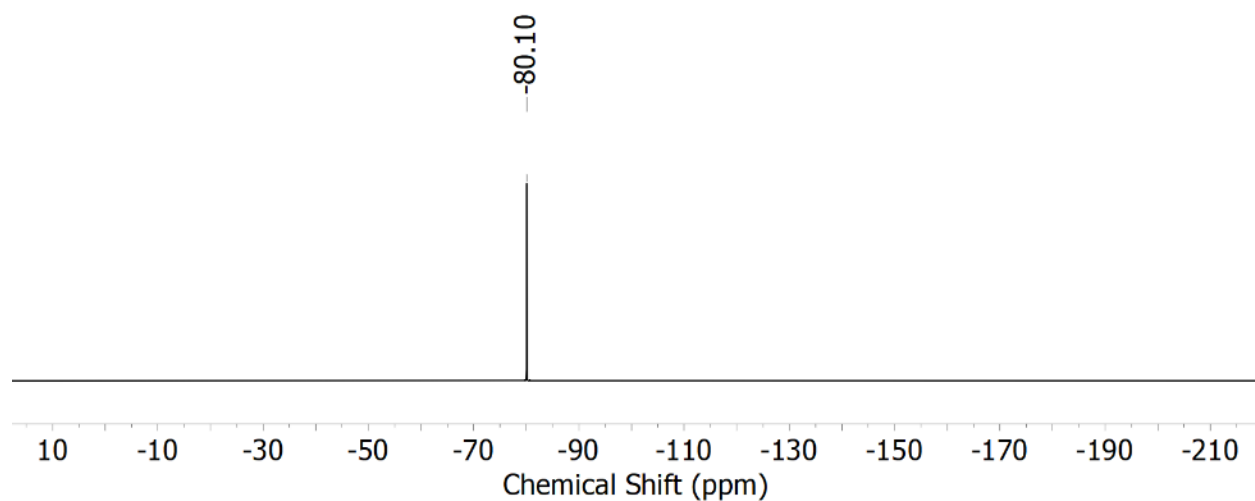


Figure S2. $^{19}\text{F}\{^1\text{H}\}$ NMR spectrum (376 MHz, CD_3CN) of **BaPenta**.

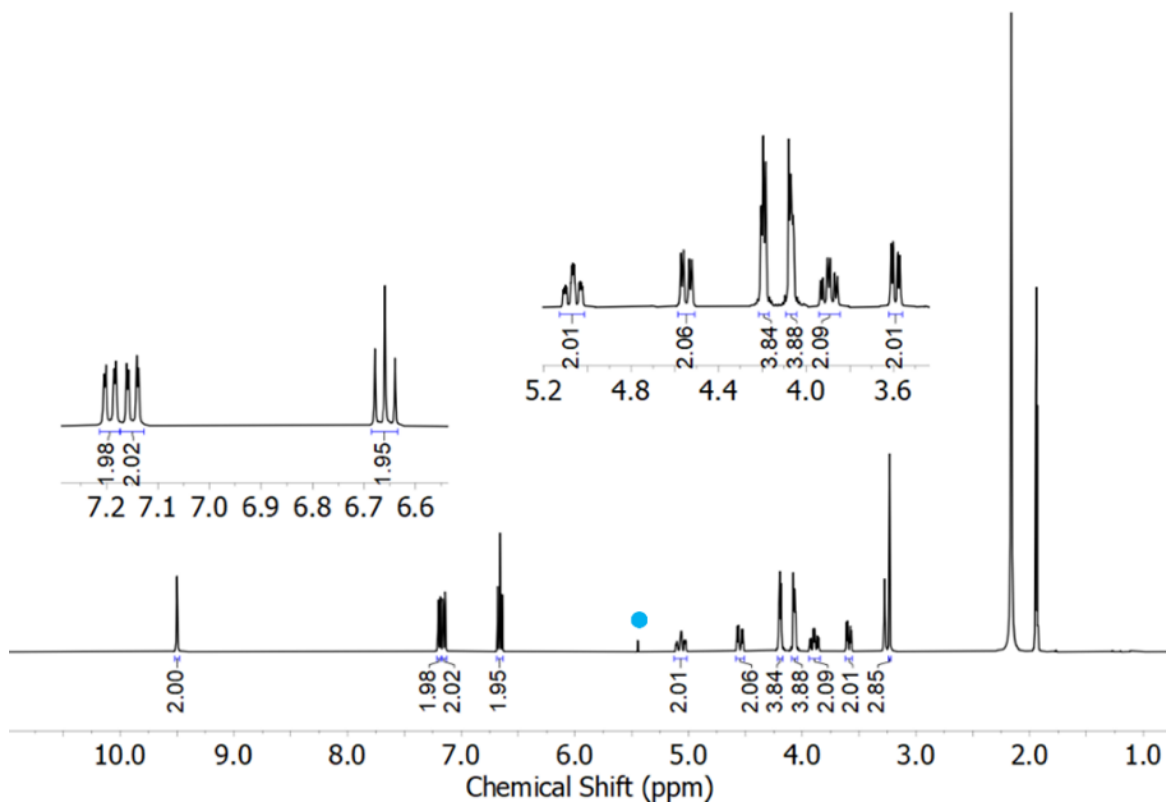


Figure S3. ^1H NMR spectrum (500 MHz, CD_3CN) of L^5UO_2 . The blue dot indicates the peak associated with the dichloromethane solvent.

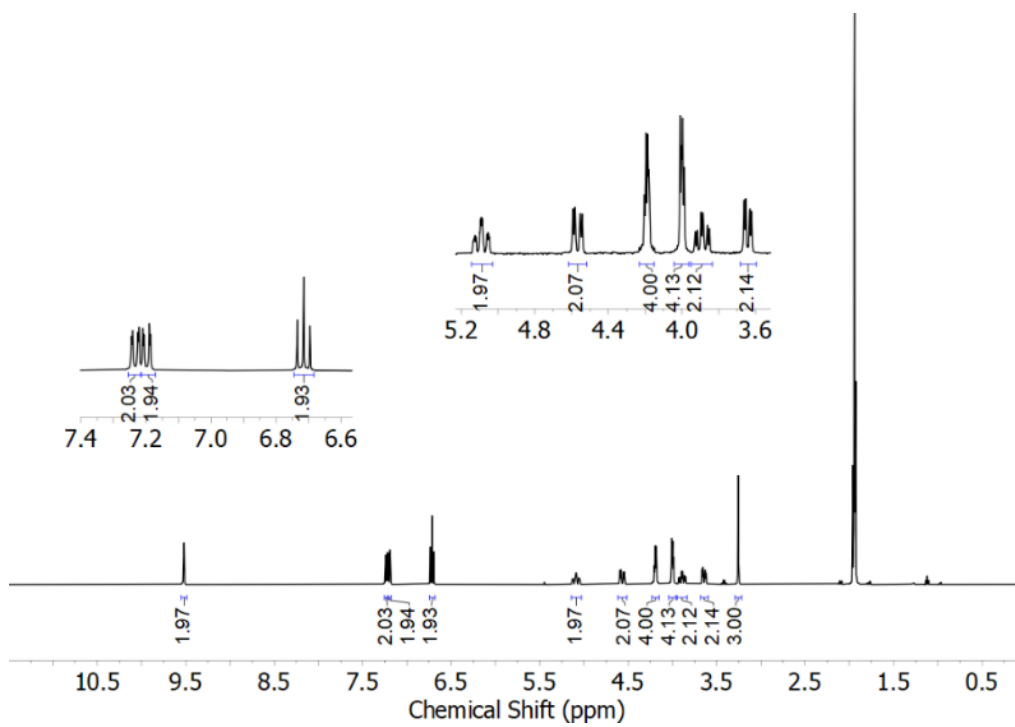


Figure S4. ^1H NMR spectrum (500 MHz, CD_3CN) of *in situ* generated $\text{L}^5\text{UO}_2\text{Cs}$.

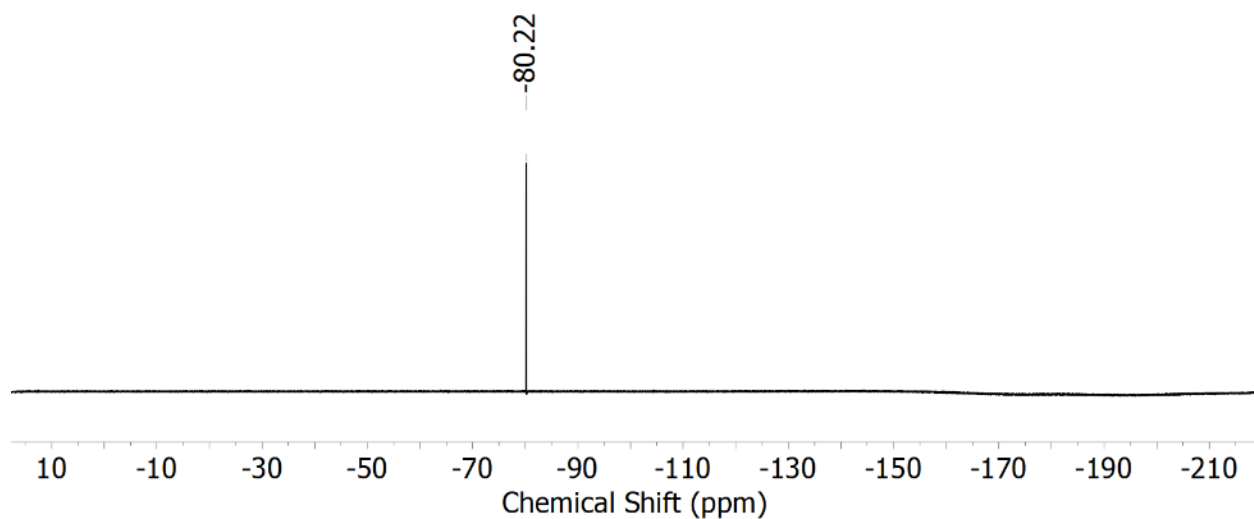


Figure S7. $^{19}\text{F}\{^1\text{H}\}$ NMR spectrum (471 MHz, CD_3CN) of *in situ* generated $\text{L}^5\text{UO}_2\text{Rb}$.

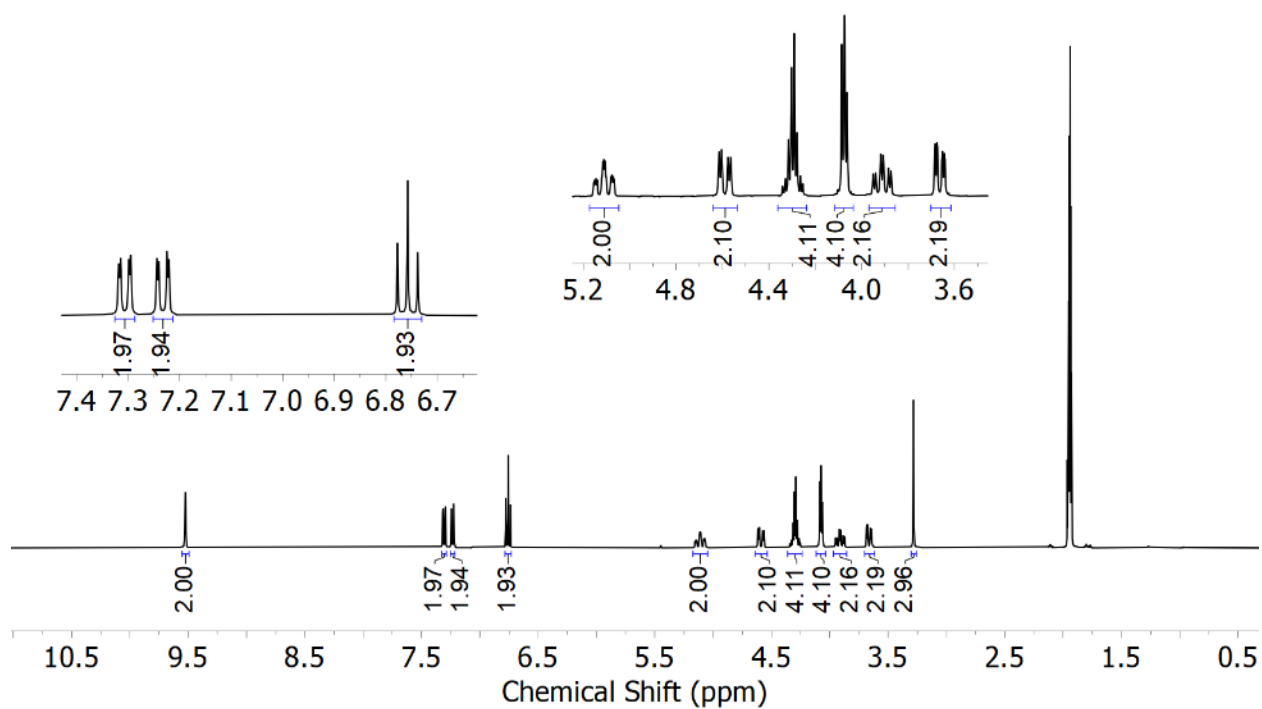


Figure S8. ^1H NMR spectrum (500 MHz, CD_3CN) of *in situ* generated $\text{L}^5\text{UO}_2\text{K}$.

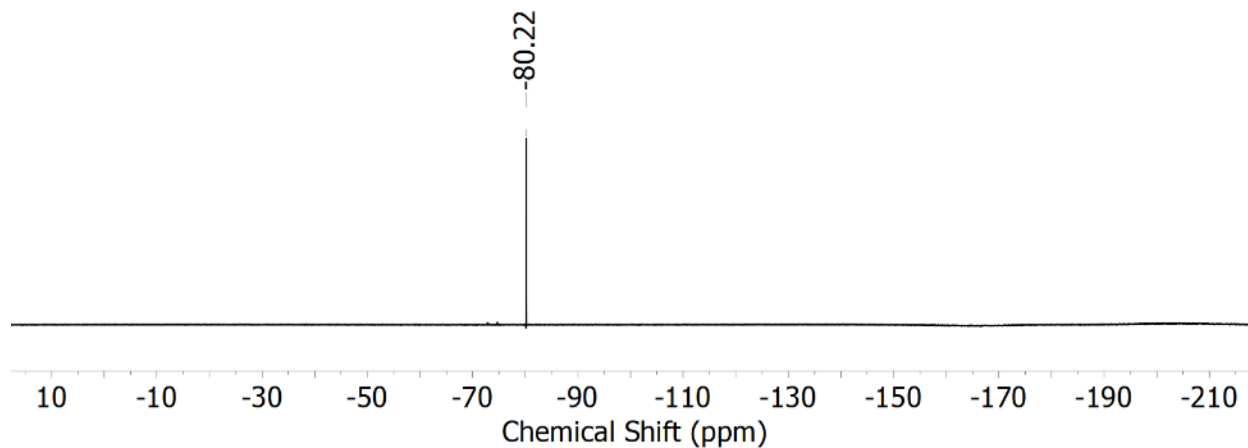


Figure S9. $^{19}\text{F}\{^1\text{H}\}$ NMR spectrum (471 MHz, CD_3CN) of *in situ* generated $\text{L}^5\text{UO}_2\text{K}$.

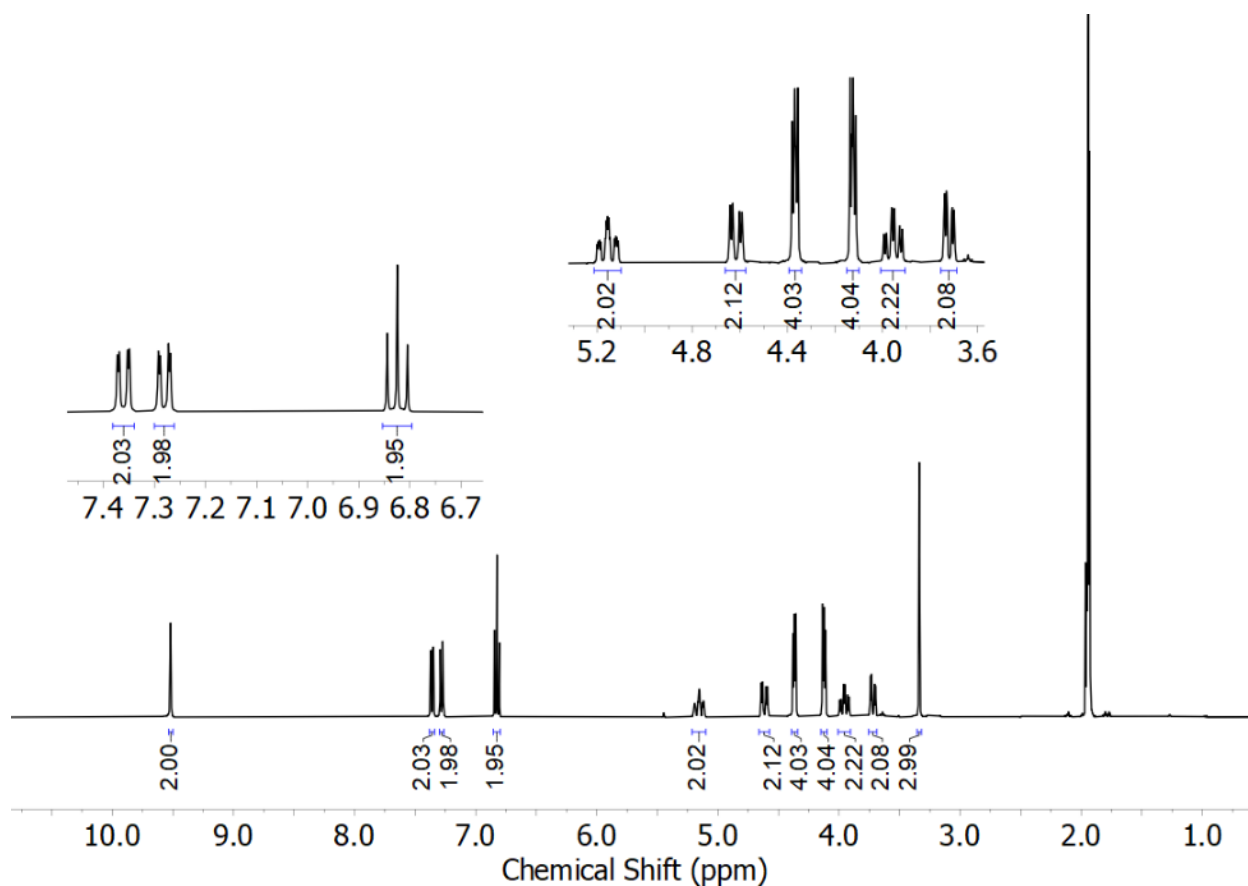


Figure S10. ^1H NMR spectrum (500 MHz, CD_3CN) of *in situ* generated $\text{L}^5\text{UO}_2\text{Na}$.

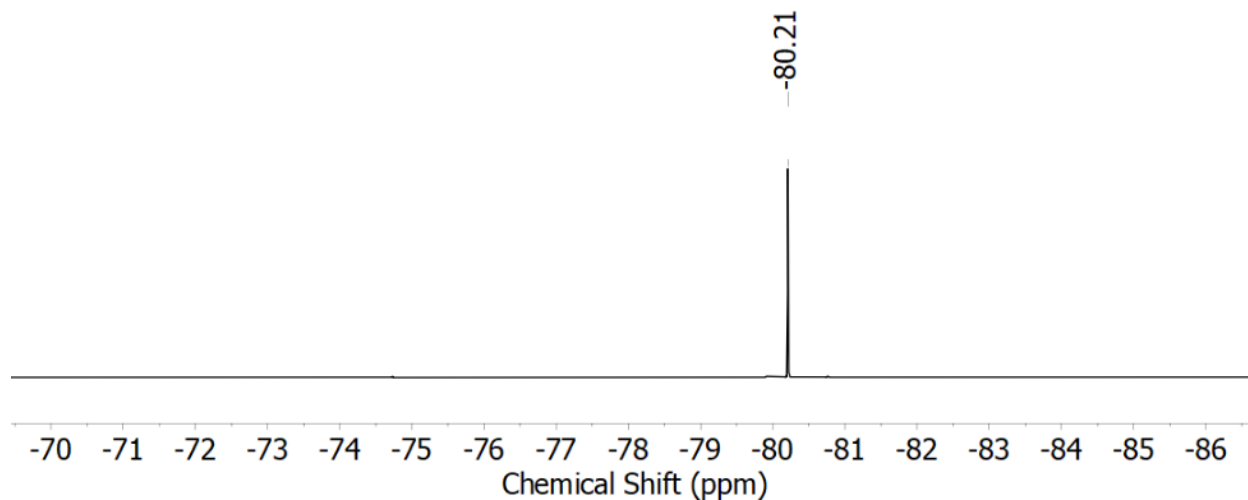


Figure S11. $^{19}\text{F}\{^1\text{H}\}$ NMR spectrum (471 MHz, CD_3CN) of *in situ* generated $\text{L}^5\text{UO}_2\text{Na}$.

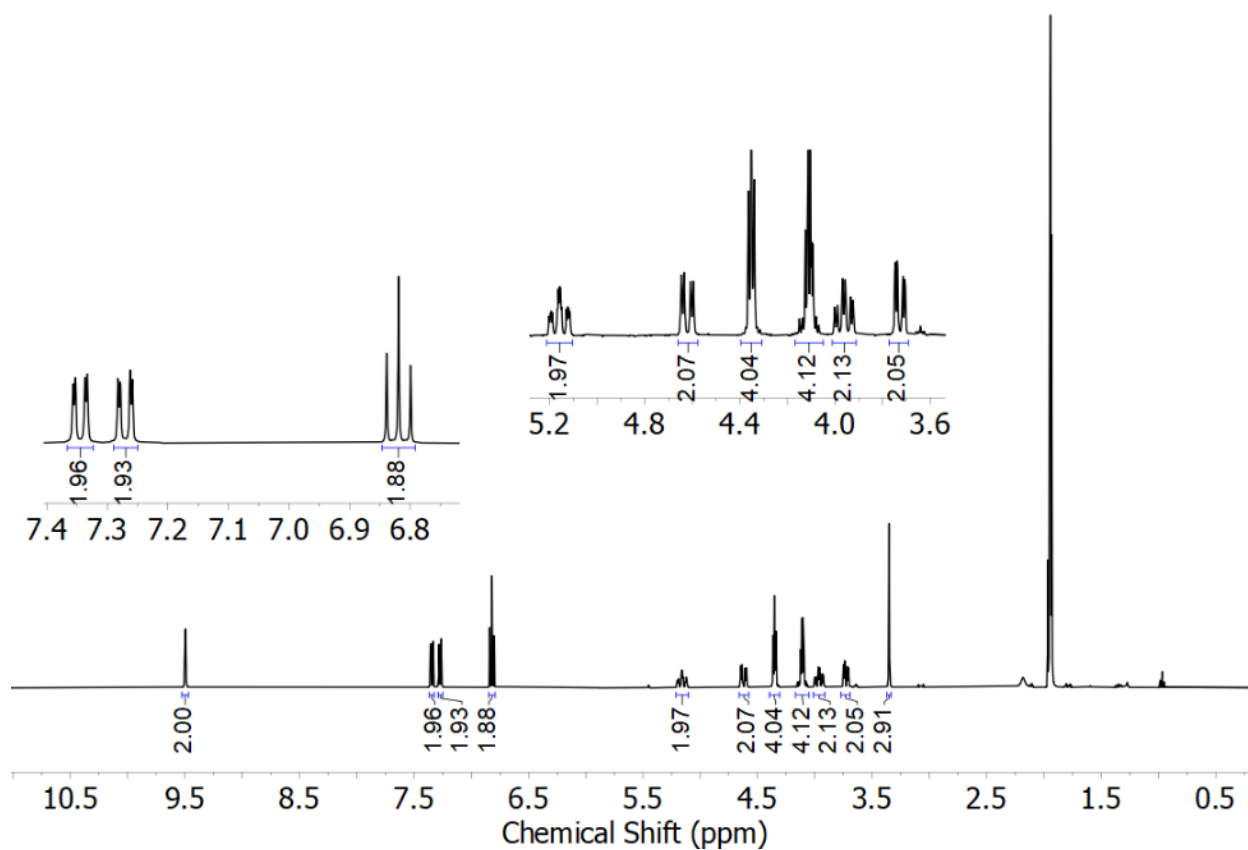


Figure S12. ^1H NMR spectrum (500 MHz, CD_3CN) of *in situ* generated $\text{L}^5\text{UO}_2\text{Li}$.

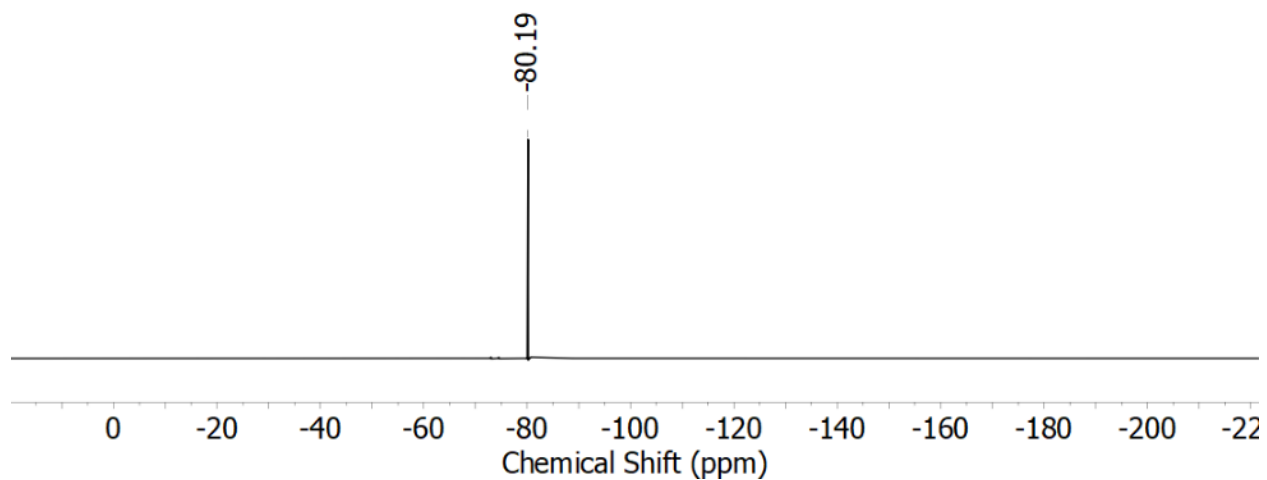


Figure S13. $^{19}\text{F}\{^1\text{H}\}$ NMR spectrum (471 MHz, CD_3CN) of *in situ* generated $\text{L}^5\text{UO}_2\text{Li}$.

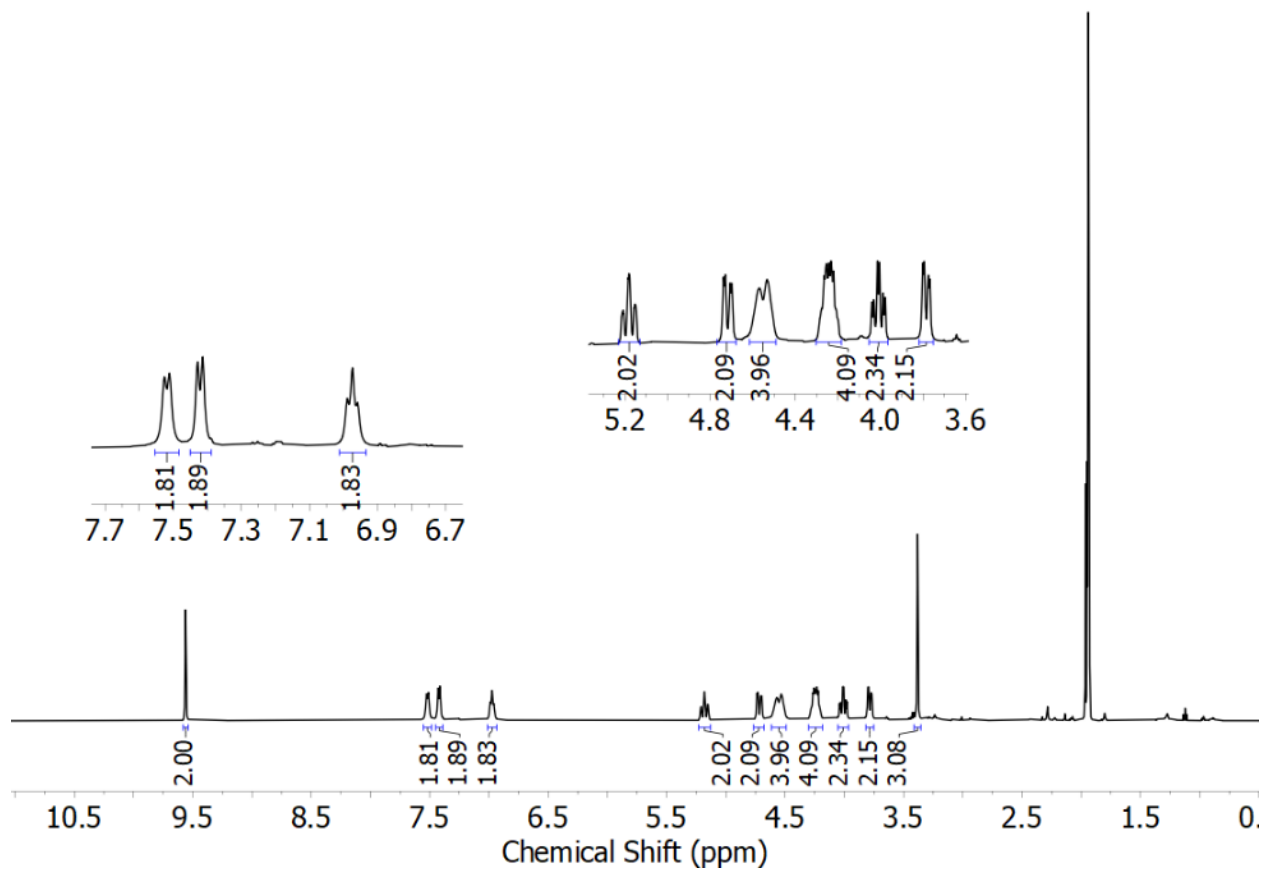


Figure S14. ^1H NMR spectrum (500 MHz, CD_3CN) of *in situ* generated $\text{L}^5\text{UO}_2\text{Ca}$.

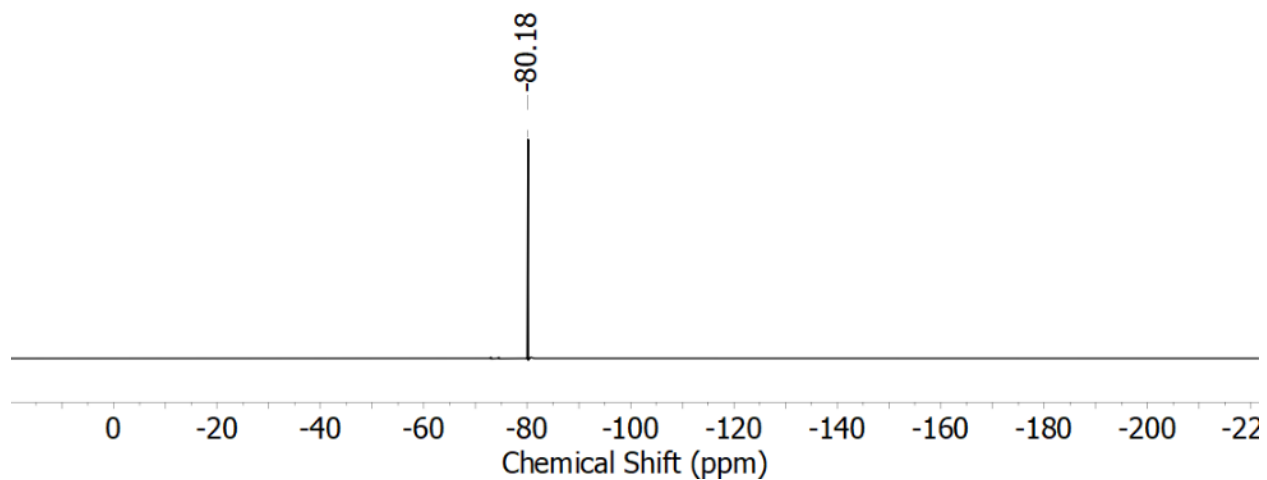


Figure S15. $^{19}\text{F}\{^1\text{H}\}$ NMR spectrum (471 MHz, CD_3CN) of *in situ* generated $\text{L}^5\text{UO}_2\text{Ca}$.

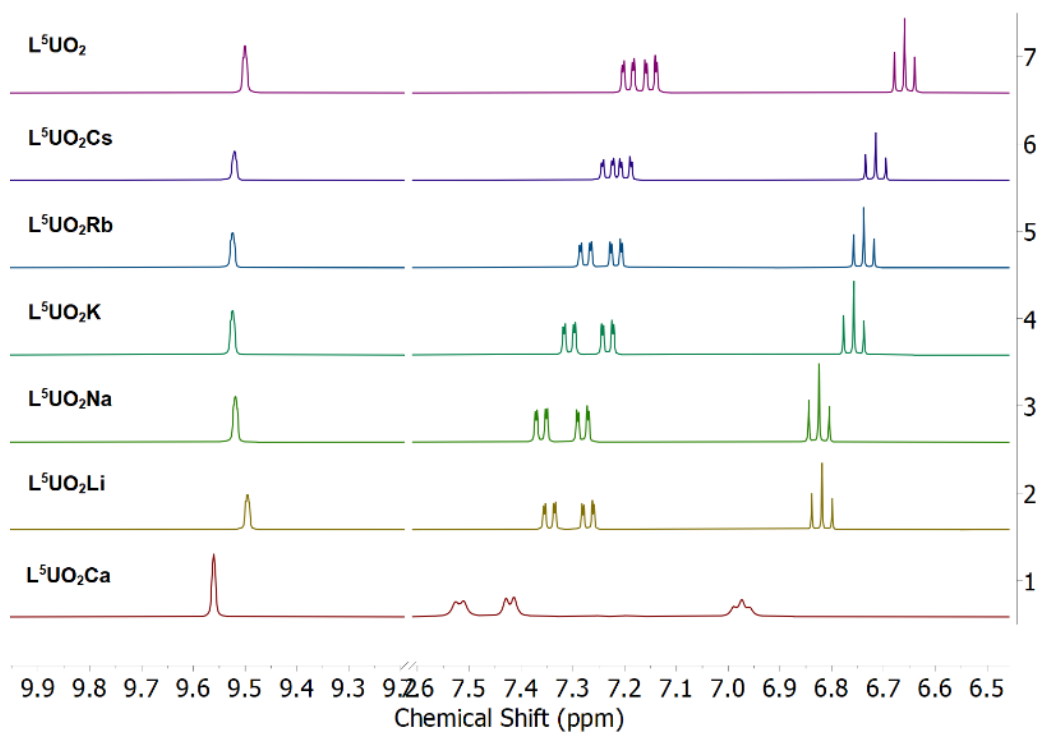


Figure S16. Stacked ^1H NMR spectra showing the aromatic and imine region of the L^5UO_2 and $\text{L}^5\text{UO}_2\text{M}$ complexes.

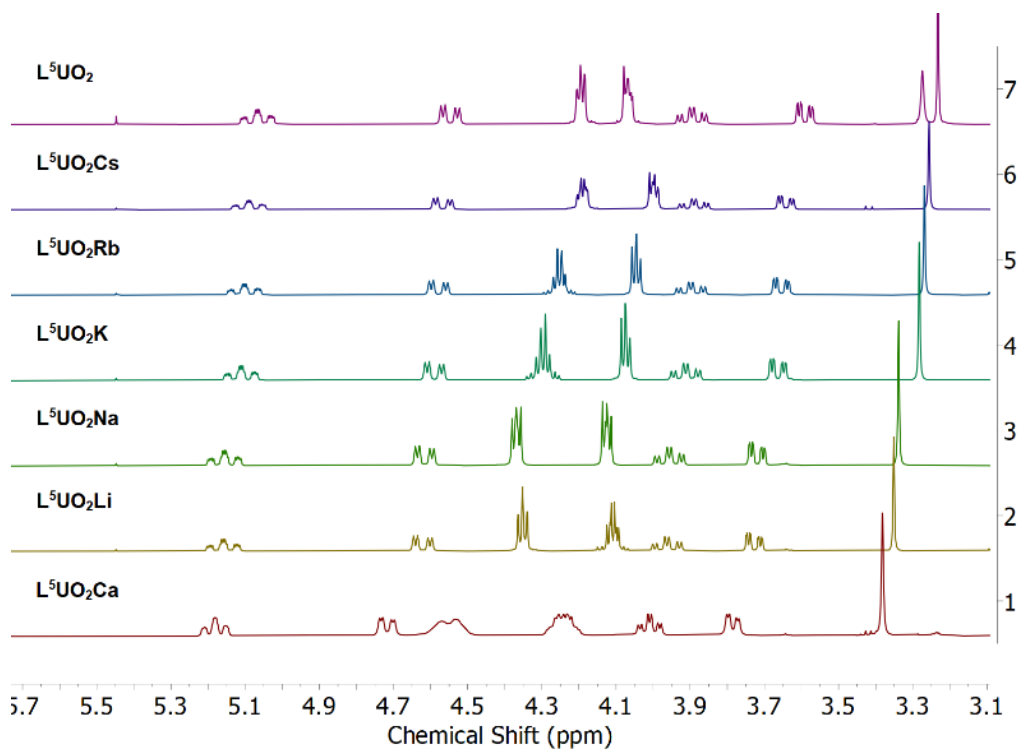


Figure S17. Stacked ^1H NMR spectra showing the aliphatic region of the $\text{L}^5\text{UO}_2\text{U}$ and $\text{L}^5\text{UO}_2\text{M}$ complexes.

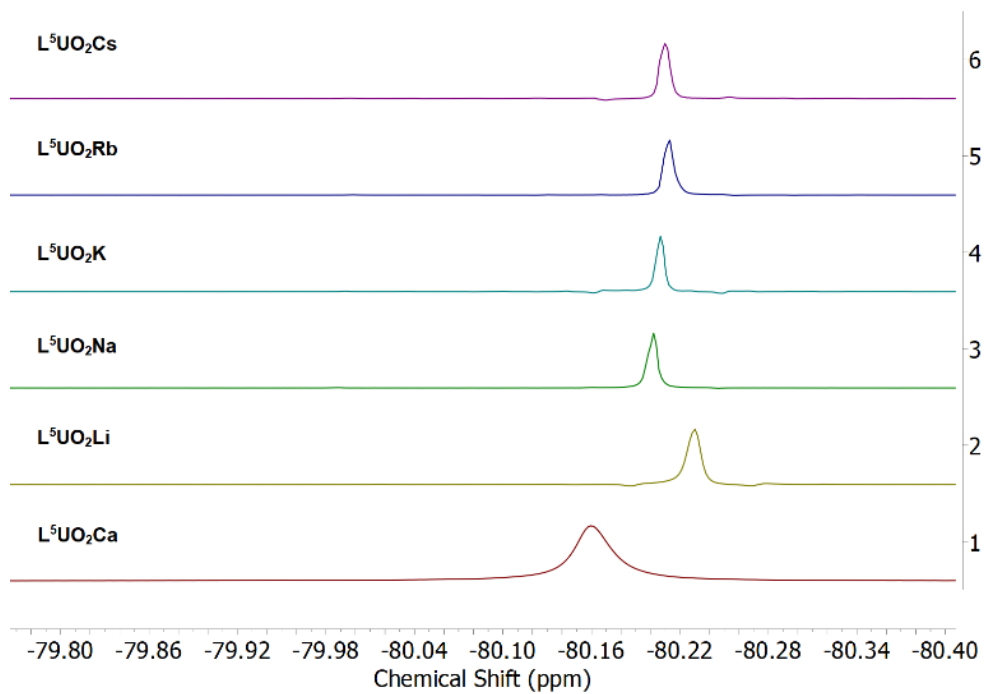


Figure S18. Stacked $^{19}\text{F}\{^1\text{H}\}$ NMR spectra for the $\text{L}^5\text{UO}_2\text{U}$ and $\text{L}^5\text{UO}_2\text{M}$ complexes.

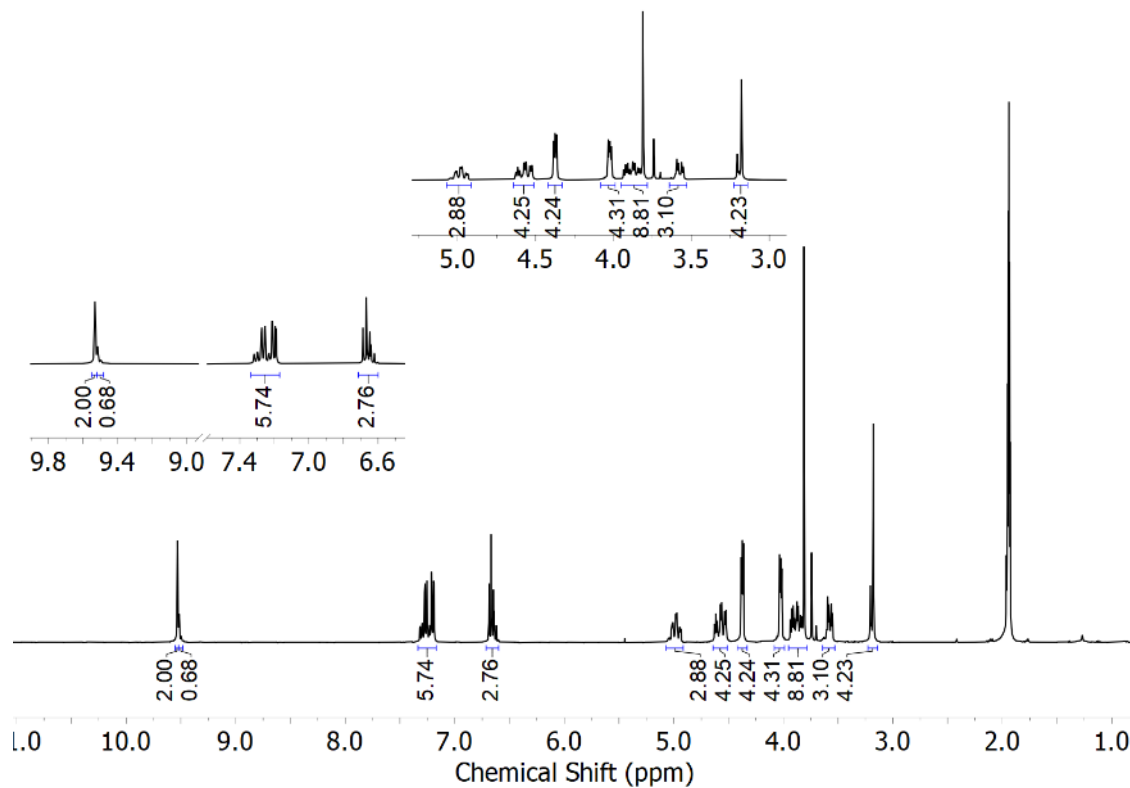


Figure S19. ^1H NMR spectrum (500 MHz, CD_3CN) of L^6UO_2 .

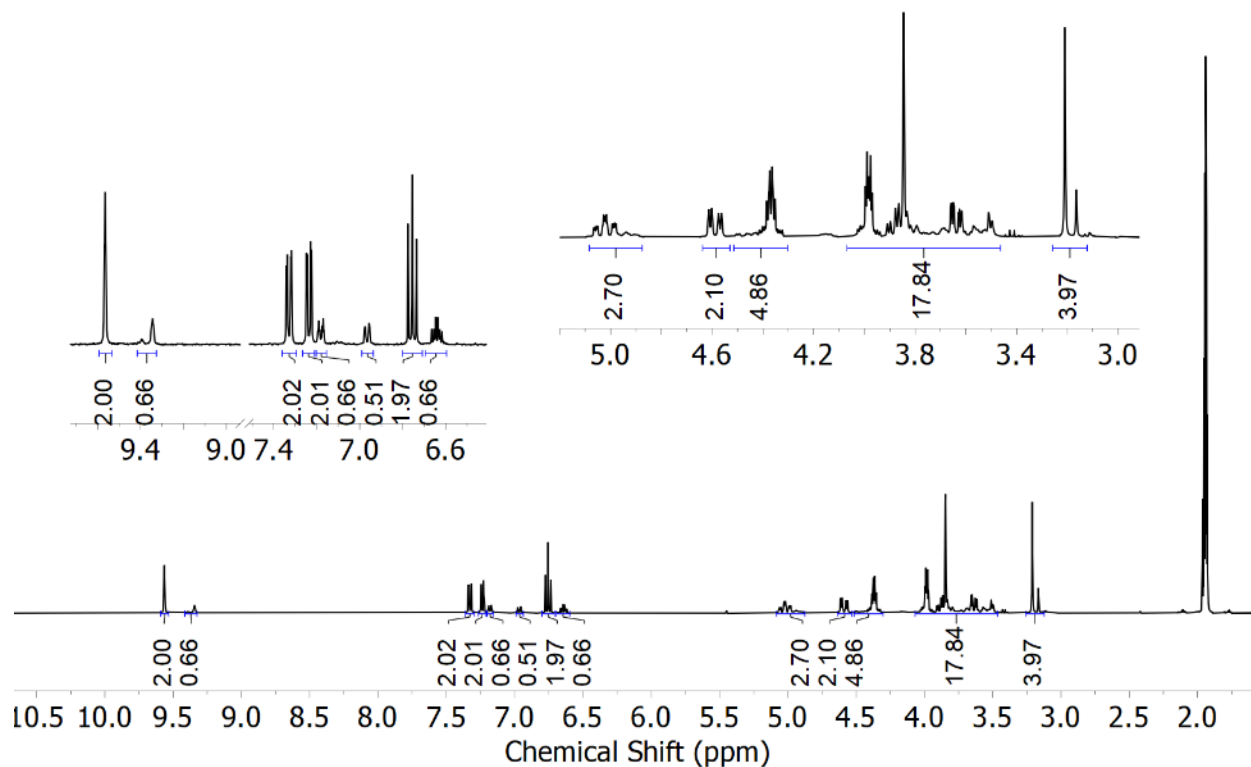


Figure S20. ^1H NMR spectrum (500 MHz, CD_3CN) of *in situ* generated $\text{L}^6\text{UO}_2\text{Cs}$.

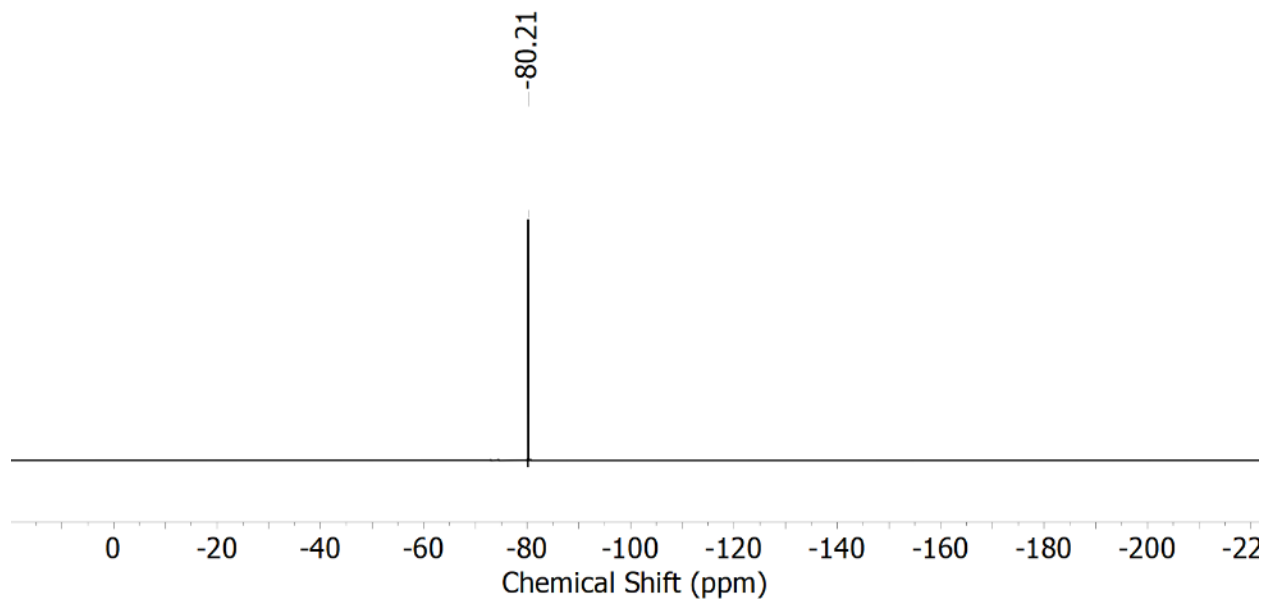


Figure S21. $^{19}\text{F}\{^1\text{H}\}$ NMR spectrum (471 MHz, CD_3CN) of *in situ* generated $\text{L}^6\text{UO}_2\text{Cs}$.

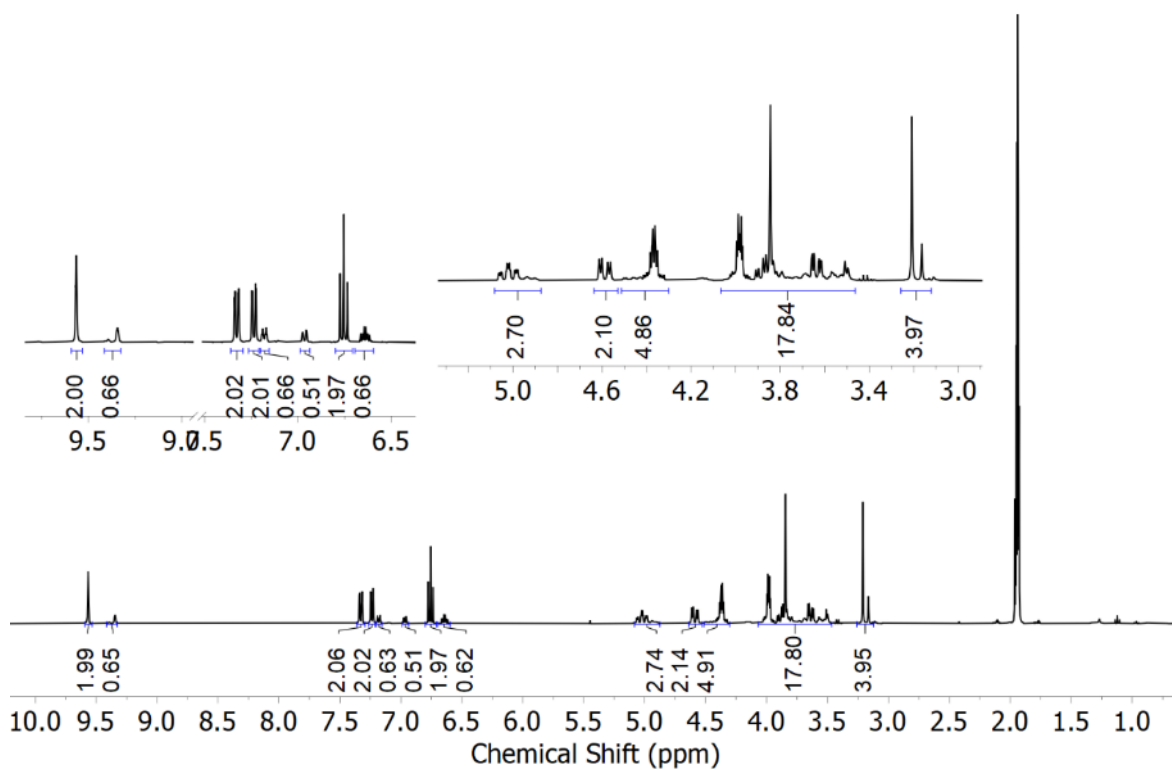


Figure S22. ^1H NMR spectrum (500 MHz, CD_3CN) of *in situ* generated $\text{L}^6\text{UO}_2\text{Rb}$.

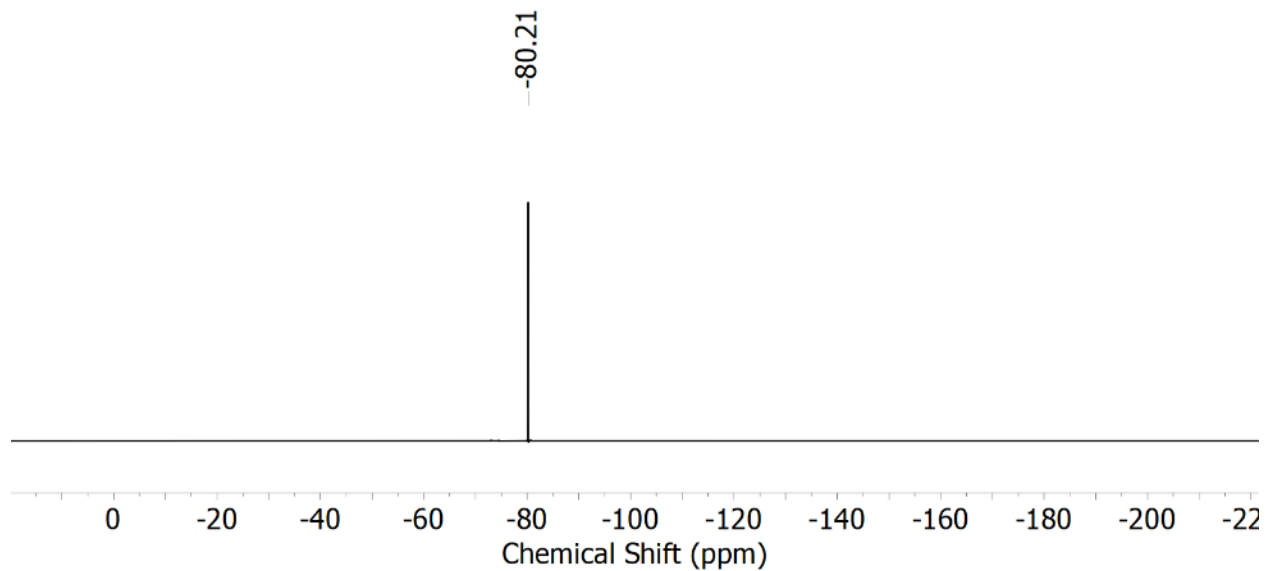


Figure S23. $^{19}\text{F}\{^1\text{H}\}$ NMR spectrum (471 MHz, CD_3CN) of *in situ* generated $\text{L}^6\text{UO}_2\text{Rb}$.

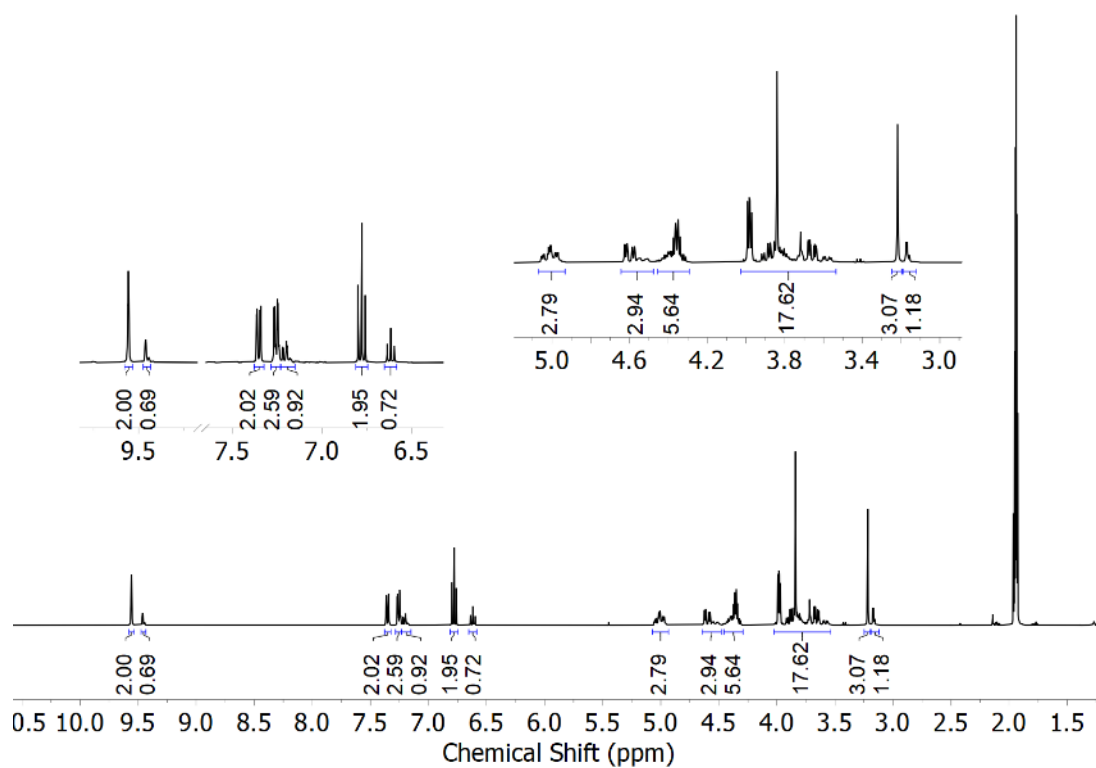


Figure S24. ^1H NMR spectrum (500 MHz, CD_3CN) of *in situ* generated $\text{L}^6\text{UO}_2\text{K}$.

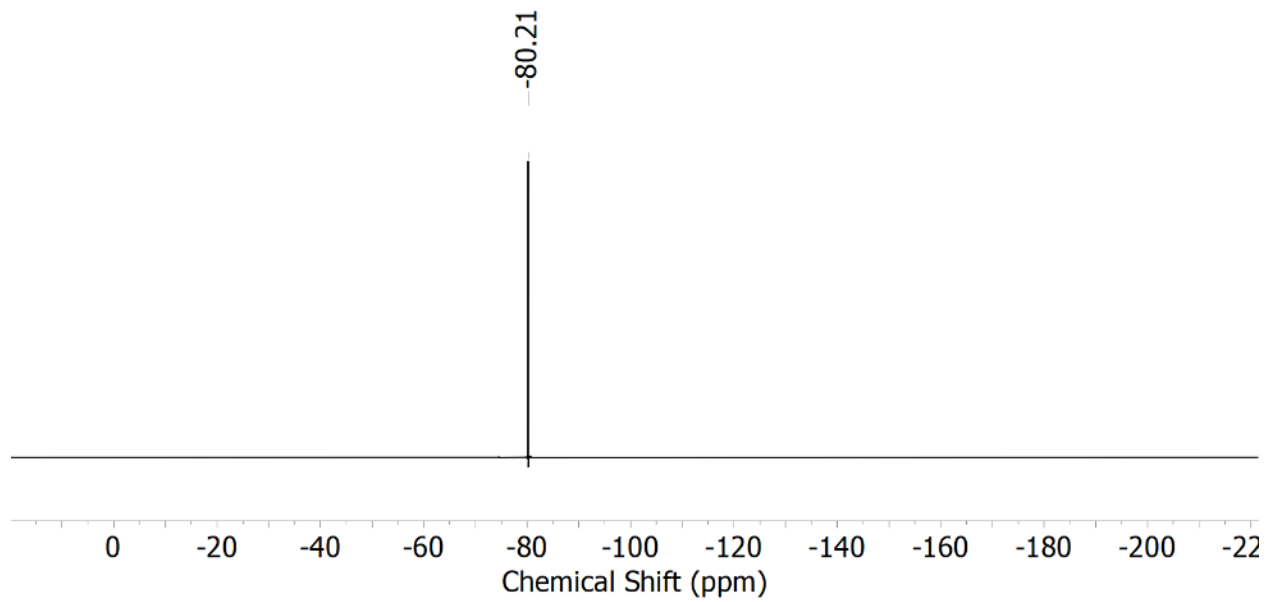


Figure S25. $^{19}\text{F}\{^1\text{H}\}$ NMR spectrum (471 MHz, CD_3CN) of *in situ* generated $\text{L}^6\text{UO}_2\text{K}$.

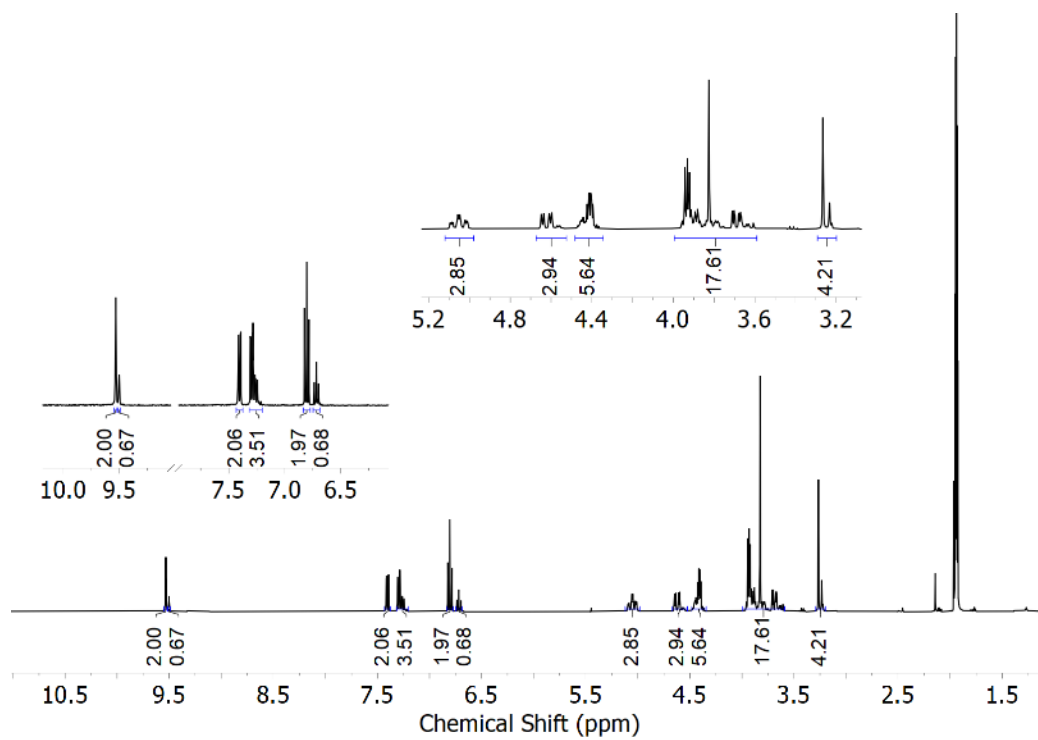


Figure S26. ^1H NMR spectrum (500 MHz, CD_3CN) of *in situ* generated $\text{L}^6\text{UO}_2\text{Na}$.

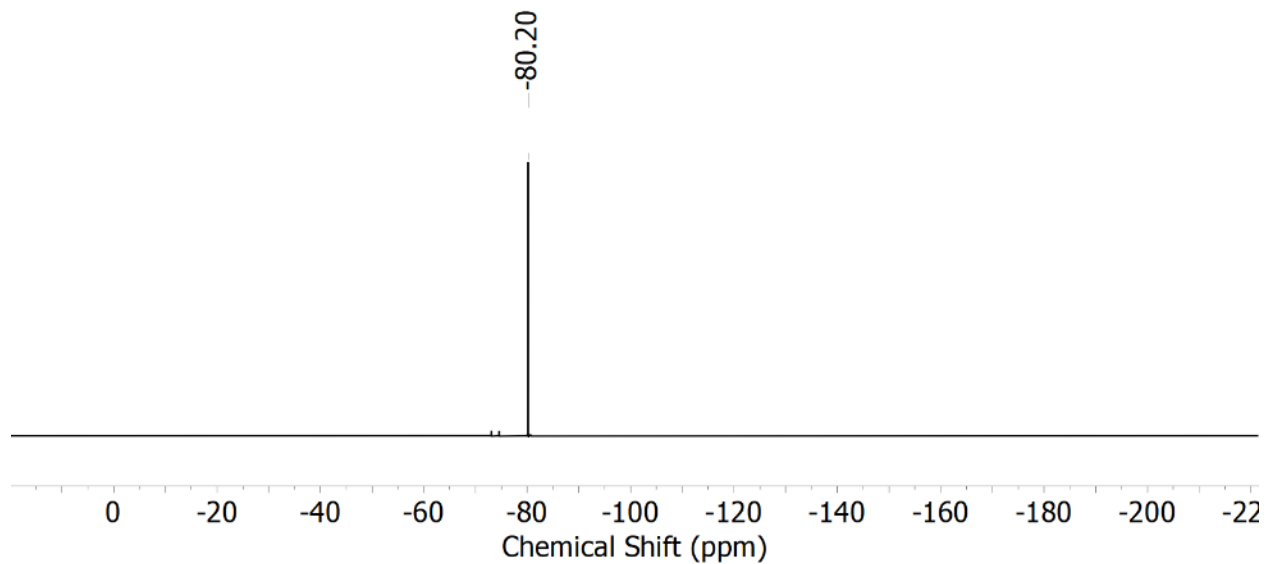


Figure S27. $^{19}\text{F}\{^1\text{H}\}$ NMR spectrum (471 MHz, CD_3CN) of *in situ* generated $\text{L}^6\text{UO}_2\text{Na}$.

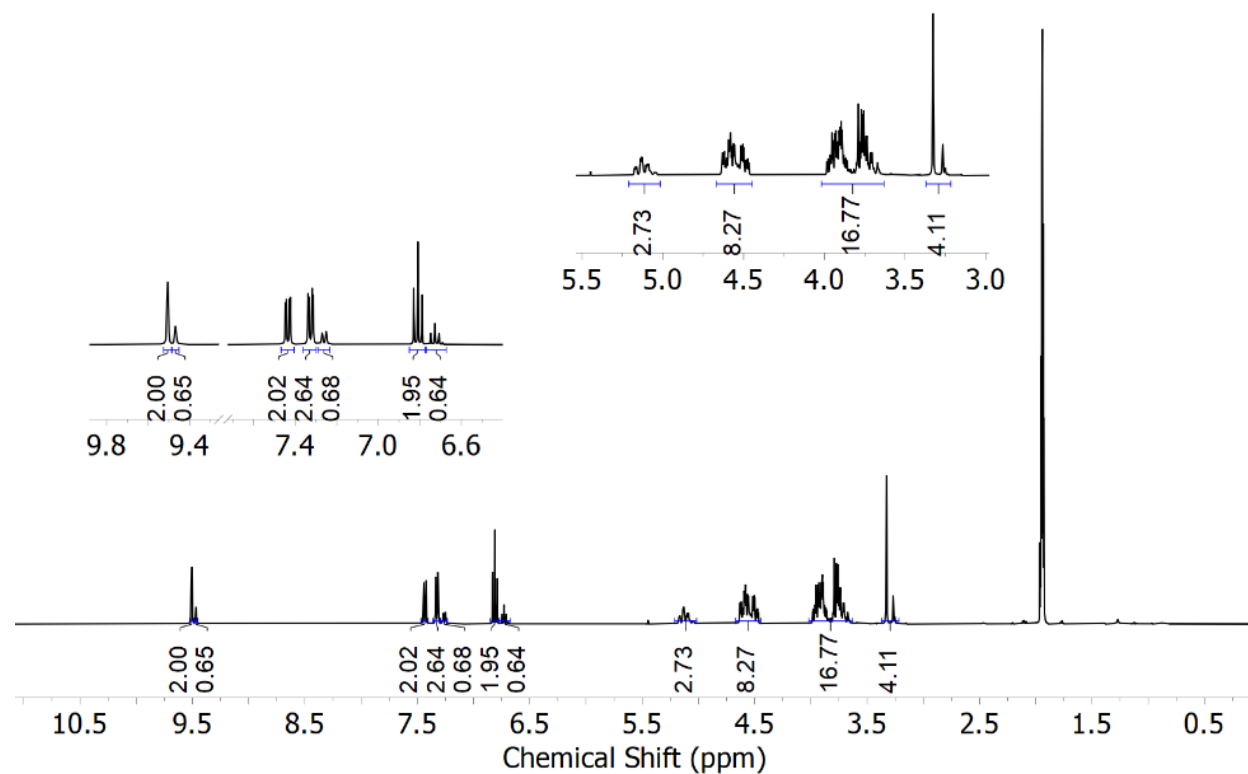


Figure S28. ^1H NMR spectrum (500 MHz, CD_3CN) of *in situ* generated $\text{L}^6\text{UO}_2\text{Li}$.

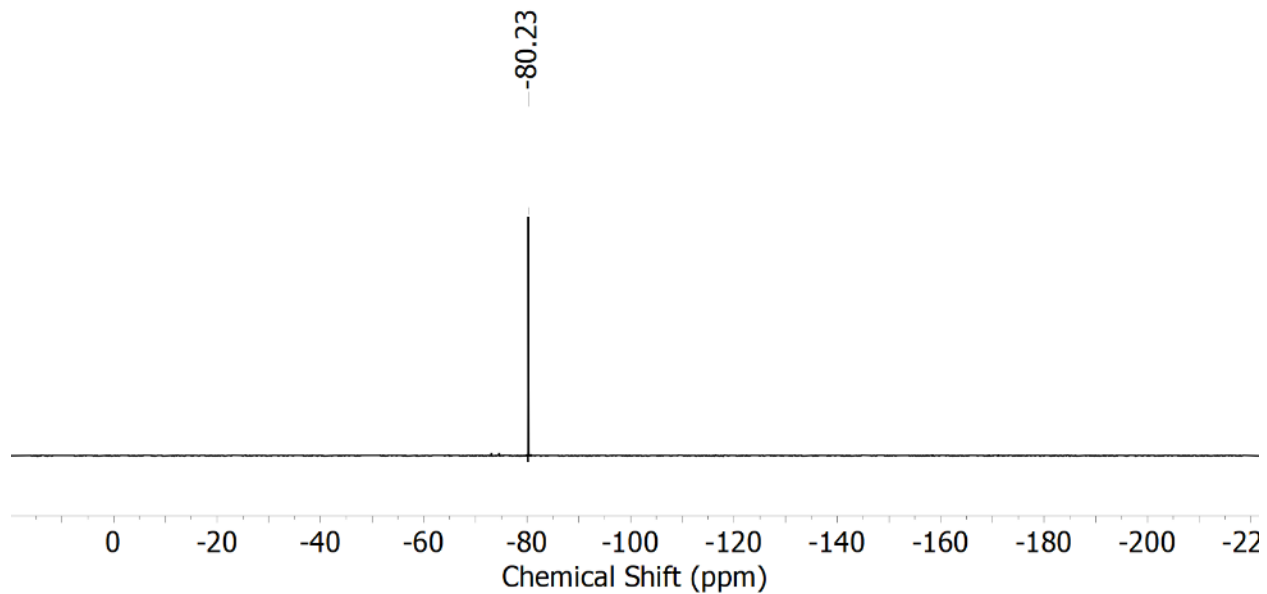


Figure S29. $^{19}\text{F}\{^1\text{H}\}$ NMR spectrum (471 MHz, CD_3CN) of *in situ* generated $\text{L}^6\text{UO}_2\text{Li}$.

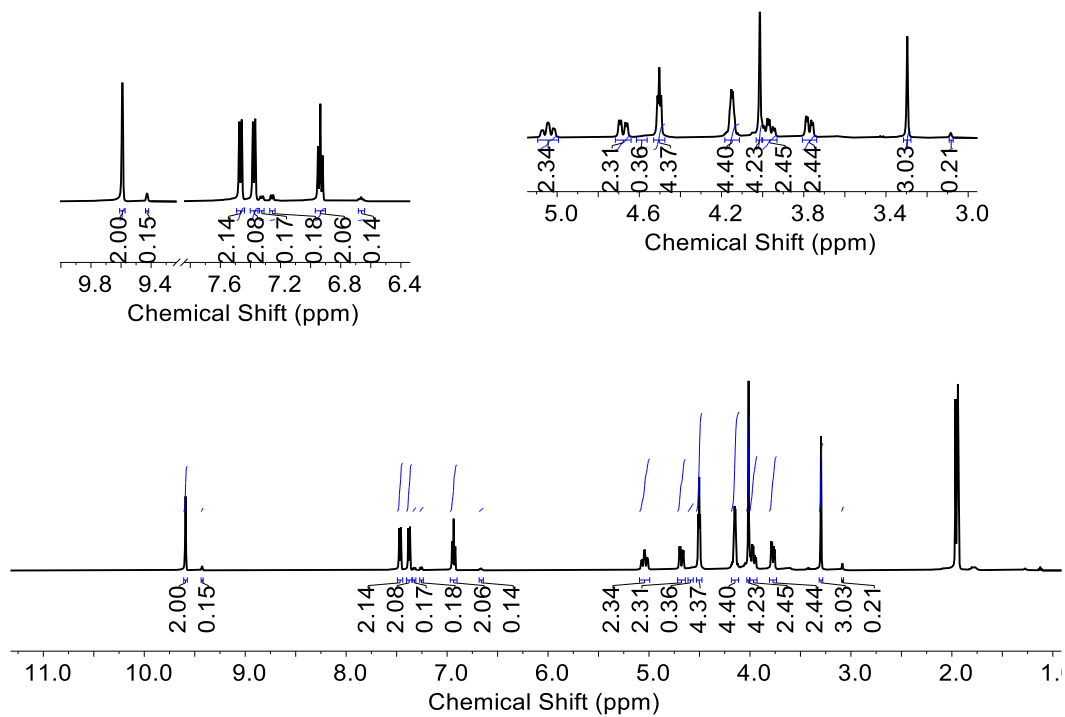


Figure S30. ^1H NMR spectrum (500 MHz, CD_3CN) of synthesized and isolated $\text{L}^6\text{UO}_2\text{Sr}$.

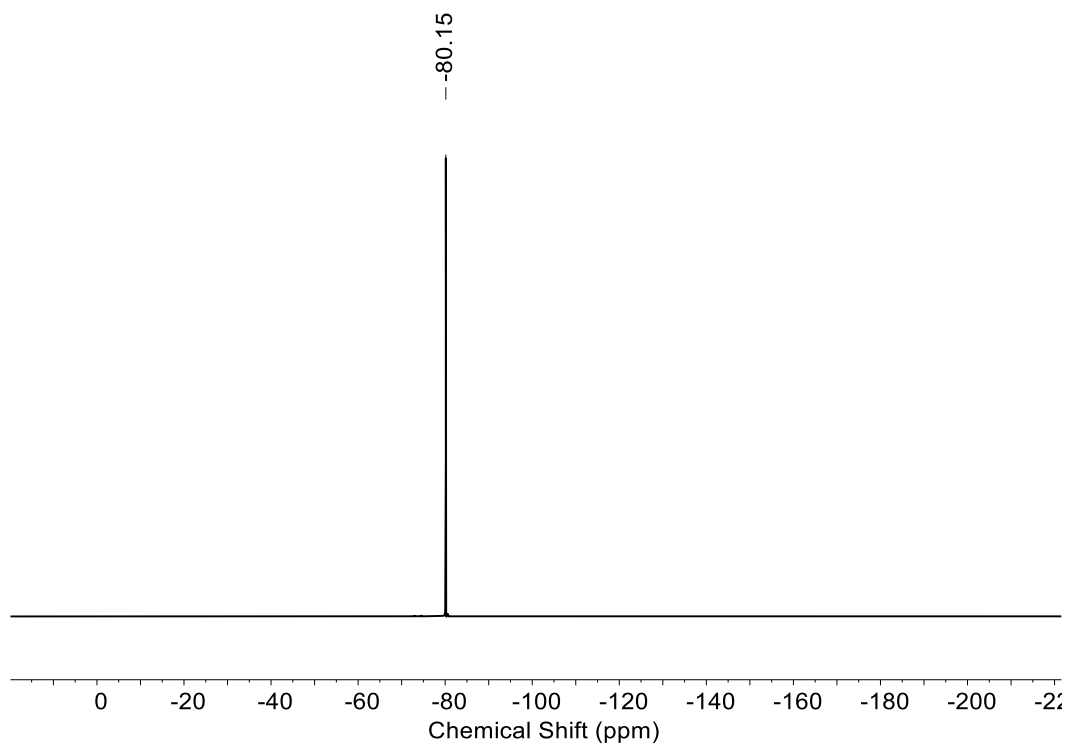


Figure S31. $^{19}\text{F}\{^1\text{H}\}$ NMR spectrum (471 MHz, CD_3CN) of synthesized and isolated $\text{L}^6\text{UO}_2\text{Sr}$.

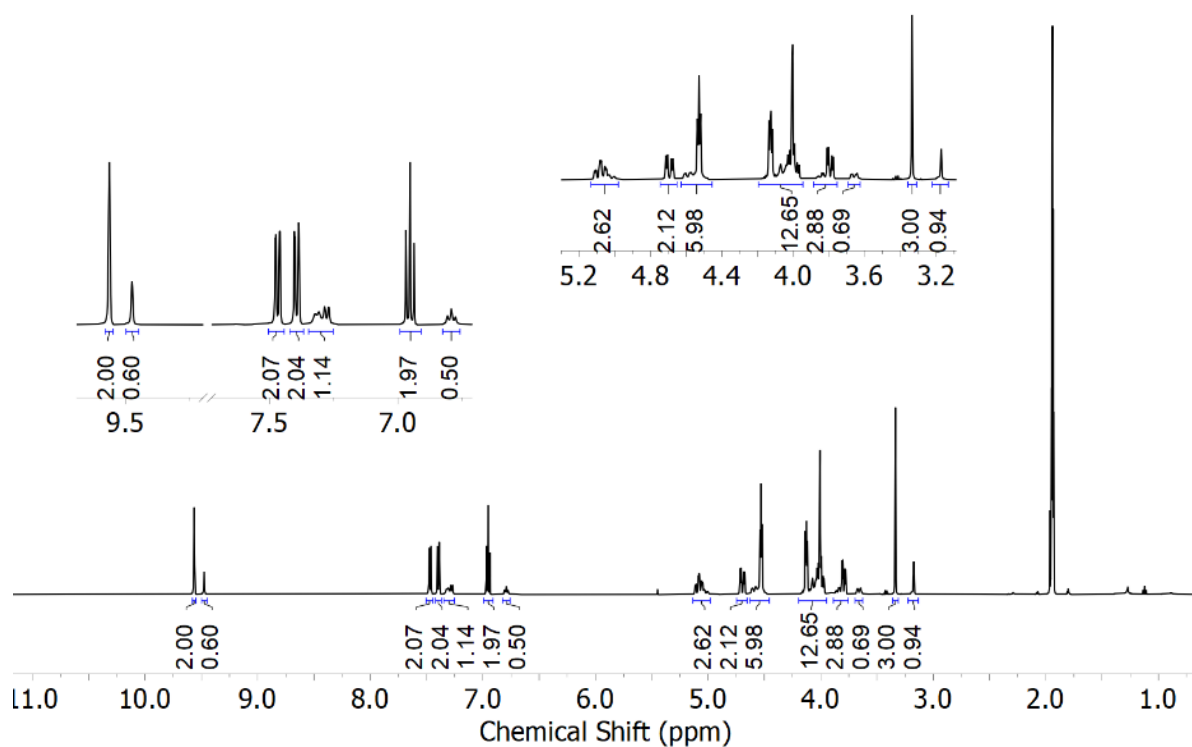


Figure S32. ^1H NMR spectrum (500 MHz, CD_3CN) of *in situ* generated $\text{L}^6\text{UO}_2\text{Ca}$.

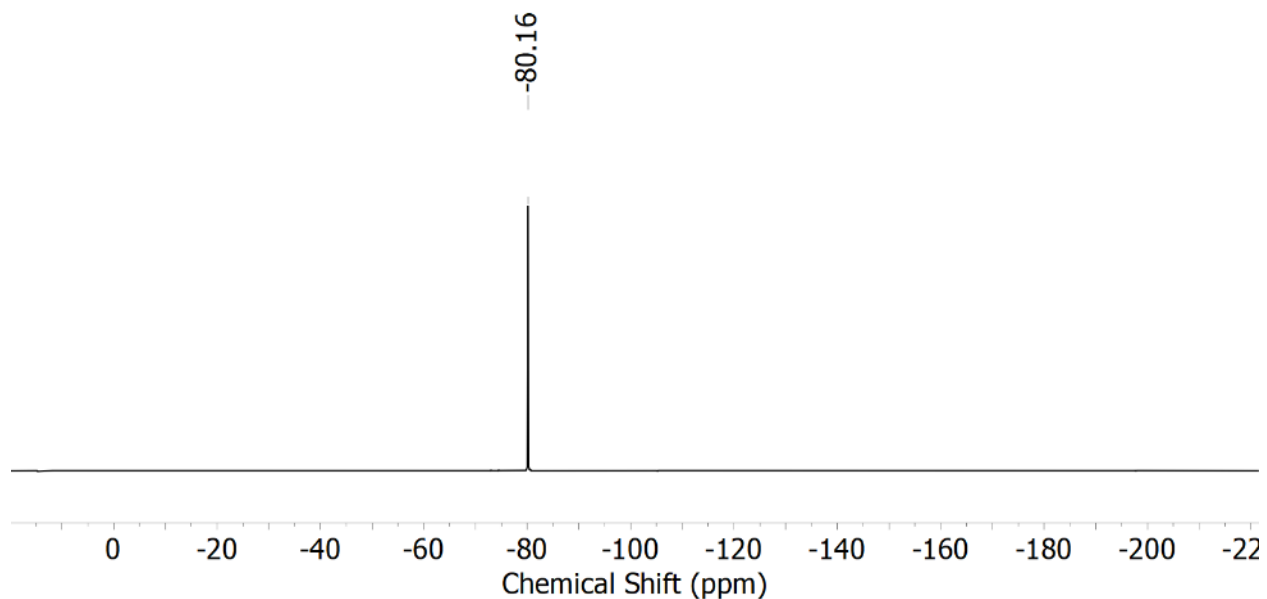


Figure S33. $^{19}\text{F}\{^1\text{H}\}$ NMR spectrum (471 MHz, CD_3CN) of *in situ* generated $\text{L}^6\text{UO}_2\text{Ca}$.

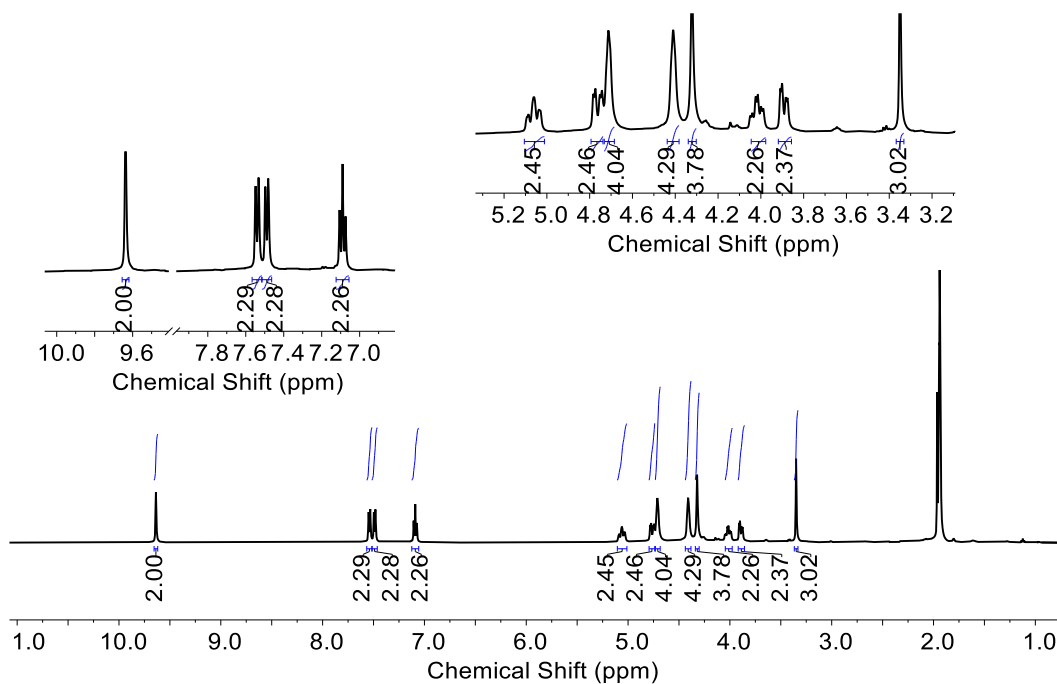


Figure S34. ^1H NMR spectrum (500 MHz, CD_3CN) of synthesized and isolated $\text{L}^6\text{UO}_2\text{La}$.

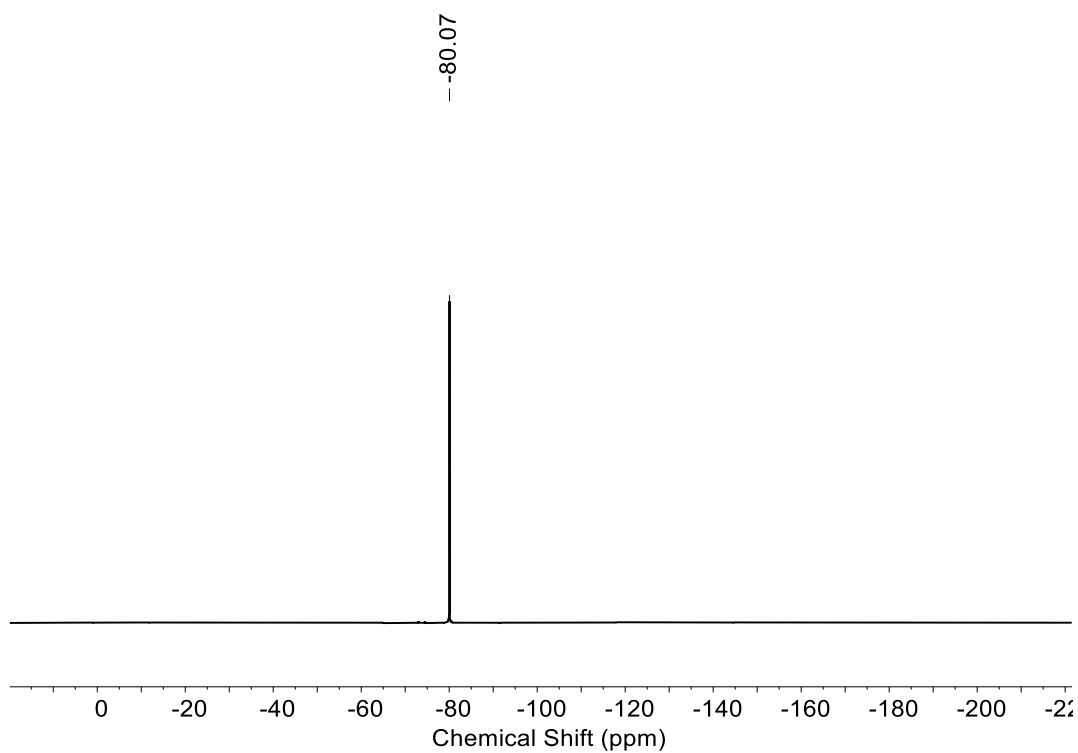


Figure S35. $^{19}\text{F}\{^1\text{H}\}$ NMR spectrum (471 MHz, CD_3CN) of synthesized and isolated $\text{L}^6\text{UO}_2\text{La}$.

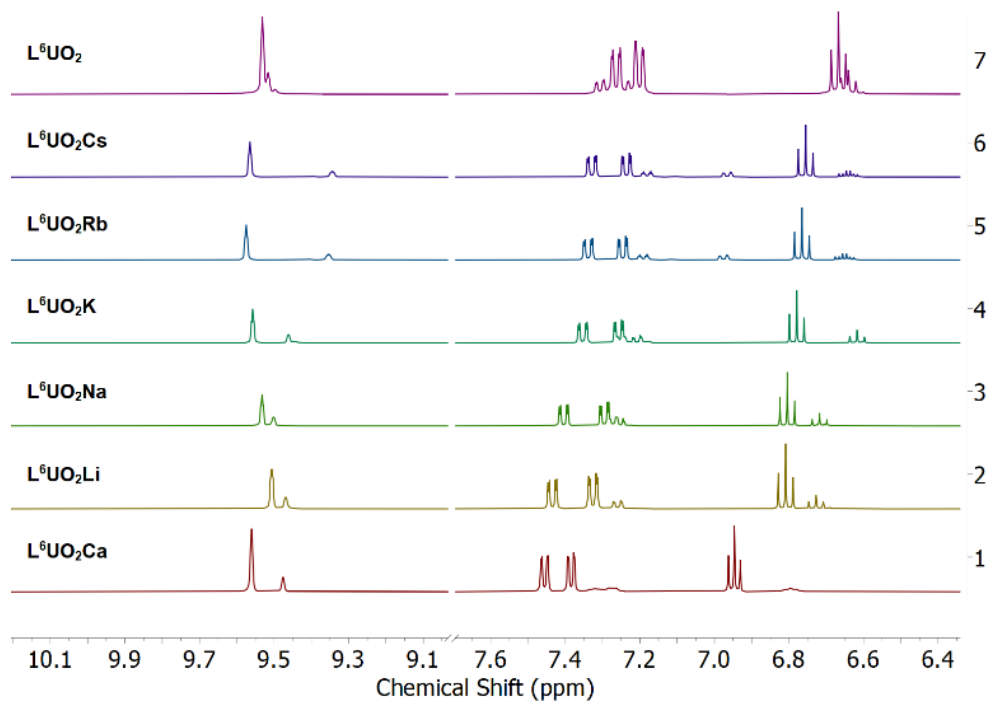


Figure S36. Stacked ^1H NMR spectra showing the aromatic and imine region of the L^6UO_2 and $\text{L}^6\text{UO}_2\text{M}$ complexes.

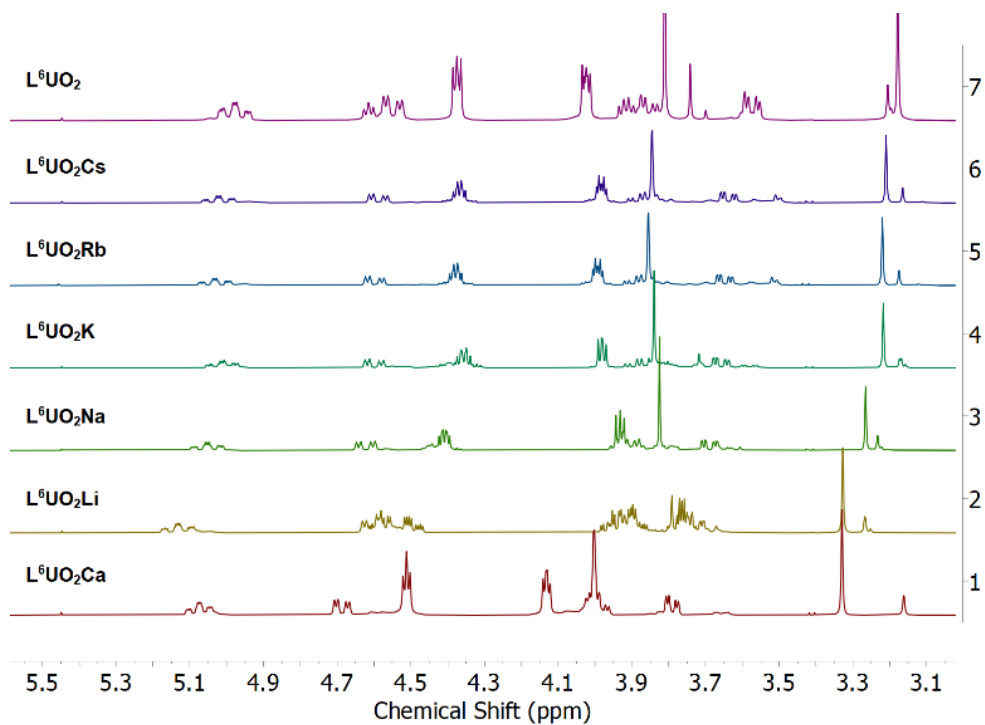


Figure S37. Stacked ^1H NMR spectra showing the aliphatic region of the L^6UO_2 and $\text{L}^6\text{UO}_2\text{M}$ complexes.

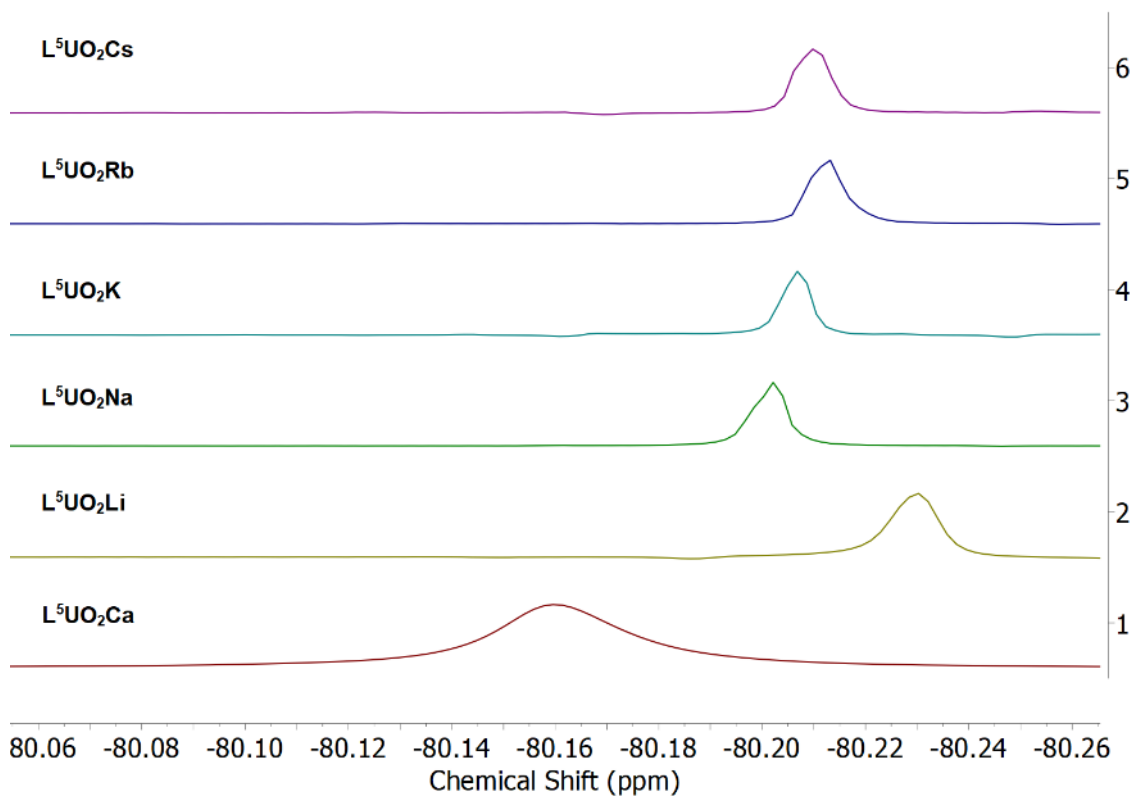


Figure S38. Stacked $^{19}\text{F}\{^1\text{H}\}$ NMR spectra for the $\text{L}^6\text{UO}_2\text{U}$ and $\text{L}^6\text{UO}_2\text{M}$ complexes.

Vibrational Analysis

Solid-state Raman Spectroscopy

Table S1. Solid-state Raman assignments for L^5UO_2M series. All values mentioned are in cm^{-1} .

L^5UO_2	L^5UO_2Rb	L^5UO_2K	L^5UO_2Na	L^5UO_2Li	L^5UO_2Sr	Assignment
584.3	576.7	575.72		581.2	575.9	Metal- O_{ligand}/N vibration
	619.1			602.1	591.7	CH in-plane bends
630.9	632.5	632.8		630.6		CH in-plane bends
741.0	739.1	740.1	735.6	741.6	740.9	CH bend; phenyl
755.1	756.6	757.8	756.7	761.3	762.9	CH bend; phenyl
772.8	774.4	775.0	771.9	774.4	775.3	Phenyl/crown positional band (crown bridges up, phenyl rings down) (CH bend)
811.7	813.3	816.7	815.7	817.4	818.7	Uranyl ν_1
	825.4				826.9	Symmetric ring breathing
840.3	839.0	842.2		841.9	835.4	Symmetric ring breathing
	864.2	863.4	862.0	864.5	859.8	Symmetric ring breathing
940.7						CH bending, phenyl
953.4						CH bending, phenyl
1029.5	1032.6	1033.4	1034.0	1031.3	1037.0	CH bend; $-(CH_2)_2-$
1079.8		1050.6		1043.1	1056.9	CH bend; $-(CH_2)_2-$

Table S2. Solid-state Raman assignments for L^6UO_2M series. All values mentioned are in cm^{-1} .

Free Ligand (L^6)	L^6UO_2	L^6UO_2Rb	L^6UO_2K	L^6UO_2Na	L^6UO_2Li	L^6UO_2Sr	L^6UO_2Ca	L^6UO_2La	Tentative Assignments
725					726				CH in-plane bends
	738	736	736	732	733	738	734	739	CH bend; phenyl
748	755	745	758	754	751	759	759	761	CH bend; phenyl
	771	756, 773, 783	777	770	767	777	771, 783	779	Phenyl/crown positional band (crown bridges up, phenyl rings down) (CH bend)
	812.5	807	811.5	811.5	811	822	824	828	Uranyl ν_1
836	838					840	840	841	Symm. ring breathing
	853	858	858	856	859	861	862	857	Symm. ring breathing
					896.5				Uranyl ν_3
	942						914	910	CH bending, phenyl
1014									CH bend; $-(CH_2)_2-$
				1030	1027			1034	CH bend; $-(CH_2)_2-$
1077									CH bend; $-(CH_2)_2-$

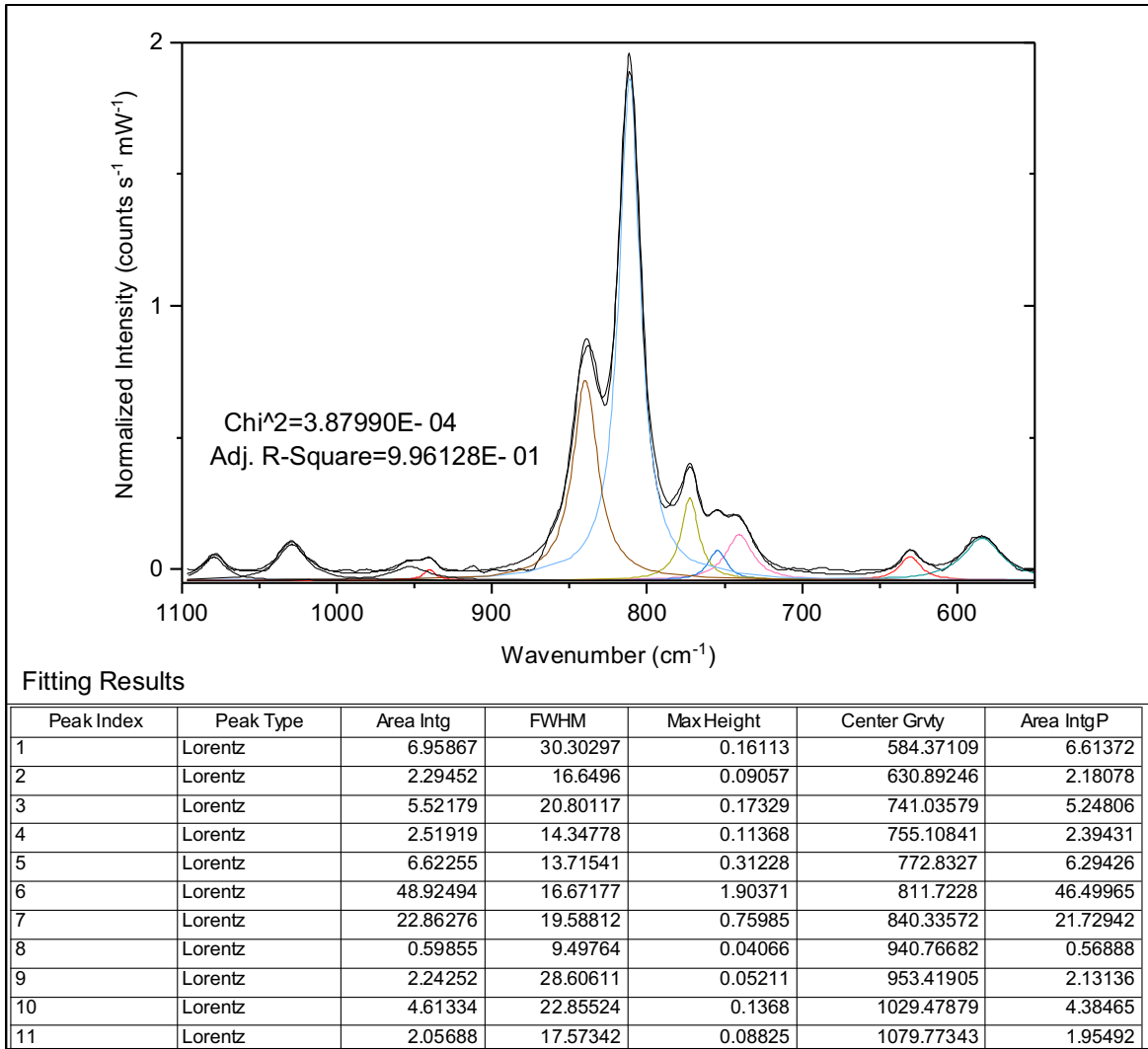


Figure S39. Solid-state Raman spectrum for L⁵UO₂.

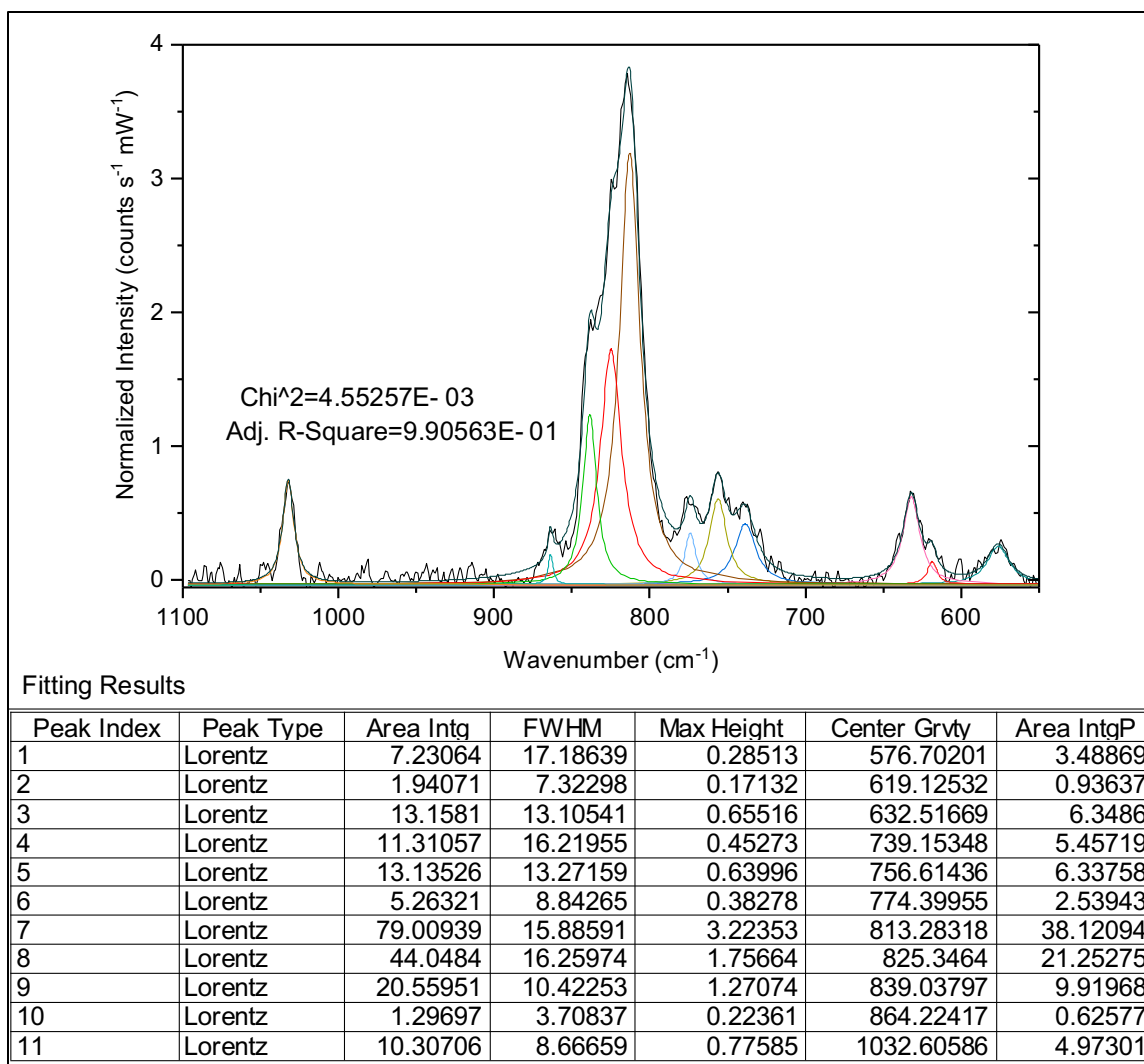


Figure S40. Solid-state Raman spectrum for L^5UO_2Rb .

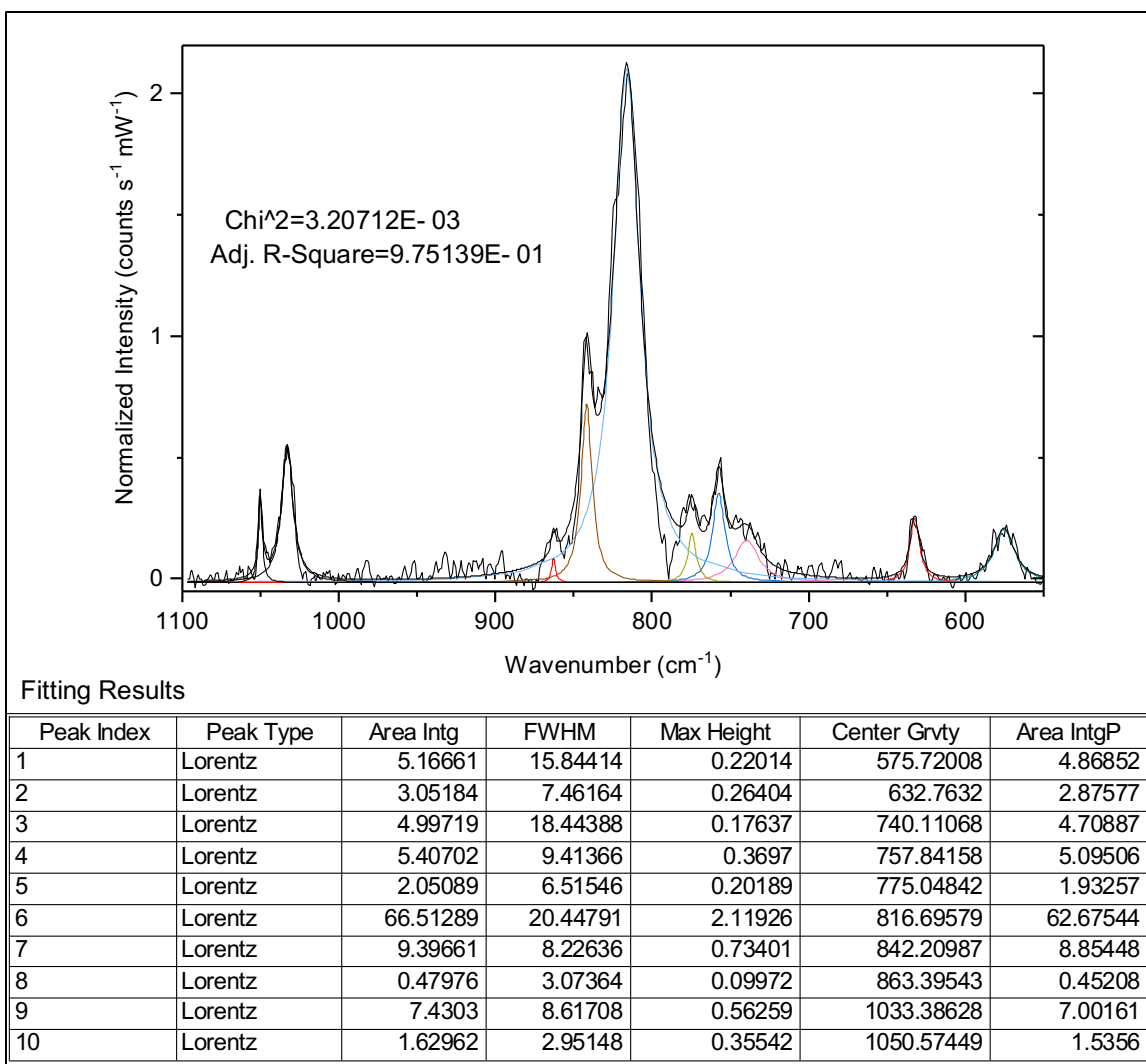


Figure S41: Solid-state Raman spectrum for L⁵UO₂K.

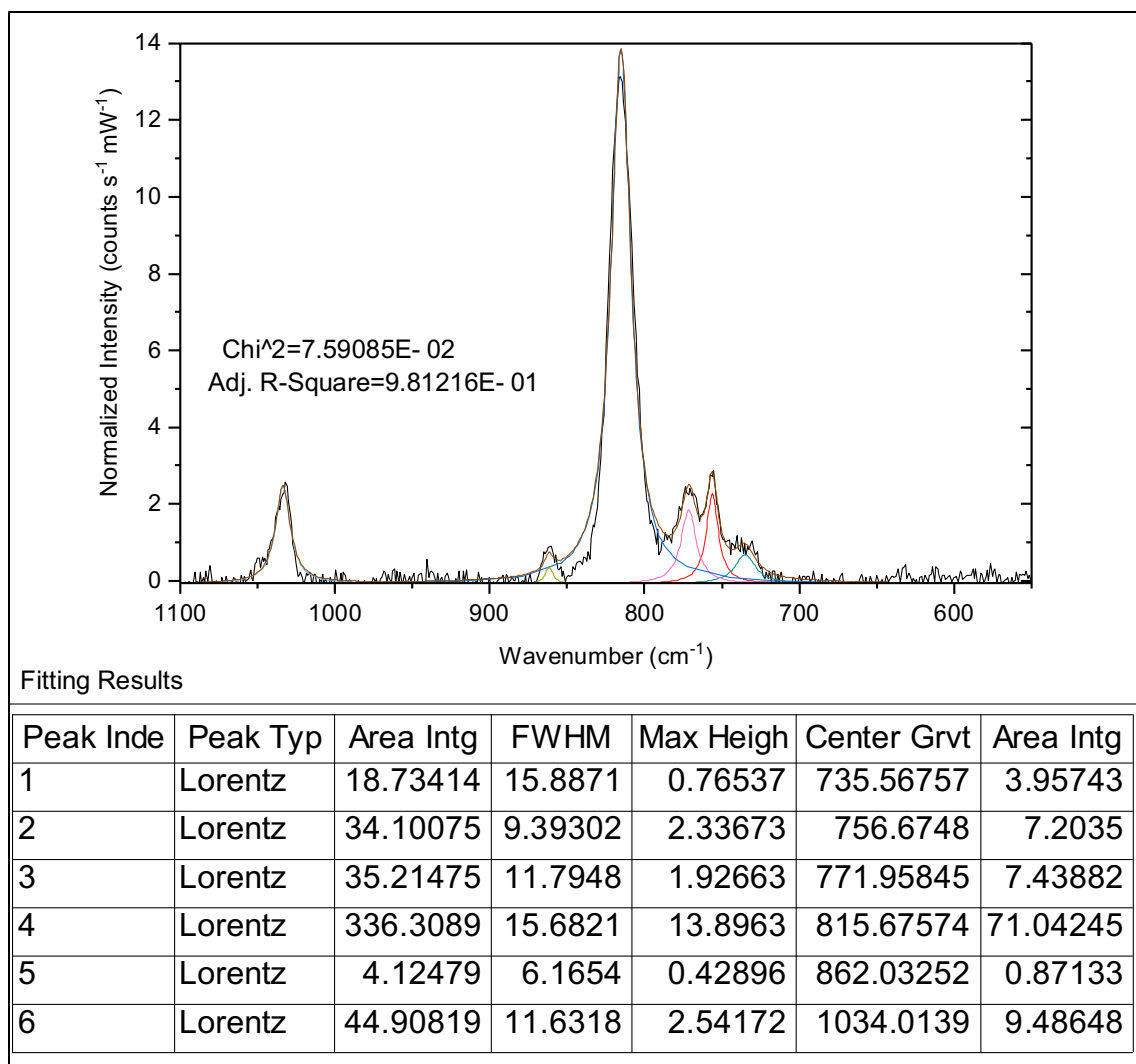


Figure S42. Solid-state Raman spectrum for L⁵UO₂Na.

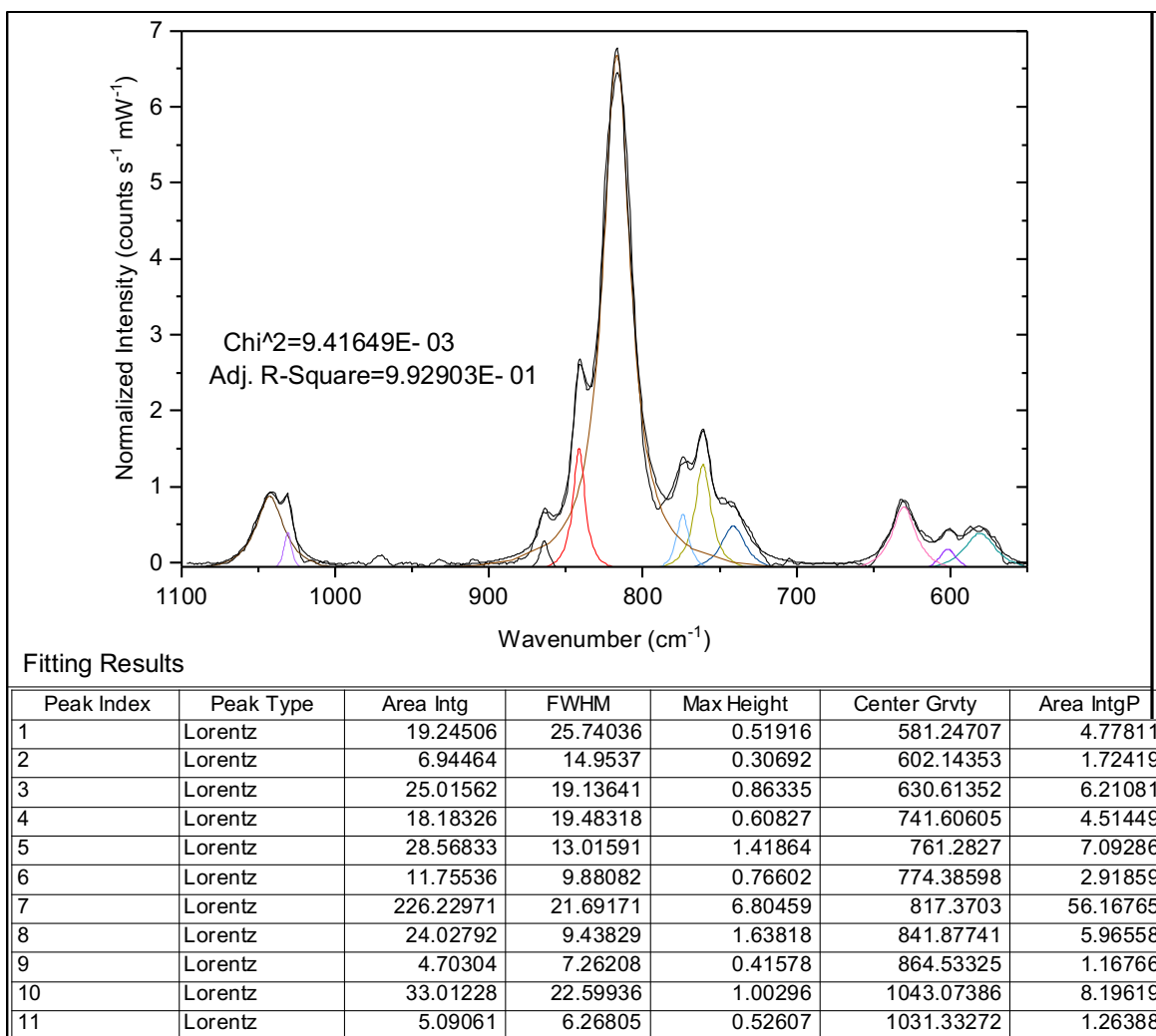


Figure S43. Solid-state Raman spectrum for L^5UO_2Li .

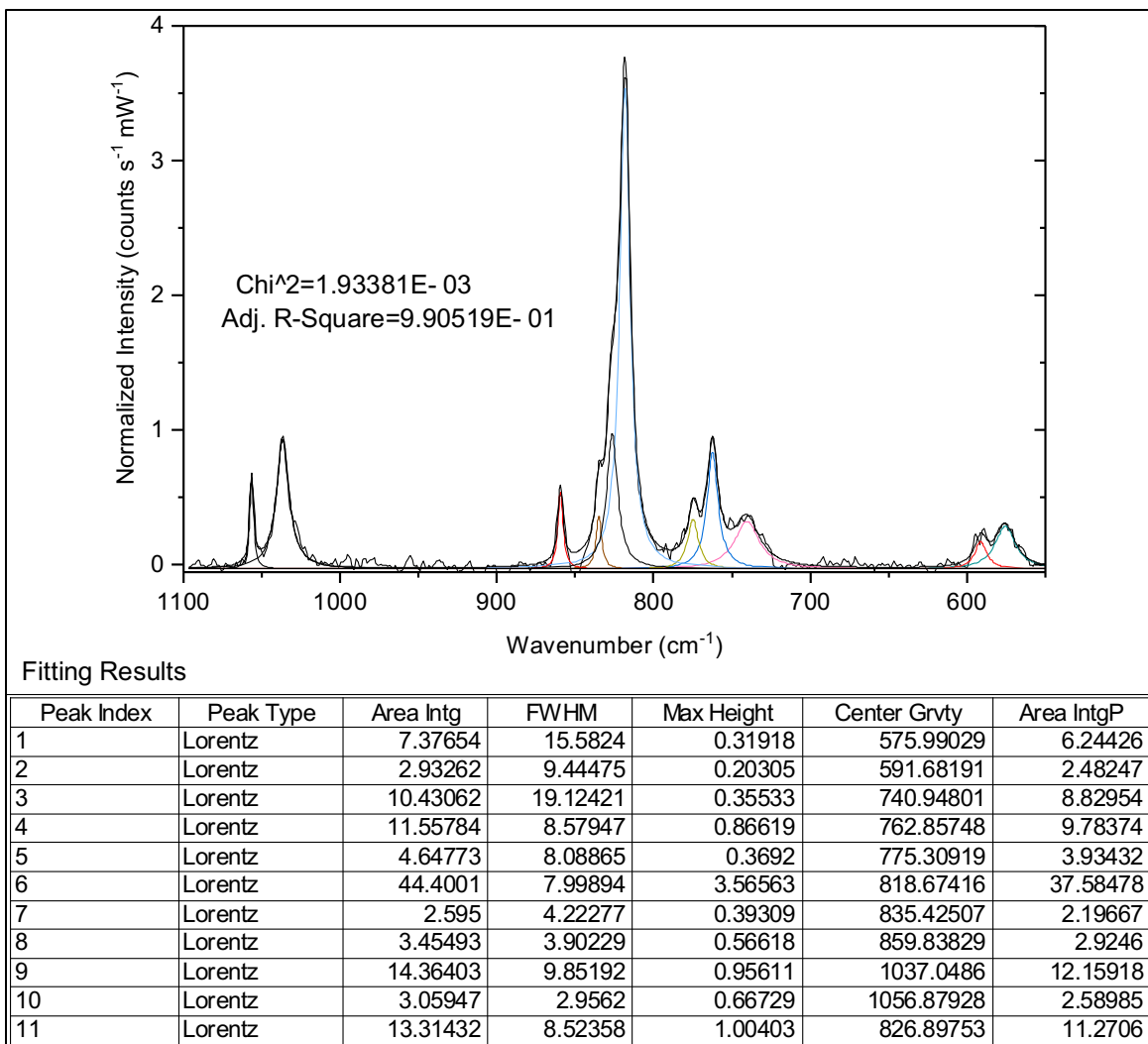


Figure S44. Solid-state Raman spectrum for L^5UO_2Sr .

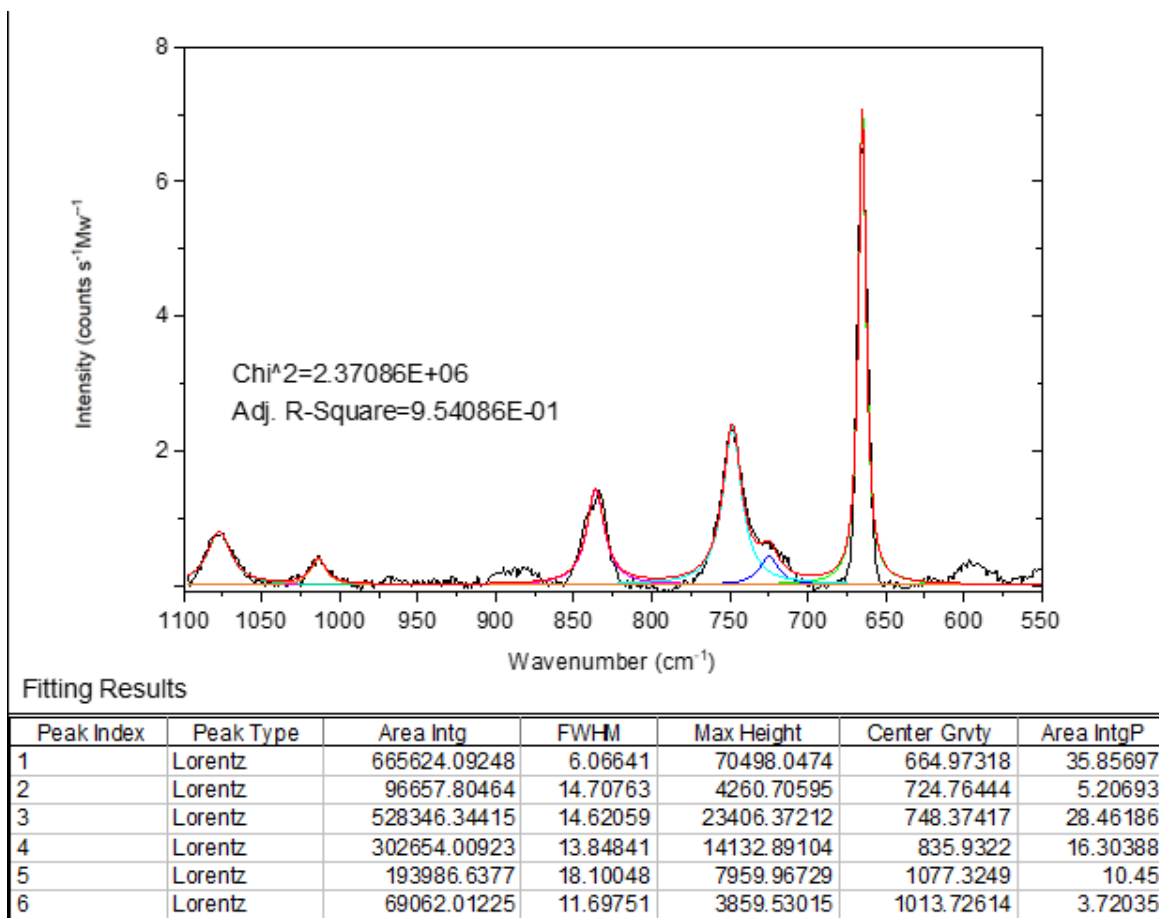


Figure S45. Solid-state Raman spectrum for L⁶ Ligand.

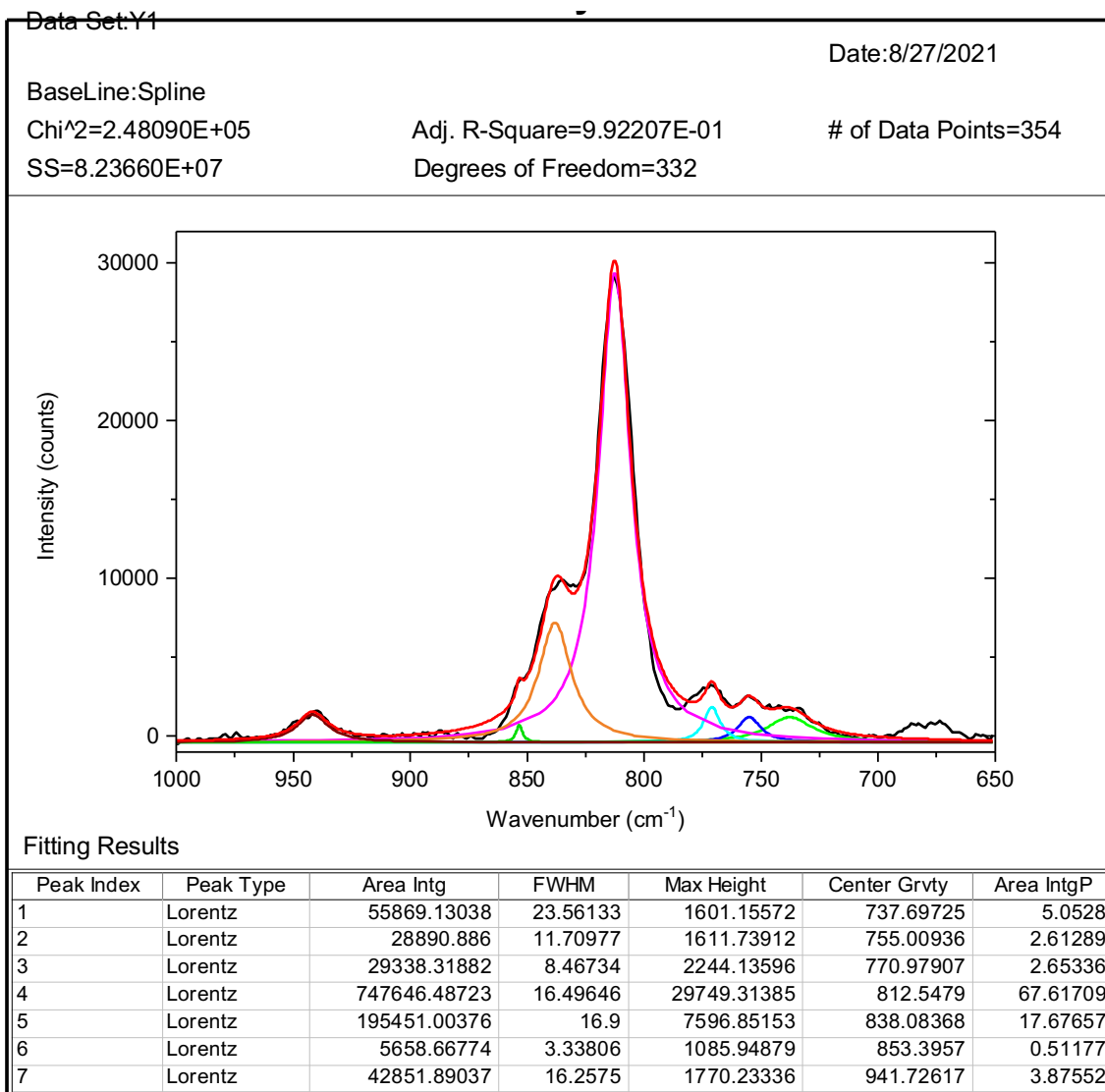


Figure S46. Solid-state Raman spectrum for L⁶UO₂.

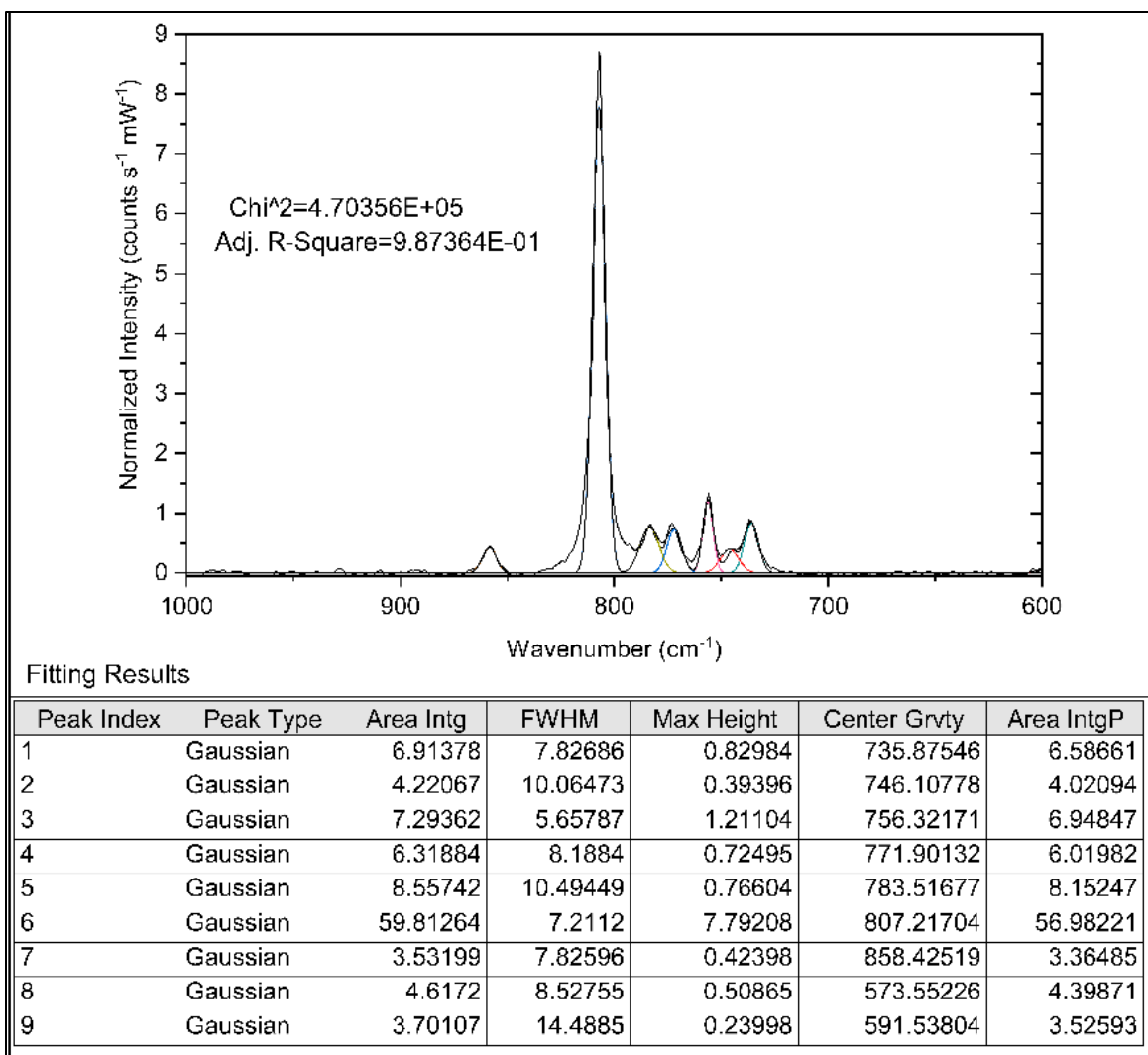


Figure S47. Solid-state Raman spectrum for L⁶UO₂Rb.

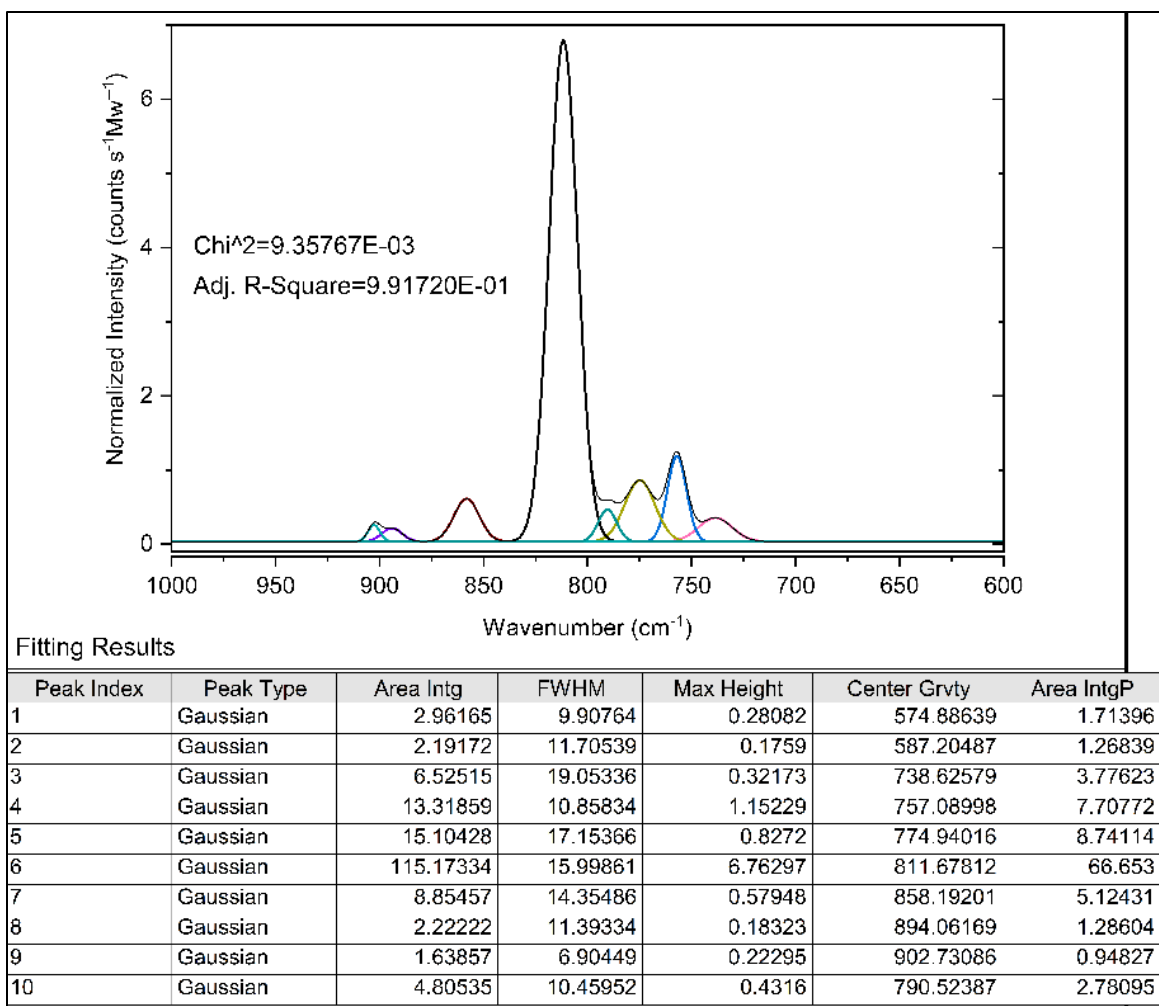


Figure S48. Solid-state Raman spectrum for L⁶UO₂K.

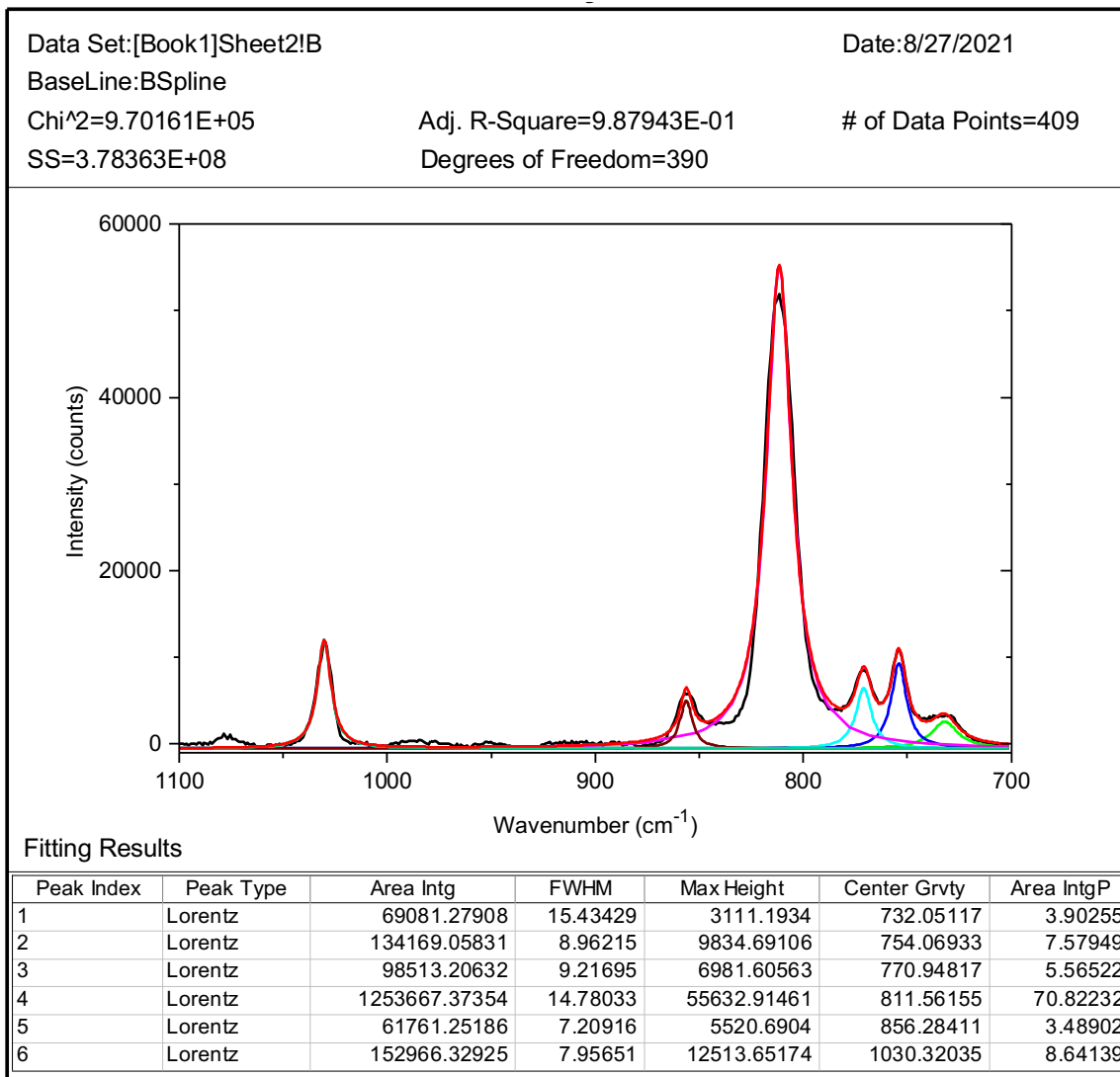


Figure S49. Solid-state Raman spectrum for L⁶UO₂Na.

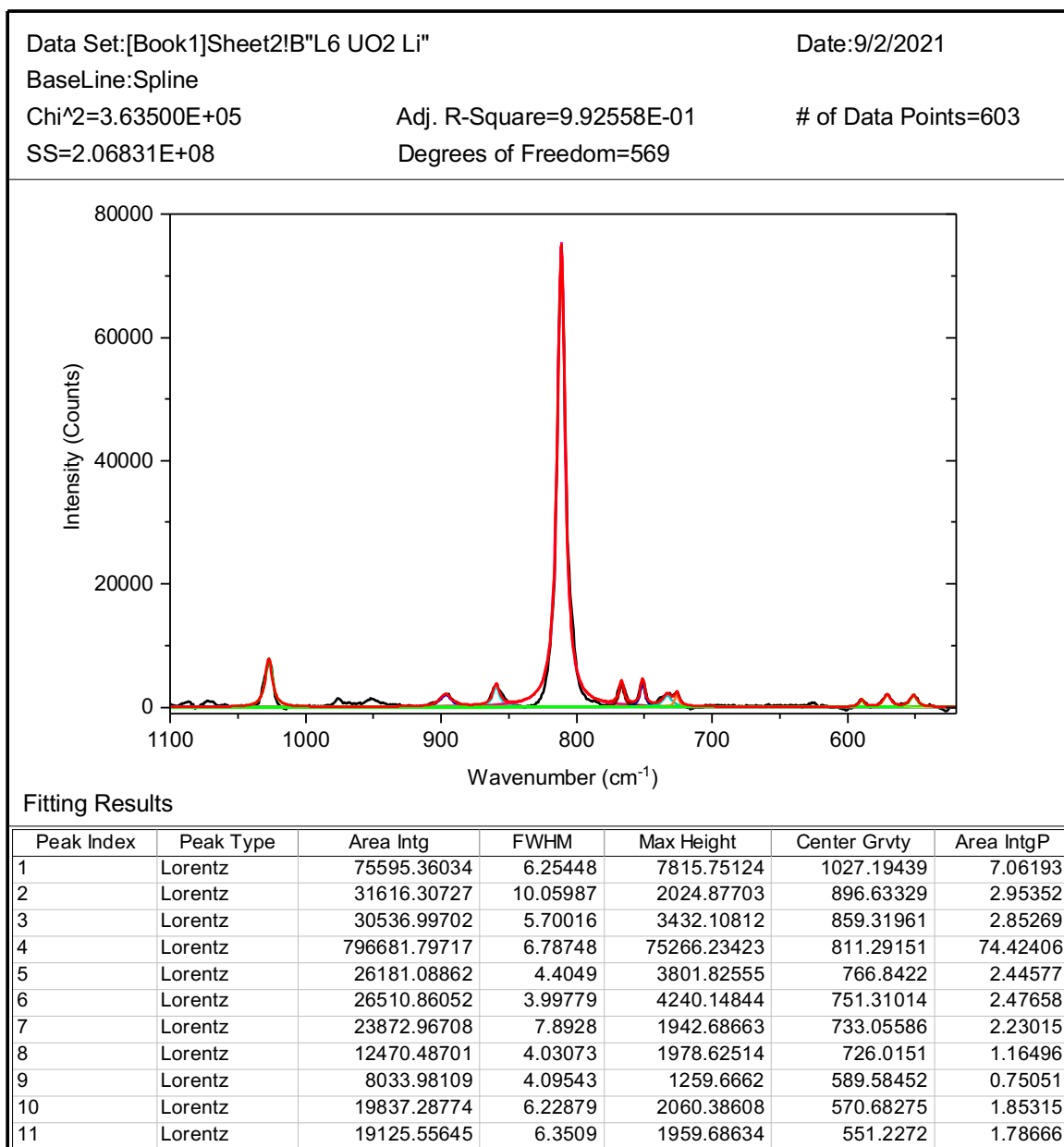


Figure S50. Solid-state Raman spectrum for L⁶UO₂Li.

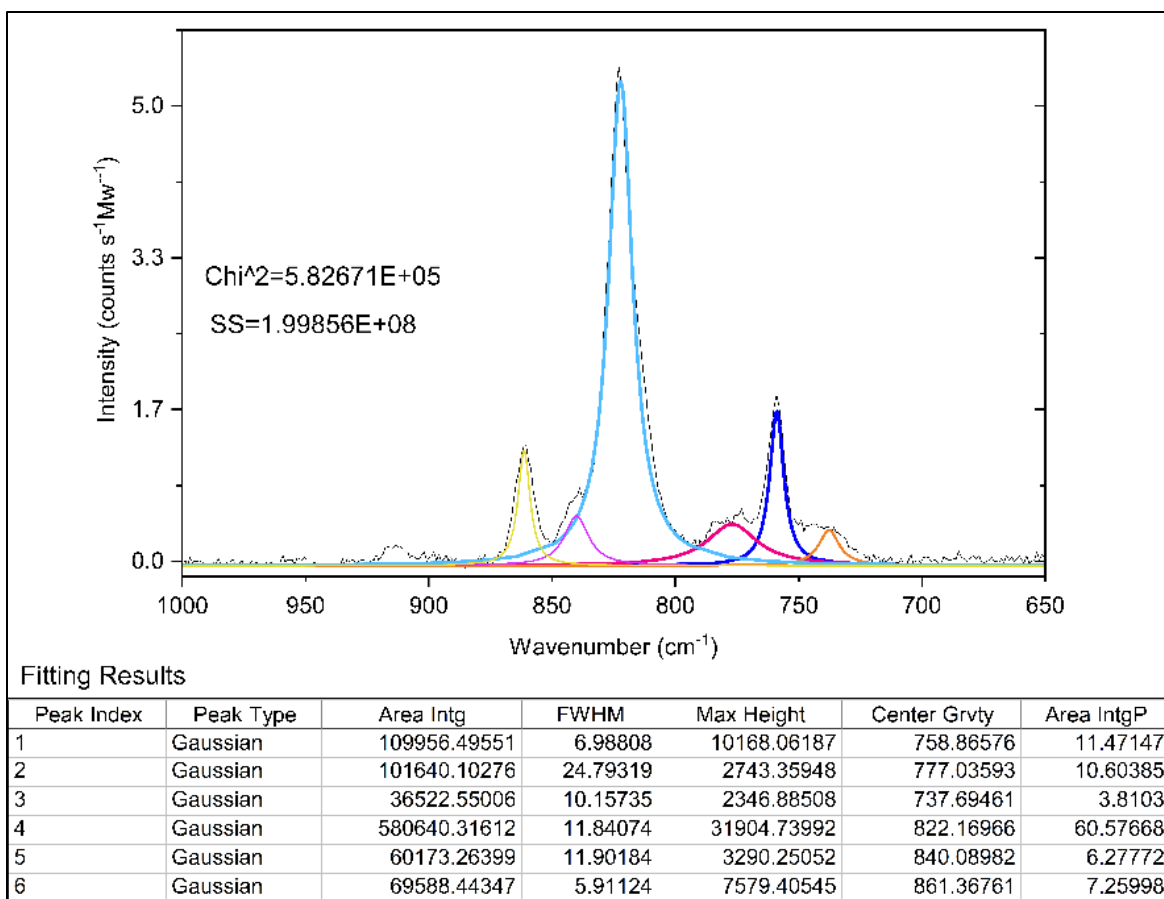


Figure S51. Solid-state Raman spectrum for L⁶UO₂Sr.

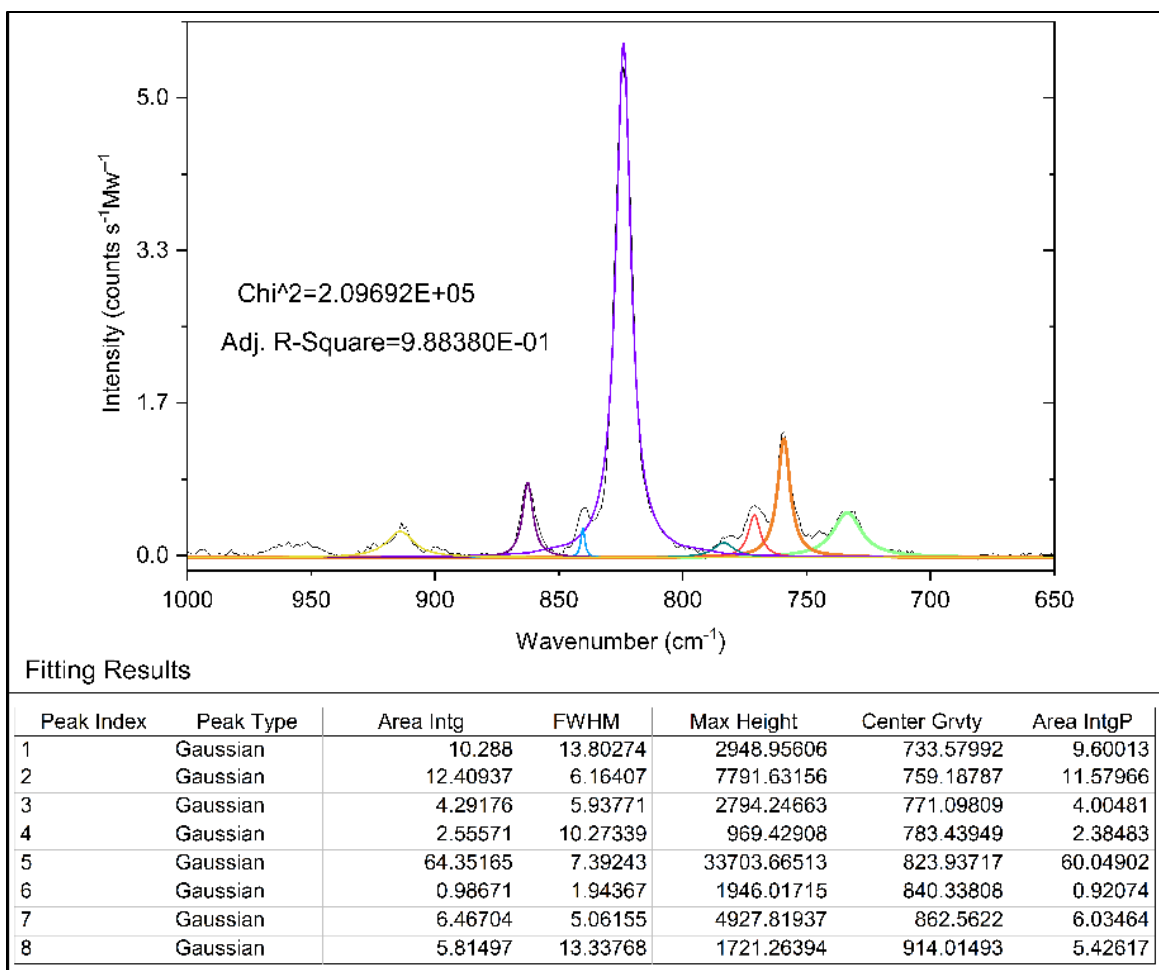


Figure S52. Solid-state Raman spectrum for L⁶UO₂Ca.

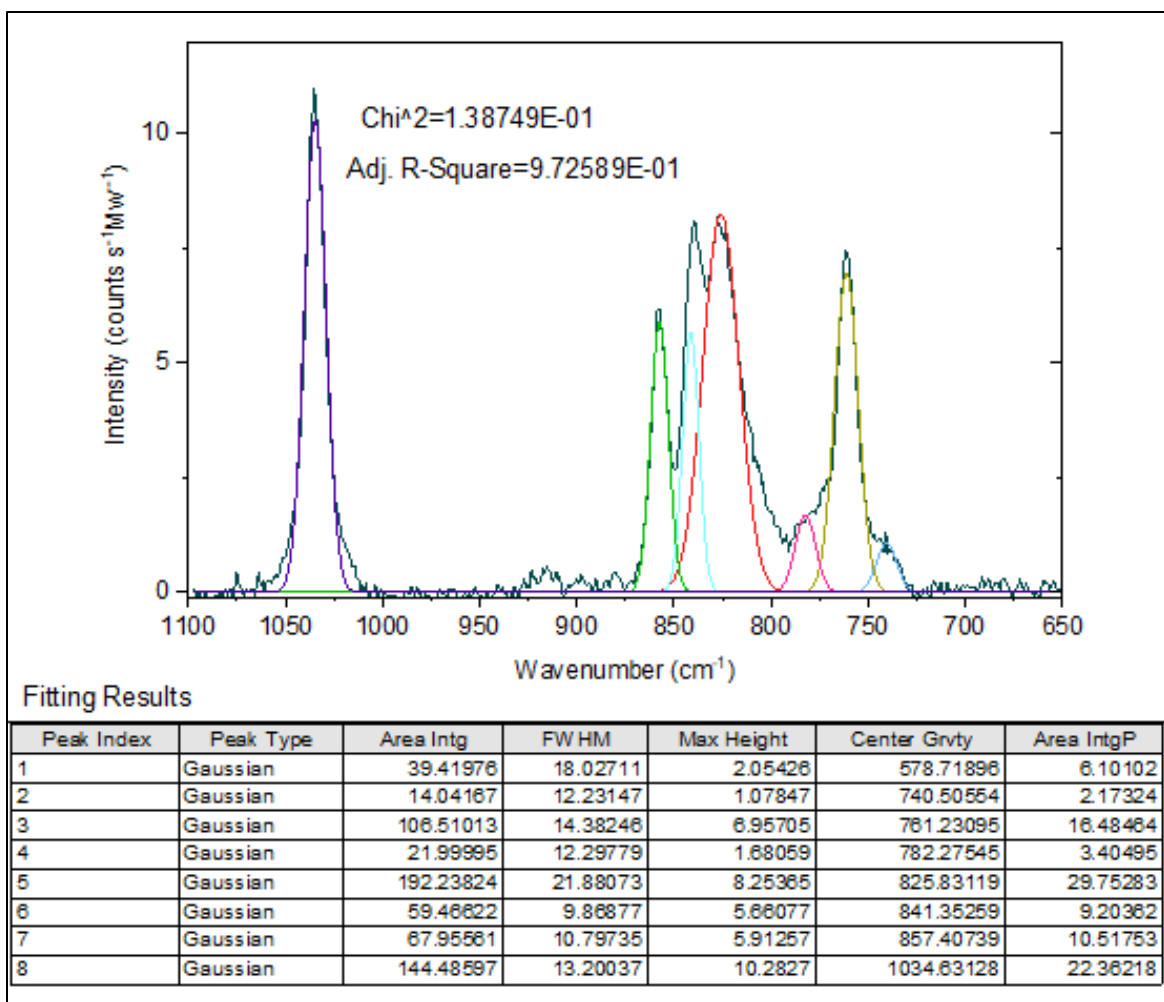


Figure S53. Solid-state Raman spectrum for L⁶UO₂La.

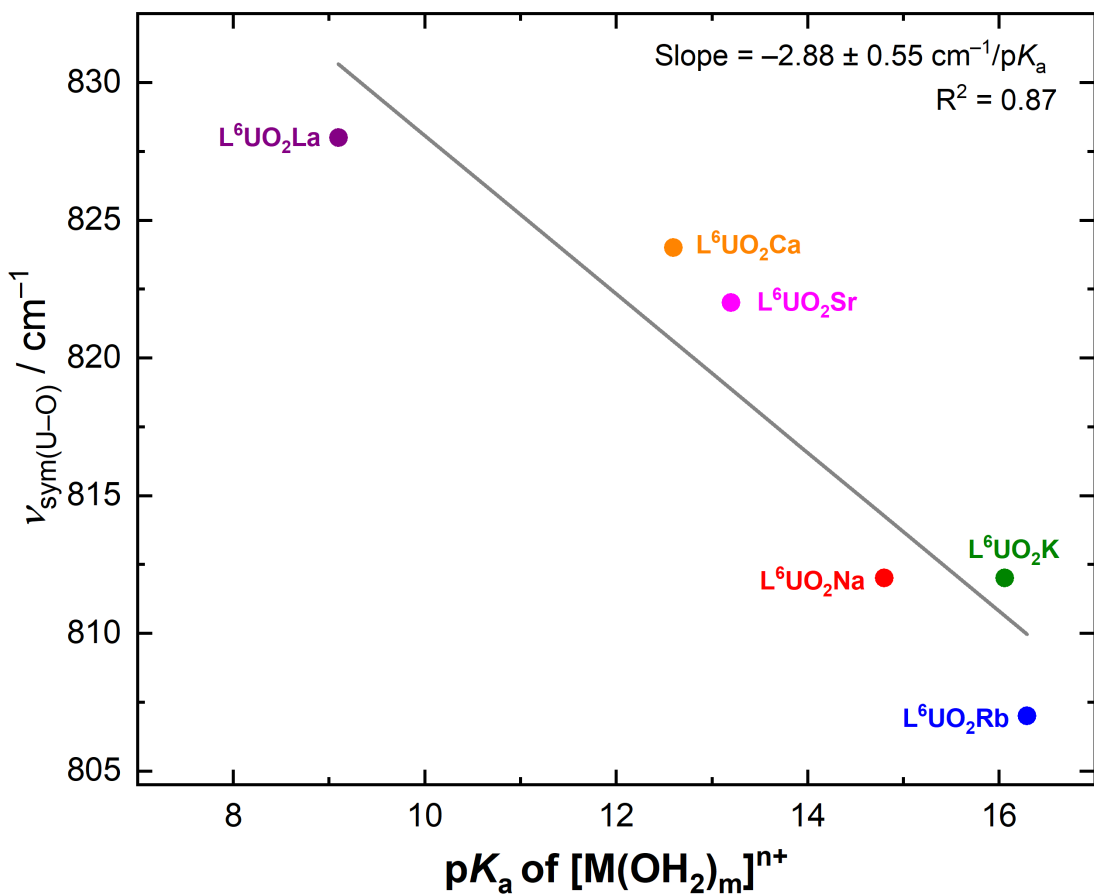


Figure S54. Dependence of the U=O symmetric stretching frequency from Raman spectroscopy of the $\text{L}^6\text{UO}_2\text{M}$ complexes including $\text{L}^6\text{UO}_2\text{La}$ on the Lewis acidity ($\text{p}K_a$) of the corresponding metal aqua complexes.

Solution Raman Spectroscopy

Table S3. Solution-state Raman assignments for L^6UO_2M series. All values mentioned are in cm^{-1} .

Complex	ν_{sym}
L^6UO_2	814.4
L^6UO_2Rb	816.0
L^6UO_2K	815.9
L^6UO_2Na	819.3
L^6UO_2Li	821.3
L^6UO_2Sr	825.0
L^6UO_2Ca	824.5
L^6UO_2La	826.8

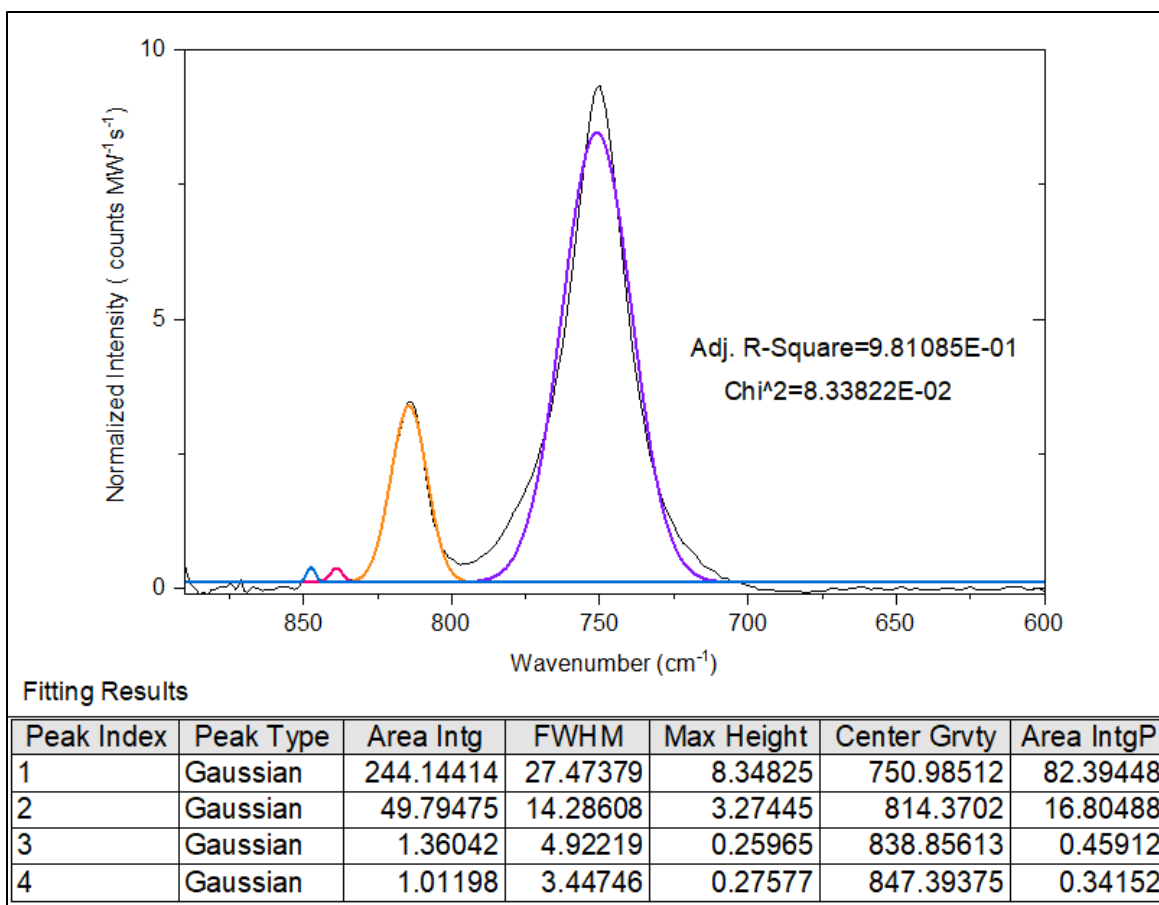


Figure S55. Fitted solution Raman spectrum for L⁶UO₂ in MeCN.

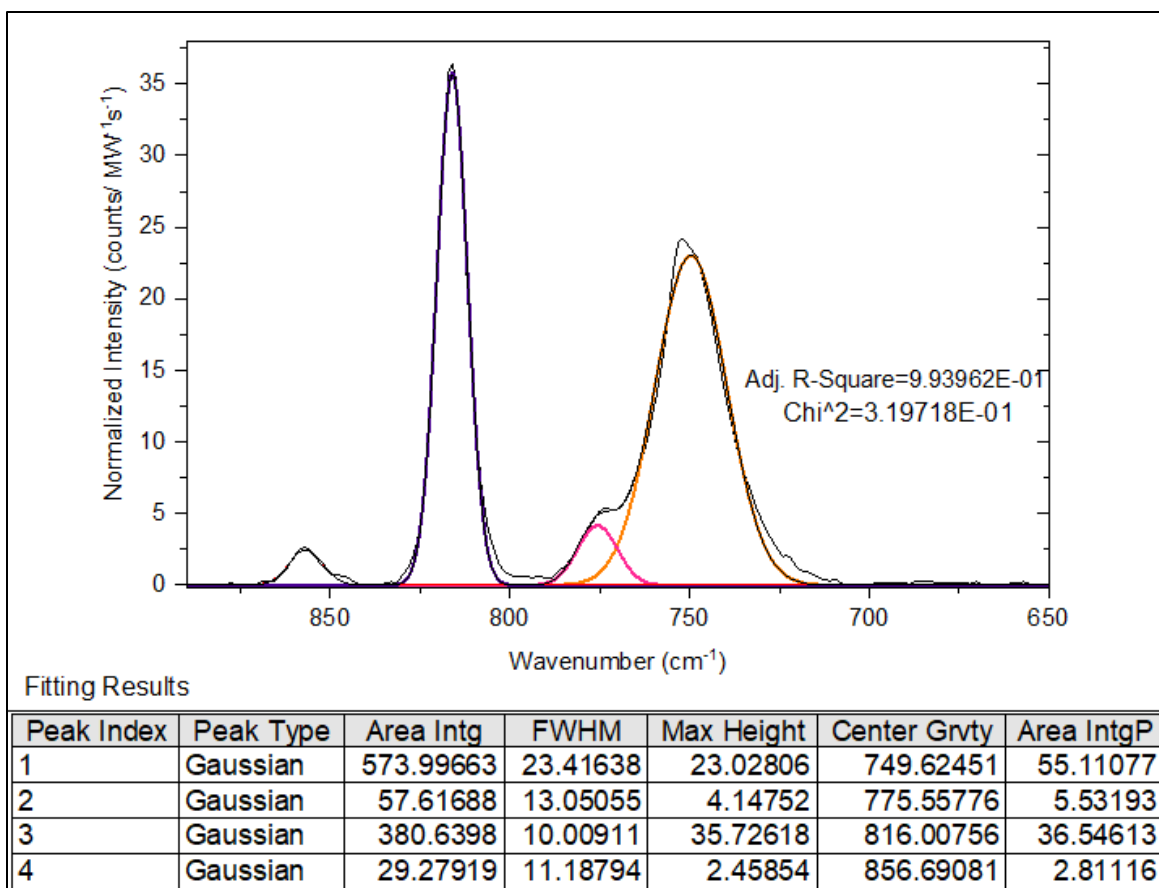
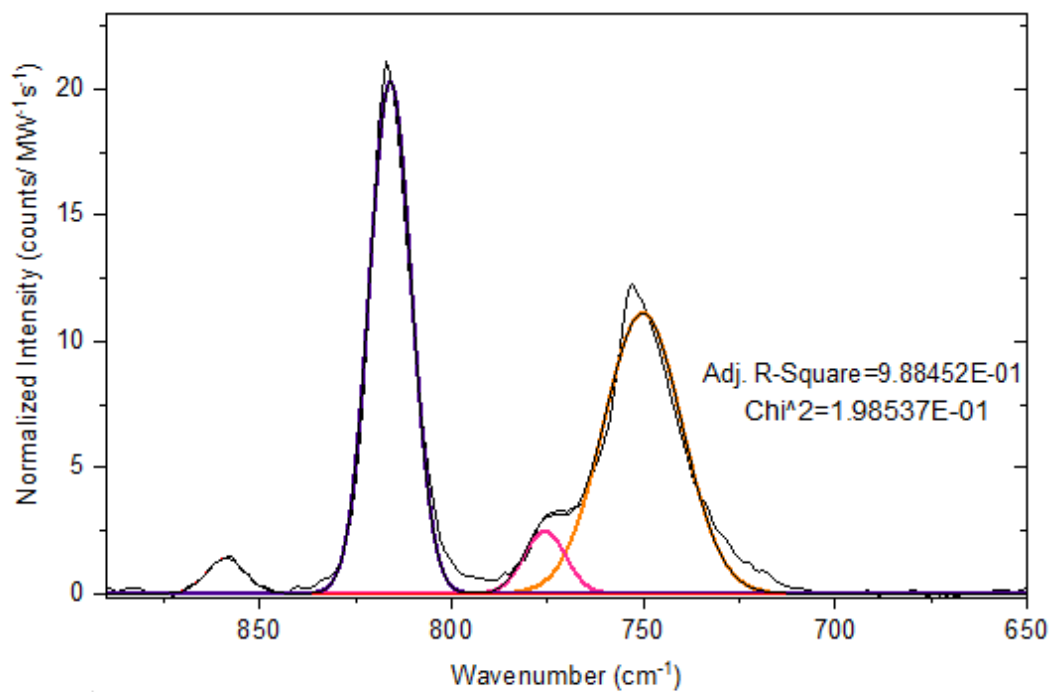


Figure S56. Fitted solution Raman spectrum for **L⁶UO₂Rb** in MeCN.



Fitting Results

Peak Index	Peak Type	Area Intg	FWHM	Max Height	Center Grvty	Area IntgP
1	Gaussian	284.67768	24.07666	11.10772	750.15812	46.37071
2	Gaussian	33.51788	12.75496	2.46868	775.66978	5.45968
3	Gaussian	278.10088	12.87584	20.29058	815.90398	45.29942
4	Gaussian	17.62061	11.81314	1.40127	858.68885	2.87019

Figure S57. Fitted solution Raman spectrum for L⁶UO₂K in MeCN.

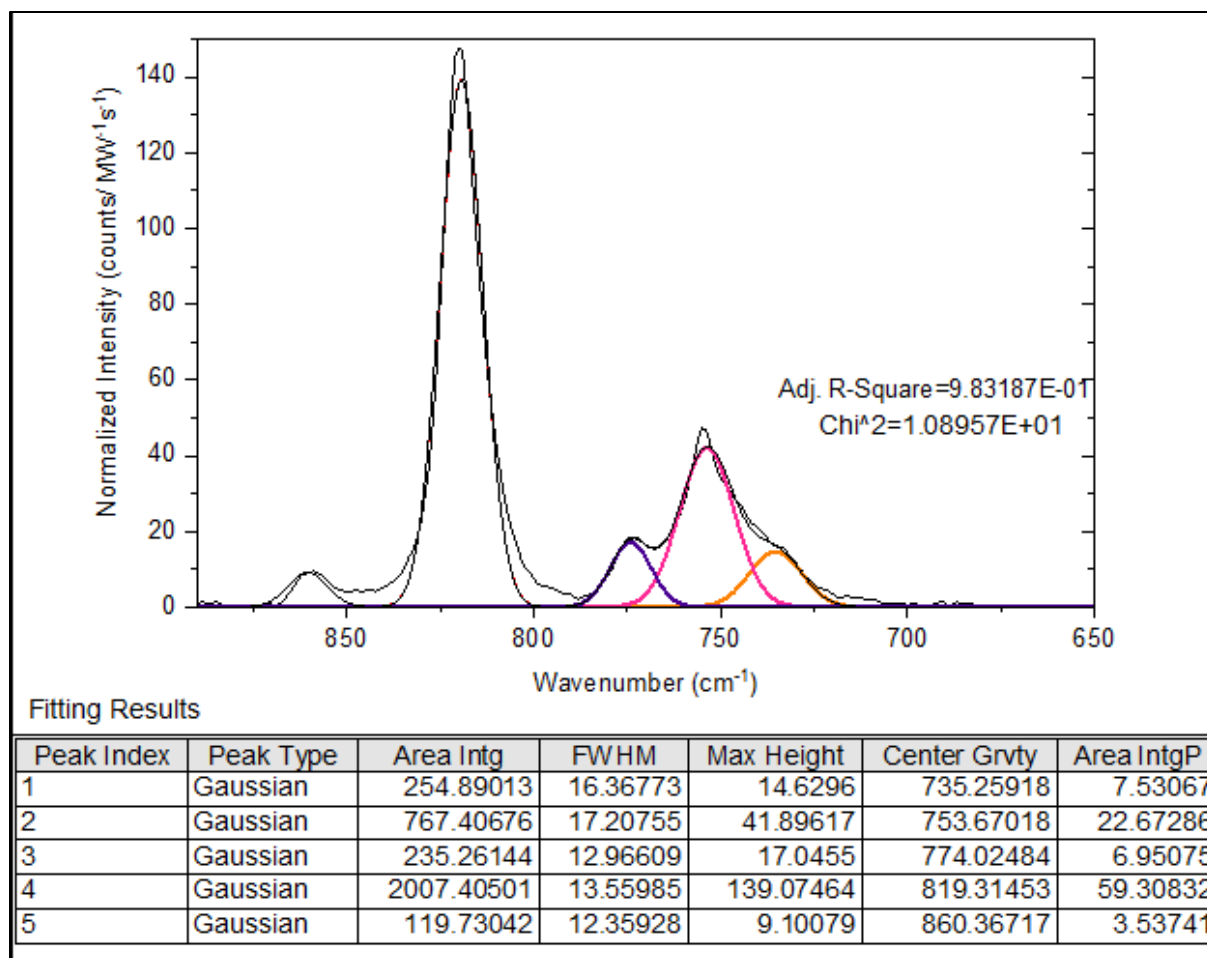


Figure S58. Fitted solution Raman spectrum for L⁶UO₂Na in MeCN.

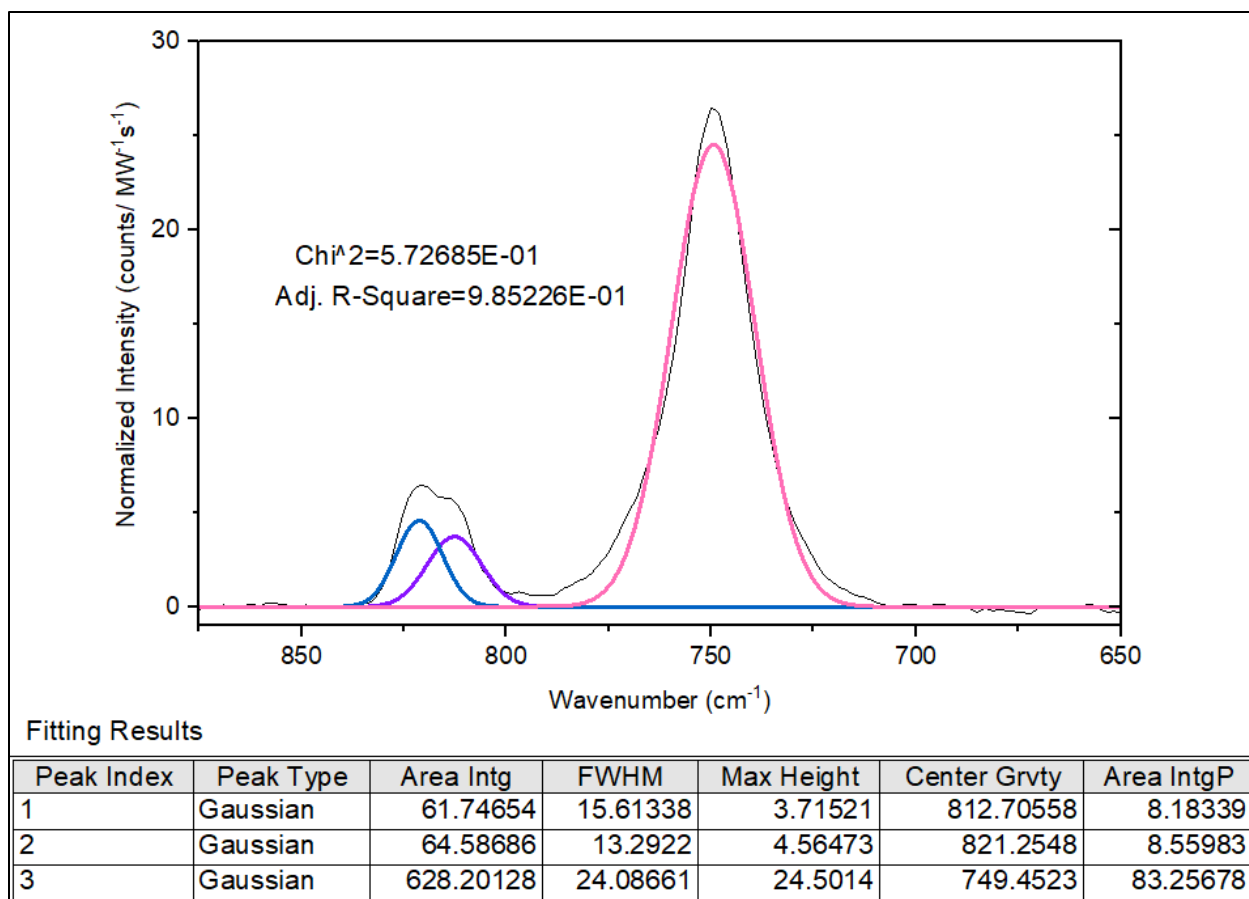


Figure S59. Fitted solution Raman spectrum for L^6UO_2Li in MeCN.

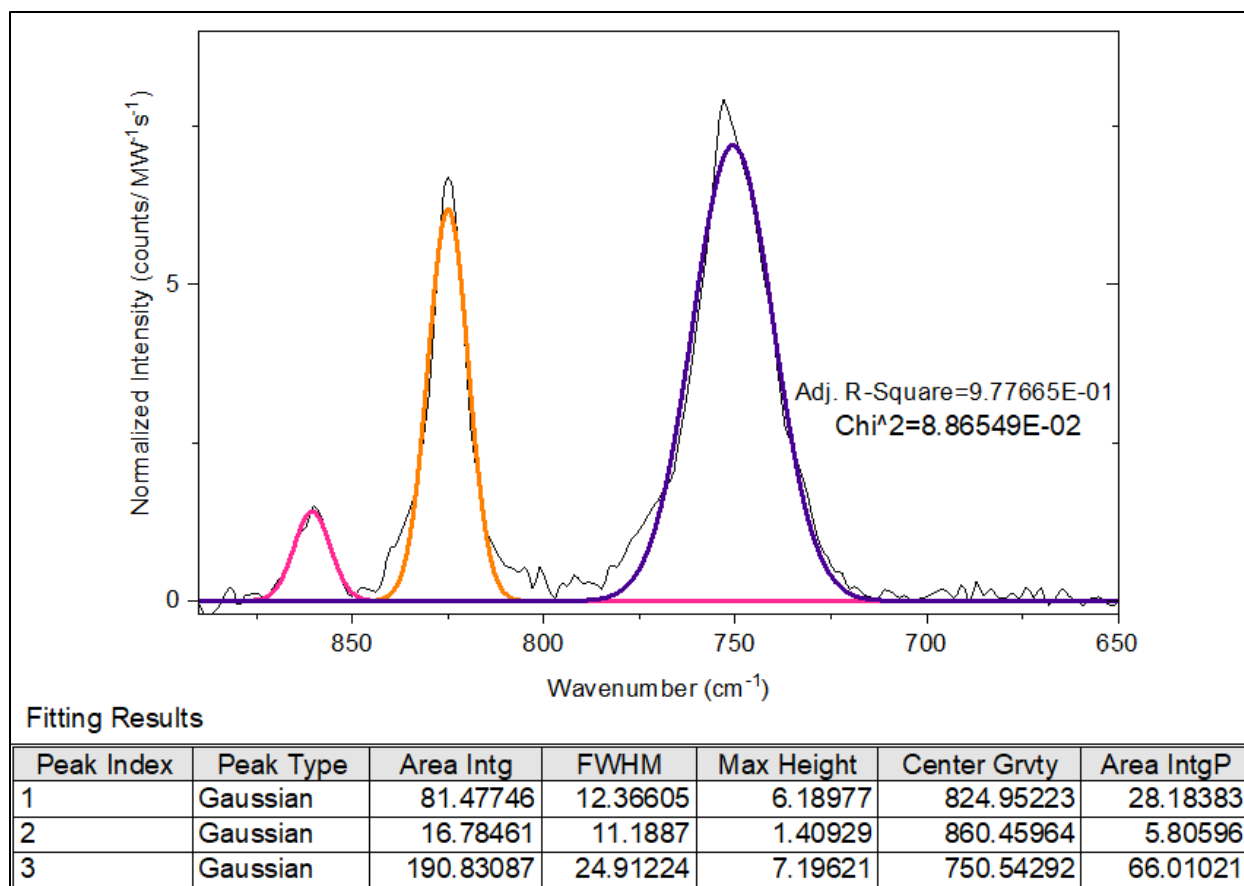


Figure S60. Fitted solution Raman spectrum for L⁶UO₂Sr in MeCN.

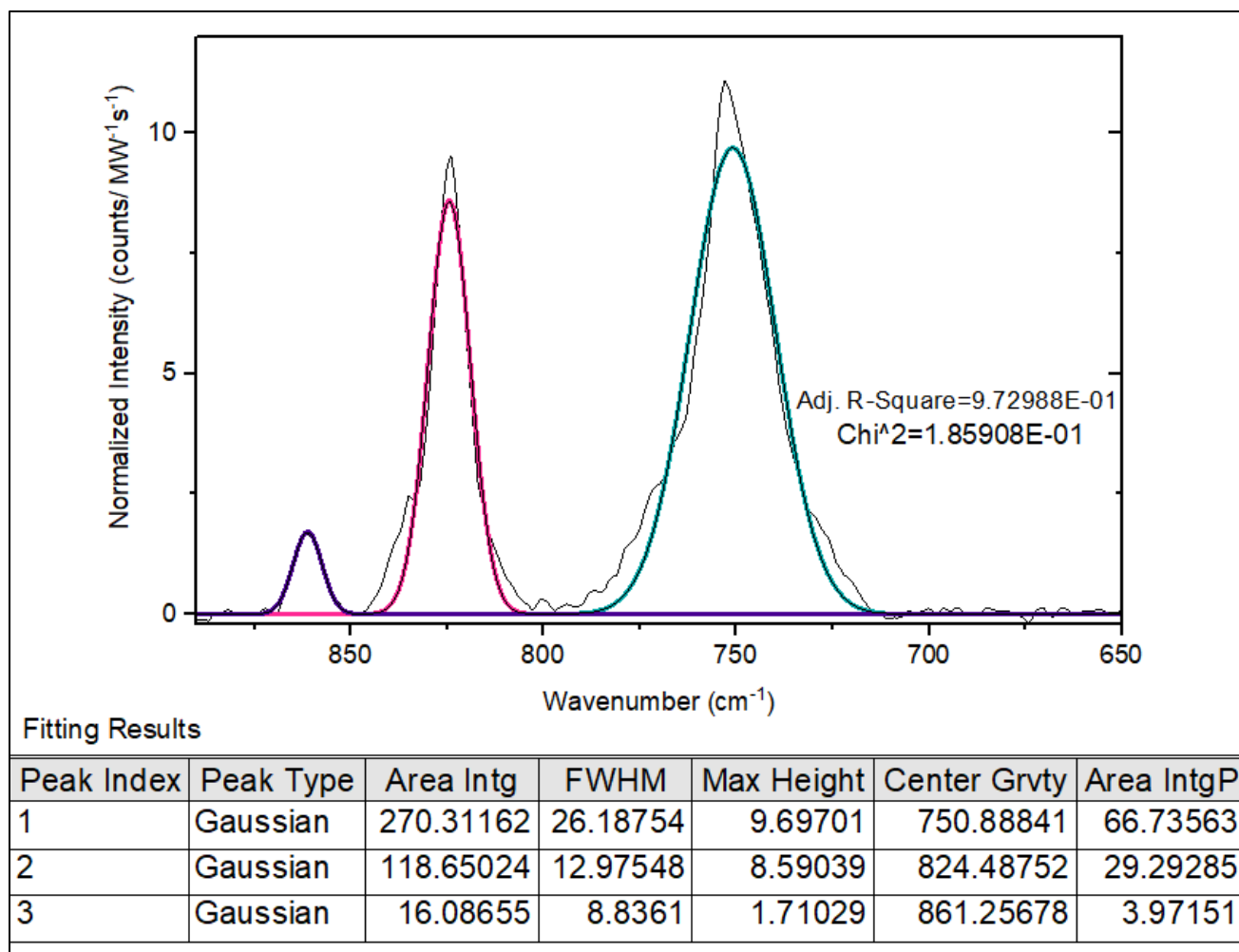


Figure S61. Fitted solution Raman spectrum for L^6UO_2Ca in MeCN.

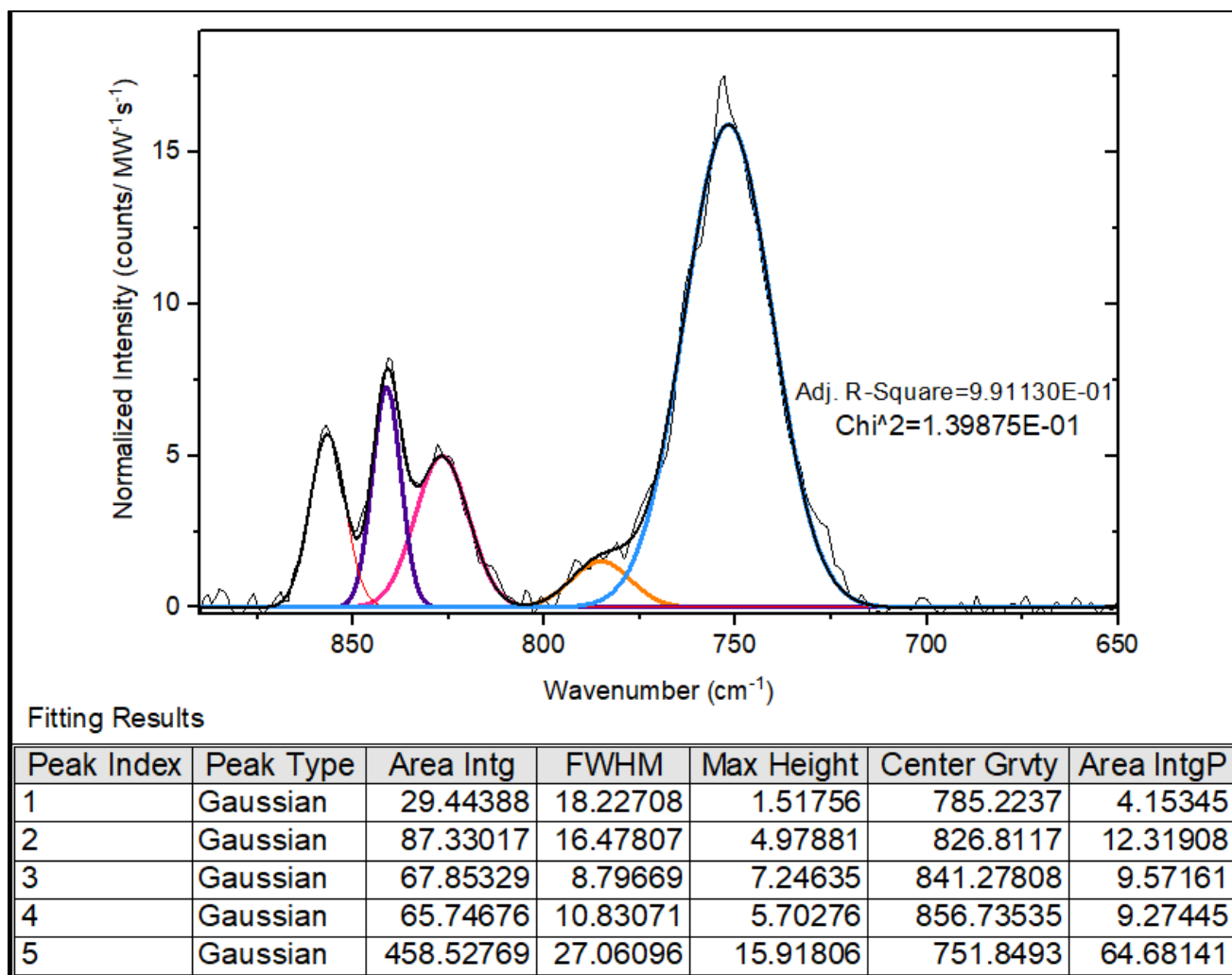


Figure S62. Fitted solution Raman spectrum for L⁶UO₂La in MeCN.

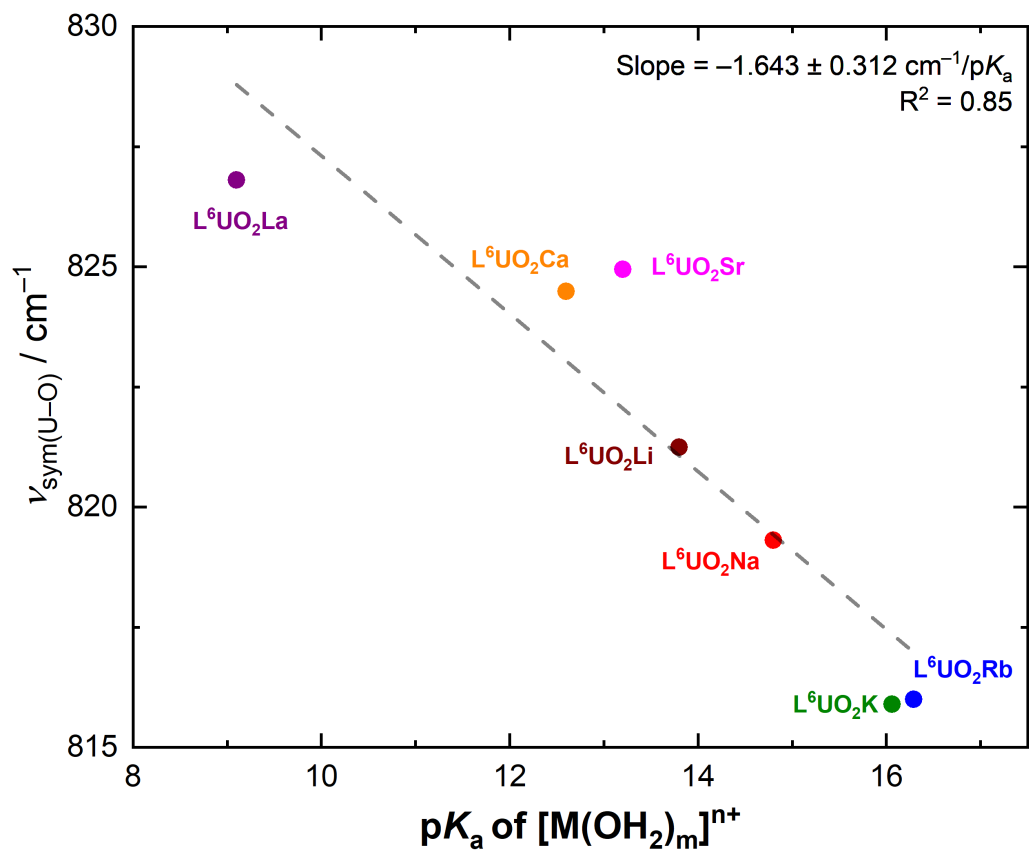


Figure S63. Dependence of the U=O symmetric stretching frequency from solution Raman spectroscopy of the $\text{L}^6\text{UO}_2\text{M}$ complexes on the Lewis acidity ($\text{p}K_a$) of the corresponding metal aqua complexes.

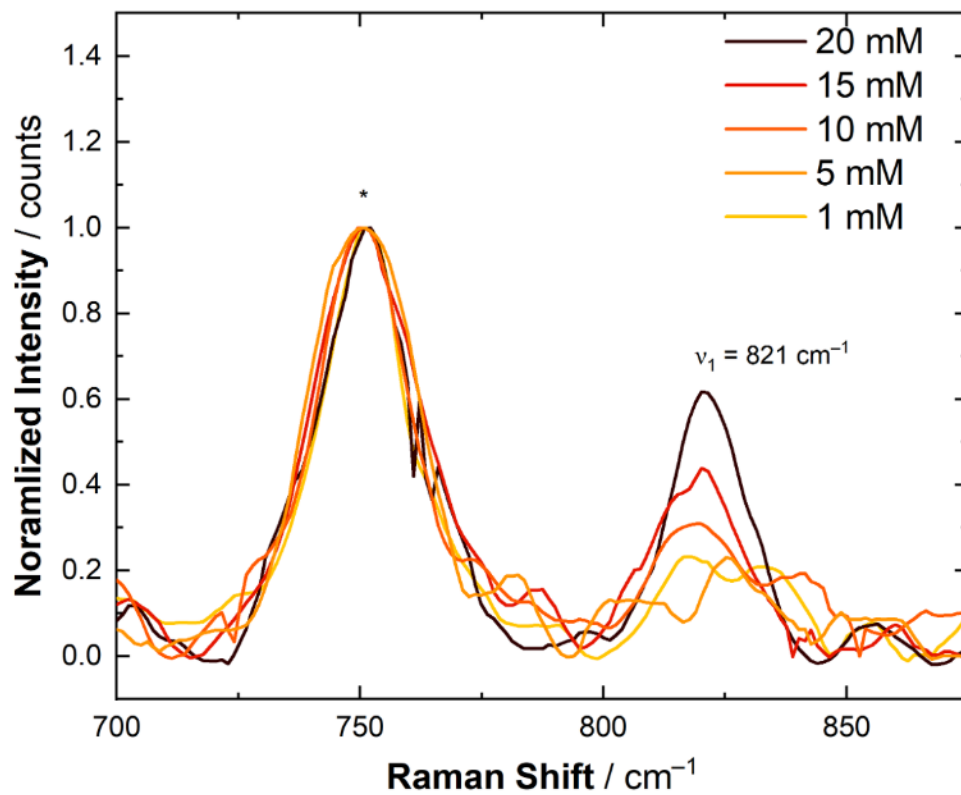


Figure S64. Filtered solution Raman spectrum of L^6UO_2Li at varied concentrations. All intensities are normalized to the MeCN signal denoted by asterisk (*).

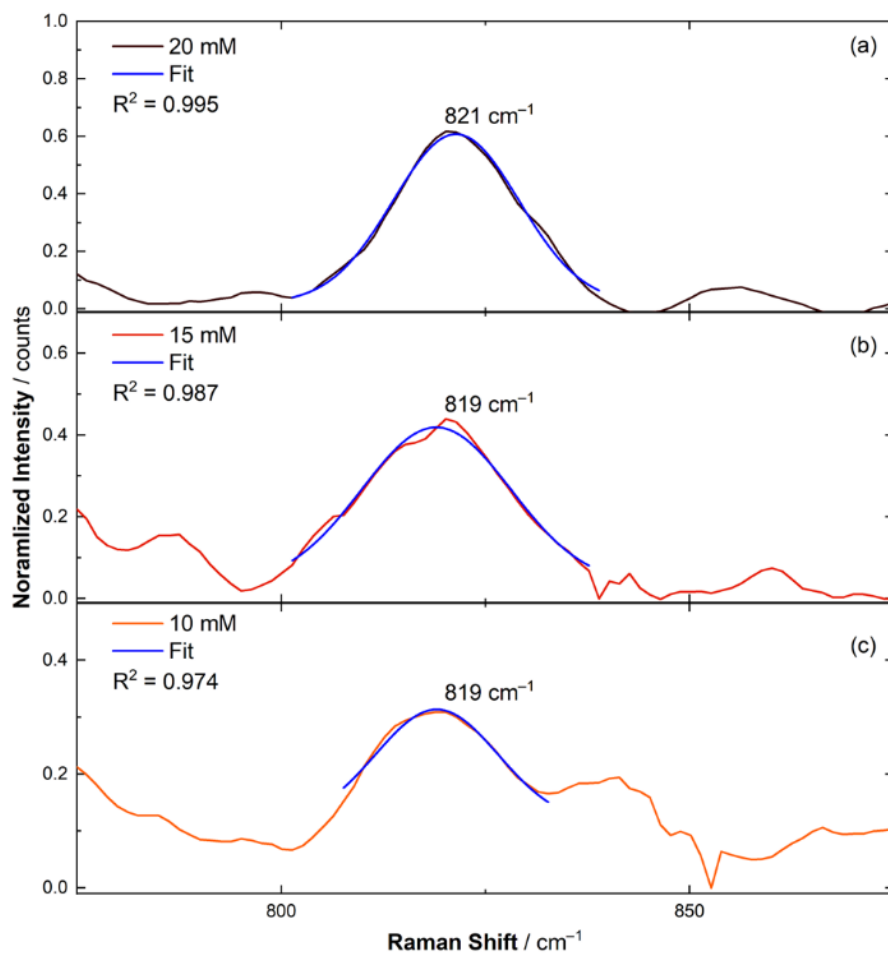
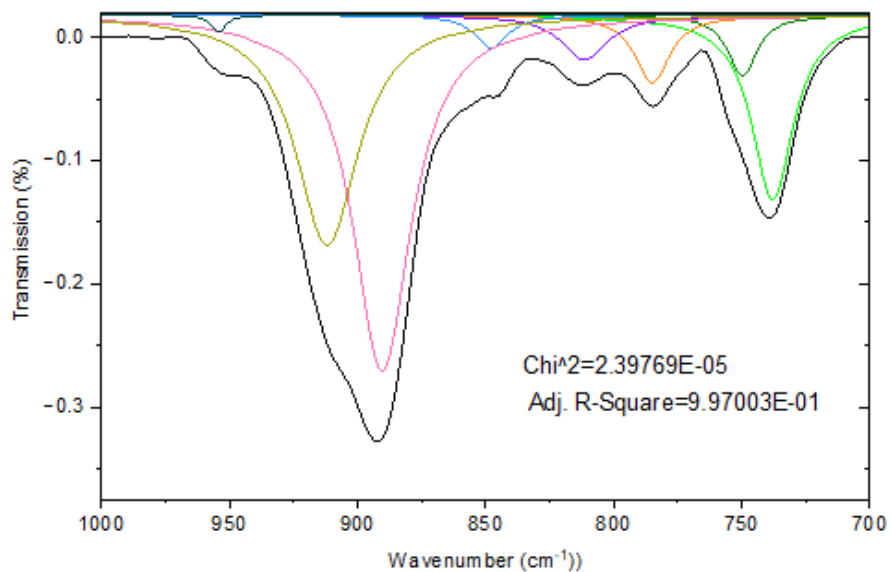


Figure S65. Filtered solution Raman spectra of $\text{L}^6\text{UO}_2\text{Li}$ at 20, 15, and 10 mM. All spectra were fitted to Gaussian curves, with the Raman shifts corresponding to the peaks of each fit listed. All intensities are normalized to the MeCN signal, denoted by an asterisk (*) in Figure S64.

Table S4. Concentrations of $\text{L}^6\text{UO}_2\text{Li}$, R^2 values of the fits, Raman shifts at the maxima of the fits, and full width at half maximum (FWHM) values for each panel in Figure S65.

Panel	Conc (mM)	R^2	xc (cm^{-1})	FWHM (cm^{-1})
a	20	0.995	821	18.2
b	15	0.987	819	21.5
c	10	0.974	819	17.7

Solid-state Infrared Spectroscopy



Fitting Results

Peak Index	Peak Type	Area Intg	FWHM	Max Height	Center Grvty	Area IntgP
1	Lorentz	-4.22189	19.7938	-0.14978	737.90506	-14.85529
2	Lorentz	-1.01632	13.7521	-0.04966	749.66259	-3.57607
3	Lorentz	-1.36893	16.5252	-0.05511	784.88624	-4.81676
4	Lorentz	-1.20174	22.1096	-0.03643	811.37009	-4.22849
5	Lorentz	-0.63546	15.6764	-0.02669	847.66698	-2.23595
6	Lorentz	-11.7359	27.6166	-0.2886	890.36494	-41.29447
7	Lorentz	-8.09054	29.8255	-0.18673	911.90973	-28.4677
8	Lorentz	-0.14928	7.07513	-0.01383	954.24867	-0.52526

Figure S66. Mid-IR spectrum for L^6UO_2 fit to Lorentzian functions.

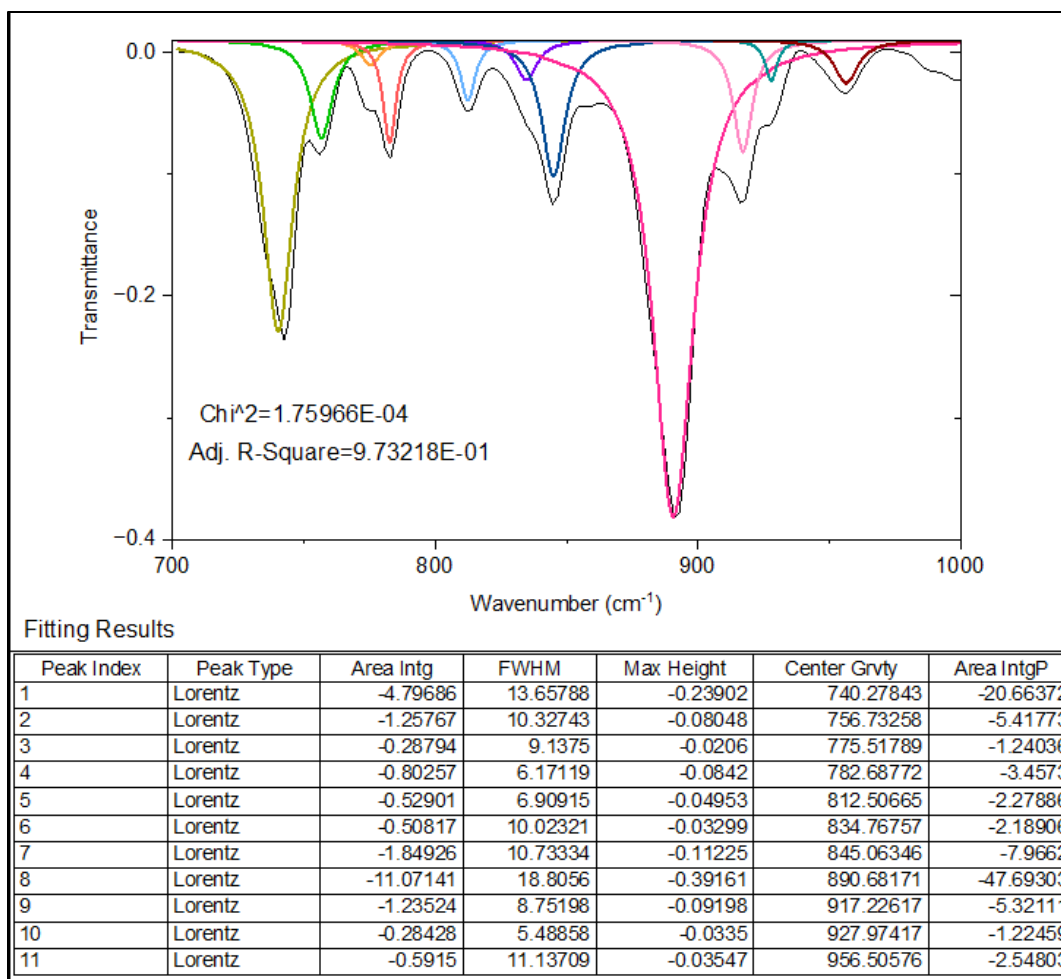
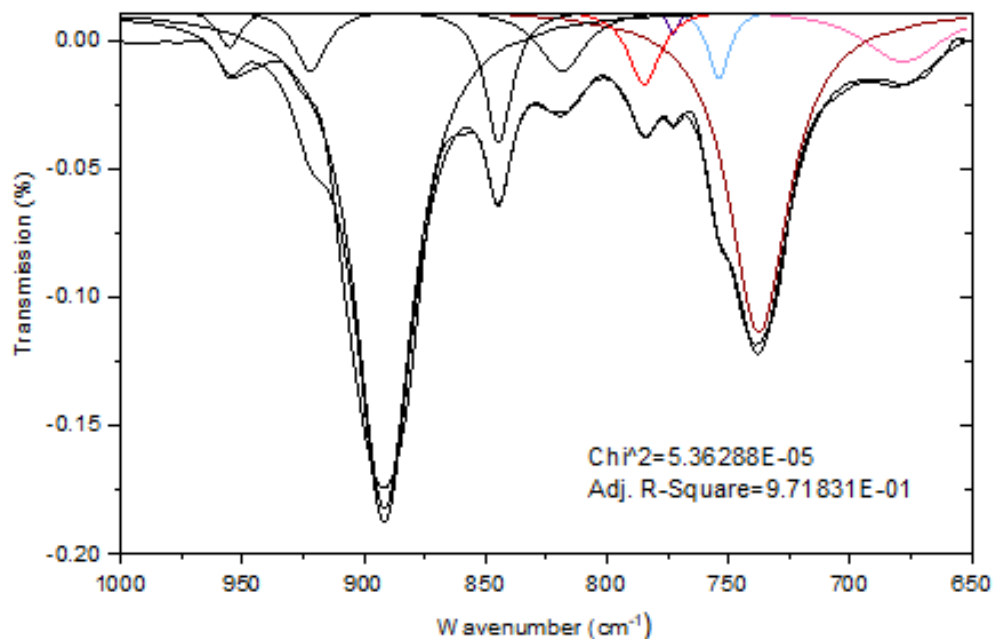


Figure S67. Mid-IR spectrum for L^6UO_2Rb fit to Lorentzian functions.



Peak Ind	Peak Ty	Area In	FWHM	Max Hei	Center Gr	Area Int
1	Lorentz	-1.03	40.711	-0.02086	678.1571	-5.4163
2	Lorentz	-5.49	29.894	-0.12614	737.4647	-28.94
3	Lorentz	-0.45	10.755	-0.02751	753.9250	-2.391
4	Lorentz	-0.09	5.3373	-0.01042	772.7444	-0.456
5	Lorentz	-0.73	16.030	-0.0298	784.6885	-3.833
6	Lorentz	-0.87	23.804	-0.02444	818.5526	-4.609
7	Lorentz	-1.09	13.614	-0.05233	844.5374	-5.752
8	Lorentz	-8.34	28.996	-0.19484	891.6063	-43.97
9	Lorentz	-0.27	11.995	-0.01514	955.3578	-1.436
10	Lorentz	-0.61	16.469	-0.02445	921.9648	-3.195

Figure S68. Mid-IR spectrum for L^6UO_2Na fit to Lorentzian functions.

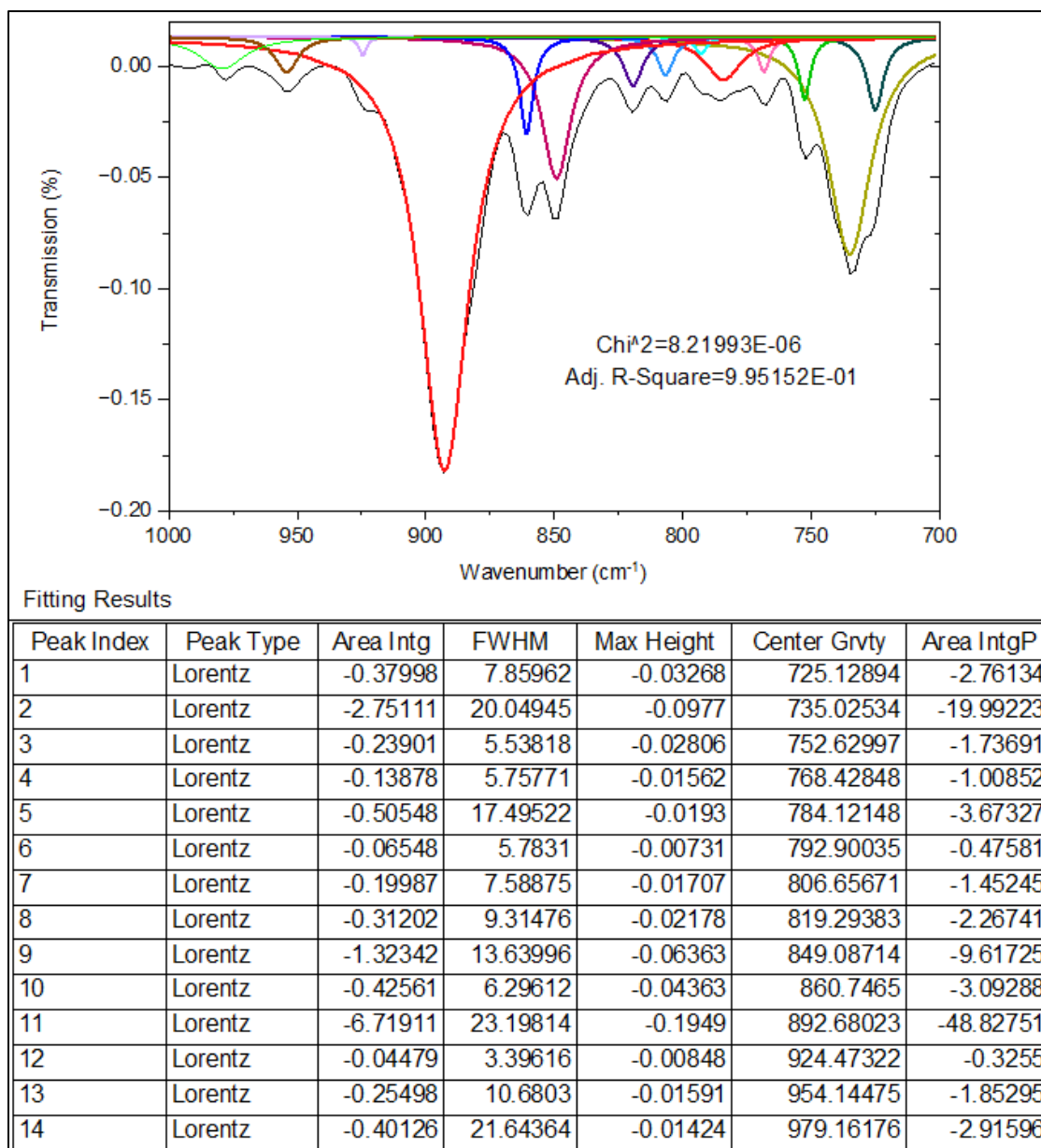


Figure S69. Mid-IR spectrum for L⁶UO₂Li fit to Lorentzian functions.

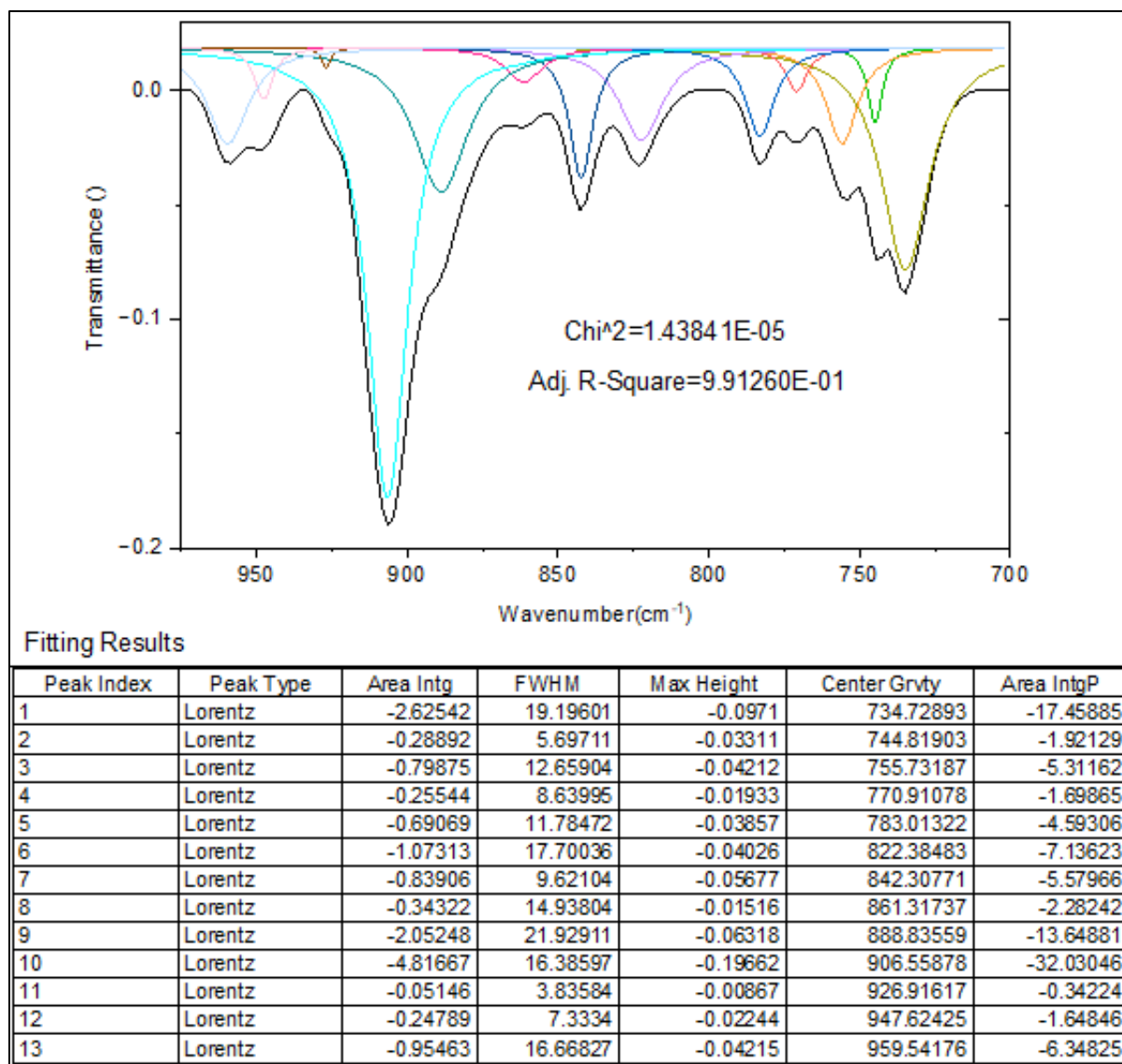


Figure S70. Mid-IR spectrum for L⁶UO₂Ca fit to Lorentzian functions.

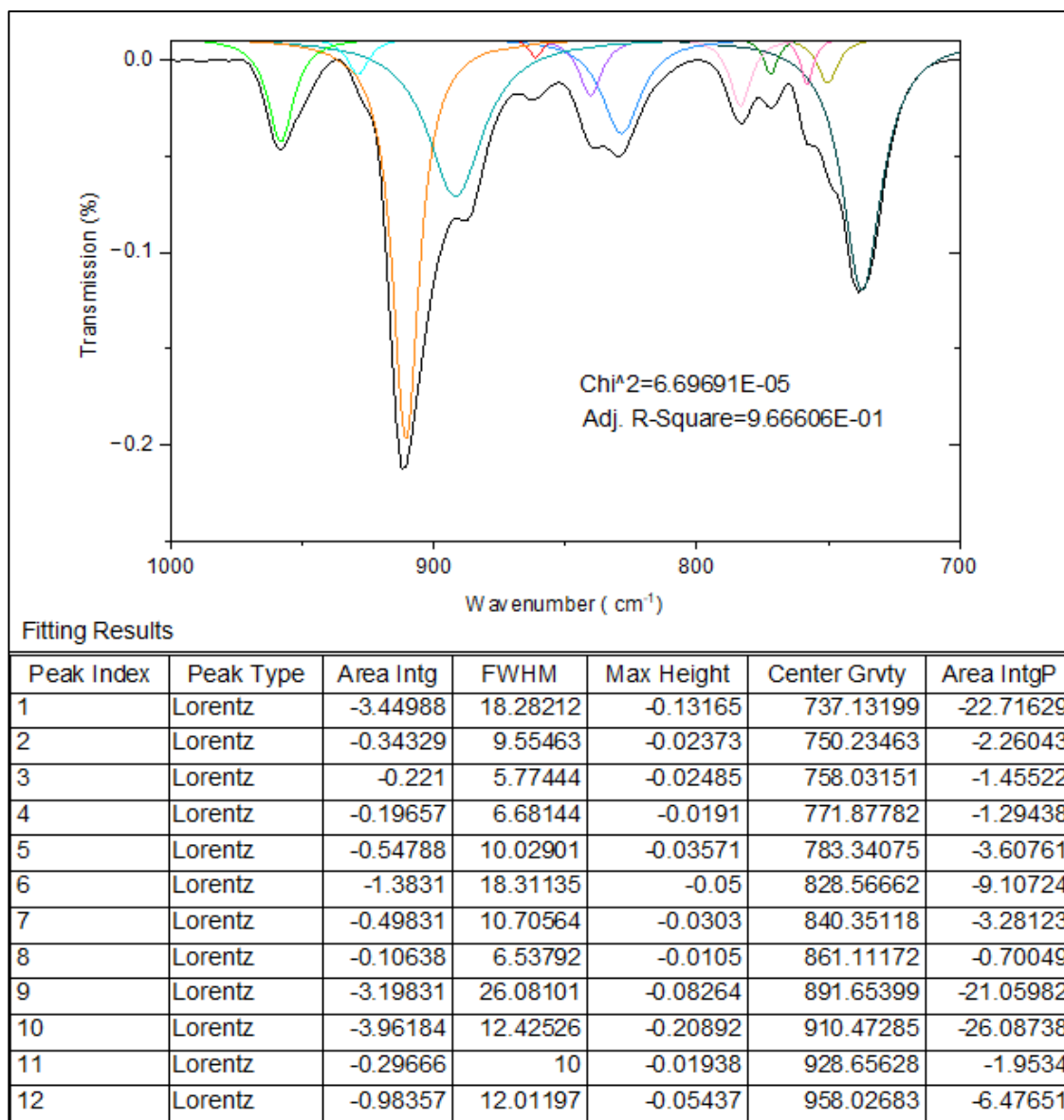


Figure S71. Mid-IR spectrum for L⁶UO₂Sr fit to Lorentzian functions.

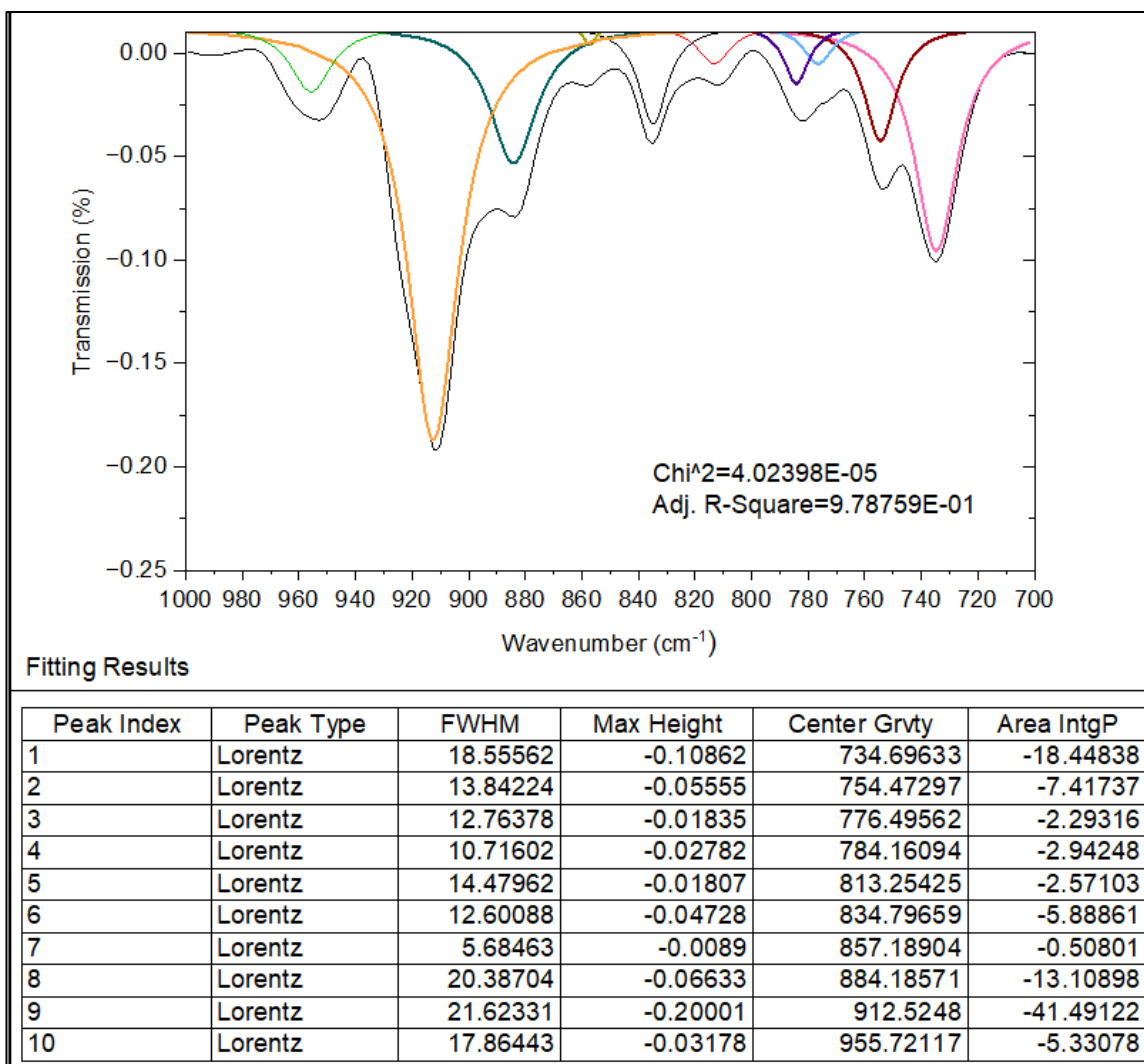


Figure S72. Mid-IR spectrum for L⁶UO₂La fit to Lorentzian functions.

Solid-state Far Infrared Spectroscopy

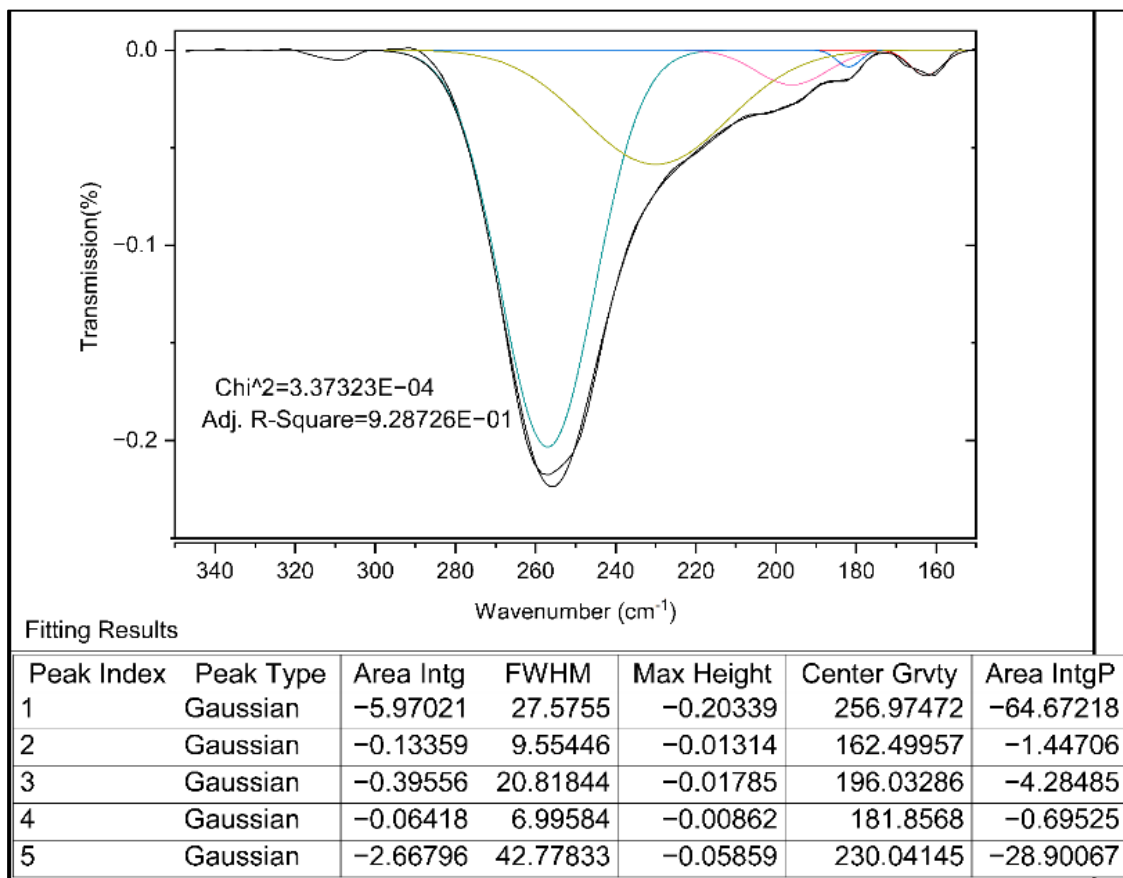


Figure S73. Far-IR spectrum for L^6UO_2 fit to Gaussian functions.

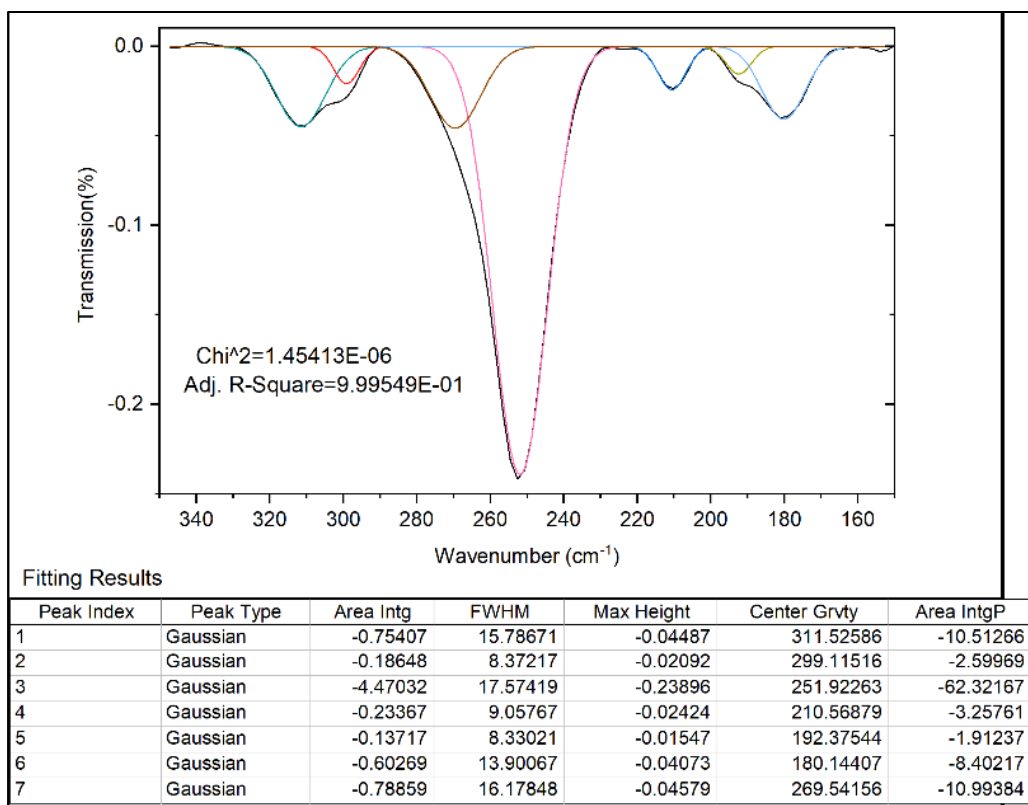


Figure S74. Far-IR spectrum for L⁶UO₂Sr fit to Gaussian functions.

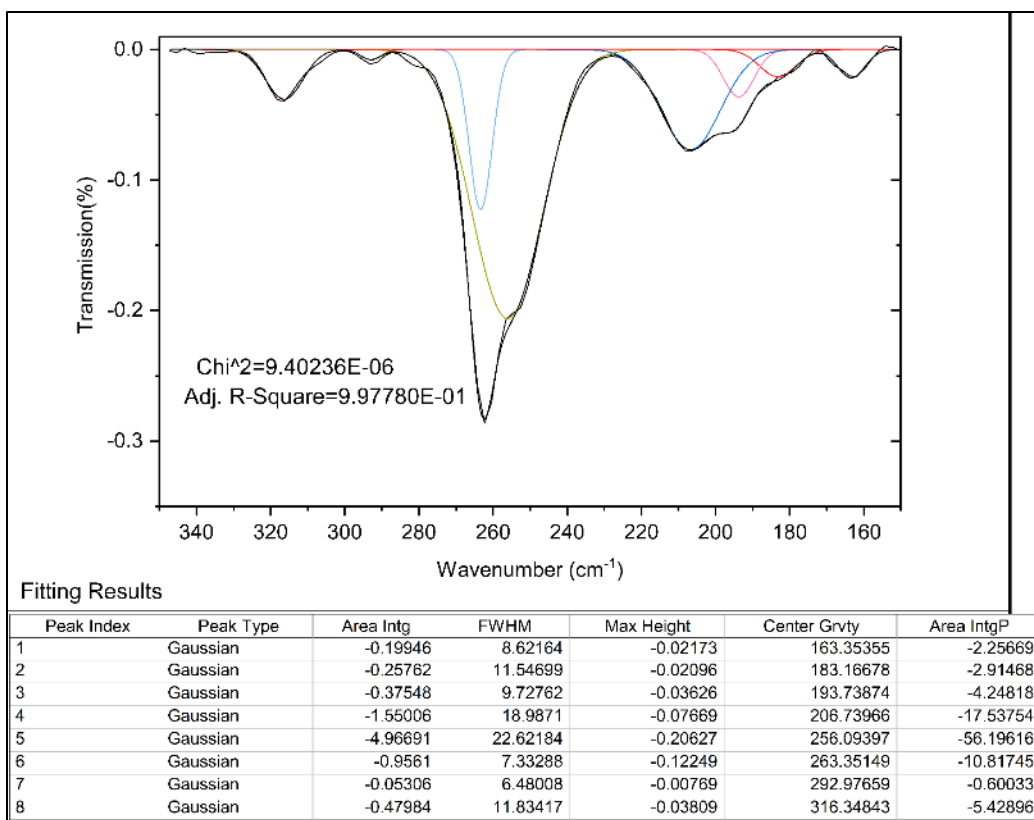


Figure S75. Far-IR spectrum for L⁶UO₂Rb fit to Gaussian functions.

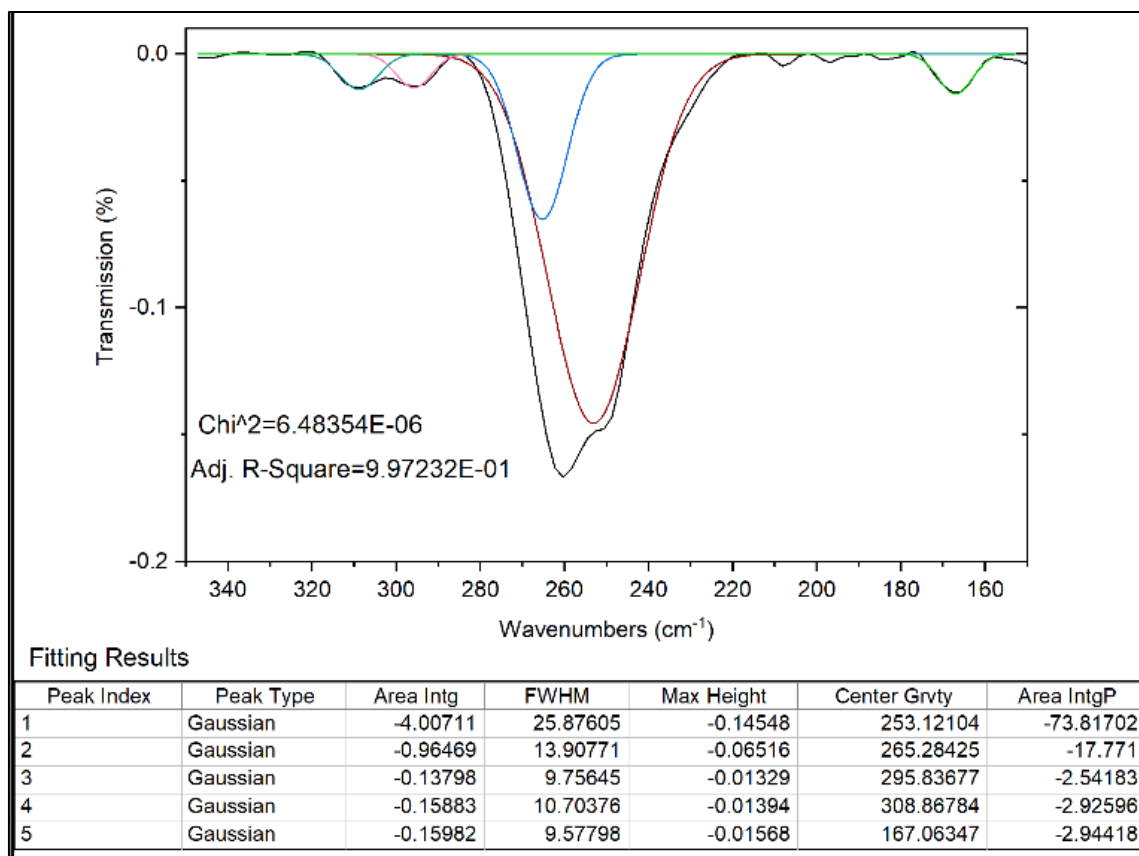


Figure S76. Far-IR spectrum for L⁶UO₂K fit to Gaussian functions.

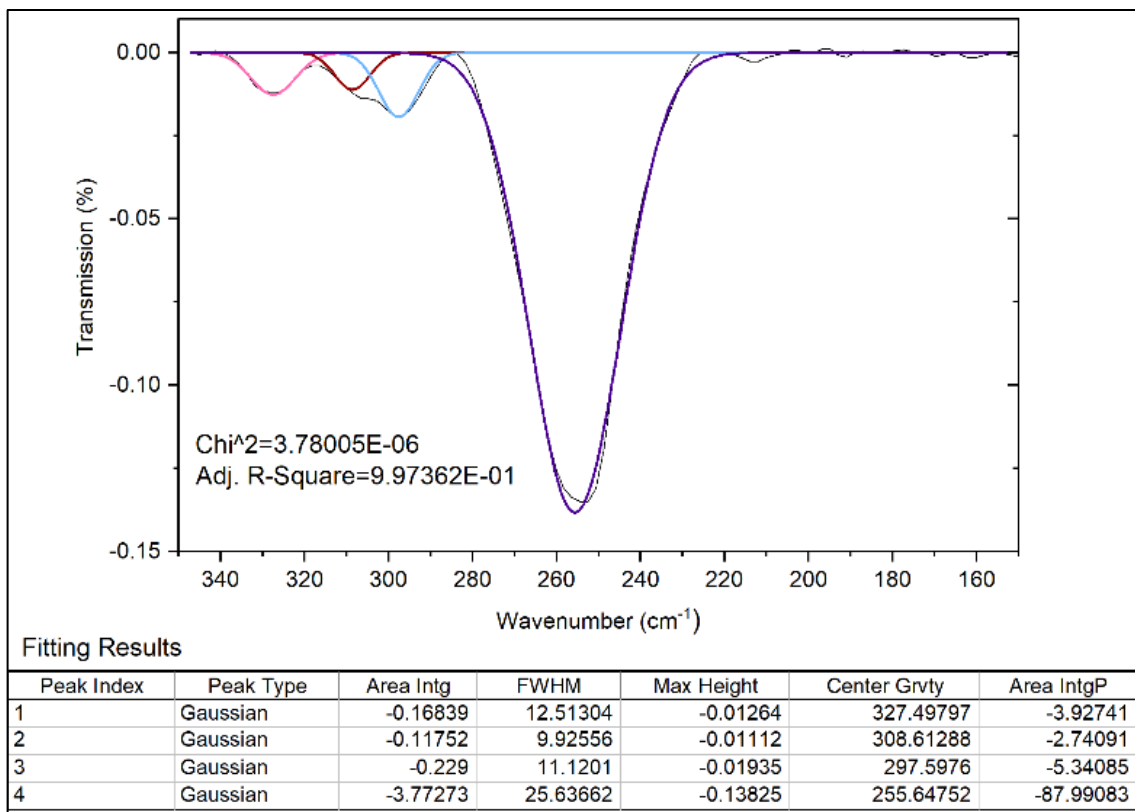


Figure S77. Far-IR spectrum for L^6UO_2Na fit to Gaussian functions.

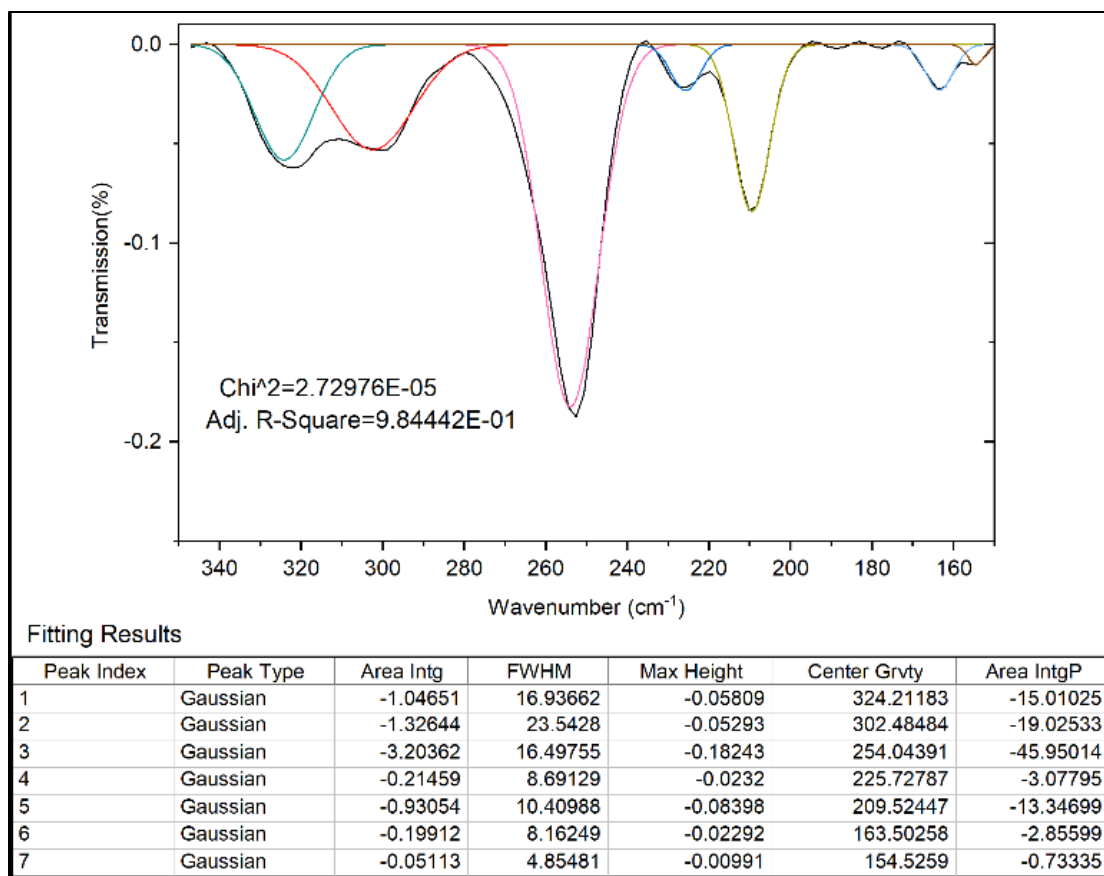


Figure S78. Far-IR spectrum for L^6UO_2Li fit to Gaussian functions.

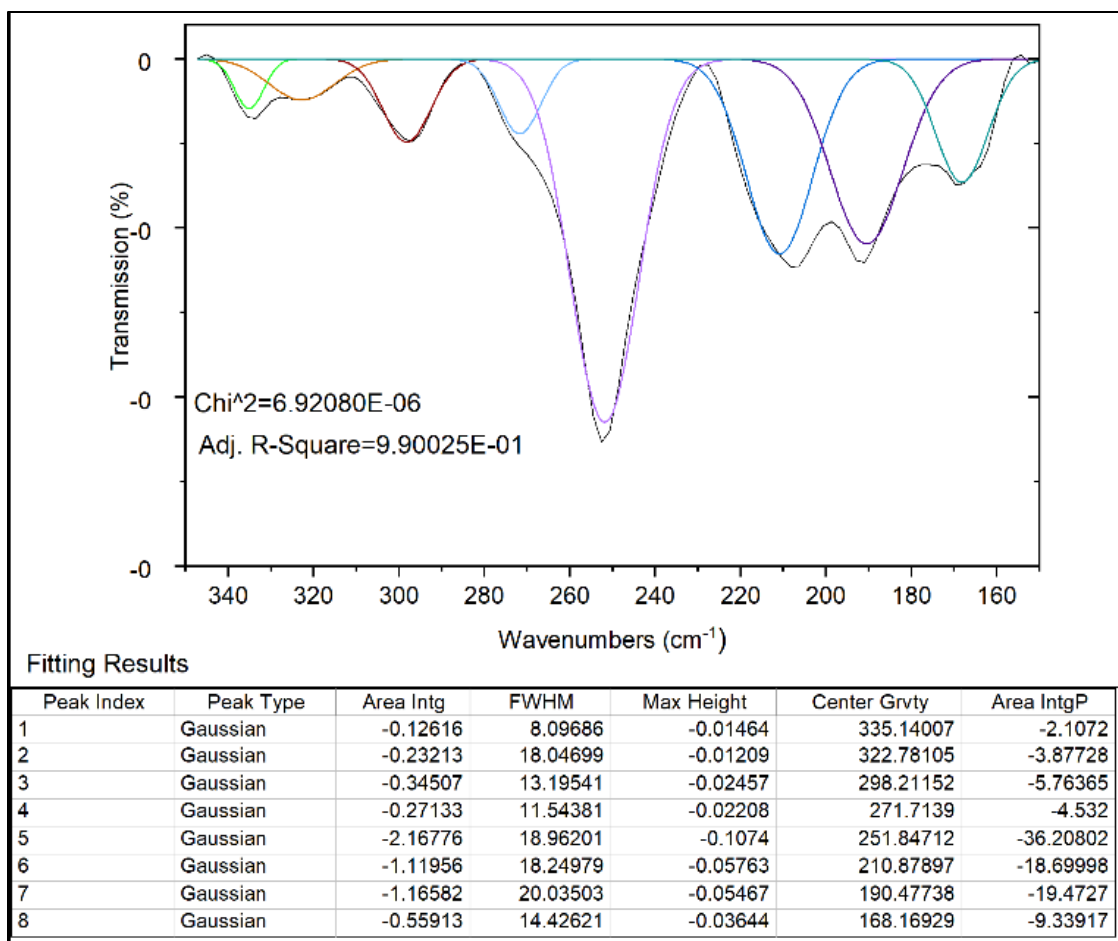


Figure S79. Far-IR spectrum for L⁶UO₂Ca fit to Gaussian functions.

Electrochemistry

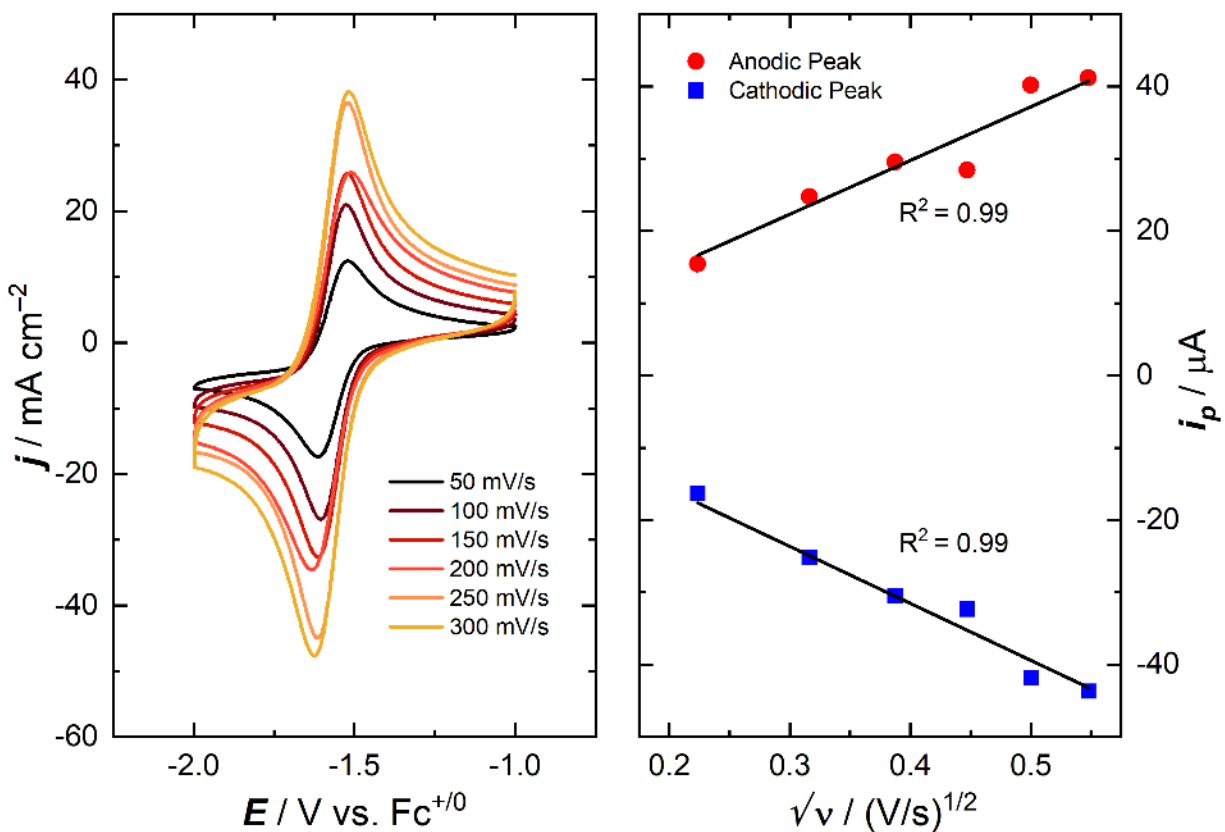


Figure S80. Left panel: scan rate dependence data for L^5UO_2 complex. Right panel: plot of peak current density vs. (scan rate)^{1/2}, demonstrating the diffusional nature of the oxidized species involved in L^5UO_2 . Diffusion coefficient of the oxidized species (calculated from the slope of the line represented by blue data points), $D_{ox} = 10.6 \times 10^{-6}$ cm²/s. Diffusion coefficient of the reduced species (calculated from the slope of the line represented by red data points), $D_{red} = 9.43 \times 10^{-6}$ cm²/s

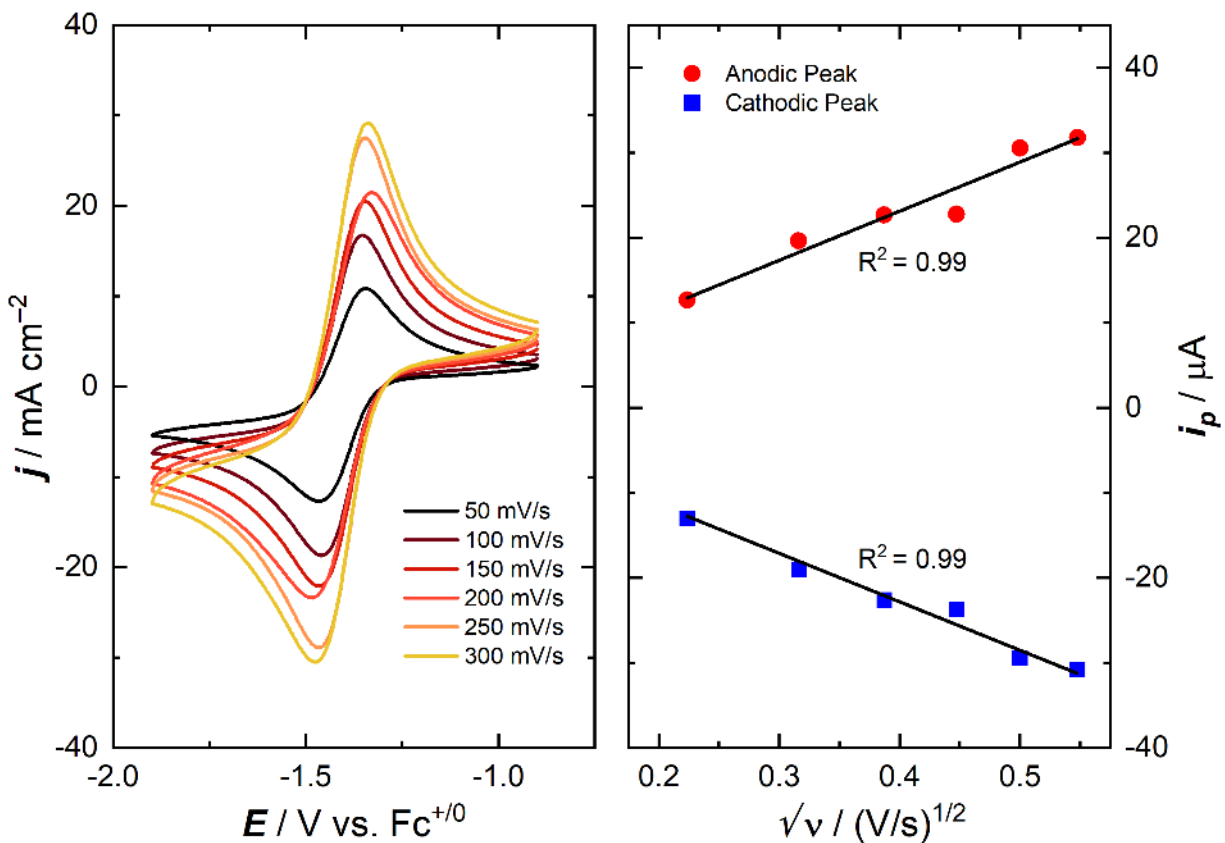


Figure S81. Left panel: scan rate dependence data for $\text{L}^5\text{UO}_2\text{Cs}$ complex. Right panel: plot of peak current density vs. $(\text{scan rate})^{1/2}$, demonstrating the diffusional nature of the oxidized species involved in $\text{L}^5\text{UO}_2\text{Cs}$. Diffusion coefficient of the oxidized species (calculated from the slope of the line represented by blue data points), $D_{\text{ox}} = 5.55 \times 10^{-6} \text{ cm}^2/\text{s}$. Diffusion coefficient of the reduced species (calculated from the slope of the line represented by red data points), $D_{\text{red}} = 5.70 \times 10^{-6} \text{ cm}^2/\text{s}$

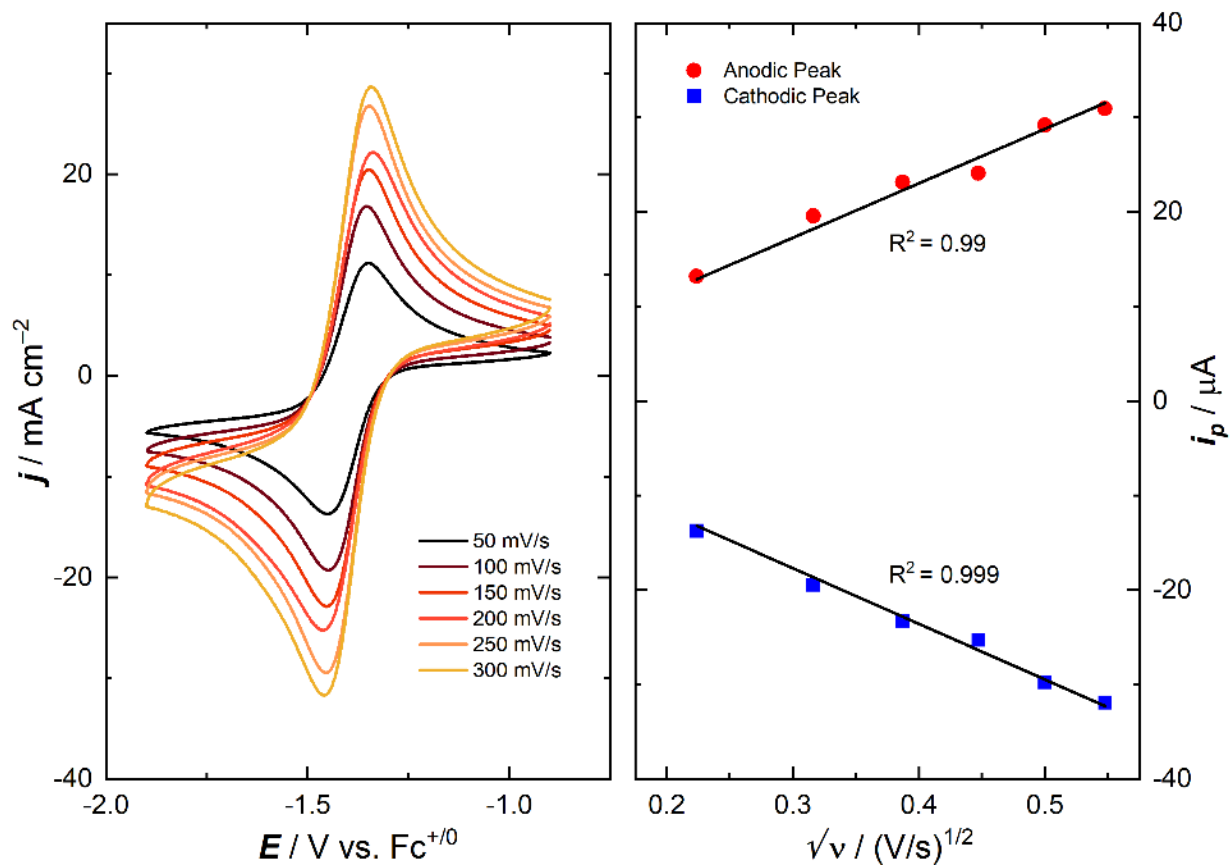


Figure S82. Left panel: scan rate dependence data for $\text{L}^5\text{UO}_2\text{Rb}$ complex. Right panel: plot of peak current density vs. $(\text{scan rate})^{1/2}$, demonstrating the diffusional nature of the oxidized species involved in $\text{L}^5\text{UO}_2\text{Rb}$. Diffusion coefficient of the oxidized species (calculated from the slope of the line represented by blue data points), $D_{\text{ox}} = 5.92 \times 10^{-6} \text{ cm}^2/\text{s}$. Diffusion coefficient of the reduced species (calculated from the slope of the line represented by red data points), $D_{\text{red}} = 5.65 \times 10^{-6} \text{ cm}^2/\text{s}$

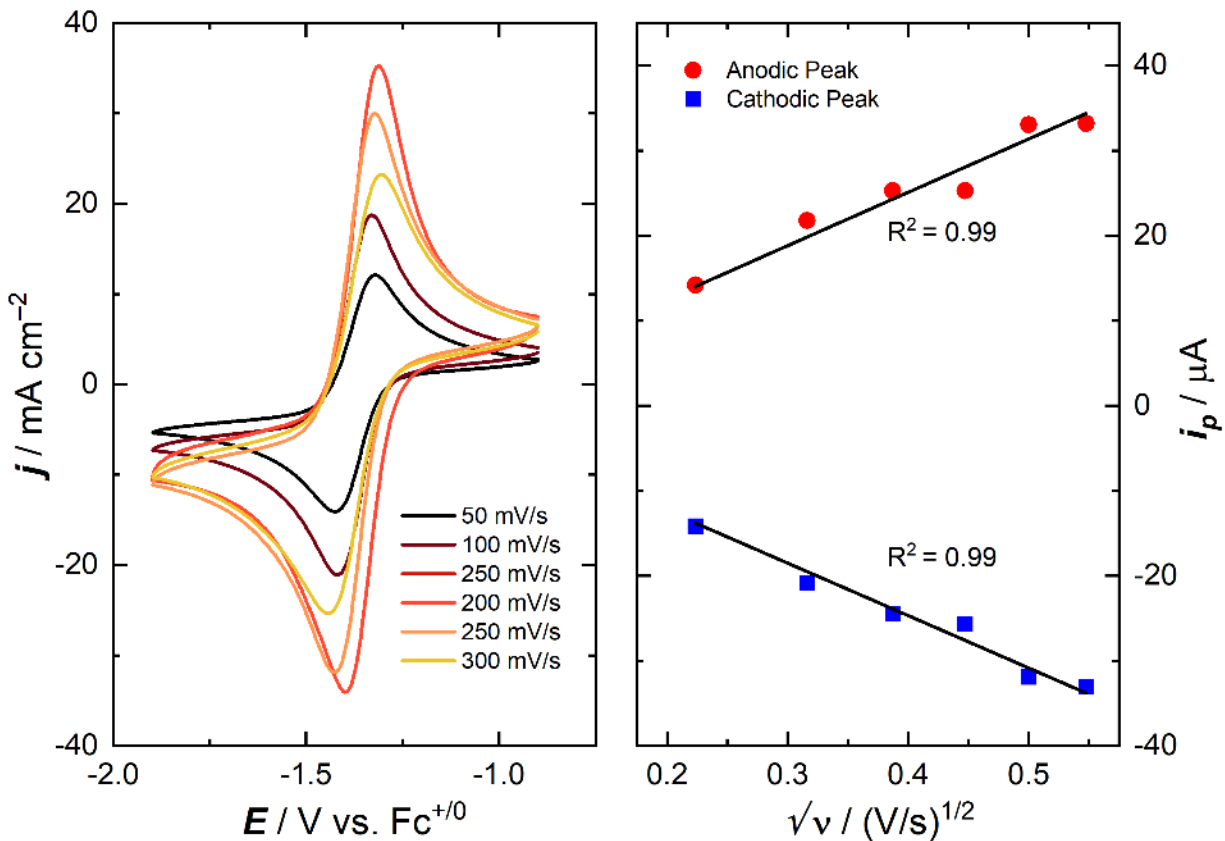


Figure S83. Left panel: scan rate dependence data for L^5UO_2K complex. Right panel: plot of peak current density vs. (scan rate)^{1/2}, demonstrating the diffusional nature of the oxidized species involved in L^5UO_2K . Diffusion coefficient of the oxidized species (calculated from the slope of the line represented by blue data points), $D_{ox} = 6.49 \times 10^{-6}$ cm²/s. Diffusion coefficient of the reduced species (calculated from the slope of the line represented by red data points), $D_{red} = 6.71 \times 10^{-6}$ cm²/s

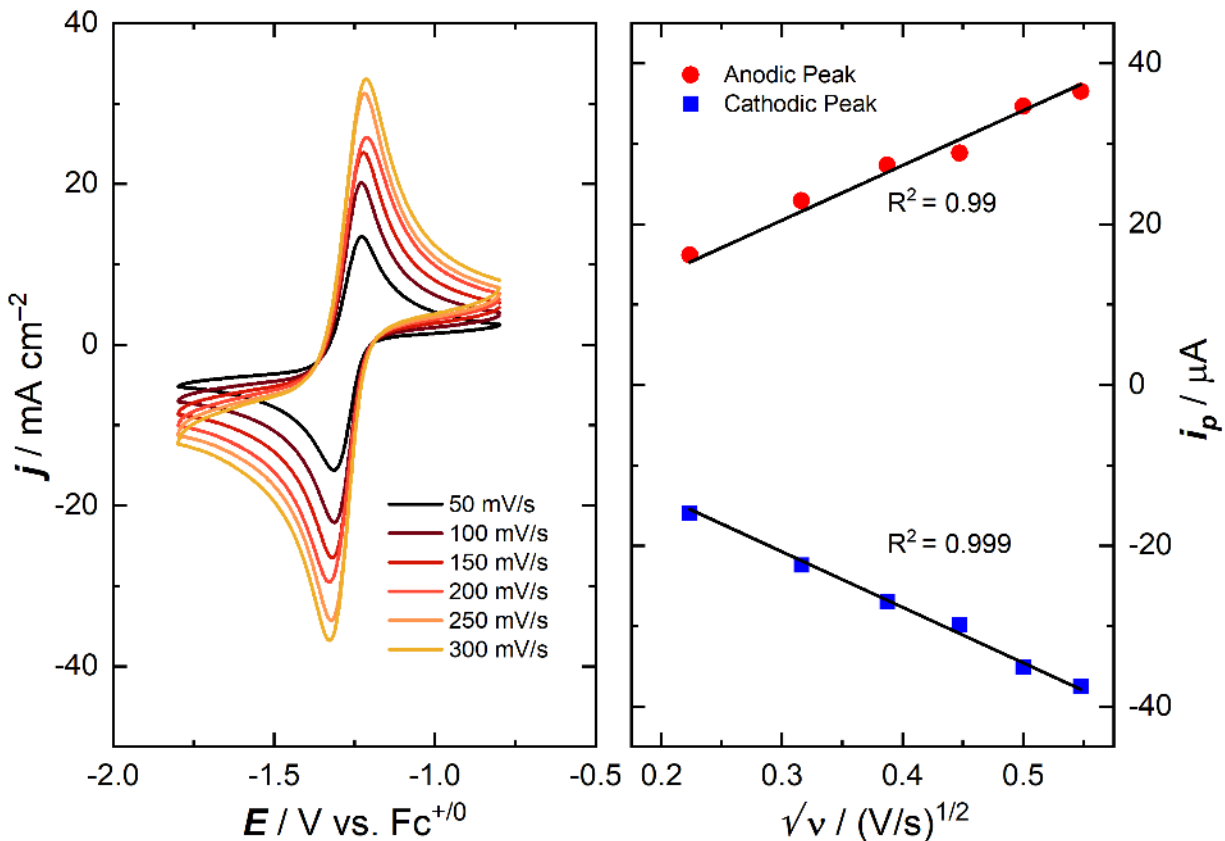


Figure S84. Left panel: scan rate dependence data for L^5UO_2Na complex. Right panel: plot of peak current density vs. $(\text{scan rate})^{1/2}$, demonstrating the diffusional nature of the oxidized species involved in L^5UO_2Na . Diffusion coefficient of the oxidized species (calculated from the slope of the line represented by blue data points), $D_{ox} = 8.15 \times 10^{-6} \text{ cm}^2/\text{s}$. Diffusion coefficient of the reduced species (calculated from the slope of the line represented by red data points), $D_{red} = 7.94 \times 10^{-6} \text{ cm}^2/\text{s}$

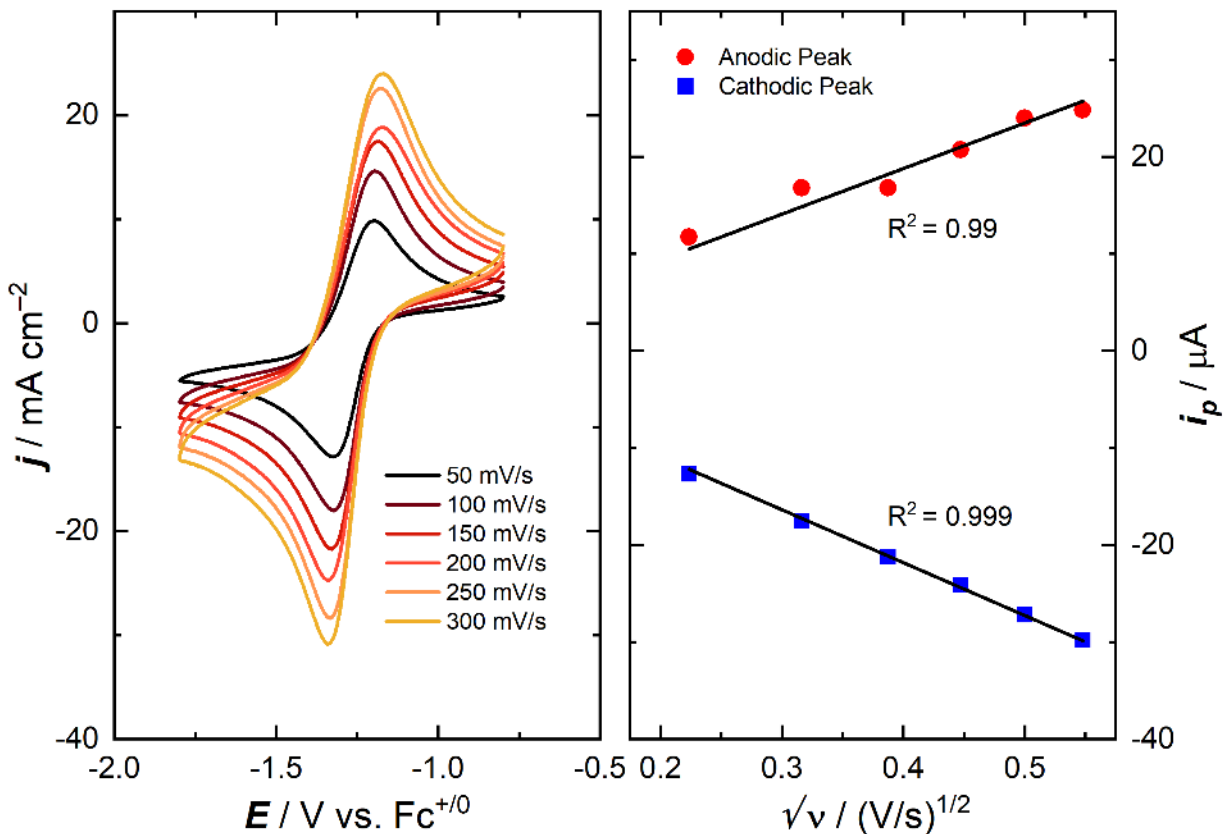


Figure S85. Left panel: scan rate dependence data for L^5UO_2Li complex. Right panel: plot of peak current density vs. $(\text{scan rate})^{1/2}$, demonstrating the diffusional nature of the oxidized species involved in L^5UO_2Li . Diffusion coefficient of the oxidized species (calculated from the slope of the line represented by blue data points), $D_{ox} = 5.07 \times 10^{-6} \text{ cm}^2/\text{s}$. Diffusion coefficient of the reduced species (calculated from the slope of the line represented by red data points), $D_{red} = 3.76 \times 10^{-6} \text{ cm}^2/\text{s}$

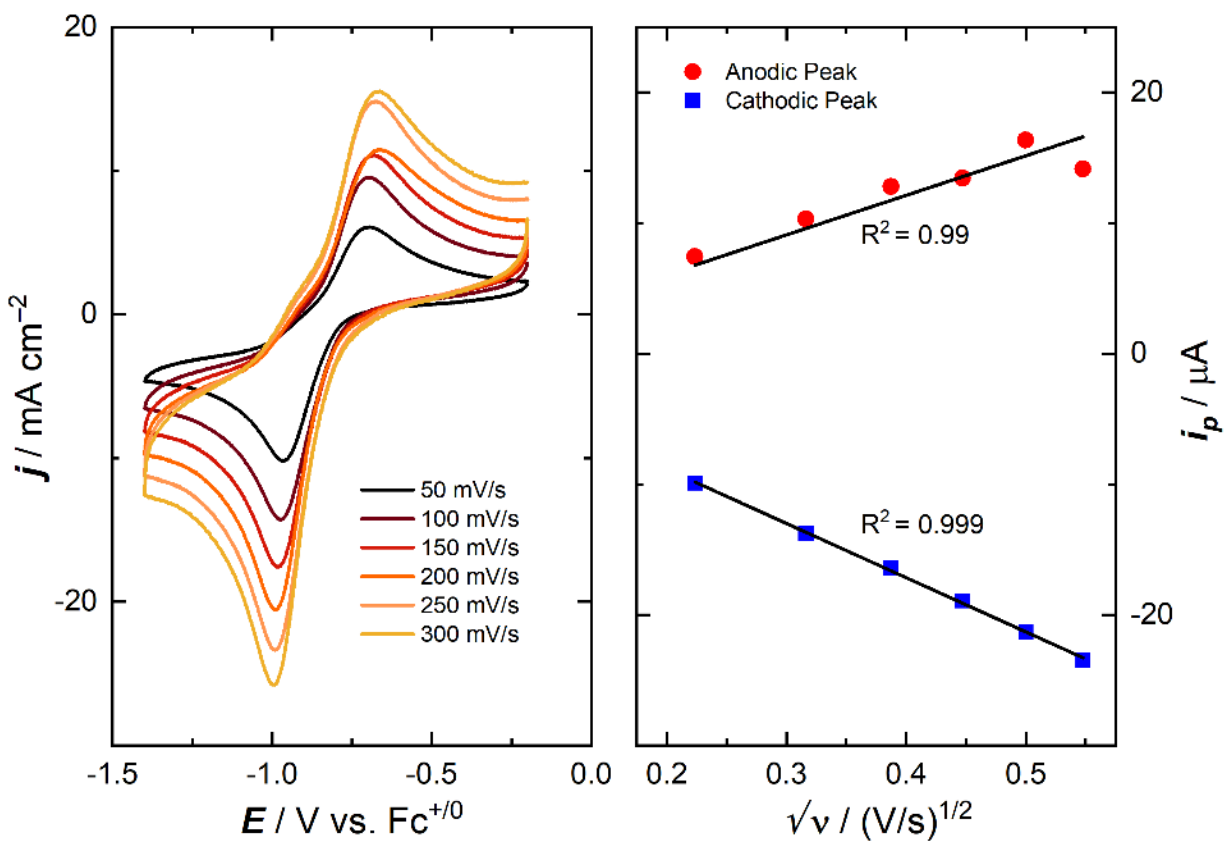


Figure S86. Left panel: scan rate dependence data for $\text{L}^5\text{UO}_2\text{Ca}$ complex. Right panel: plot of peak current density vs. $(\text{scan rate})^{1/2}$, demonstrating the diffusional nature of the oxidized species involved in $\text{L}^5\text{UO}_2\text{Ca}$. Diffusion coefficient of the oxidized species (calculated from the slope of the line represented by blue data points), $D_{\text{ox}} = 3.12 \times 10^{-6} \text{ cm}^2/\text{s}$. Diffusion coefficient of the reduced species (calculated from the slope of the line represented by red data points), $D_{\text{red}} = 1.56 \times 10^{-6} \text{ cm}^2/\text{s}$.

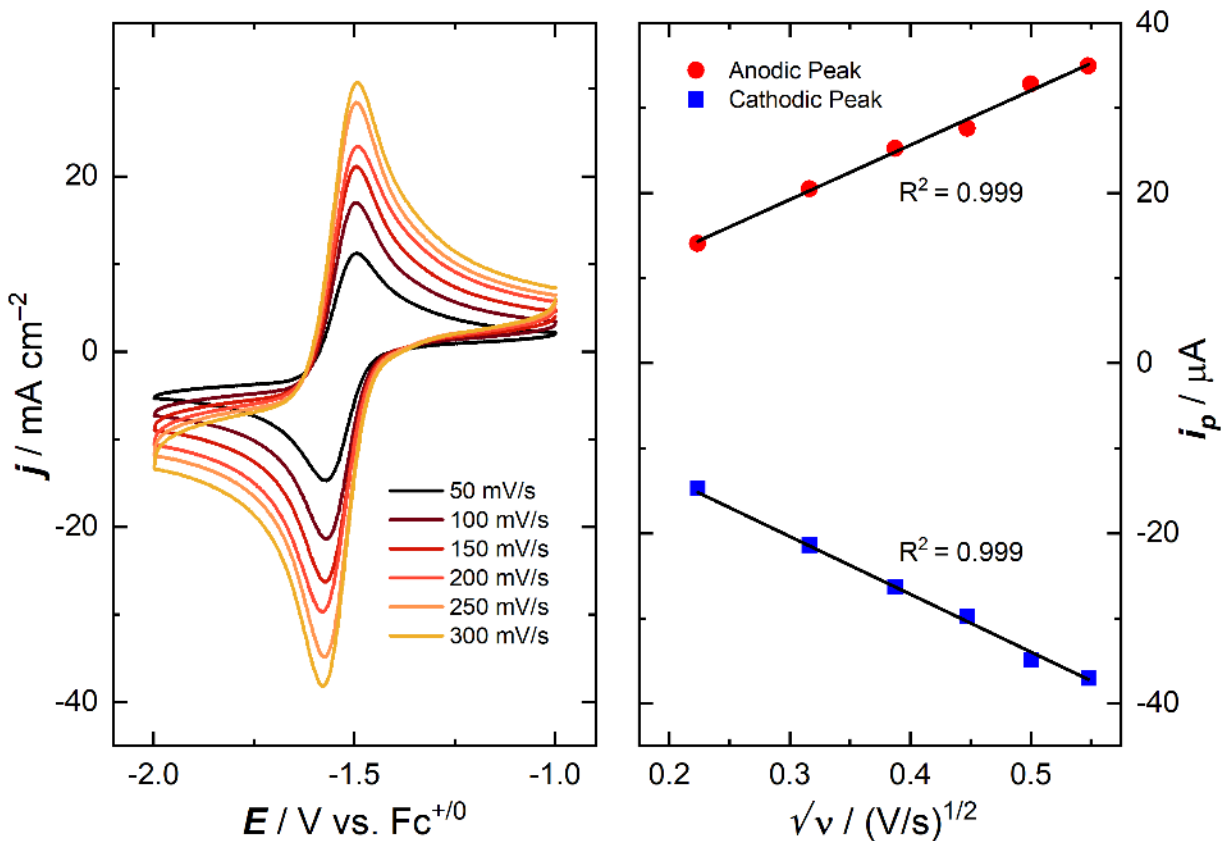


Figure S87. Left panel: scan rate dependence data for L^6UO_2 complex. Right panel: plot of peak current density vs. $(\text{scan rate})^{1/2}$, demonstrating the diffusional nature of the oxidized species involved in L^6UO_2 . Diffusion coefficient of the oxidized species (calculated from the slope of the line represented by blue data points), $D_{\text{ox}} = 7.86 \times 10^{-6} \text{ cm}^2/\text{s}$. Diffusion coefficient of the reduced species (calculated from the slope of the line represented by red data points), $D_{\text{red}} = 7.01 \times 10^{-6} \text{ cm}^2/\text{s}$.

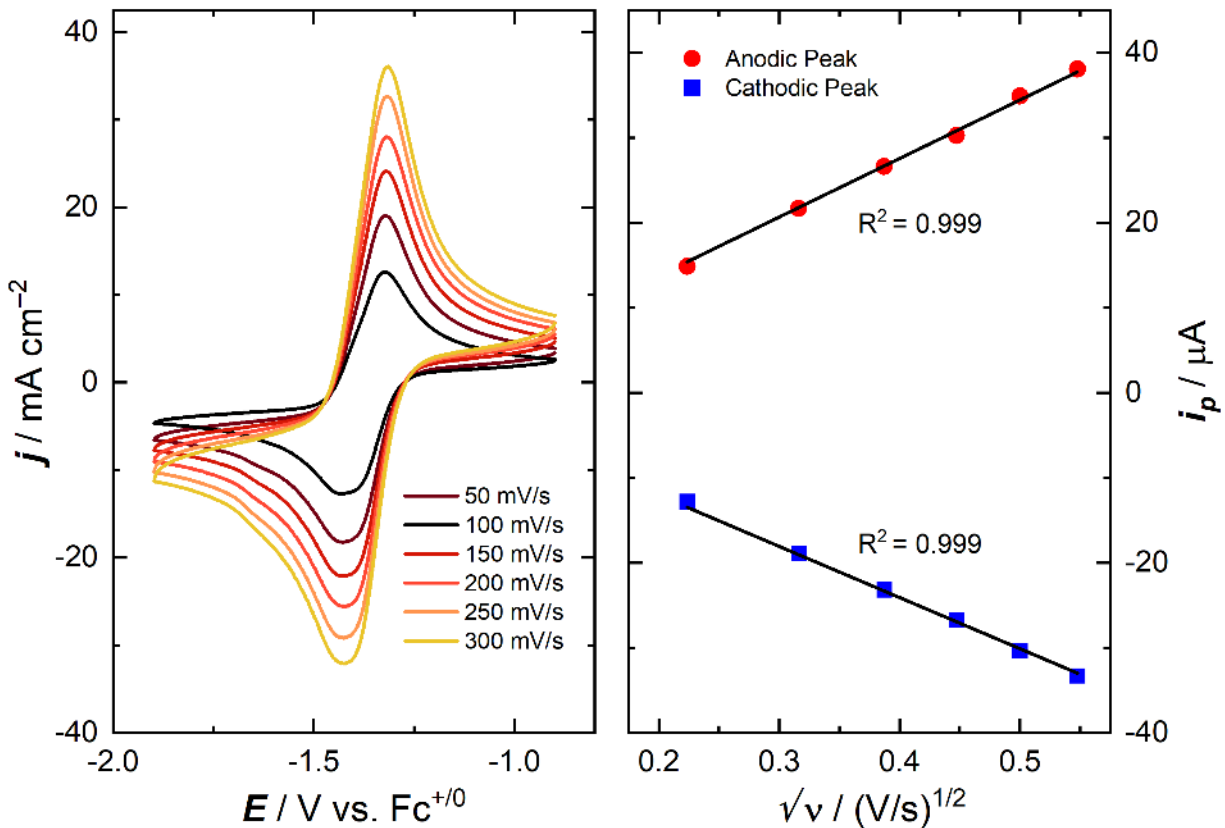


Figure S88. Left panel: scan rate dependence data for $\text{L}^6\text{UO}_2\text{Cs}$ complex. Right panel: plot of peak current density vs. $(\text{scan rate})^{1/2}$, demonstrating the diffusional nature of the oxidized species involved in $\text{L}^6\text{UO}_2\text{Cs}$. Diffusion coefficient of the oxidized species (calculated from the slope of the line represented by blue data points), $D_{\text{ox}} = 6.18 \times 10^{-6} \text{ cm}^2/\text{s}$. Diffusion coefficient of the reduced species (calculated from the slope of the line represented by red data points), $D_{\text{red}} = 8.09 \times 10^{-6} \text{ cm}^2/\text{s}$.

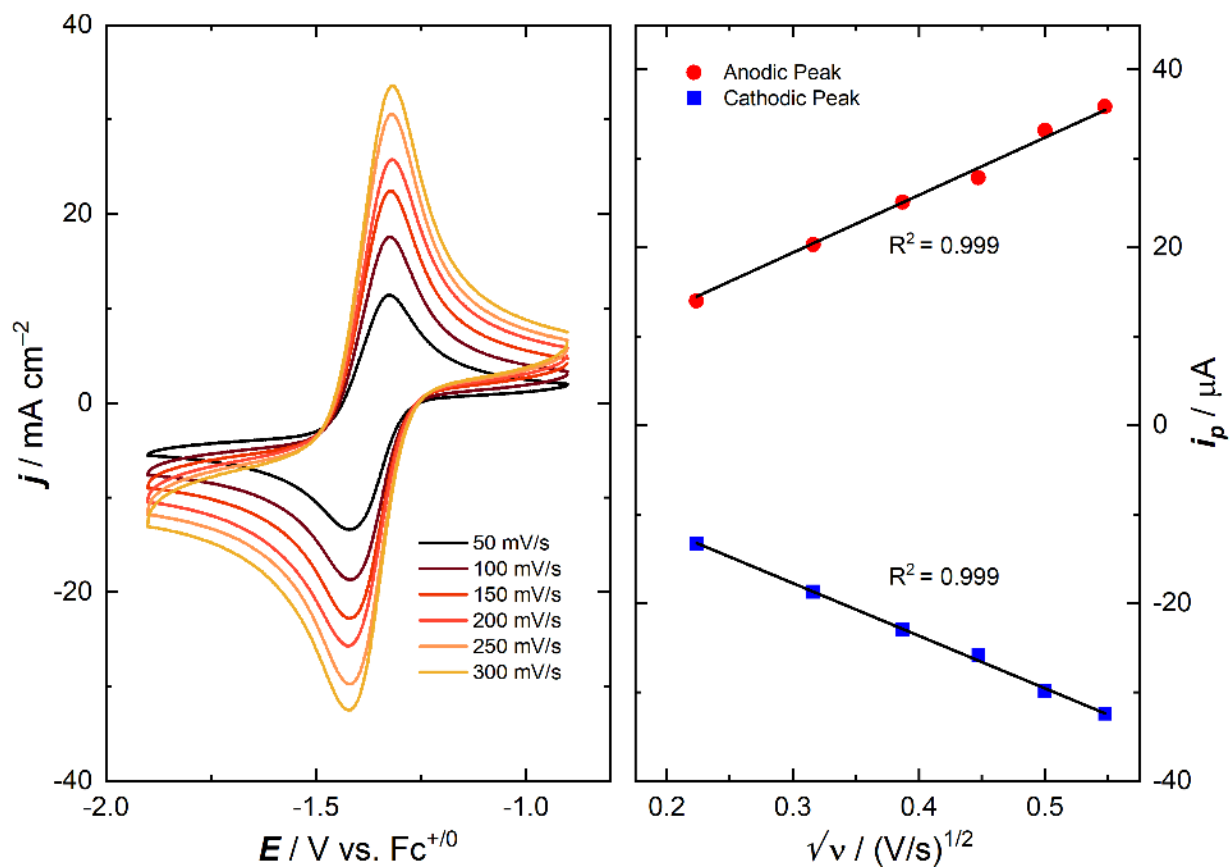


Figure S89. Left panel: scan rate dependence data for L^6UO_2Rb complex. Right panel: plot of peak current density vs. $(\text{scan rate})^{1/2}$, demonstrating the diffusional nature of the oxidized species involved in L^6UO_2Rb . Diffusion coefficient of the oxidized species (calculated from the slope of the line represented by blue data points), $D_{ox} = 5.96 \times 10^{-6} \text{ cm}^2/\text{s}$. Diffusion coefficient of the reduced species (calculated from the slope of the line represented by red data points), $D_{red} = 7.14 \times 10^{-6} \text{ cm}^2/\text{s}$.

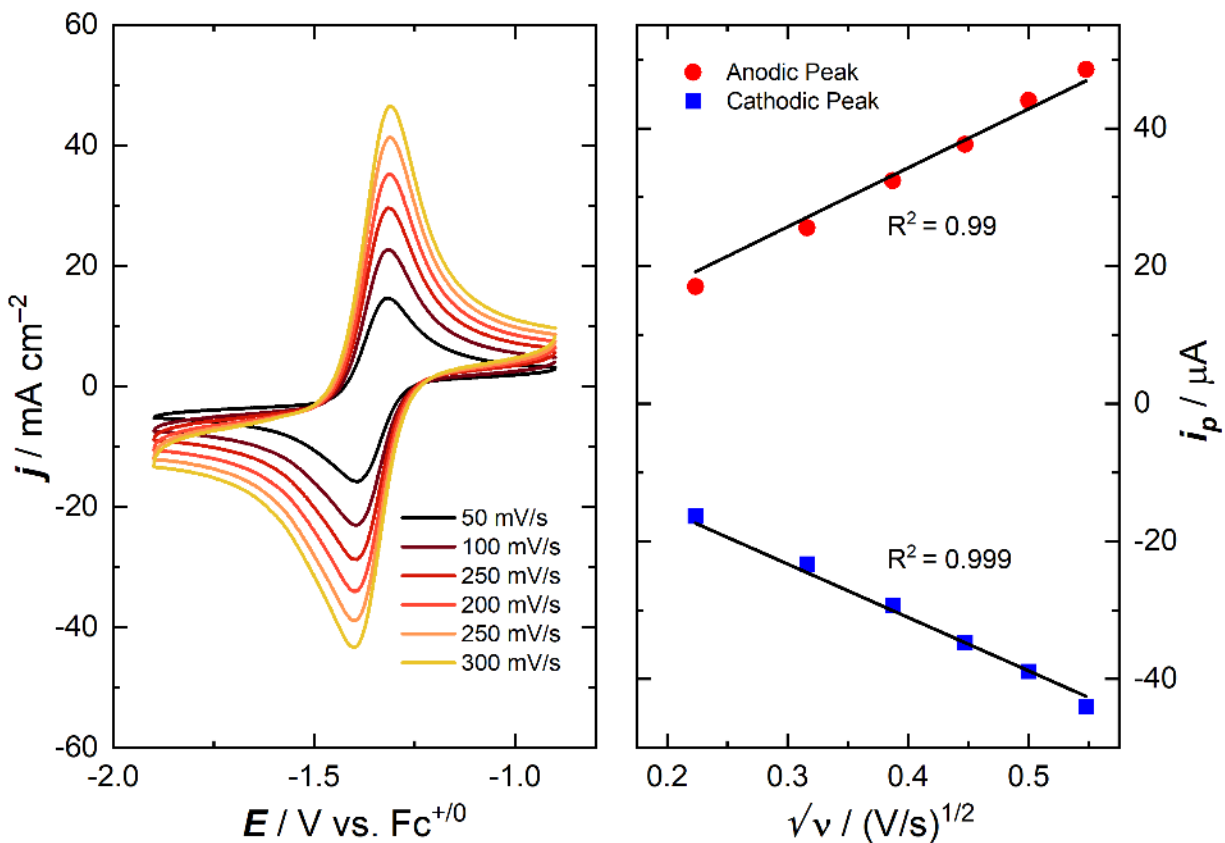


Figure S90. Left panel: scan rate dependence data for L^6UO_2K complex. Right panel: plot of peak current density vs. $(\text{scan rate})^{1/2}$, demonstrating the diffusional nature of the oxidized species involved in L^6UO_2K . Diffusion coefficient of the oxidized species (calculated from the slope of the line represented by blue data points), $D_{\text{ox}} = 10.3 \times 10^{-6} \text{ cm}^2/\text{s}$. Diffusion coefficient of the reduced species (calculated from the slope of the line represented by red data points), $D_{\text{red}} = 12.5 \times 10^{-6} \text{ cm}^2/\text{s}$.

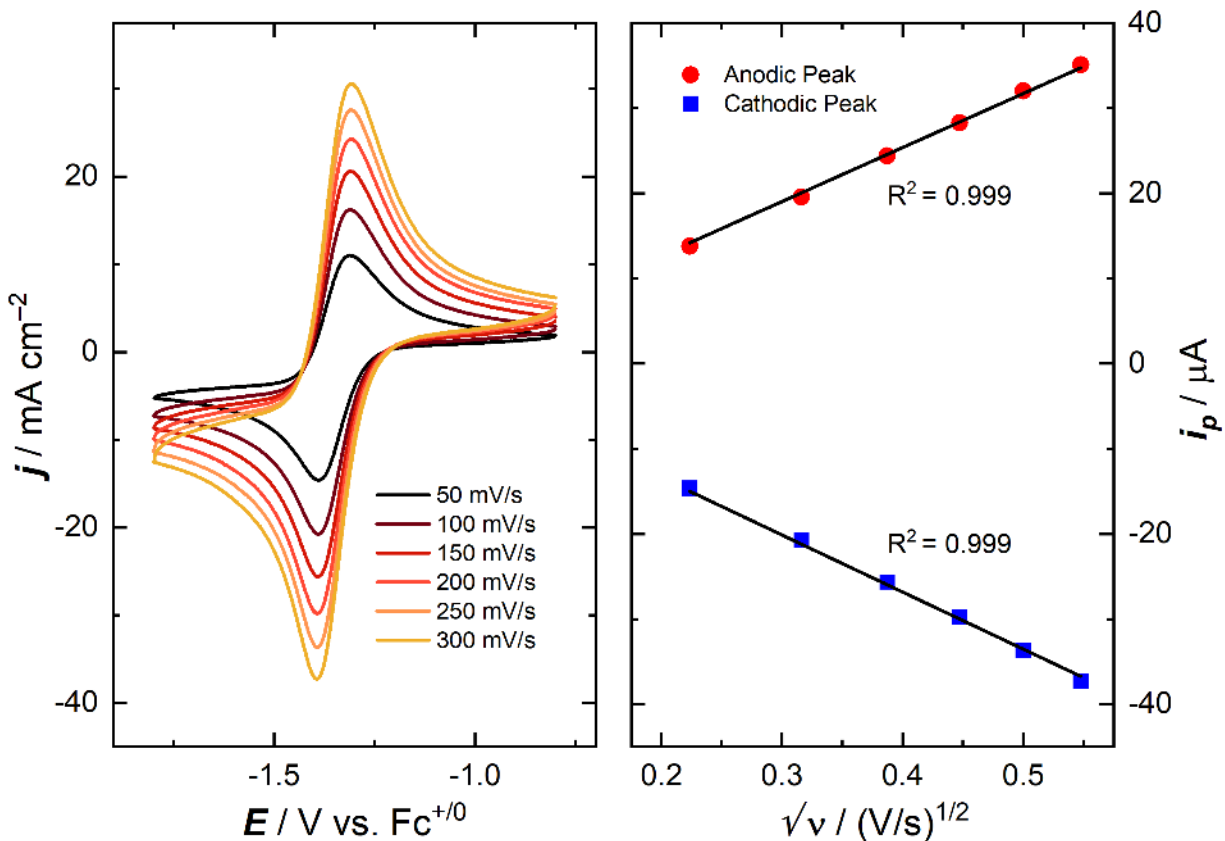


Figure S91. Left panel: scan rate dependence data for L^6UO_2Na complex. Right panel: plot of peak current density vs. $(\text{scan rate})^{1/2}$, demonstrating the diffusional nature of the oxidized species involved in L^6UO_2Na . Diffusion coefficient of the oxidized species (calculated from the slope of the line represented by blue data points), $D_{\text{ox}} = 7.67 \times 10^{-6} \text{ cm}^2/\text{s}$. Diffusion coefficient of the reduced species (calculated from the slope of the line represented by red data points), $D_{\text{red}} = 6.86 \times 10^{-6} \text{ cm}^2/\text{s}$.

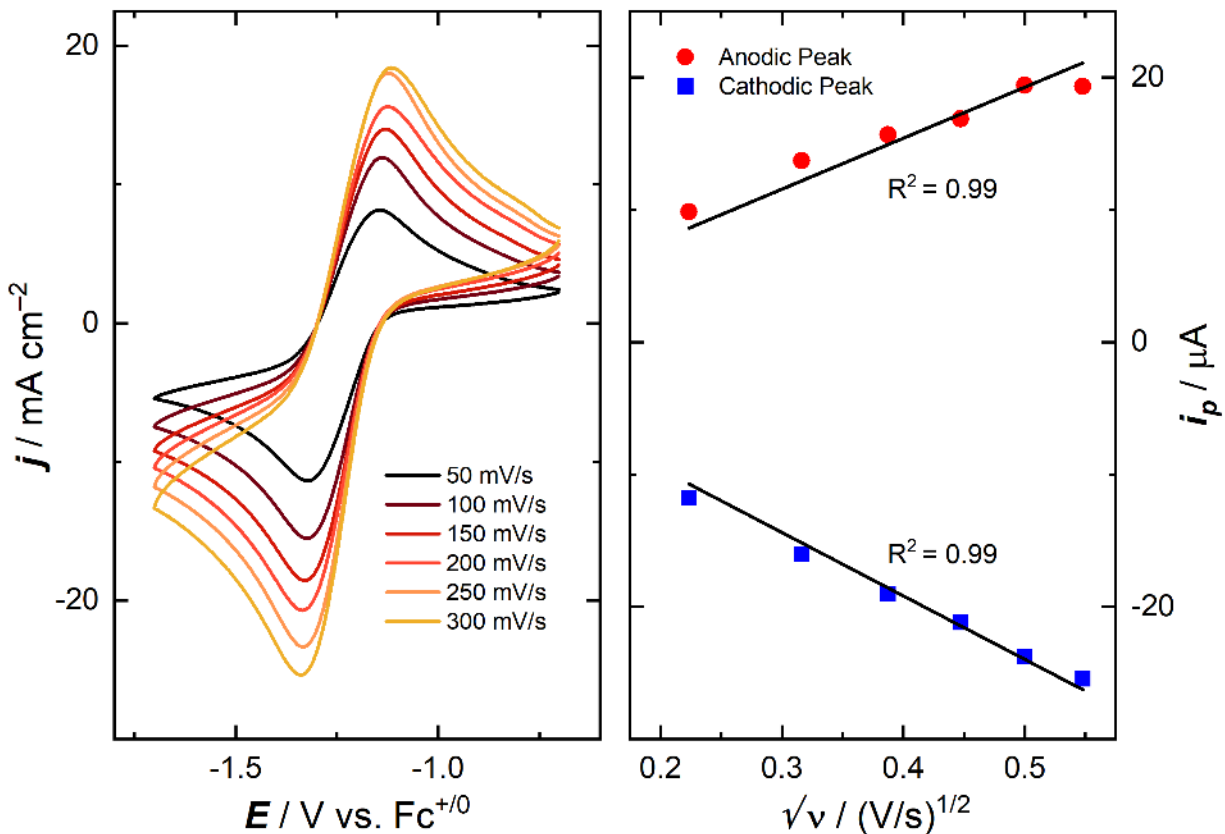


Figure S92. Left panel: scan rate dependence data for $\text{L}^6\text{UO}_2\text{Li}$ complex. Right panel: plot of peak current density vs. $(\text{scan rate})^{1/2}$, demonstrating the diffusional nature of the oxidized species involved in $\text{L}^6\text{UO}_2\text{Li}$. Diffusion coefficient of the oxidized species (calculated from the slope of the line represented by blue data points), $D_{\text{ox}} = 3.92 \times 10^{-6} \text{ cm}^2/\text{s}$. Diffusion coefficient of the reduced species (calculated from the slope of the line represented by red data points), $D_{\text{red}} = 2.53 \times 10^{-6} \text{ cm}^2/\text{s}$.

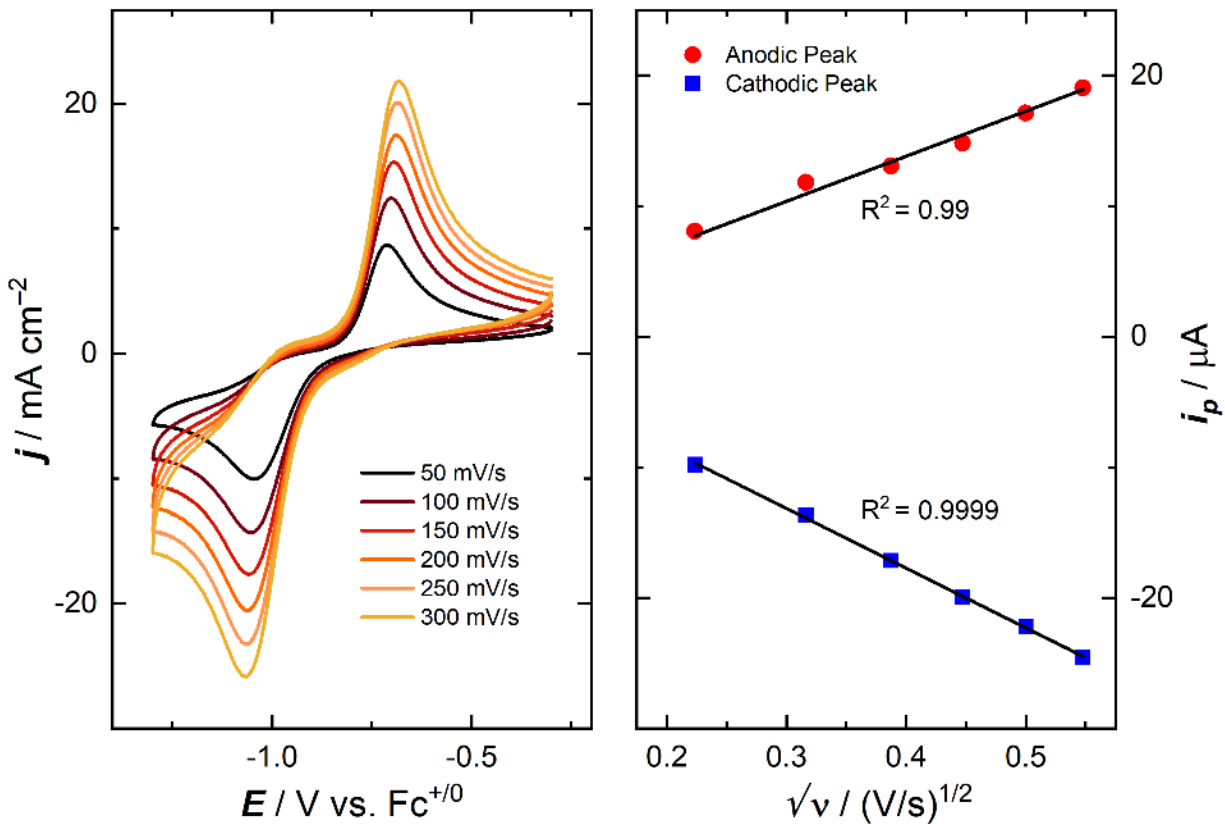


Figure S93. Left panel: scan rate dependence data for $\text{L}^6\text{UO}_2\text{Ca}$ complex. Right panel: plot of peak current density vs. $(\text{scan rate})^{1/2}$, demonstrating the diffusional nature of the oxidized species involved in $\text{L}^6\text{UO}_2\text{Ca}$. Diffusion coefficient of the oxidized species (calculated from the slope of the line represented by blue data points), $D_{\text{ox}} = 3.36 \times 10^{-6} \text{ cm}^2/\text{s}$. Diffusion coefficient of the reduced species (calculated from the slope of the line represented by red data points), $D_{\text{red}} = 2.03 \times 10^{-6} \text{ cm}^2/\text{s}$.

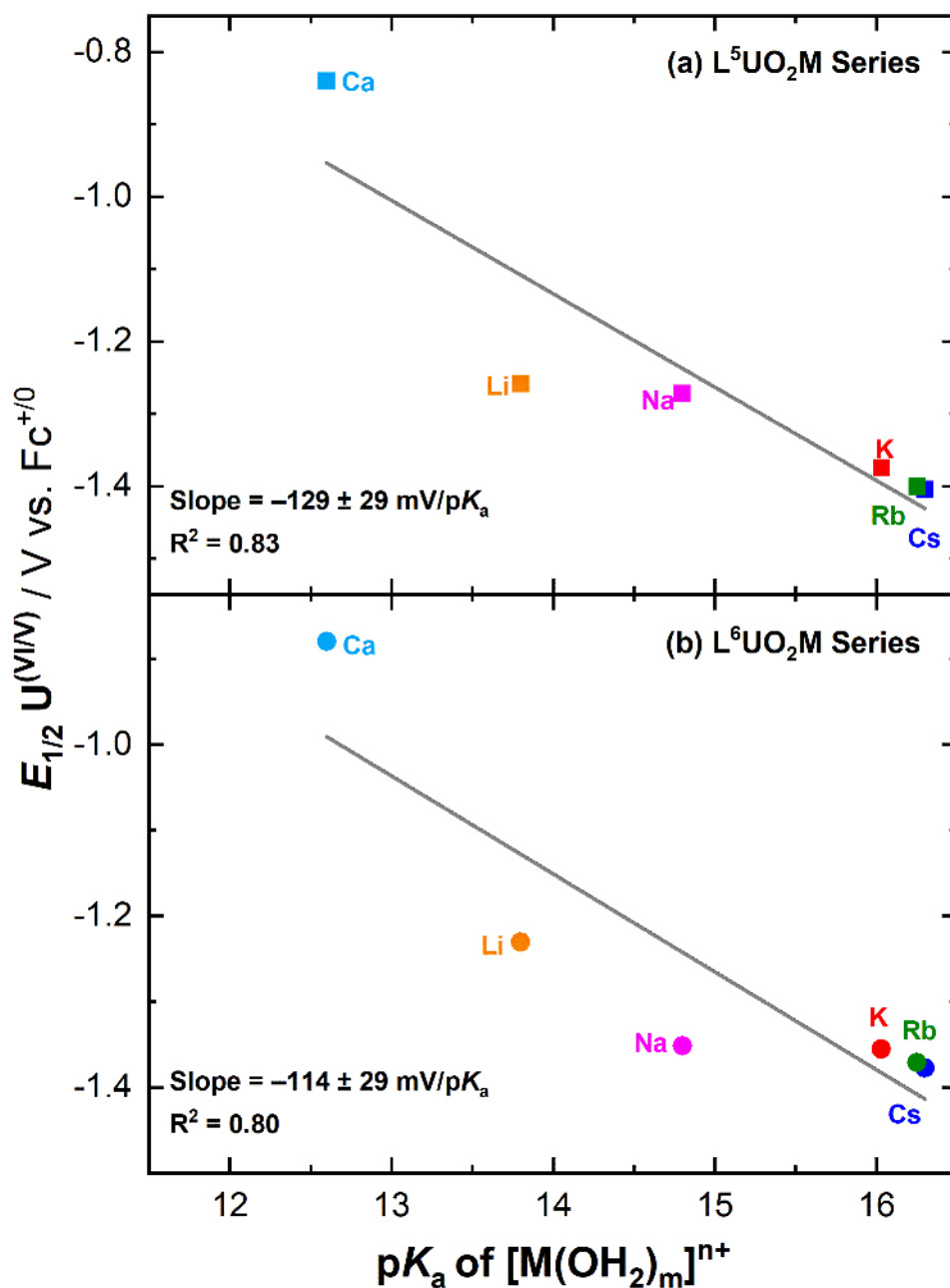


Figure S94. Plot of $E_{1/2}(U^{VI/V})$ vs. pK_a of $[M(H_2O)_m]^{n+}$ for L^5UO_2M complexes (a, top) and L^6UO_2M complexes (b, bottom), including L^5UO_2Ca and L^6UO_2Ca . Noted uncertainties on the correlations/slopes were determined to be ± 29 mV/ pK_a for each unique data set; the identical uncertainty in each case represents a coincidental identical value for each data set.

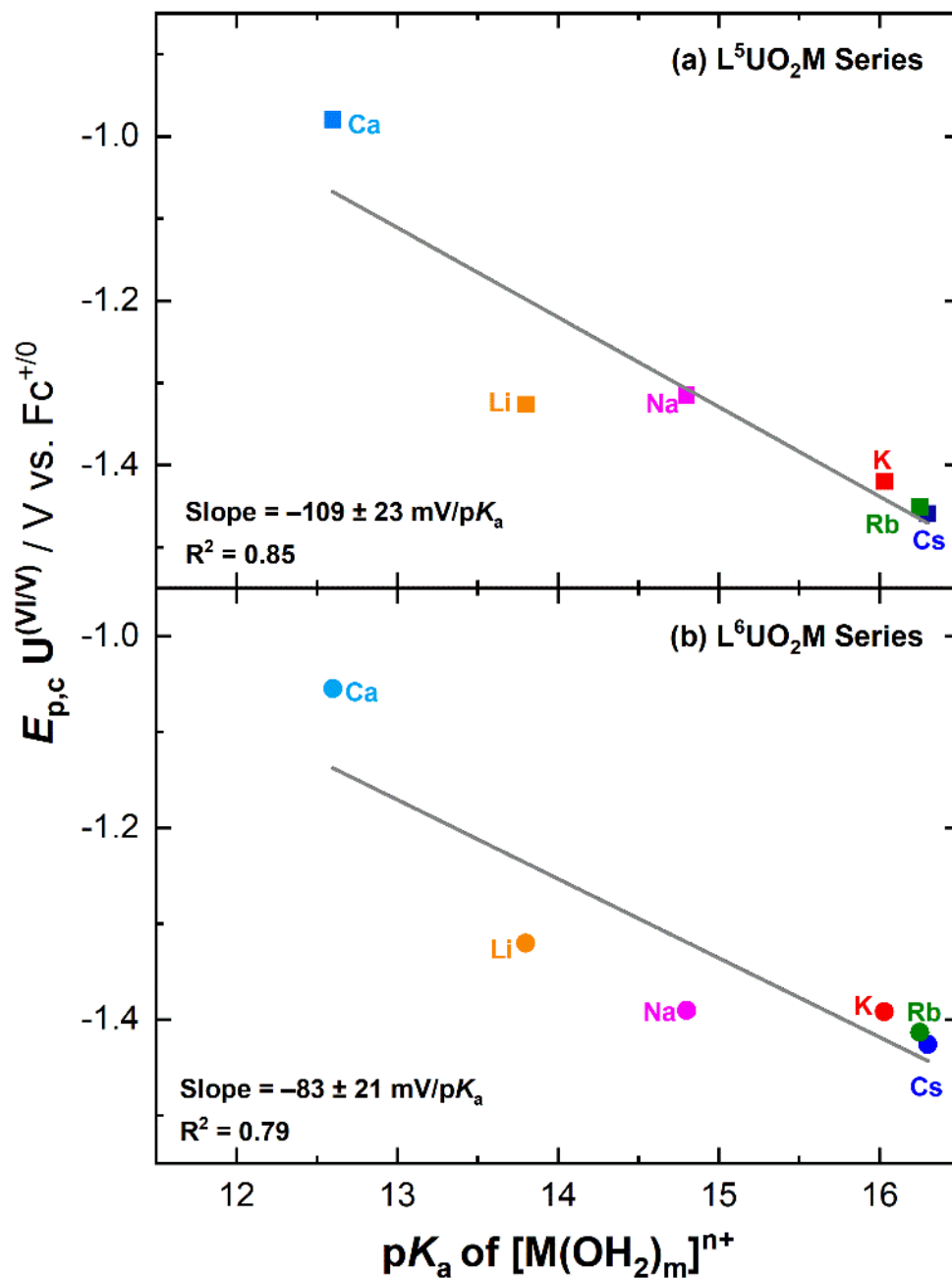


Figure S95. Plot of $E_{p,c}(U^{VI/V})$ vs. pK_a of $[M(H_2O)_m]^{n+}$ for L^5UO_2M complexes (a, top) and L^6UO_2M complexes (b, bottom), including L^5UO_2Ca and L^6UO_2Ca .

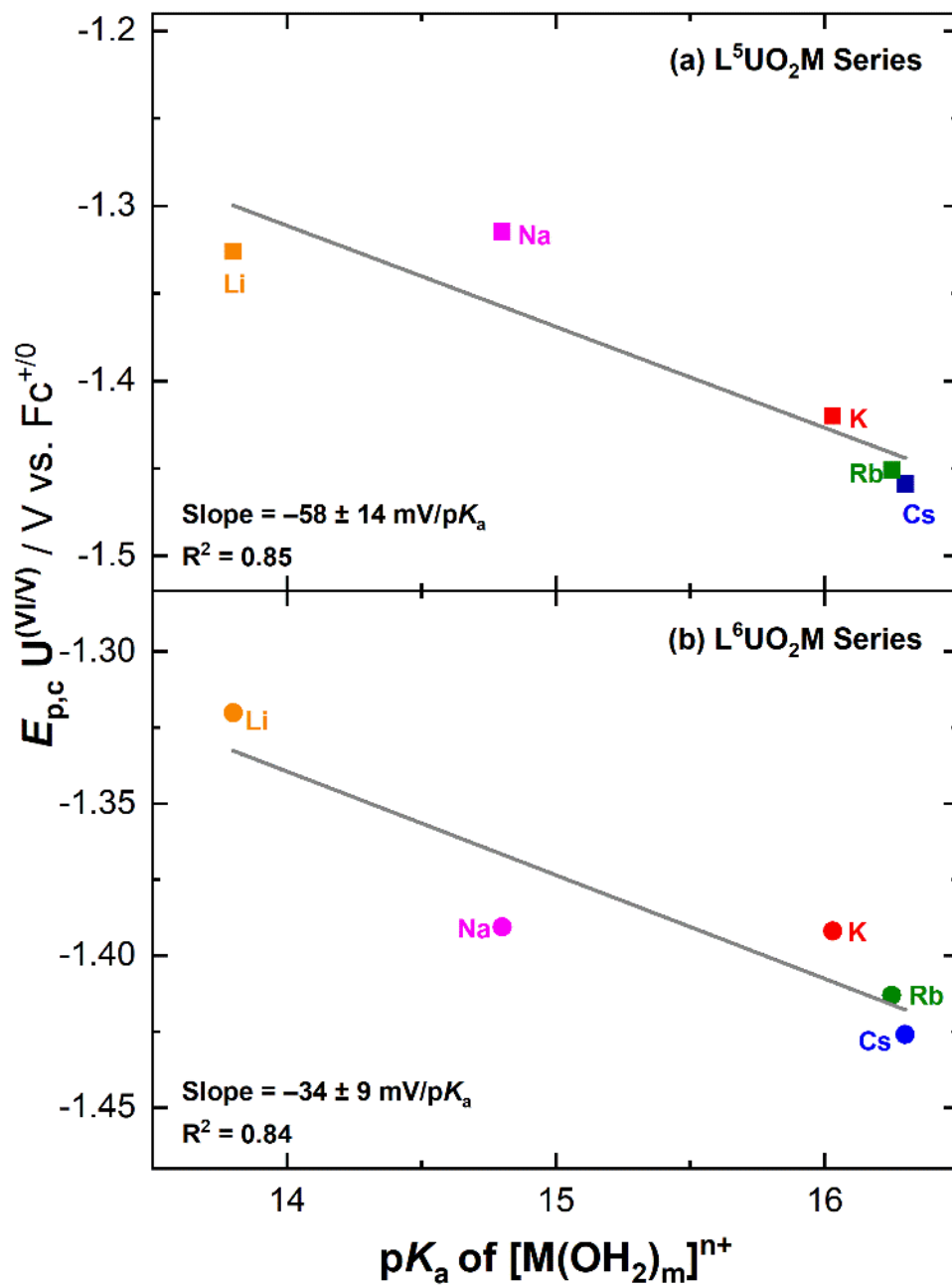


Figure S96. Plot of $E_{p,c}(U^{VI/V})$ vs. pK_a of $[M(H_2O)_m]^{n+}$ for L^5UO_2M complexes (a, top) and L^6UO_2M complexes (b, bottom).

Electrochemical Titrations

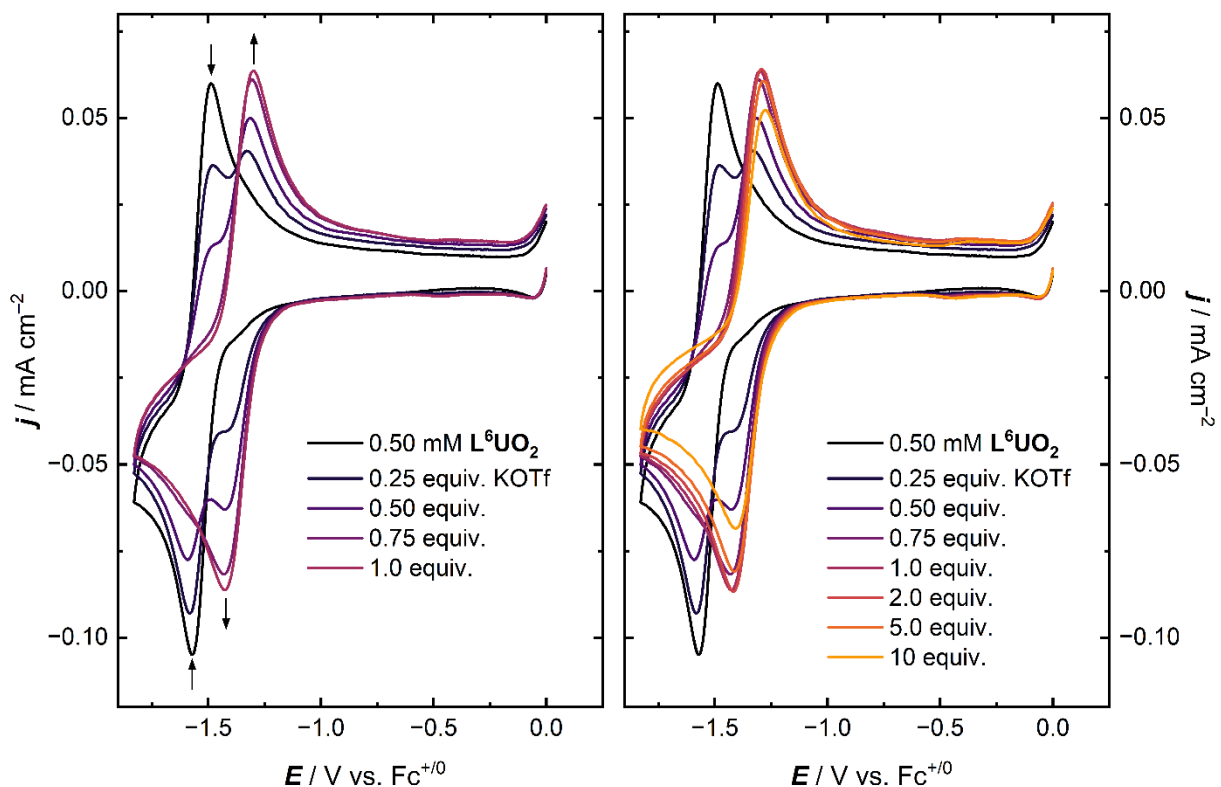


Figure S97. Left panel: electrochemical titration of L^6UO_2 with increasing equivalents of KOTf up to 1 equiv. Right panel: Further additions of KOTf up to 10 equiv. demonstrating the redox behavior of the U(VI)/U(V) couple in the presence of excess $[K^+]$. Three consecutive cyclic voltammograms were collected for each addition of $[K^+]$, first cycles plotted above. Conditions: 0.5 mM L^6UO_2 in 0.1 M tetrabutylammonium hexafluorophosphate in acetonitrile; stock solution of KOTf prepared in acetonitrile electrolyte; 100 mV/s scan rate.

Table S5. Selected metrics for the electrochemical titration of L^6UO_2 with KOTf.

Concentration of $[K^+]$ ^a (μ M)	$E_{1/2}$ ($L^6UO_2/L^6UO_2^-$) ^b (V vs. $Fc^{+/0}$)	ΔE_p ^c (mV)	$E_{1/2}$ ($L^6UO_2K/L^6UO_2K^-$) ^b (V vs. $Fc^{+/0}$)	ΔE_p ^c (mV)
0	-1.53	80		
120	-1.53	100	-1.38	90
240	-1.54	110	-1.37	110
360			-1.37	130
480			-1.37	130
950			-1.36	120
2200			-1.35	130
4100			-1.34	140

^aConcentration of $[K^+]$ corrected for dilution during the course of the experiment.

^bhalf-wave potentials were determined for isolated redox events with clean corresponding anodic and cathodic peak potentials.

^cPeak anodic and cathodic potential difference

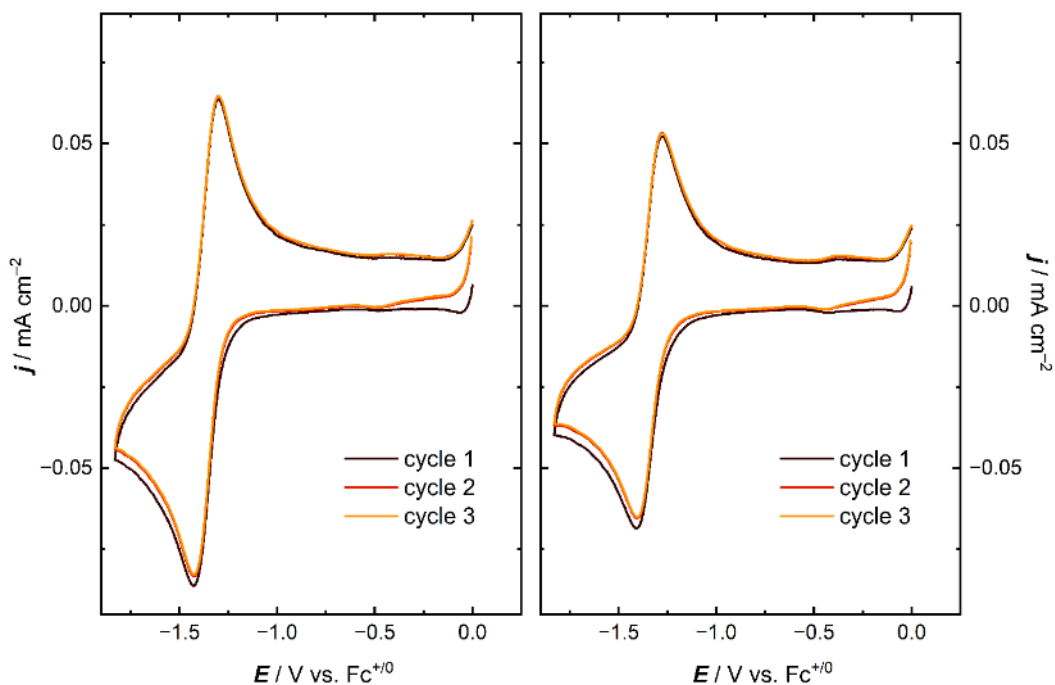


Figure S98. Left panel: 3 consecutive cyclic voltammograms of L^6UO_2 in the presence of 1 equiv. of KOTf. Right panel: 10 equiv. of KOTf. Conditions: 0.5 mM L^6UO_2 in tetrabutylammonium hexafluorophosphate in acetonitrile; 100 mV/s scan rate.

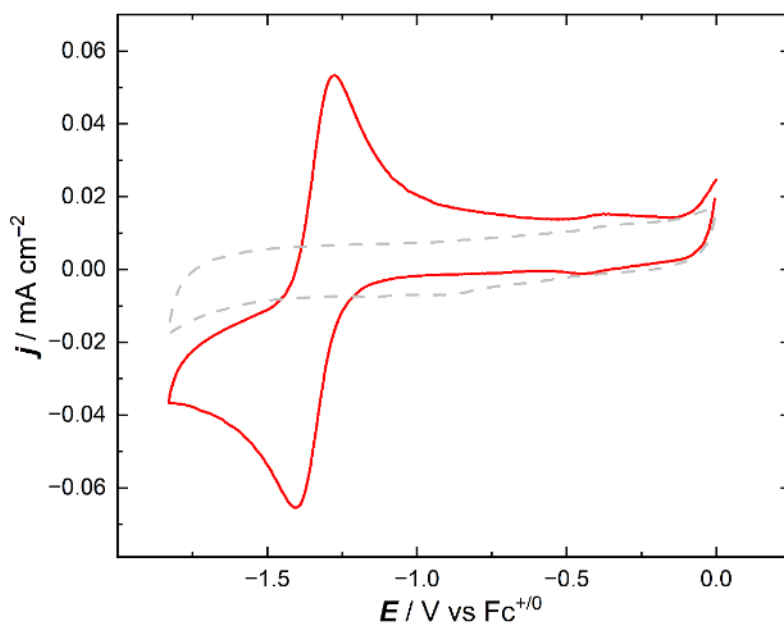


Figure S99. Red trace: cyclic voltammogram of 0.5 mM L^6UO_2 in the presence of 10 equiv. of KOTf. Dashed trace: cyclic voltammogram of blank tetrabutylammonium hexafluorophosphate in acetonitrile with 10 equiv. of KOTf added with respect to the concentration of L^6UO_2 . 100 mV/s scan rate.

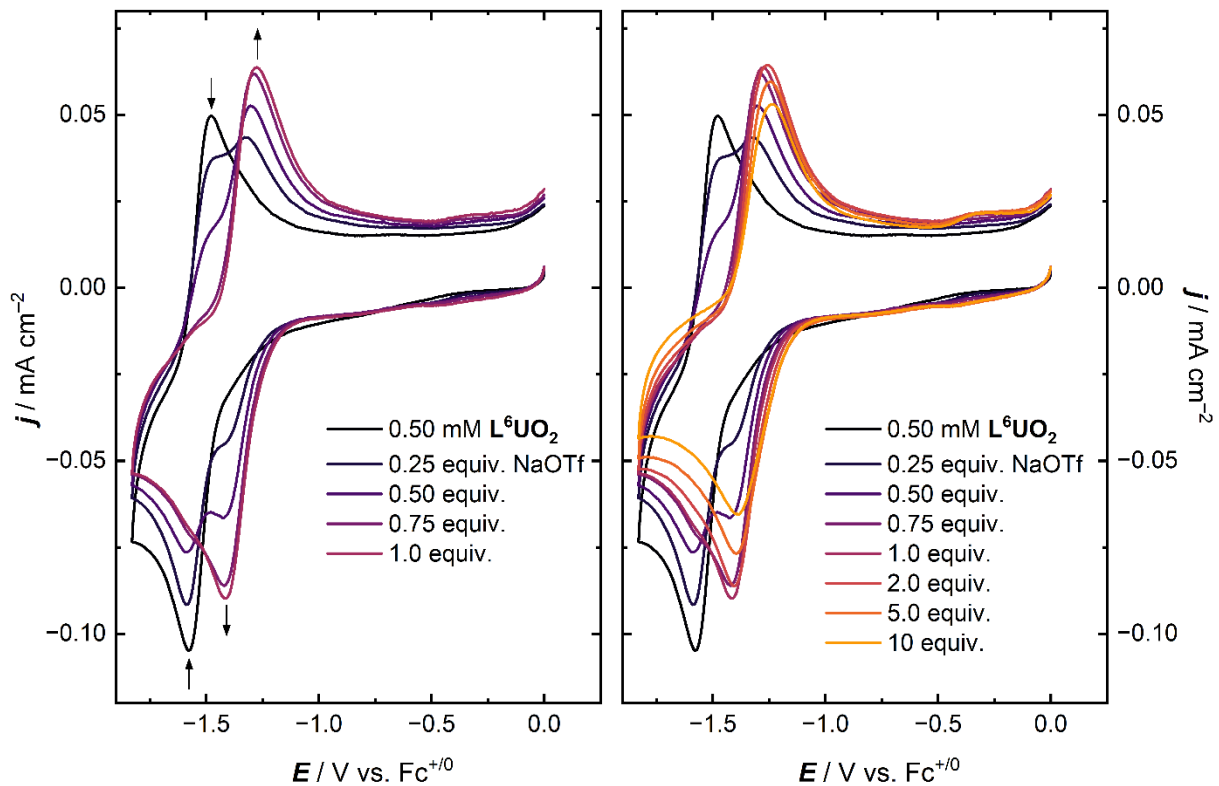


Figure S100. Left panel: electrochemical titration of L^6UO_2 with increasing equivalents of NaOTf up to 1 equiv. Right panel: Further additions of NaOTf up to 10 equiv. demonstrating the redox behavior of the U(VI)/U(V) couple in the presence of excess $[Na^+]$. Three consecutive cyclic voltammograms were collected for each addition of $[Na^+]$, first cycles plotted above. Conditions: 0.5 mM L^6UO_2 in 0.1 M tetrabutylammonium hexafluorophosphate in acetonitrile; stock solution of NaOTf prepared in acetonitrile electrolyte; 100 mV/s scan rate.

Table S6. Selected metrics for the electrochemical titration of L^6UO_2 with NaOTf.

Concentration of [Na ⁺] ^a (μ M)	$E_{1/2}$ ($L^6UO_2/L^6UO_2^-$) ^b (V vs. $Fc^{+/0}$)	ΔE_p^c (mV)	$E_{1/2}$ ($L^6UO_2Na/L^6UO_2Na^-$) ^b (V vs. $Fc^{+/0}$)	ΔE_p^c (mV)
0	-1.53	100		
120	-1.53	130	-1.38	100
240	-1.54	110	-1.37	130
360			-1.36	130
480			-1.34	140
950			-1.33	140
2200			-1.32	150
4100			-1.31	150

^aConcentration of [Na⁺] corrected for dilution during the course of the experiment.

^bhalf-wave potentials were determined for isolated redox events with clean corresponding anodic and cathodic peak potentials.

^cPeak anodic and cathodic potential difference

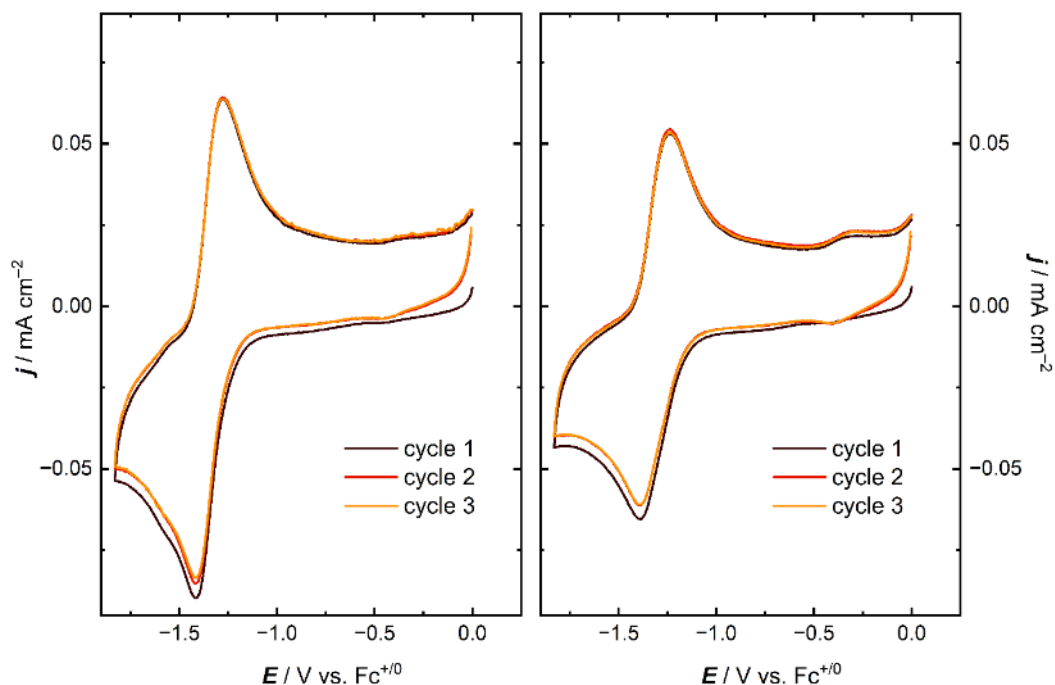


Figure S101. Left panel: 3 consecutive cyclic voltammograms of L^6UO_2 in the presence of 1 equiv. of NaOTf. Right panel: 10 equiv. of NaOTf. Conditions: 0.5 mM L^6UO_2 in tetrabutylammonium hexafluorophosphate in acetonitrile; 100 mV/s scan rate.

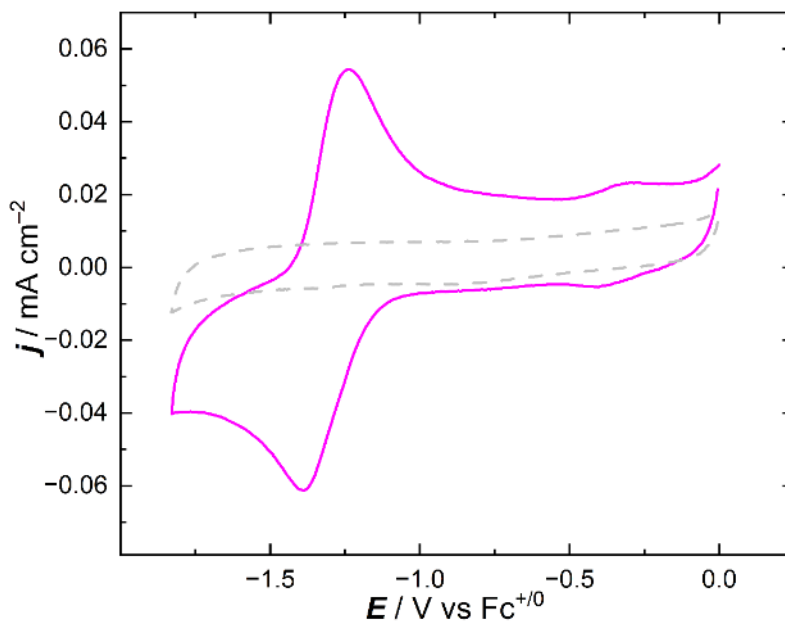


Figure S102. Magenta trace: cyclic voltammogram of 0.5 mM L^6UO_2 in the presence of 10 equiv. of NaOTf. Dashed trace: cyclic voltammogram of blank tetrabutylammonium hexafluorophosphate in acetonitrile with 10 equiv. of NaOTf added with respect to the concentration of L^6UO_2 . 100 mV/s scan rate.

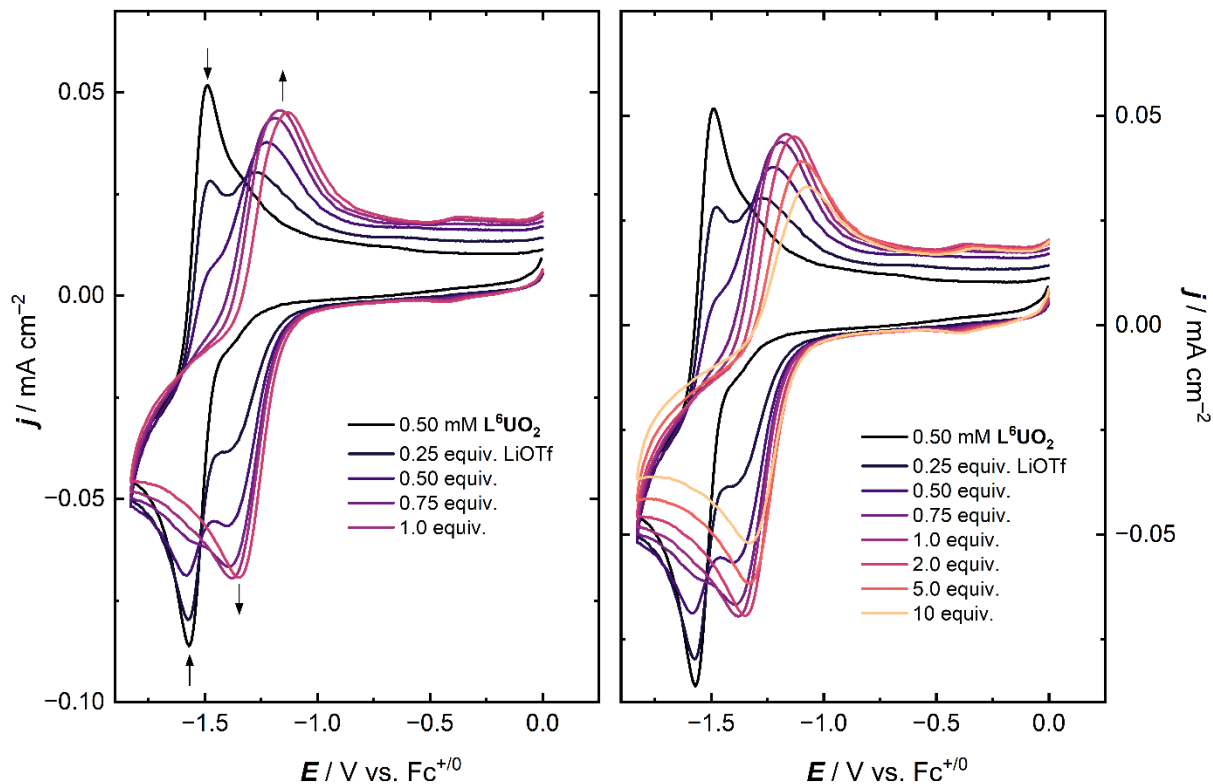


Figure S103. Left panel: electrochemical titration of L^6UO_2 with increasing equivalents of LiOTf up to 1 equiv. Right panel: Further additions of LiOTf up to 10 equiv. demonstrating the redox behavior of the U(VI)/U(V) couple in the presence of excess $[\text{Li}^+]$. A single cyclic voltammogram was collected for each addition of $[\text{Li}^+]$. Conditions: 0.5 mM L^6UO_2 in 0.1 M tetrabutylammonium hexafluorophosphate in acetonitrile; stock solution of LiOTf prepared in acetonitrile electrolyte; 100 mV/s scan rate.

Table S7. Selected metrics for the electrochemical titration of L^6UO_2 with LiOTf (single cycles).

Concentration of [Li ⁺] ^a (μM)	$E_{1/2}$ ($\text{L}^6\text{UO}_2/\text{L}^6\text{UO}_2^-$) ^b (V vs. $\text{Fc}^{+/0}$)	ΔE_p^c (mV)	$E_{1/2}$ ($\text{L}^6\text{UO}_2\text{Li}/\text{L}^6\text{UO}_2\text{Li}^-$) ^b (V vs. $\text{Fc}^{+/0}$)	ΔE_p^c (mV)
0	-1.53	80		
120	-1.52	100	-1.34	140
240			-1.31	180
360			-1.29	180
480			-1.27	220
950			-1.24	220
2200			-1.21	240
4100			-1.20	260

^aConcentration of [Li⁺] corrected for dilution during the course of the experiment.

^bhalf-wave potentials were determined for isolated redox events with clean corresponding anodic and cathodic peak potentials.

^cPeak anodic and cathodic potential difference

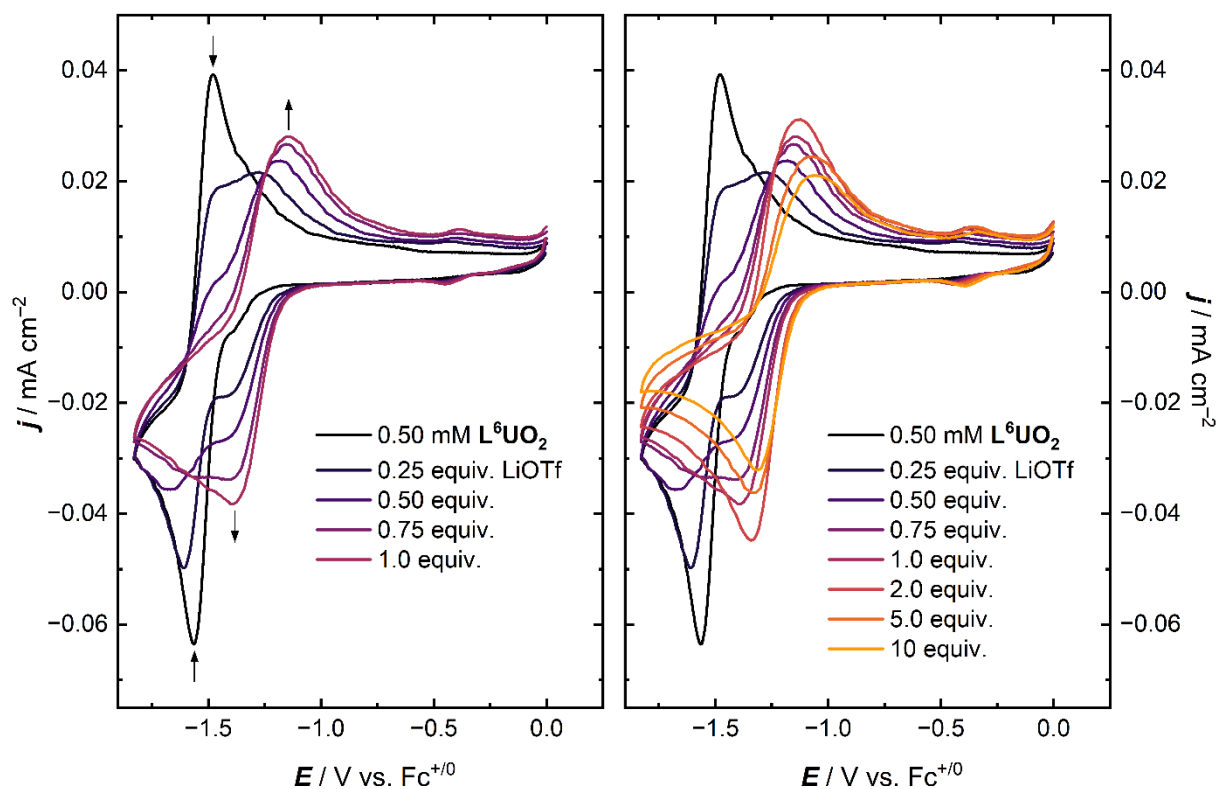


Figure S104. Left panel: electrochemical titration of L^6UO_2 with increasing equivalents of LiOTf up to 1 equiv. Right panel: Further additions of LiOTf up to 10 equiv. demonstrating the redox behavior of the U(VI)/U(V) couple in the presence of excess $[\text{Li}^+]$. Three consecutive cyclic voltammograms were collected for each addition of $[\text{Li}^+]$ followed by wiping the working electrode to remove putative absorbed species, second cycles plotted above. There appears to be little influence of $[\text{Li}^+]$ on the reduction-induced formation of heterogenous material based on the similarity of these data to those shown in Figure S103 for $[\text{Li}^+]$ titration without wiping the electrode. Conditions: 0.5 mM L^6UO_2 in 0.1 M tetrabutylammonium hexafluorophosphate in acetonitrile; stock solution of LiOTf prepared in acetonitrile electrolyte; 100 mV/s scan rate.

Table S8. Selected metrics for the electrochemical titration of L^6UO_2 with LiOTf (working electrode wiped).

Concentration of $[\text{Li}^+]^a$ (μM)	$E_{1/2}$ ($\text{L}^6\text{UO}_2/\text{L}^6\text{UO}_2^-$) ^b (V vs. $\text{Fc}^{+/0}$)	ΔE_p^c (mV)	$E_{1/2}$ ($\text{L}^6\text{UO}_2\text{Li}/\text{L}^6\text{UO}_2\text{Li}^-$) ^b (V vs. $\text{Fc}^{+/0}$)	ΔE_p^c (mV)
0	-1.52	80		
120	-1.52	180	-1.35	160
240			-1.32	270
360			-1.28	260
480			-1.27	260
950			-1.23	220
2200			-1.20	260
4100			-1.19	260

^aConcentration of $[\text{Li}^+]$ corrected for dilution during the course of the experiment.

^bhalf-wave potentials were determined for isolated redox events with clean corresponding anodic and cathodic peak potentials.

^cPeak anodic and cathodic potential difference

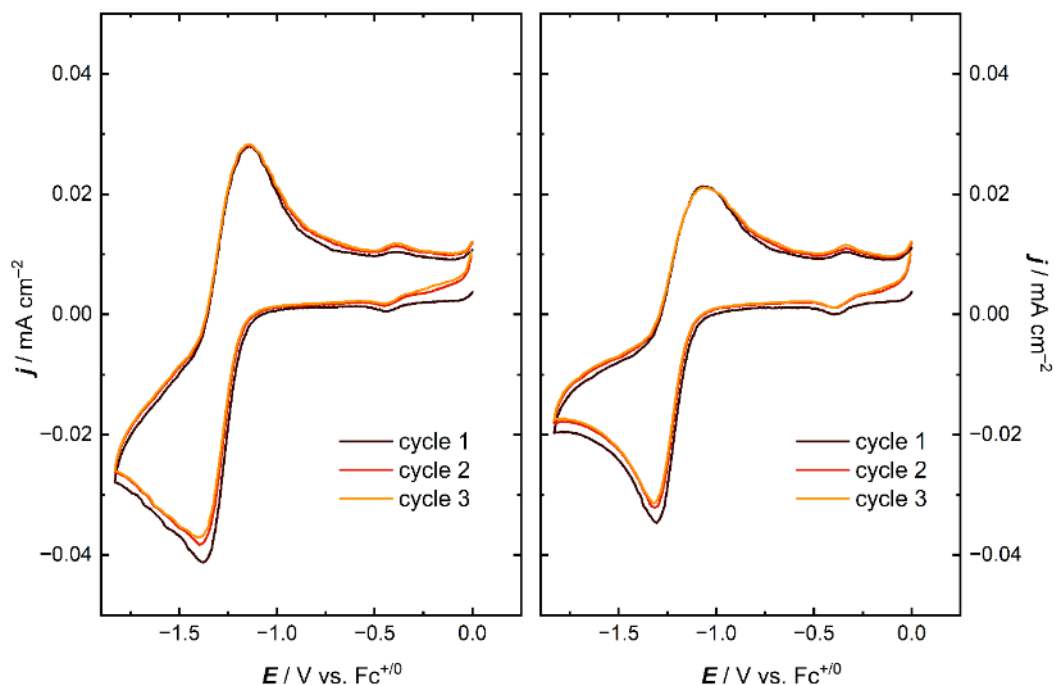


Figure S105. Left panel: 3 consecutive cyclic voltammograms of L^6UO_2 in the presence of 1 equiv. of LiOTf. Right panel: 10 equiv. of LiOTf. The working electrode was wiped in between additions of LiOTf. Conditions: 0.5 mM L^6UO_2 in tetrabutylammonium hexafluorophosphate in acetonitrile; 100 mV/s scan rate.

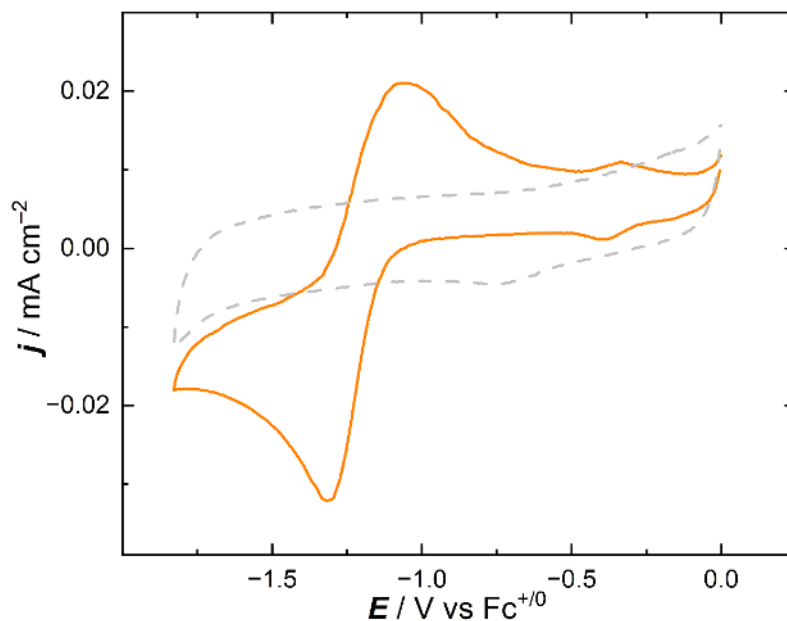


Figure S106. Orange trace: cyclic voltammogram of 0.5 mM L^6UO_2 in the presence of 10 equiv. of LiOTf. Dashed trace: cyclic voltammogram of blank tetrabutylammonium hexafluorophosphate in acetonitrile with 10 equiv. of LiOTf added with respect to the concentration of L^6UO_2 . 100 mV/s scan rate.

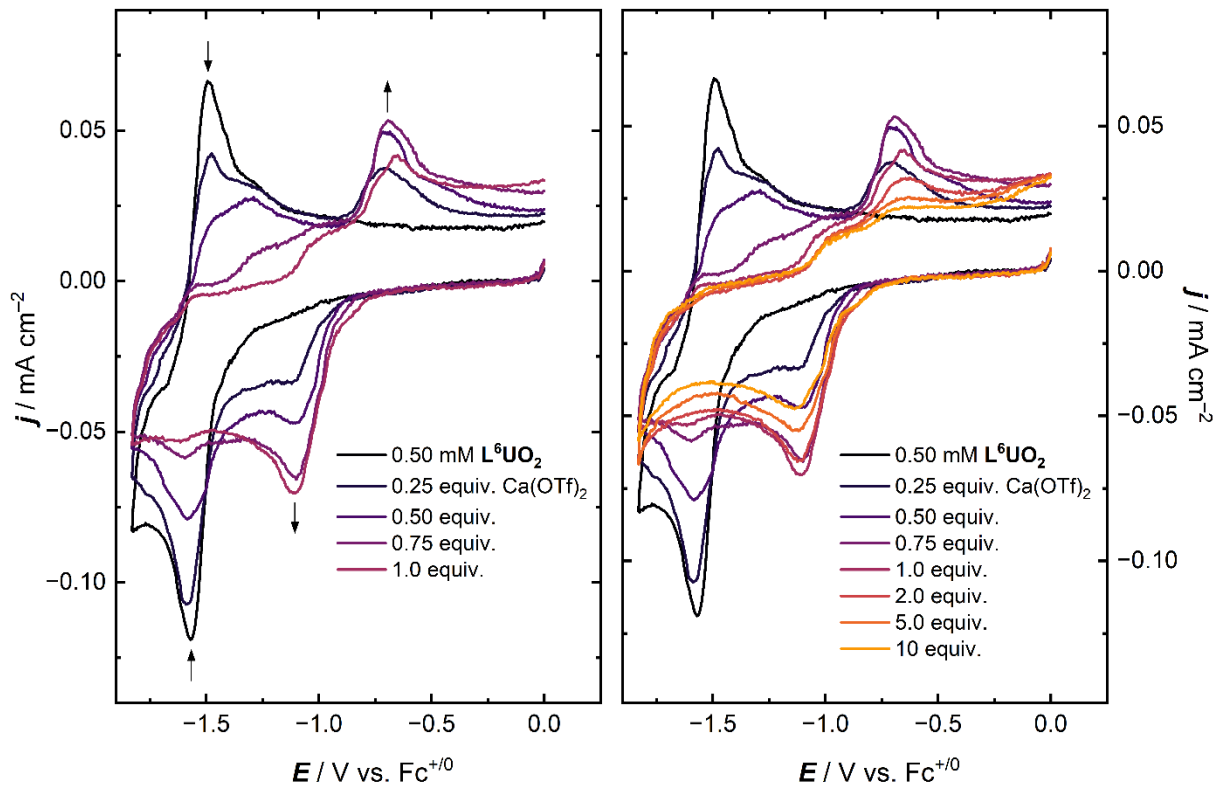


Figure S107. Left panel: electrochemical titration of L^6UO_2 with increasing equivalents of $\text{Ca}(\text{OTf})_2$ up to 1 equiv. Right panel: Further additions of $\text{Ca}(\text{OTf})_2$ up to 10 equiv. demonstrating the redox behavior of the U(VI)/U(V) couple in the presence of excess $[\text{Ca}^{2+}]$. A single cyclic voltammogram was collected for each addition of $[\text{Ca}^{2+}]$. Conditions: 0.5 mM L^6UO_2 in 0.1 M tetrabutylammonium hexafluorophosphate in acetonitrile; stock solution of $\text{Ca}(\text{OTf})_2$ prepared in acetonitrile electrolyte; 100 mV/s scan rate.

Table S9. Selected metrics for the electrochemical titration of L^6UO_2 with $Ca(OTf)_2$ (single cycles).

Concentration of $[Ca^{2+}]^a$ (μM)	$E_{1/2}$ ($L^6UO_2/L^6UO_2^-$) ^b (V vs. $Fc^{+/0}$)	ΔE_p^c (mV)	$E_{1/2}$ ($L^6UO_2Ca/L^6UO_2Ca^-$) ^b (V vs. $Fc^{+/0}$)	ΔE_p^c (mV)
0	-1.53	80		
120	-1.53	120	-0.93	460
240	-1.44	290	-0.90	430
360	-1.57	60	-0.90	410
480	-1.56	100	-0.88	450
950			-0.88	490
2200			-0.89	530
4100			-0.84	580

^aConcentration of $[Ca^{2+}]$ corrected for dilution during the course of the experiment.

^bhalf-wave potentials were determined for isolated redox events with clean corresponding anodic and cathodic peak potentials.

^cPeak anodic and cathodic potential difference

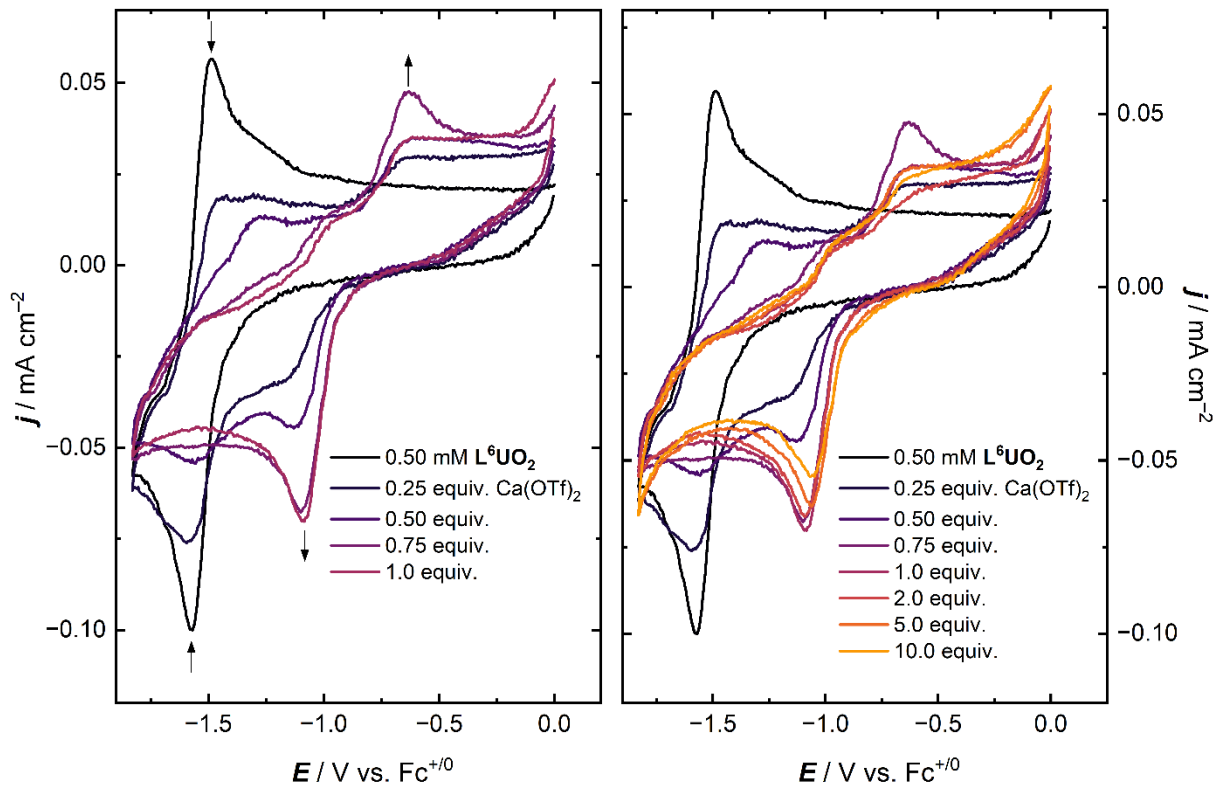


Figure S108. Left panel: electrochemical titration of L^6UO_2 with increasing equivalents of $Ca(OTf)_2$ up to 1 equiv. Right panel: Further additions of $Ca(OTf)_2$ up to 10 equiv. demonstrating the redox behavior of the U(VI)/U(V) couple in the presence of excess $[Ca^{2+}]$. Three consecutive cyclic voltammograms were collected for each addition of $[Ca^{2+}]$ followed by wiping the working electrode to remove putative absorbed species, second cycles plotted above. There appears to be little influence of $[Ca^{2+}]$ on the reduction-induced formation of heterogenous material based on the similarity of these data to those shown in figure S107 for $[Ca^{2+}]$ titration without wiping the electrode. Conditions: 0.5 mM L^6UO_2 in 0.1 M tetrabutylammonium hexafluorophosphate in acetonitrile; stock solution of $Ca(OTf)_2$ prepared in acetonitrile electrolyte; 100 mV/s scan rate.

Table S10. Selected metrics for the electrochemical titration of L^6UO_2 with $\text{Ca}(\text{OTf})_2$ (working electrode wiped).

Concentration of $[\text{Ca}^{2+}]^a$ (μM)	$E_{1/2}$ ($\text{L}^6\text{UO}_2/\text{L}^6\text{UO}_2^-$) ^b (V vs. $\text{Fc}^{+/0}$)	ΔE_p^c (mV)	$E_{1/2}$ ($\text{L}^6\text{UO}_2\text{Ca}/\text{L}^6\text{UO}_2\text{Ca}^-$) ^b (V vs. $\text{Fc}^{+/0}$)	ΔE_p^c (mV)
0	-1.53	90		
120	-1.45	280		
240	-1.41	310	-0.87	530
360			-0.87	470
480			-0.85	470
950			-0.84	510
2200			-0.84	440
4100			-0.82	500

^aConcentration of $[\text{Ca}^{2+}]$ corrected for dilution during the course of the experiment.

^bhalf-wave potentials were determined for isolated redox events with clean corresponding anodic and cathodic peak potentials.

^cPeak anodic and cathodic potential difference

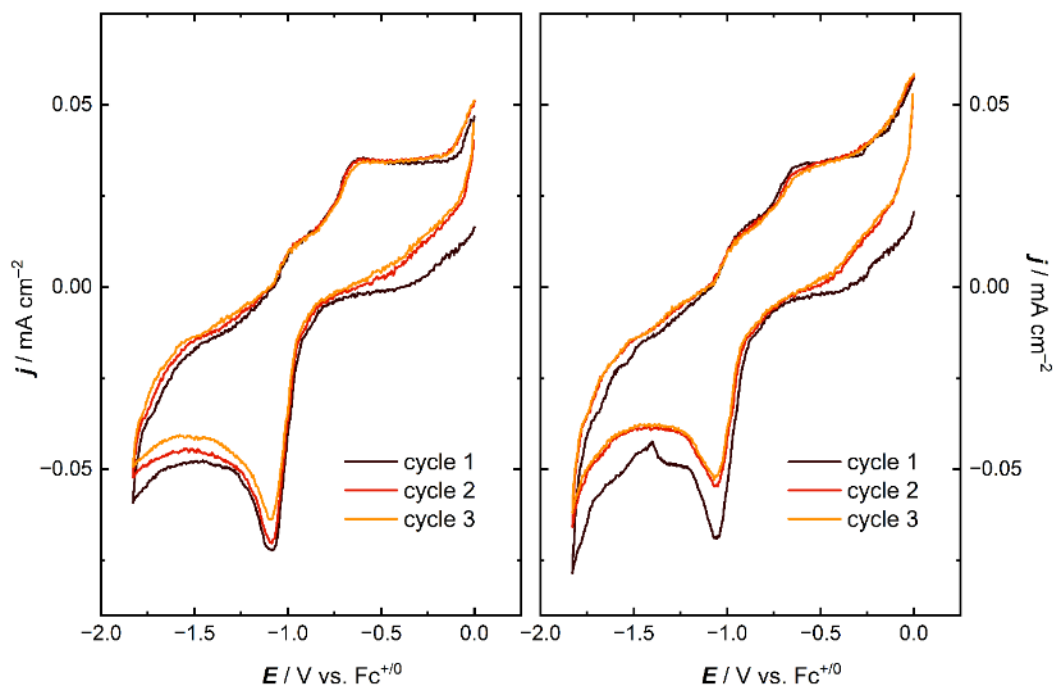


Figure S109. Left panel: 3 consecutive cyclic voltammograms of L^6UO_2 in the presence of 1 equiv. of $Ca(OTf)_2$. Right panel: 10 equiv. of $Ca(OTf)_2$. The working electrode was wiped in between additions of $Ca(OTf)_2$. Conditions: 0.5 mM L^6UO_2 in tetrabutylammonium hexafluorophosphate in acetonitrile; 100 mV/s scan rate.

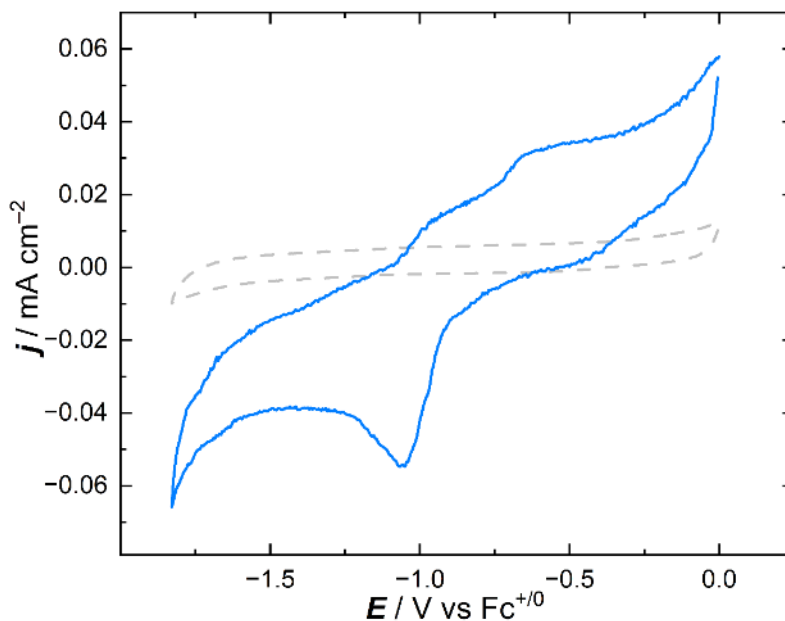


Figure S110. Blue trace: cyclic voltammogram of 0.5 mM L^6UO_2 in the presence of 10 equiv. of $Ca(OTf)_2$. Dashed trace: cyclic voltammogram of blank tetrabutylammonium hexafluorophosphate in acetonitrile with 10 equiv. of $Ca(OTf)_2$ added with respect to the concentration of L^6UO_2 . 100 mV/s scan rate.

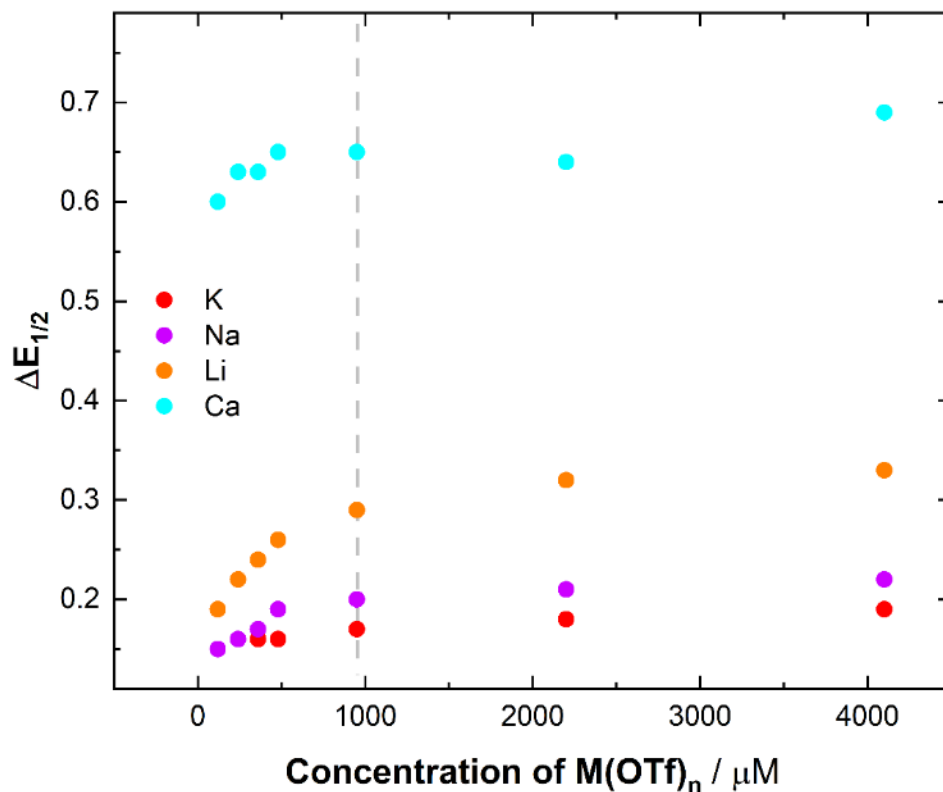


Figure S111. Dependence of the redox potential difference between L^6UO_2 and the *in-situ* generated L^6UO_2M ($\Delta E_{1/2}$) on the concentration of titrated $M(OTf)_n$. The dashed line represents the addition of 1 equiv. of $M(OTf)_n$ with respect to the concentration of L^6UO_2 . After 1 equiv. of $M(OTf)_n$ is added, there is essentially no change in the $\Delta E_{1/2}$ as revealed by plateauing behavior beyond 1000 μM of $M(OTf)_n$.

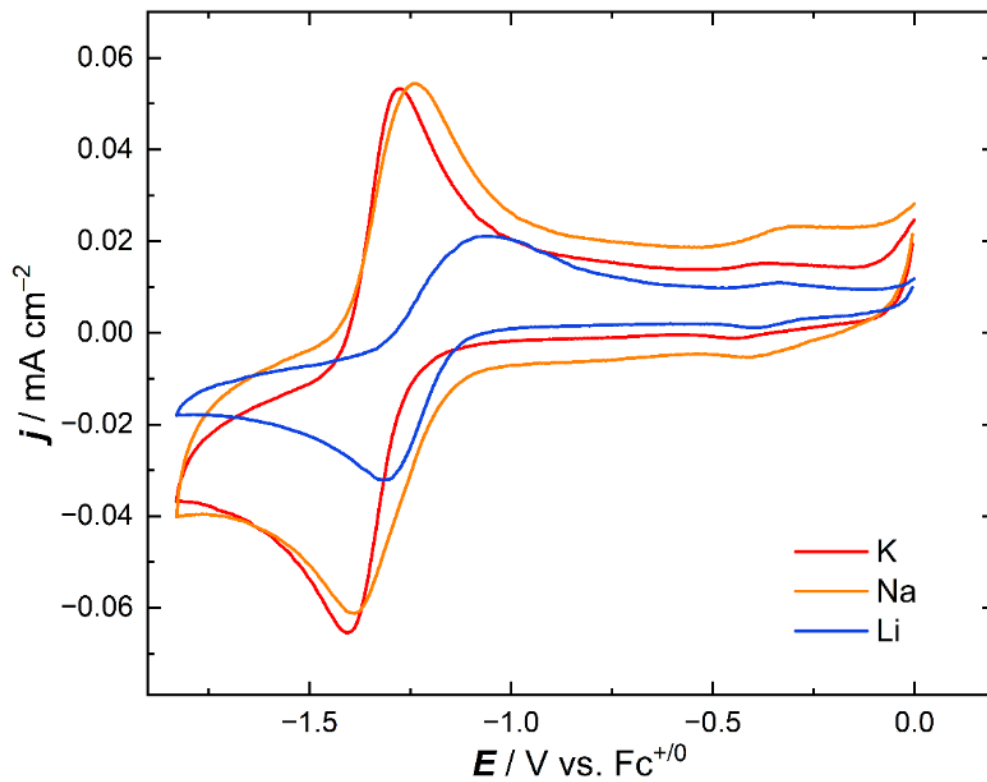


Figure S112. Cyclic voltammograms of L^6UO_2 titrated with 10 equiv. of respective $\text{M}(\text{OTf})$ to highlight the redox event that occurs at ca. 0.4 V vs. $\text{Fc}^{+/0}$. Second cycles plotted from each respective titration from figures S97, S100, and S103.

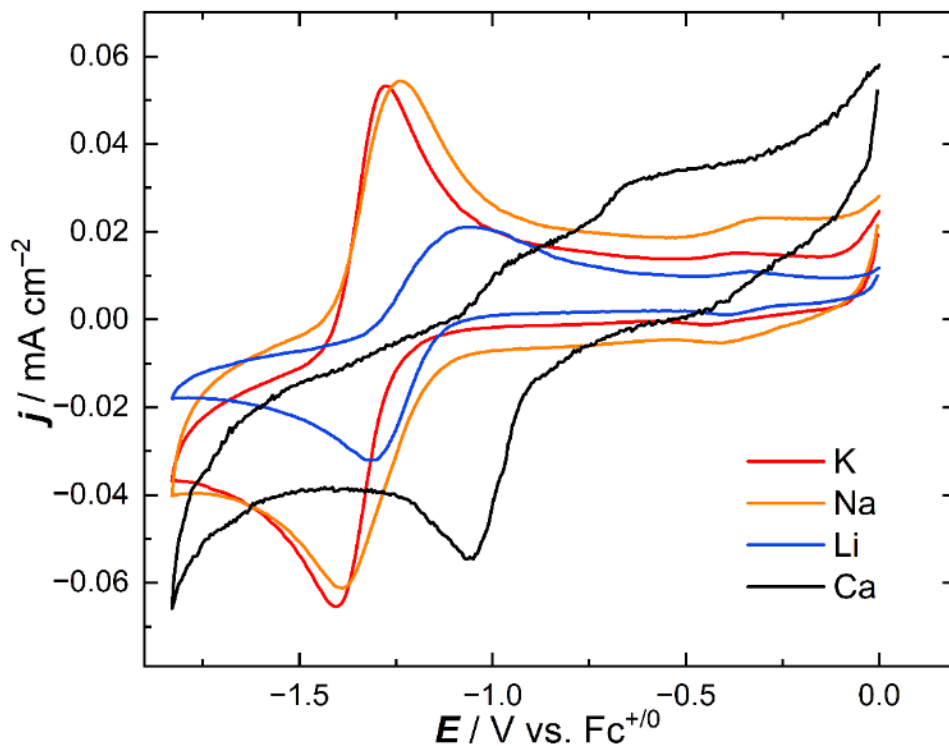


Figure S113. Cyclic voltammograms of L^6UO_2 titrated with 10 equiv. of respective $\text{M}(\text{OTf})_n$ to compare the appearance of the redox event near ca. 0.4 V vs. $\text{Fc}^{+/0}$ in the titrations with monovalent cations to the $\text{Ca}(\text{OTf})_2$ titration which appears to lack a feature in the same potential range. Second cycles plotted from each respective titration from figures S97, S100, S103, and S107.

NMR Titrations

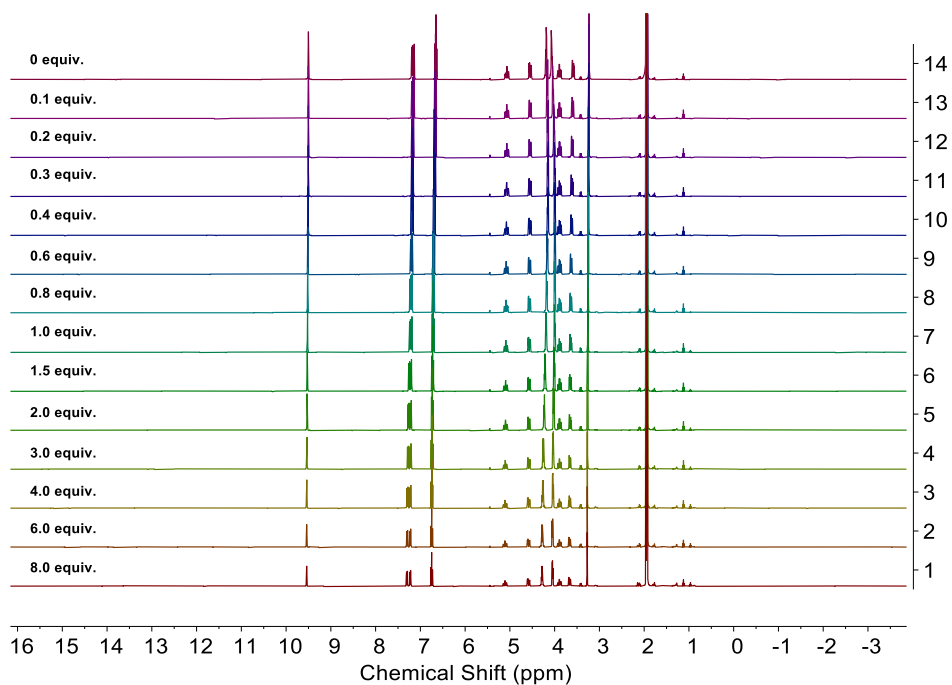


Figure S114. NMR titration experiments of L^5UO_2 with CsOTf showing the full spectra.

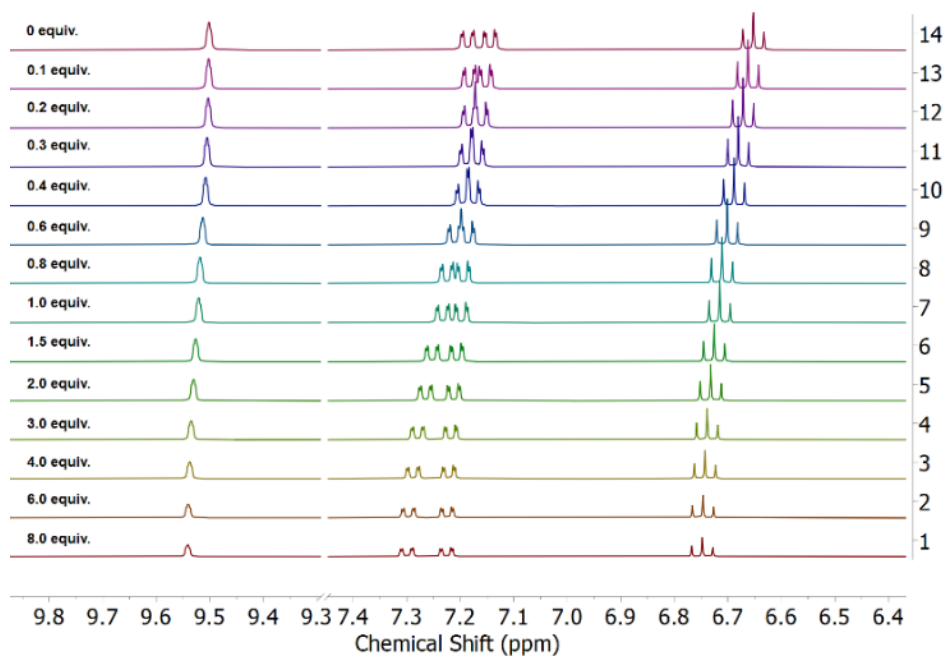


Figure S115. NMR titration experiments of L^5UO_2 with CsOTf showing the imine and aromatic region.

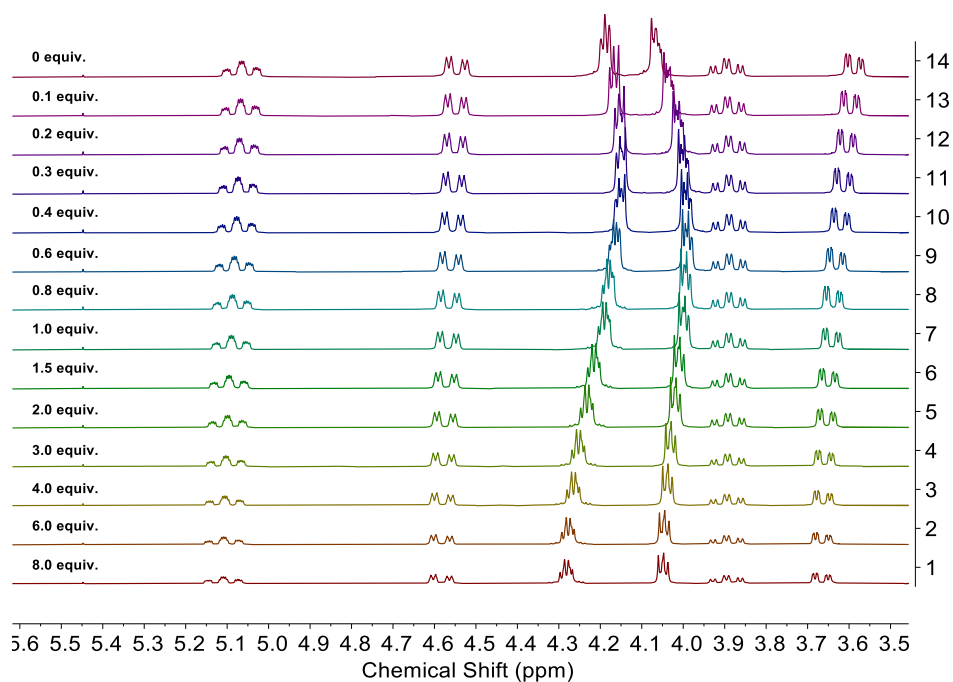


Figure S116. NMR titration experiments of L^5UO_2 with CsOTf showing the aliphatic region.

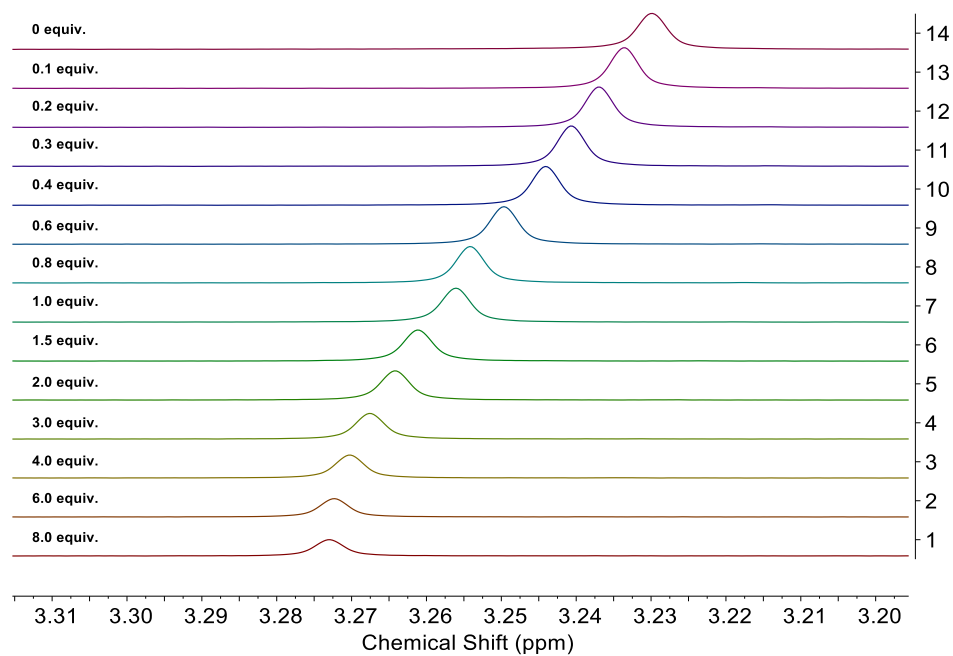


Figure S117. NMR titration experiments of L^5UO_2 with CsOTf showing the peak corresponding to the $-N-CH_3$ group used to make binding curves.

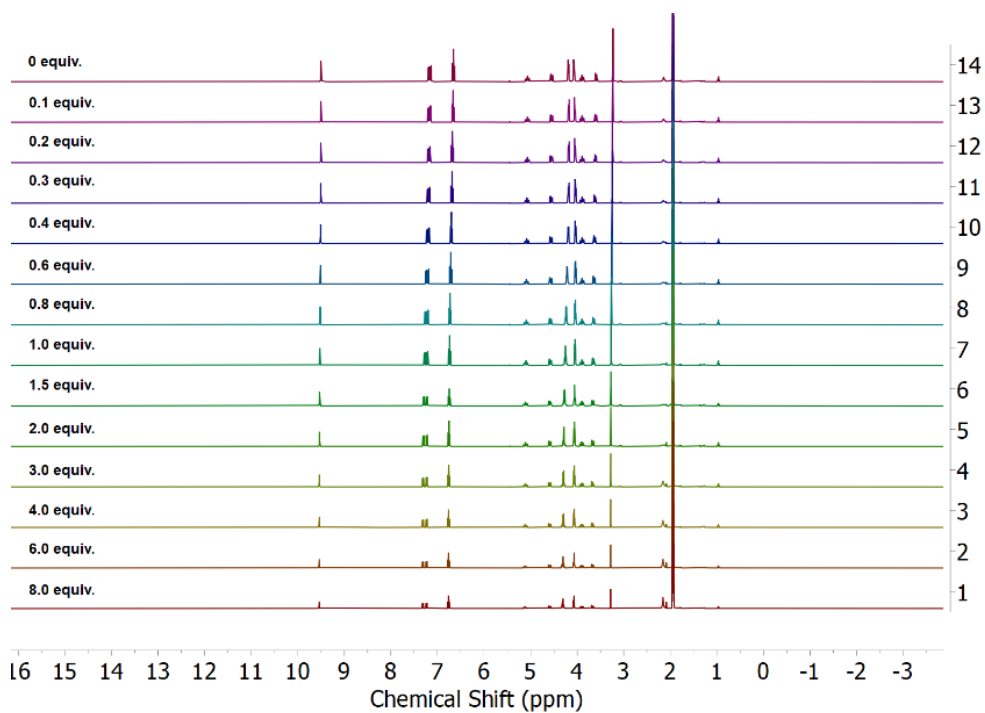


Figure S118. NMR titration experiments of L^5UO_2 with RbOTf showing the full spectra.

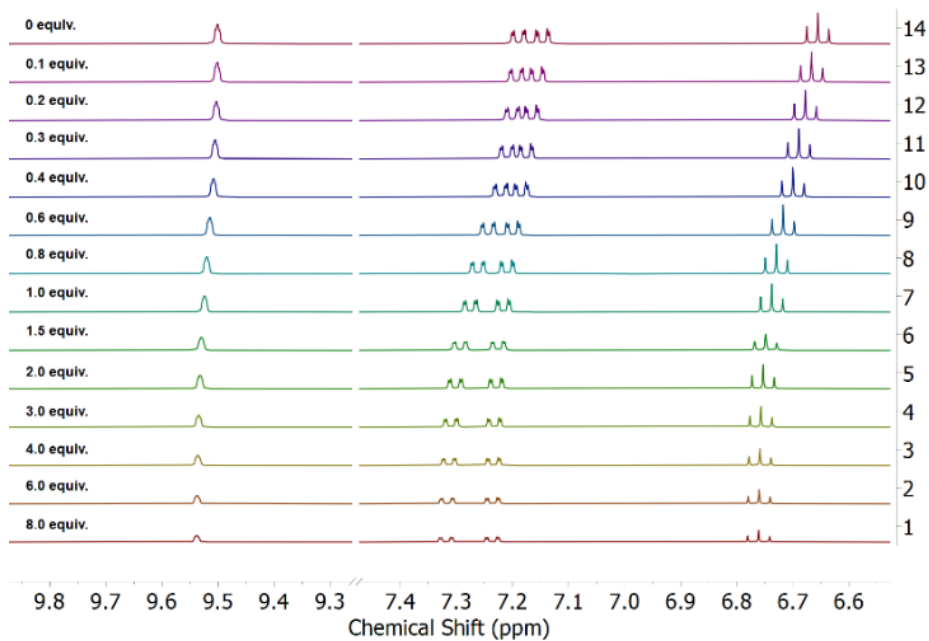


Figure S119. NMR titration experiments of L^5UO_2 with RbOTf showing the imine and aromatic region.

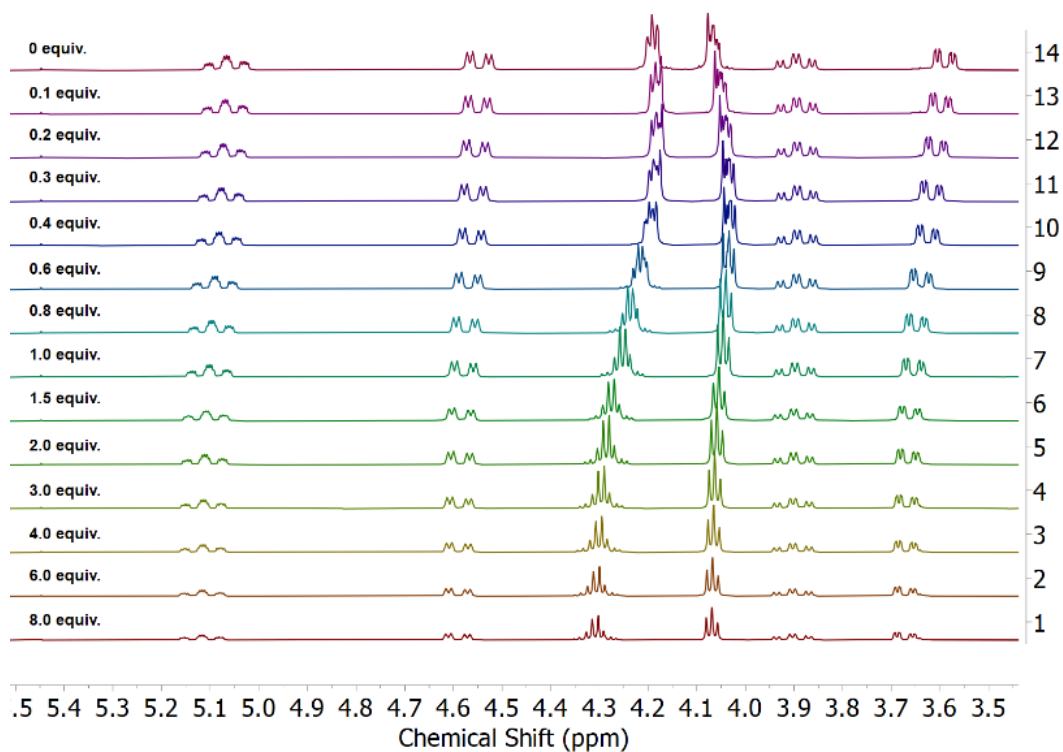


Figure S120. NMR titration experiments of L^5UO_2 with RbOTf showing the aliphatic region.

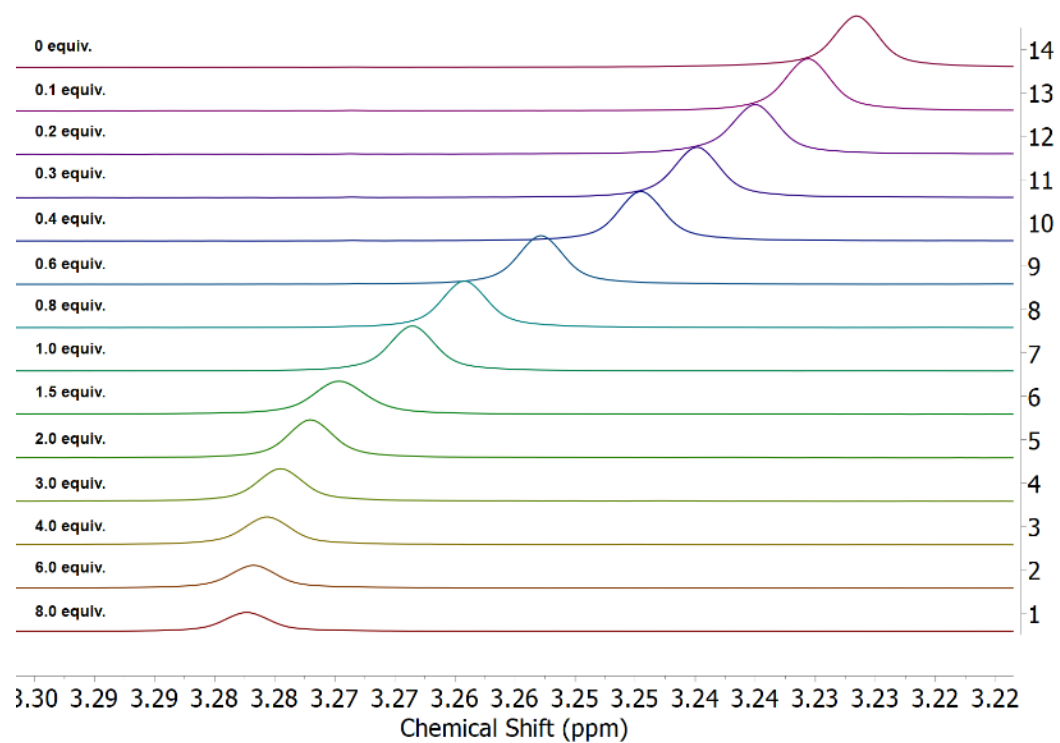


Figure S121. NMR titration experiments of L^5UO_2 with RbOTf showing the peak corresponding to the $-N-CH_3$ group used to make binding curves.

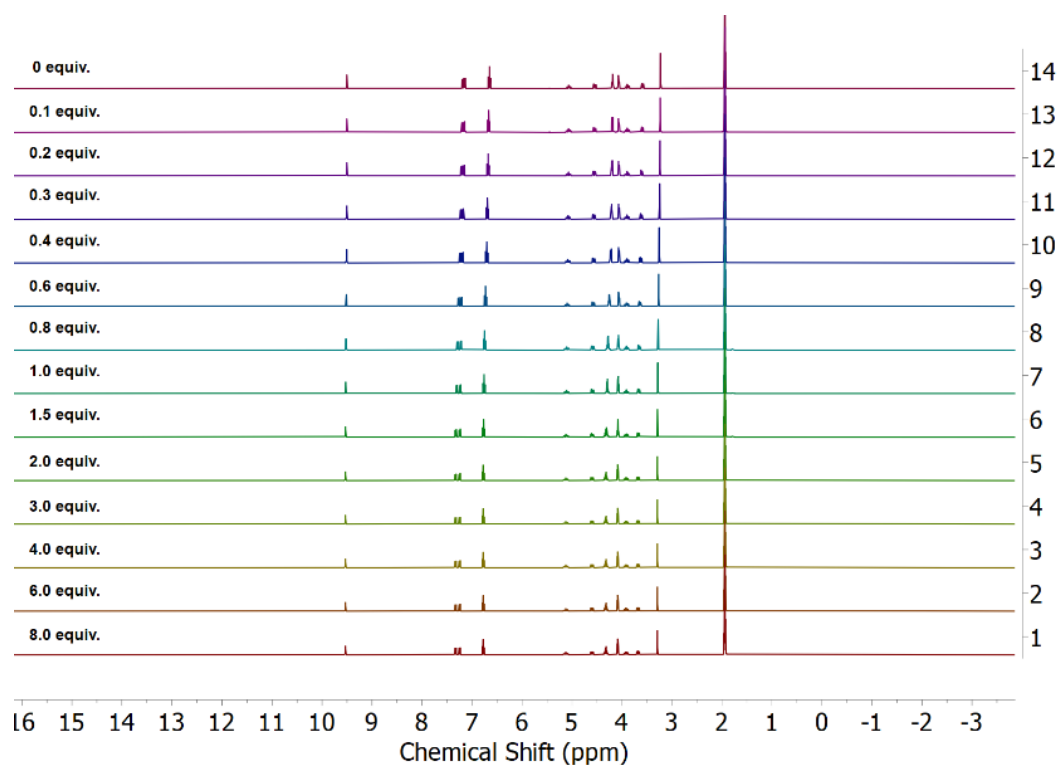


Figure S122. NMR titration experiments of L^5UO_2 with KOTf showing the full spectra.

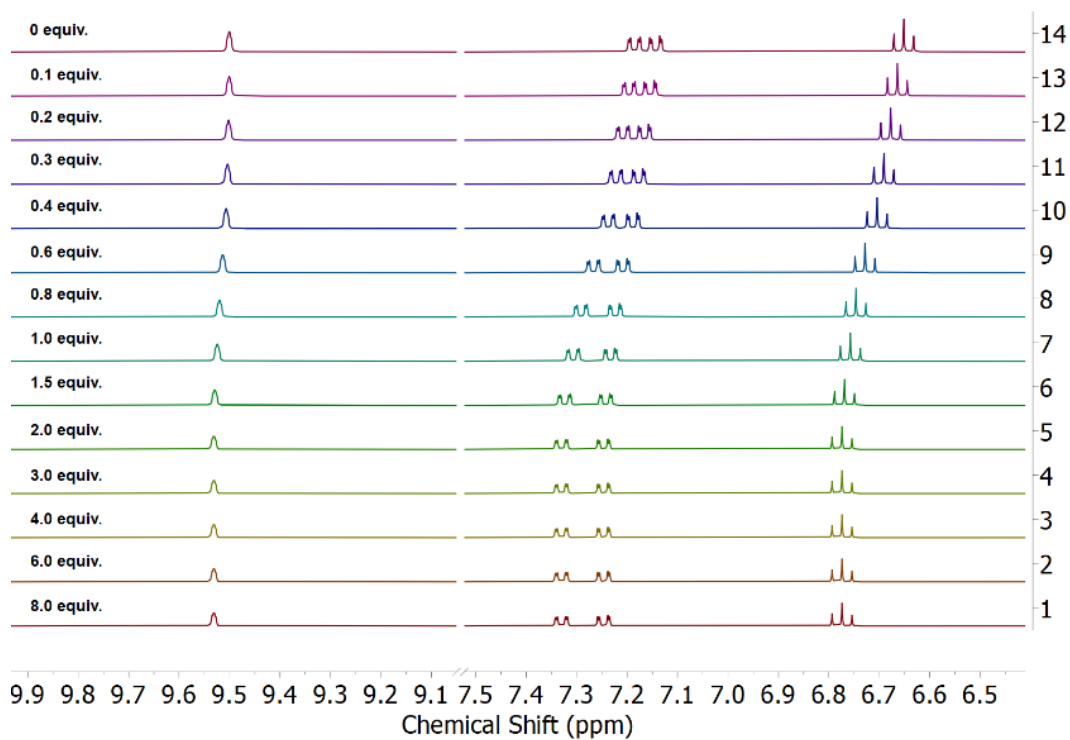


Figure S123. NMR titration experiments of L^5UO_2 with KOTf showing the imine and aromatic region.

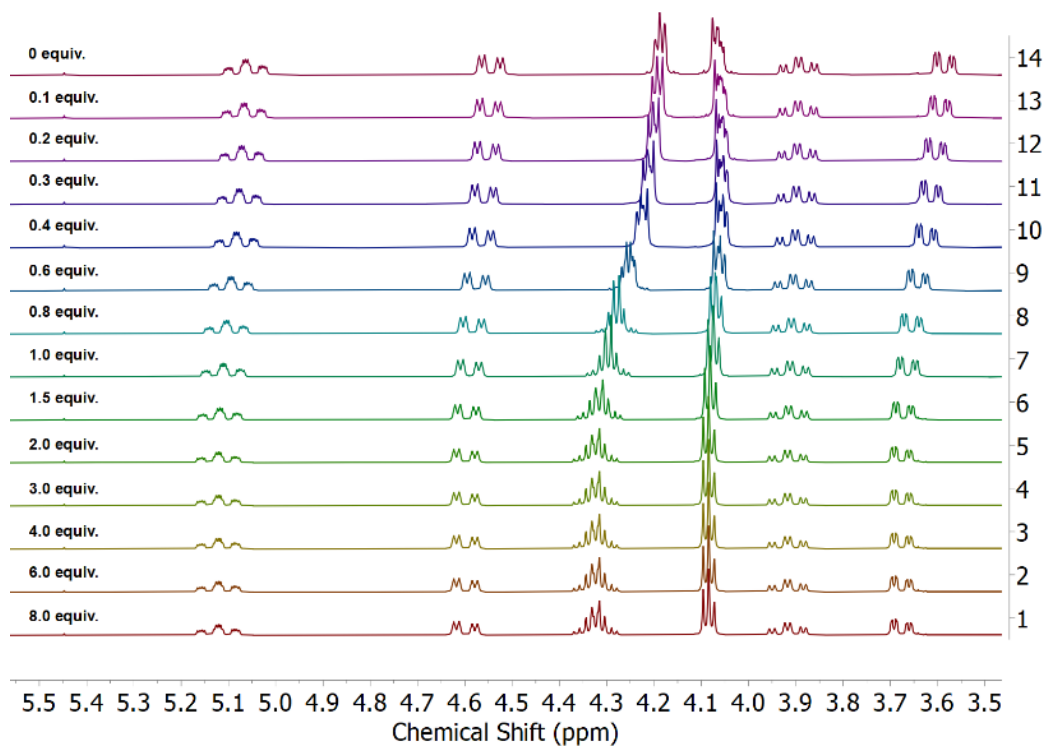


Figure S124. NMR titration experiments of L^5UO_2 with KOTf showing the aliphatic region.

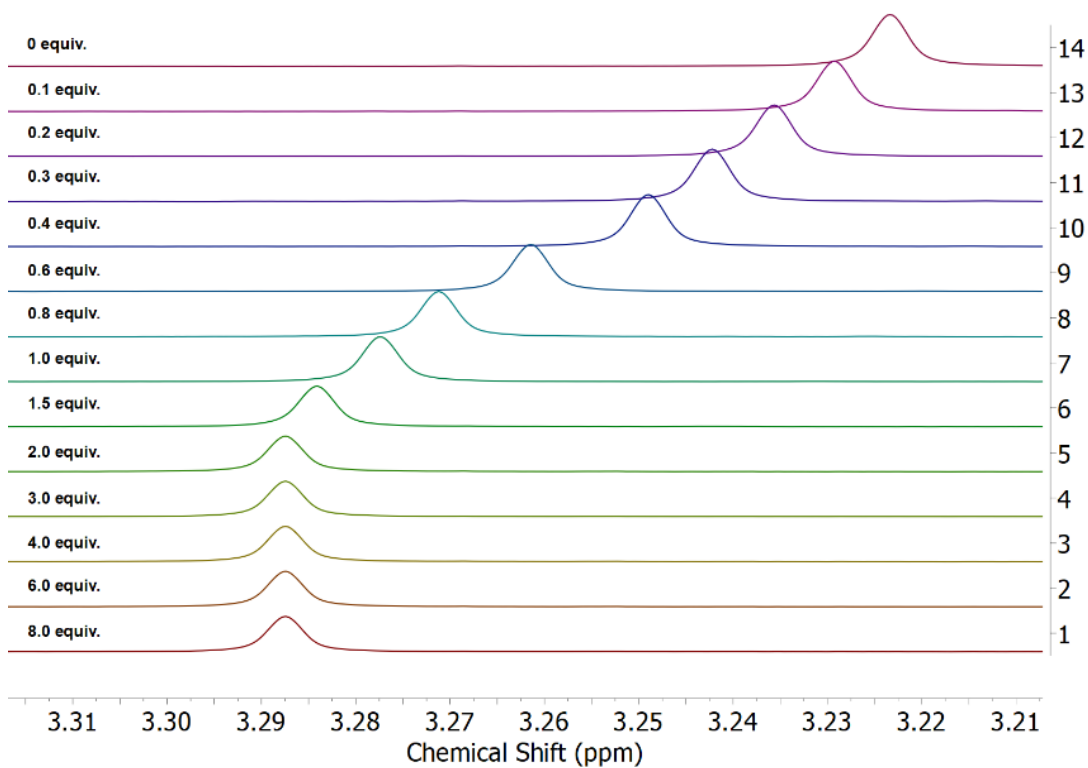


Figure S125. NMR titration experiments of L^5UO_2 with KOTf showing the peak corresponding to the $-N-CH_3$ group used to make binding curves.

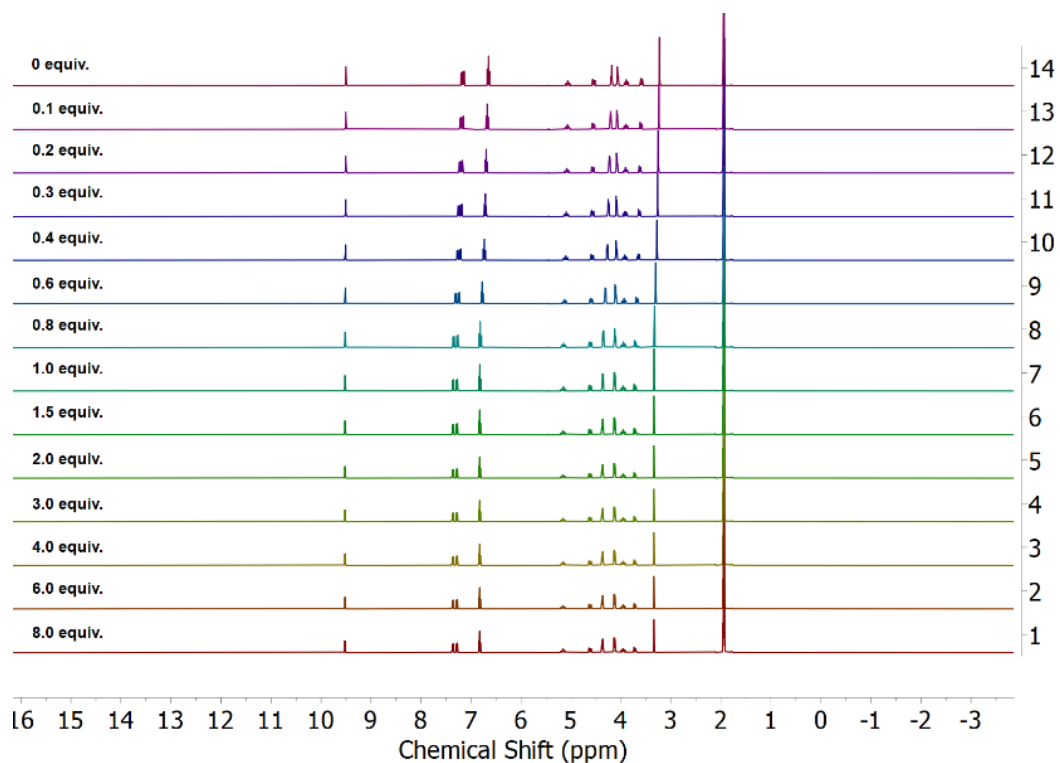


Figure S126. NMR titration experiments of L^5UO_2 with NaOTf showing the full spectra.

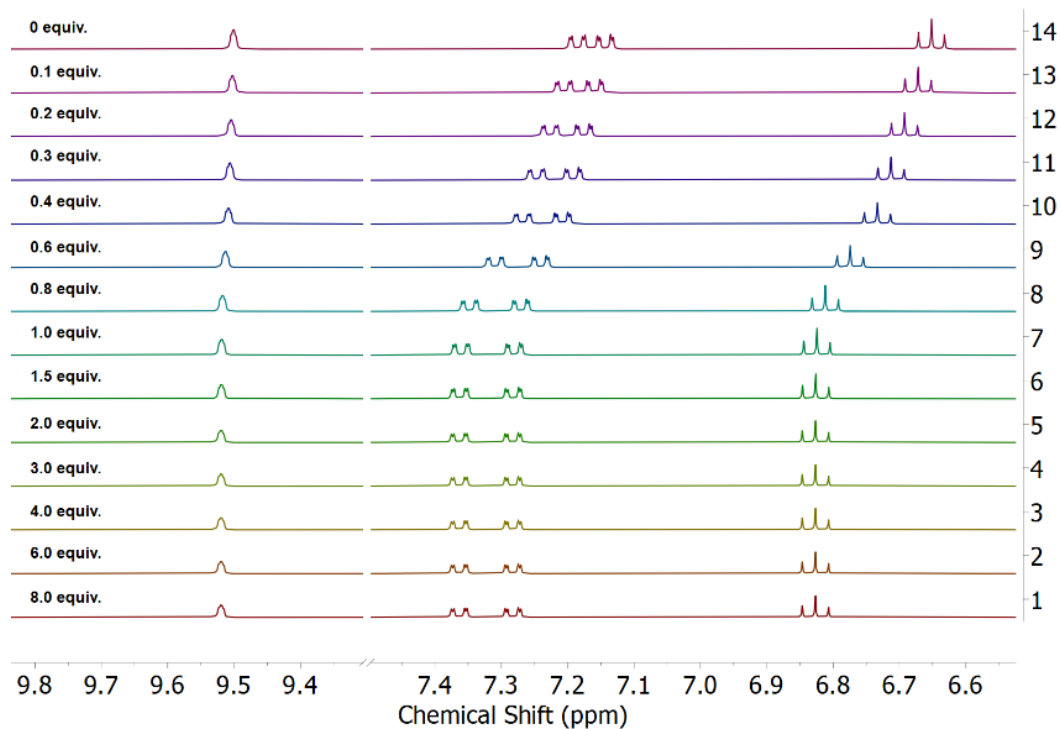


Figure S127. NMR titration experiments of L^5UO_2 with NaOTf showing the imine and aromatic region.

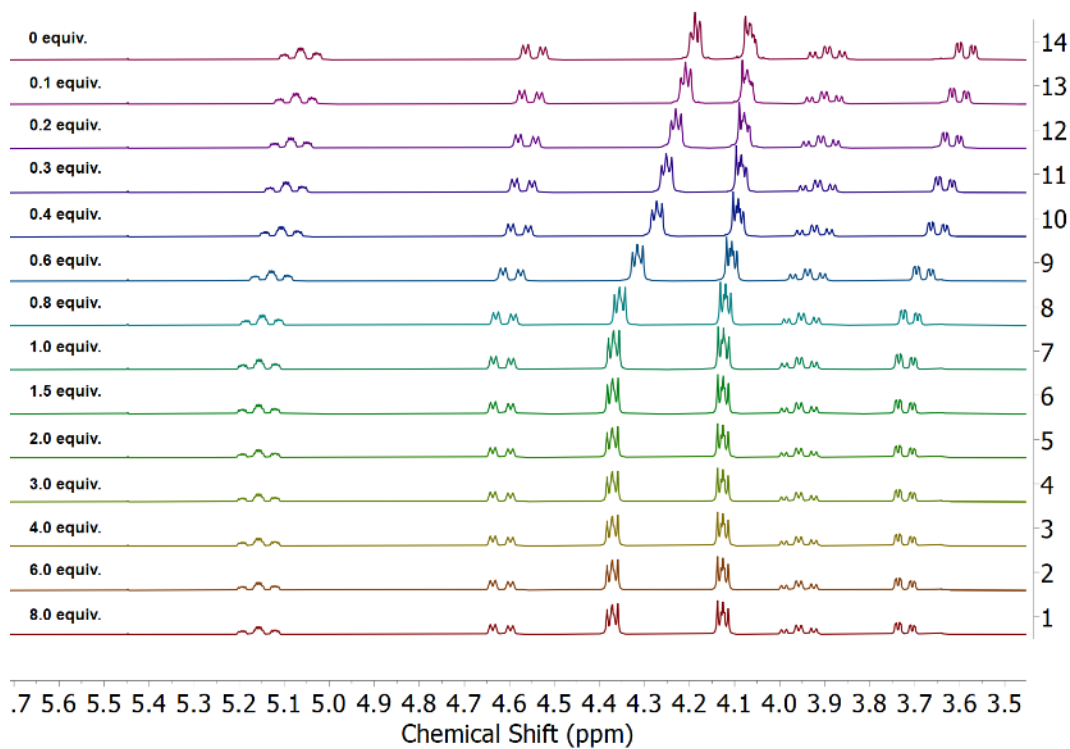


Figure S128. NMR titration experiments of L^5UO_2 with NaOTf showing the aliphatic region.

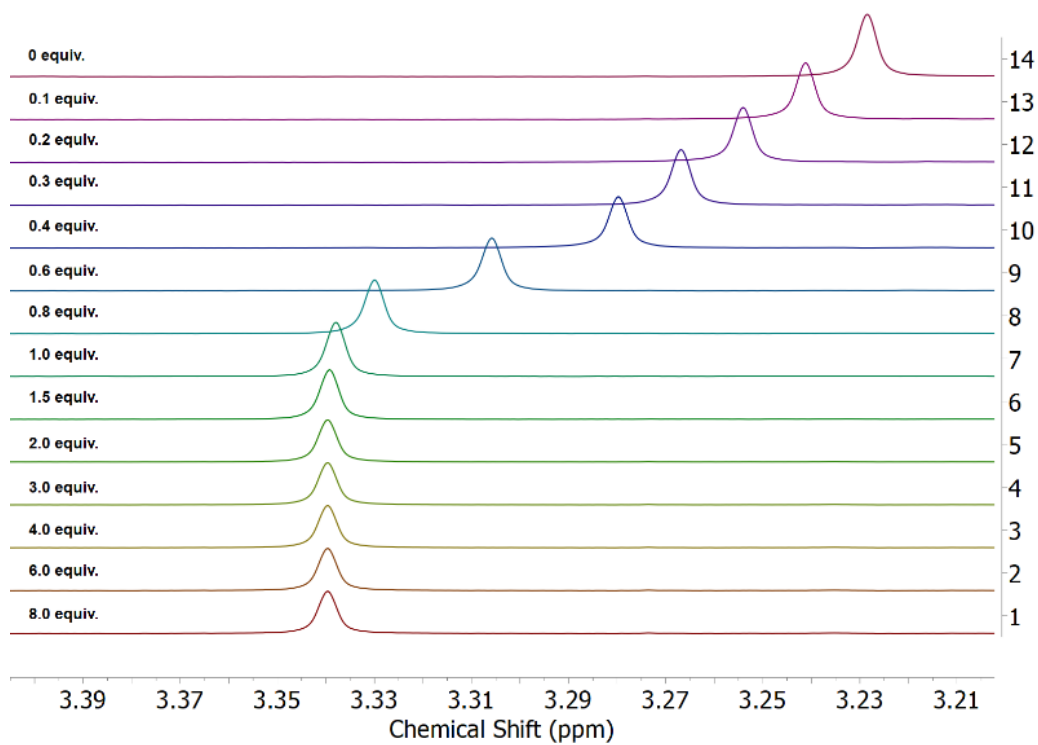


Figure S129. NMR titration experiments of L^5UO_2 with NaOTf showing the peak corresponding to the $-N-CH_3$ group used to make binding curves.

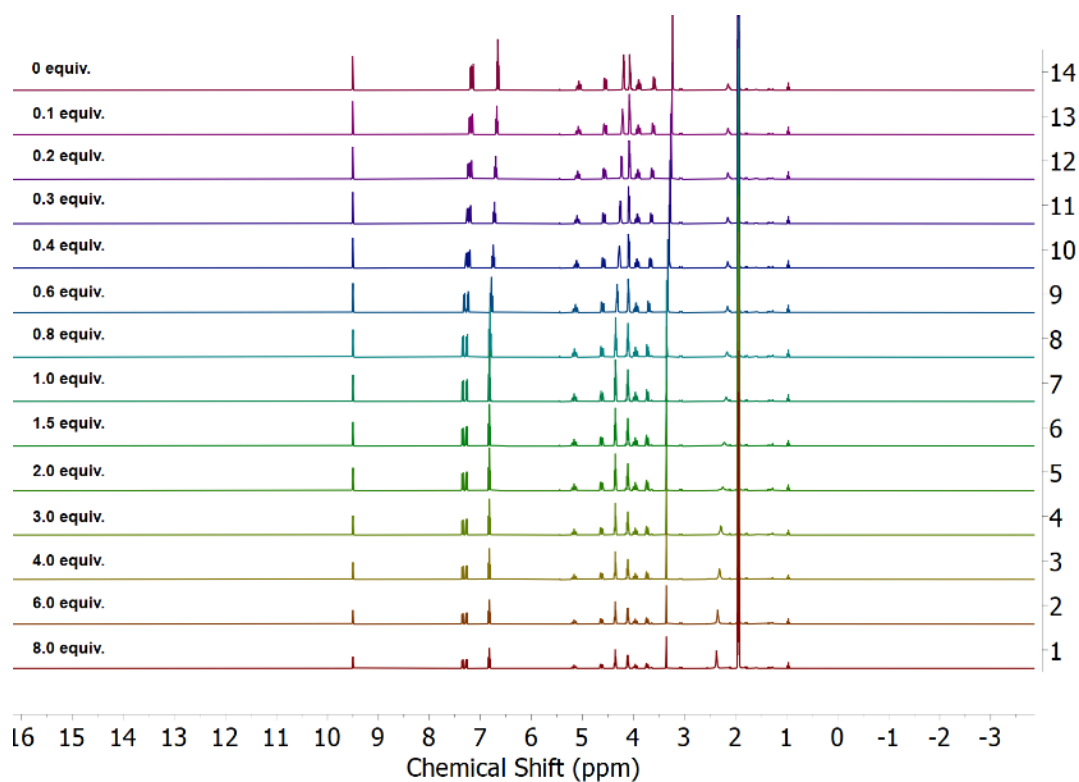


Figure S130. NMR titration experiments of L^5UO_2 with LiOTf showing the full region.

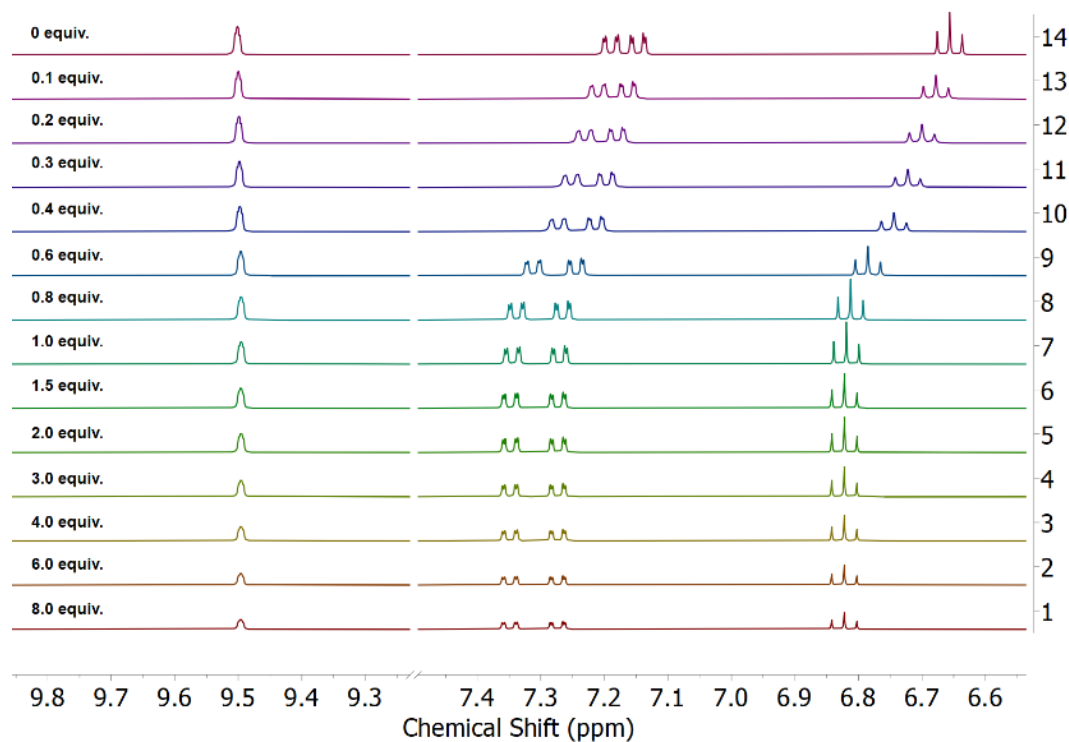


Figure S131. NMR titration experiments of L^5UO_2 with LiOTf showing the imine and aromatic region.

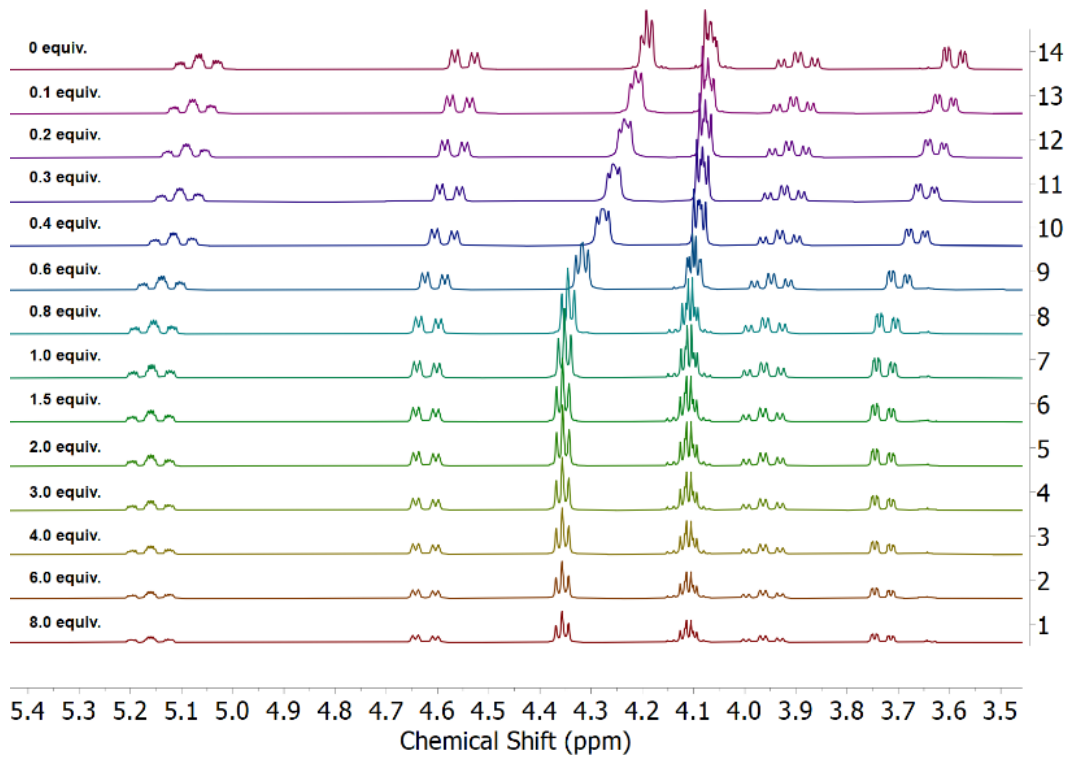


Figure S132. NMR titration experiments of L^5UO_2 with LiOTf showing the aliphatic region.

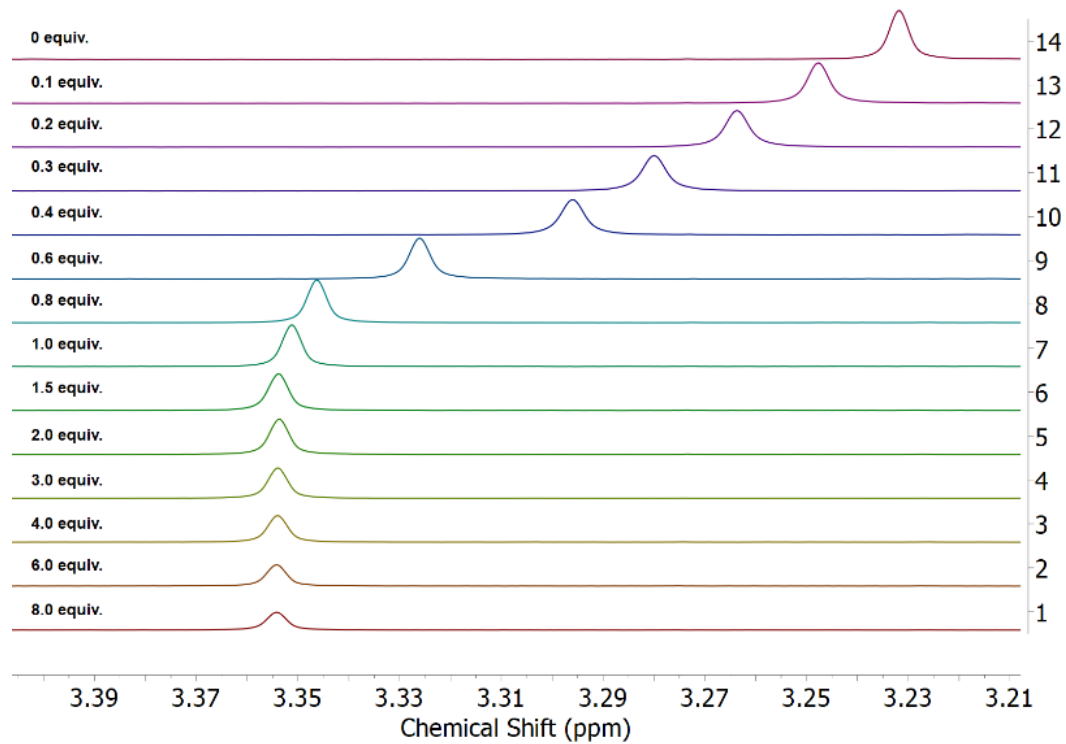


Figure S133. NMR titration experiments of L^5UO_2 with LiOTf showing the peak corresponding to the $-N-CH_3$ group used to make binding curves.

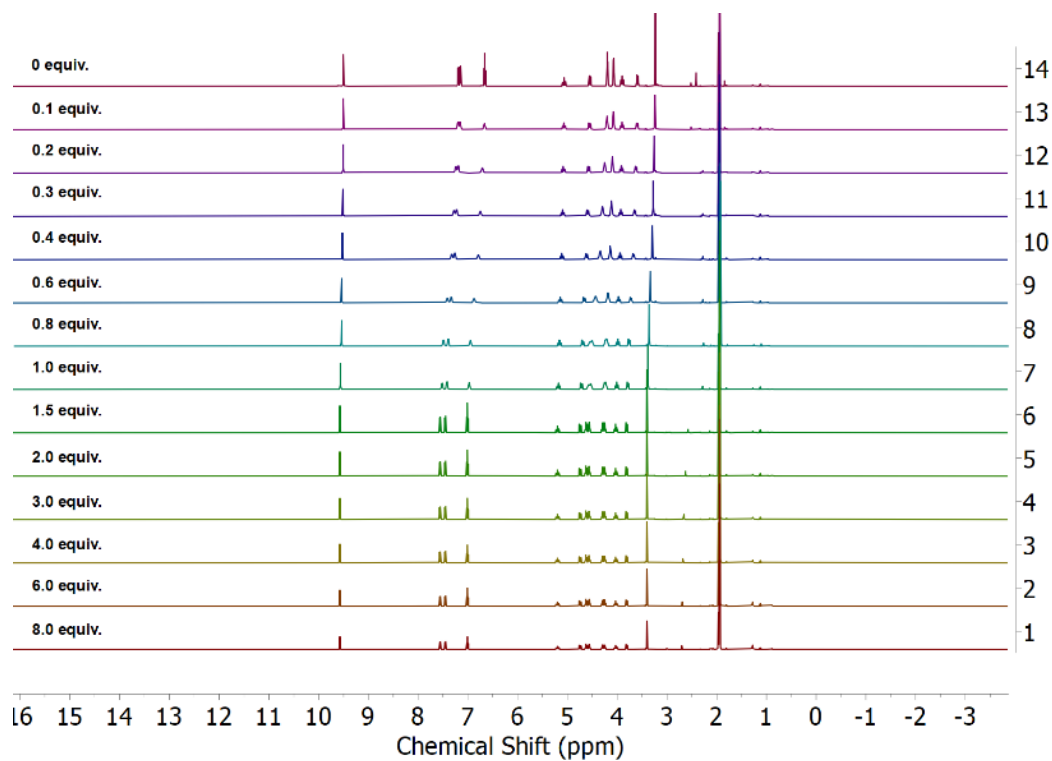


Figure S134. NMR titration experiments of L^5UO_2 with $Ca(OTf)_2$ showing the full region.

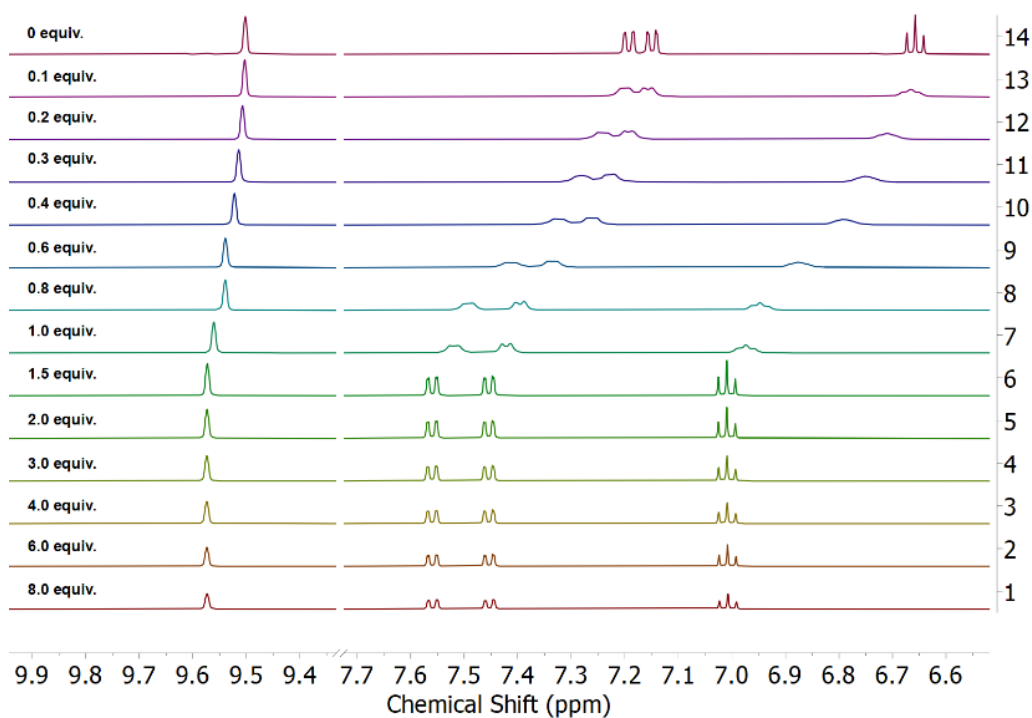


Figure S135. NMR titration experiments of L^5UO_2 with $Ca(OTf)_2$ showing the imine and aromatic region.

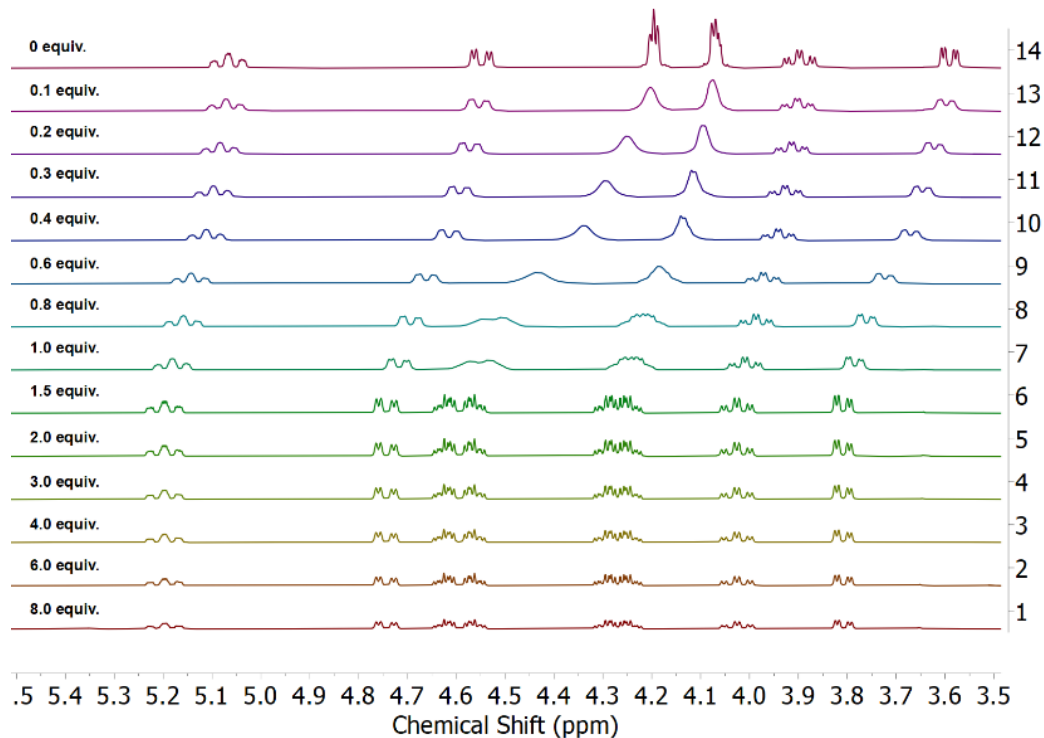


Figure S136. NMR titration experiments of L^5UO_2 with $Ca(OTf)_2$ showing the aliphatic region.

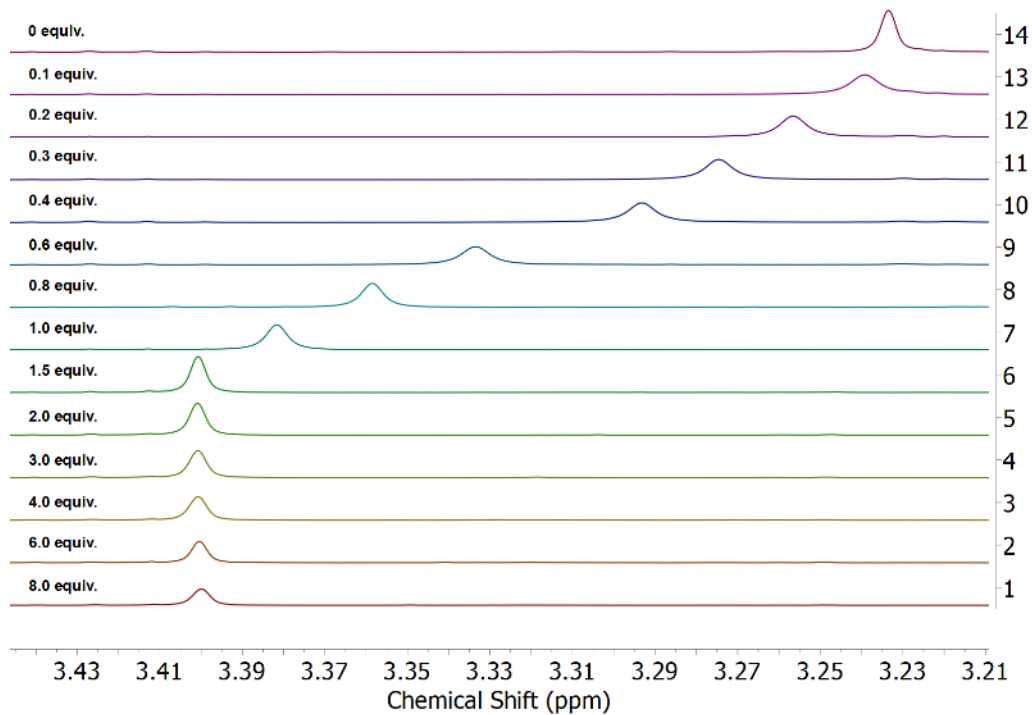


Figure S137. NMR titration experiments of L^5UO_2 with $Ca(OTf)_2$ showing the peak corresponding to the $-N-CH_3$ group used to make binding curves.

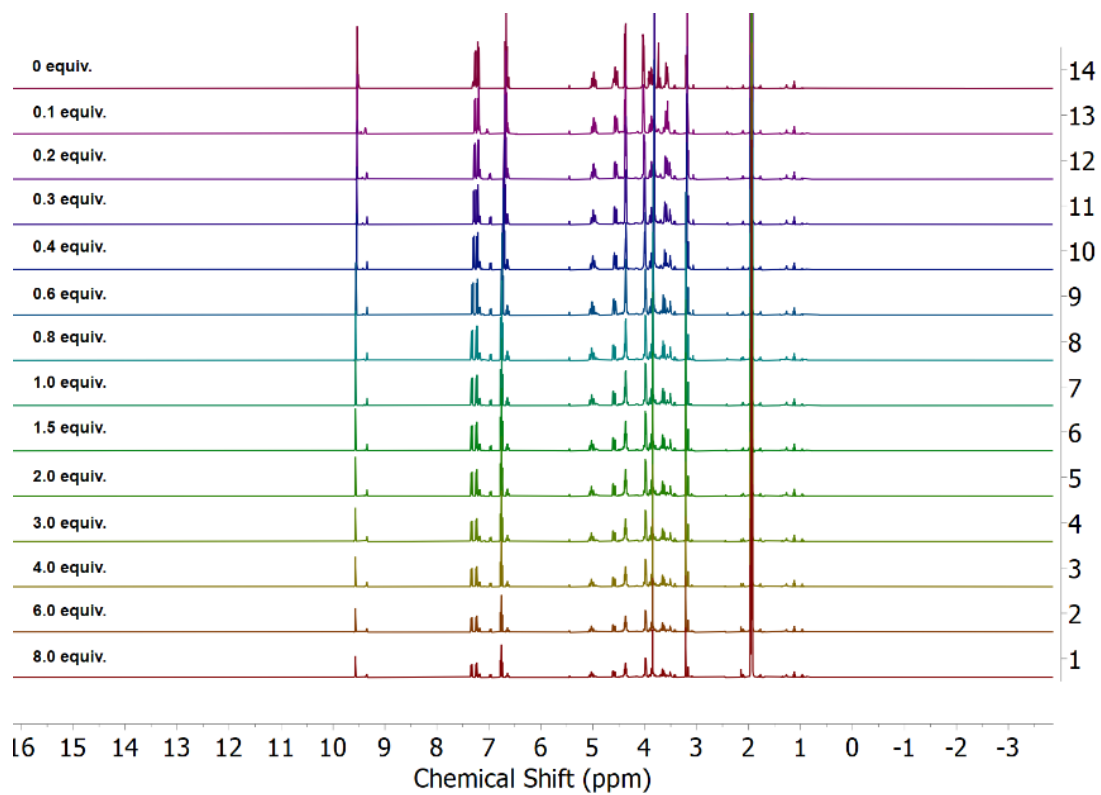


Figure S138. NMR titration experiments of L^6UO_2 with CsOTf showing the full spectra.

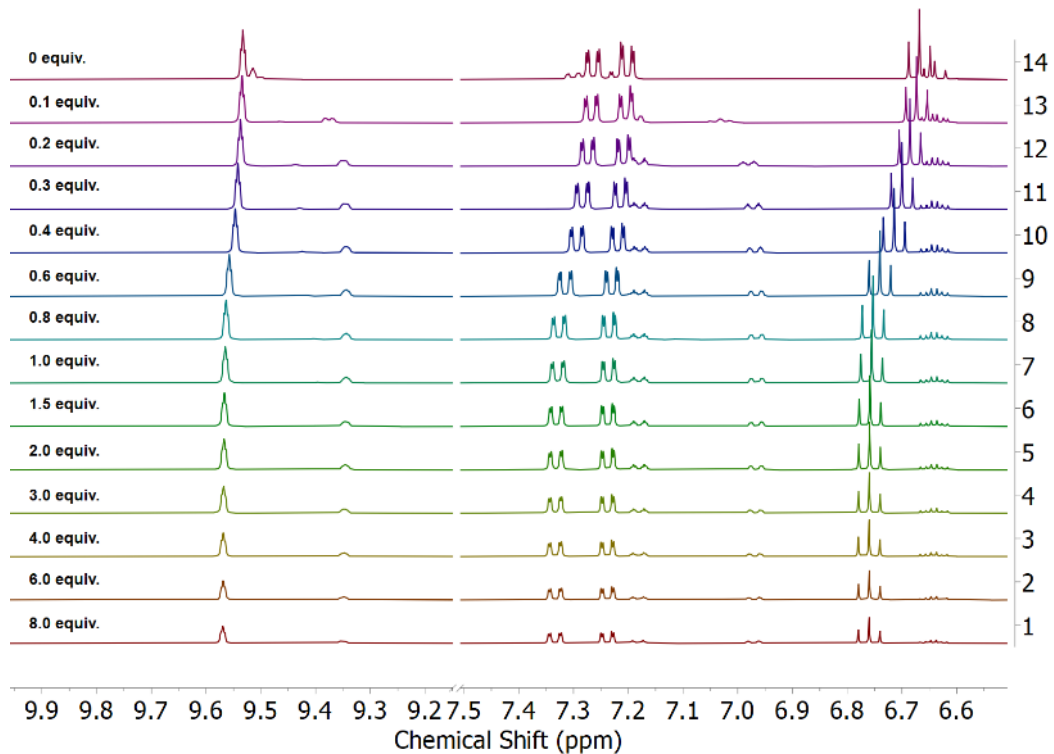


Figure S139. NMR titration experiments of L^6UO_2 with CsOTf showing the imine and aromatic region.

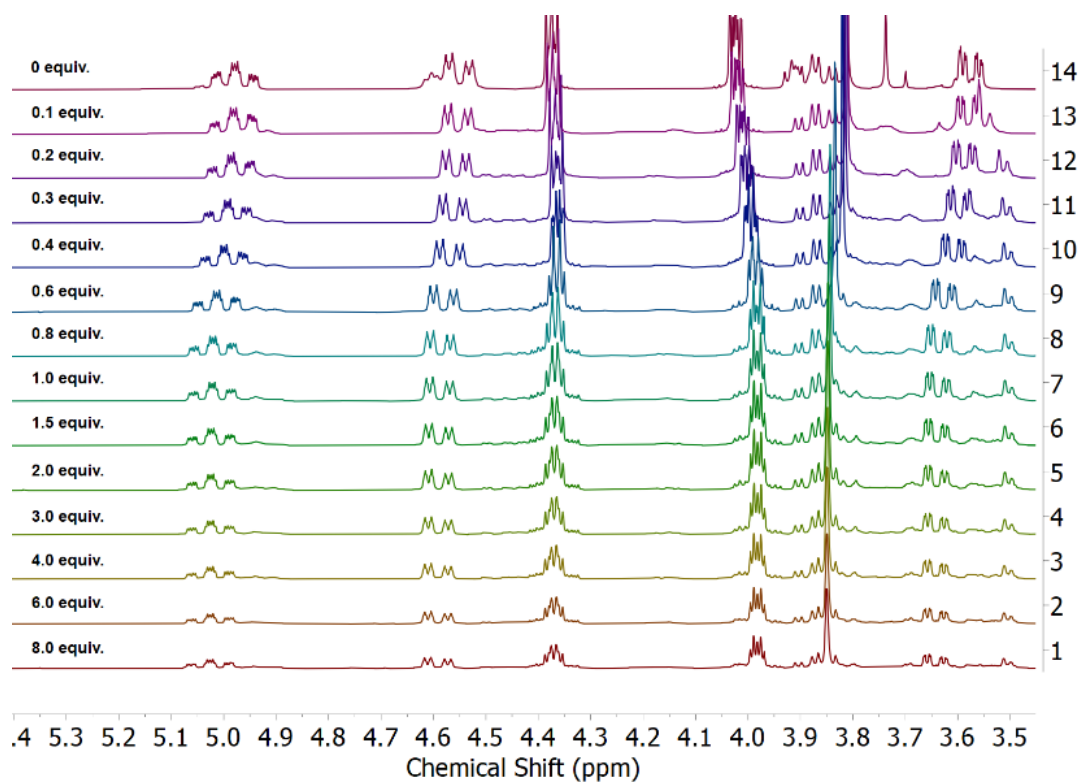


Figure S140. NMR titration experiments of L^6UO_2 with CsOTf showing the aliphatic region.

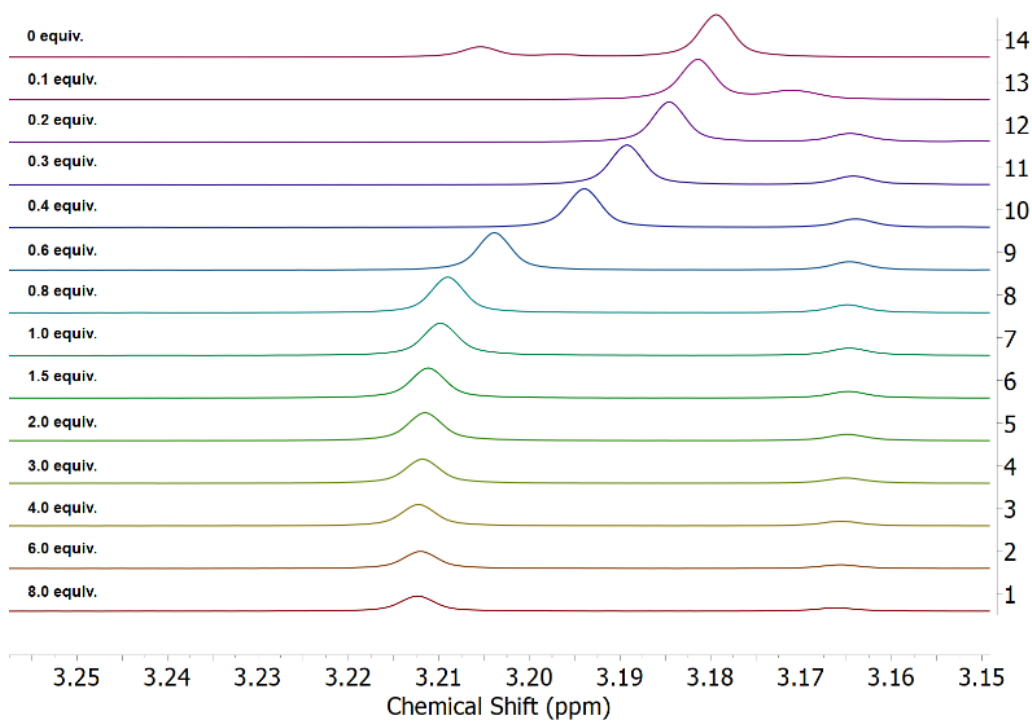


Figure S141. NMR titration experiments of L^6UO_2 with CsOTf showing the peak corresponding to the $-N-CH_3$ group used to make binding curves.

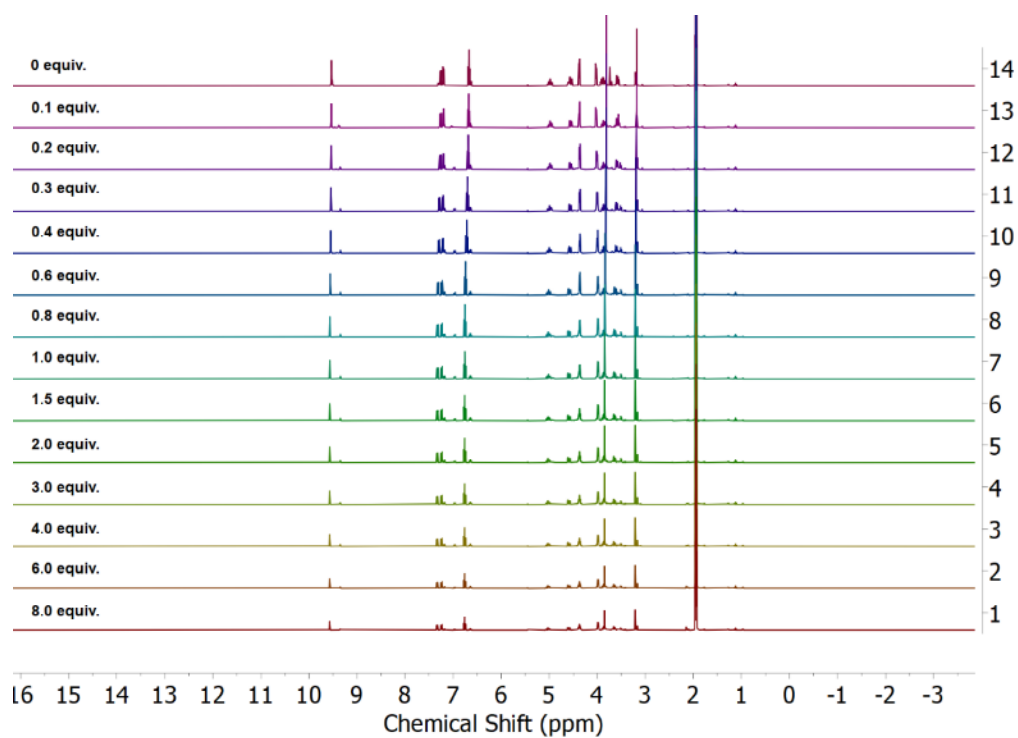


Figure S142. NMR titration experiments with L^6UO_2 with RbOTf showing the full spectra.

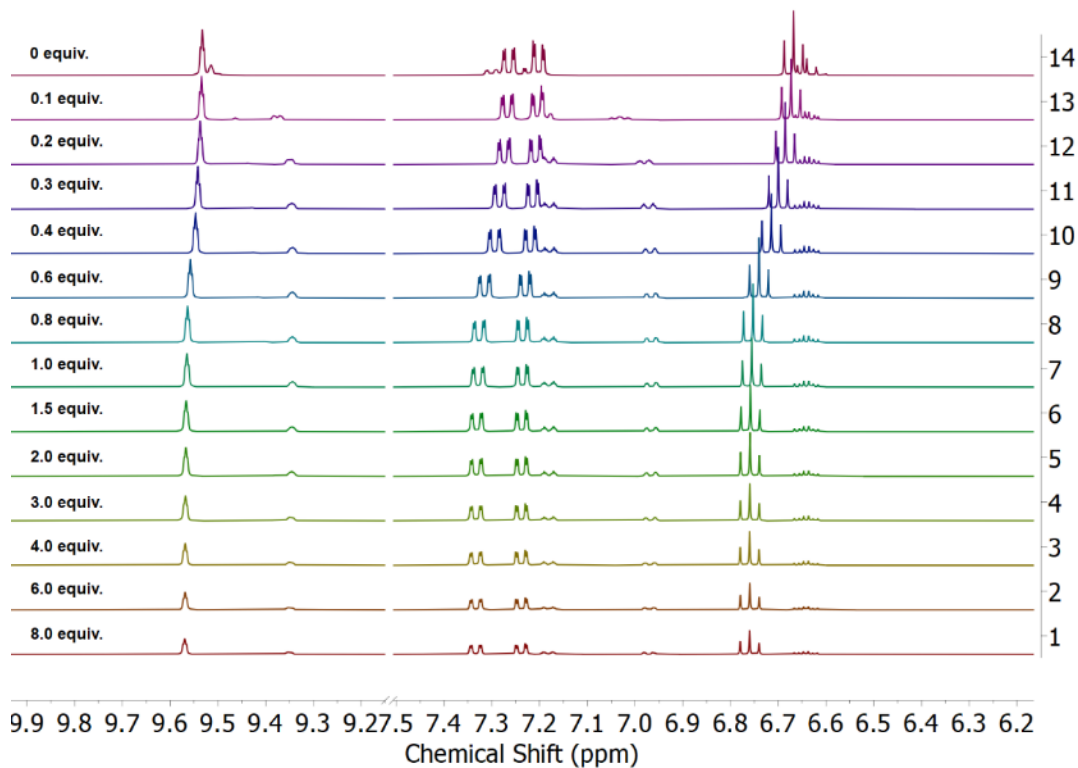


Figure S143. NMR titration experiments with L^6UO_2 with RbOTf showing the imine and aromatic region.

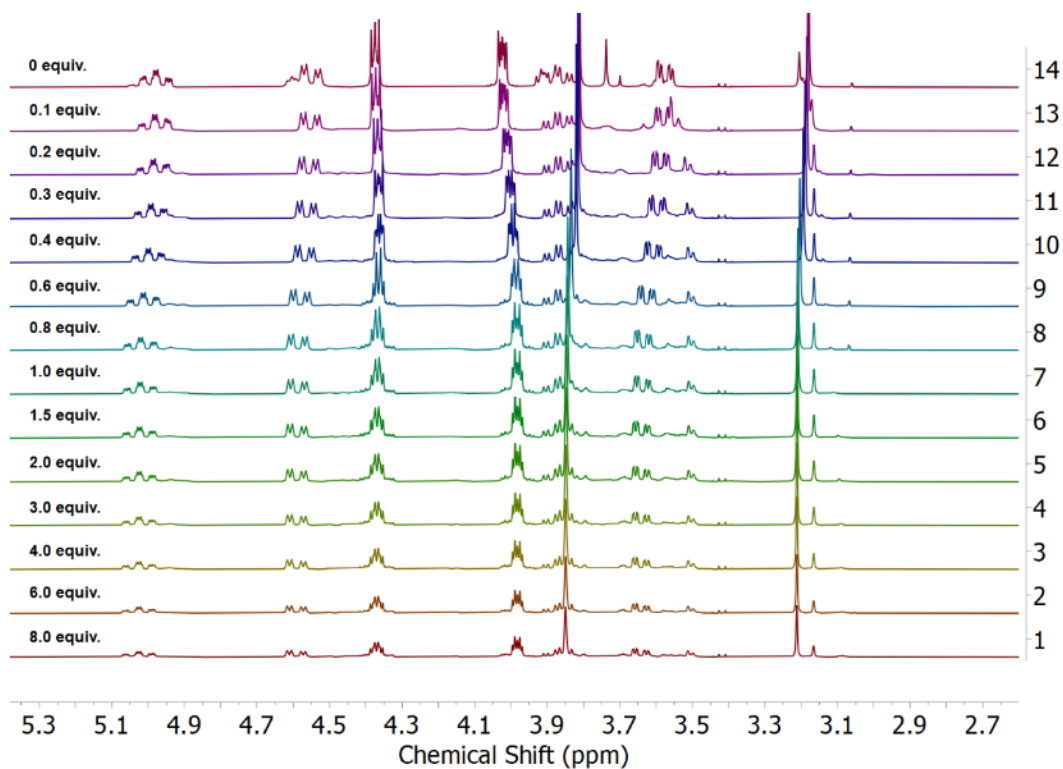


Figure S144. NMR titration experiments with L^6UO_2 with RbOTf showing the aliphatic region.

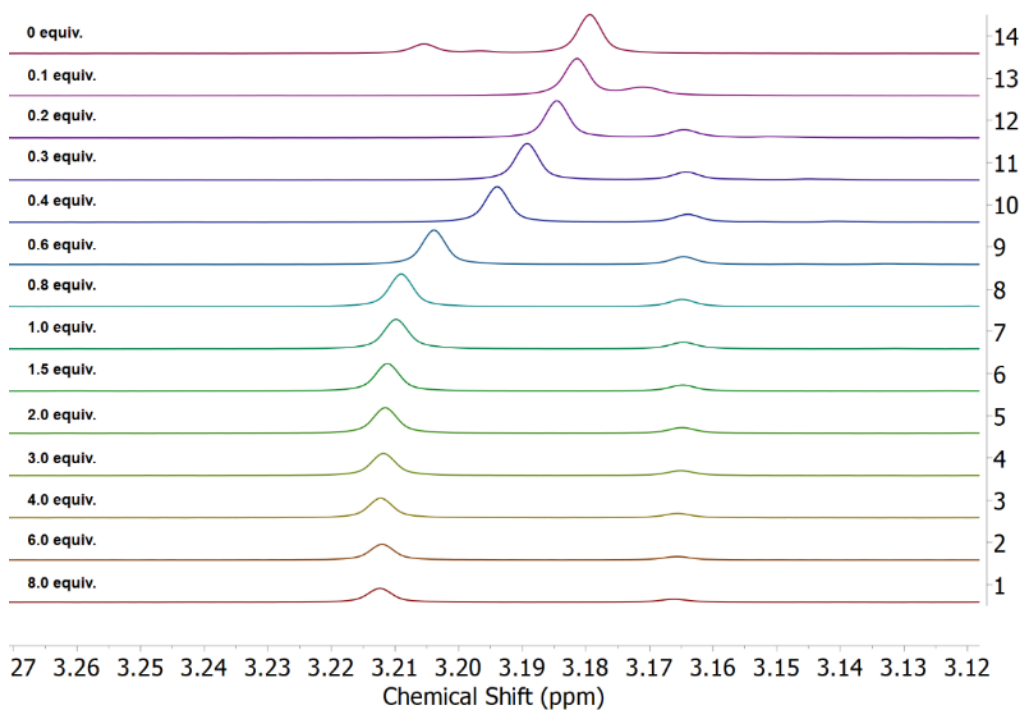


Figure S145. NMR titration experiments with L^6UO_2 with RbOTf showing the peak corresponding to the $-N-CH_3$ group used to make binding curves.

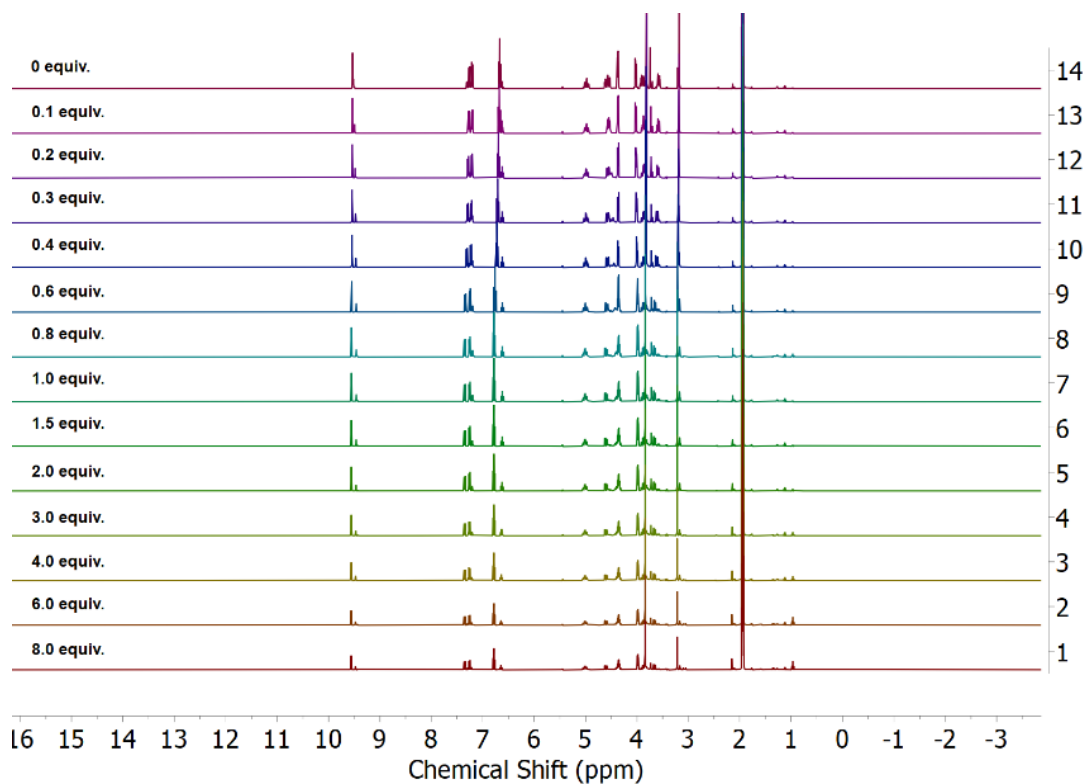


Figure S146. NMR titration experiments of L^6UO_2 with KOTf showing the full region.

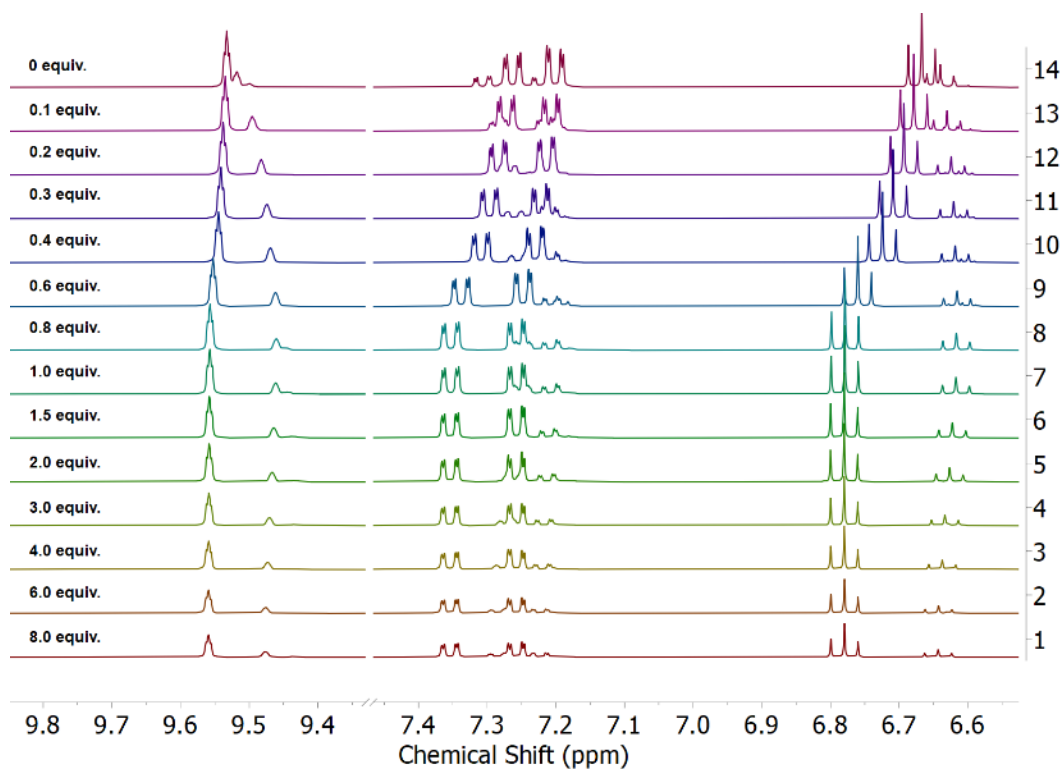


Figure S147. NMR titration experiments of L^6UO_2 with KOTf showing the imine and aromatic region.

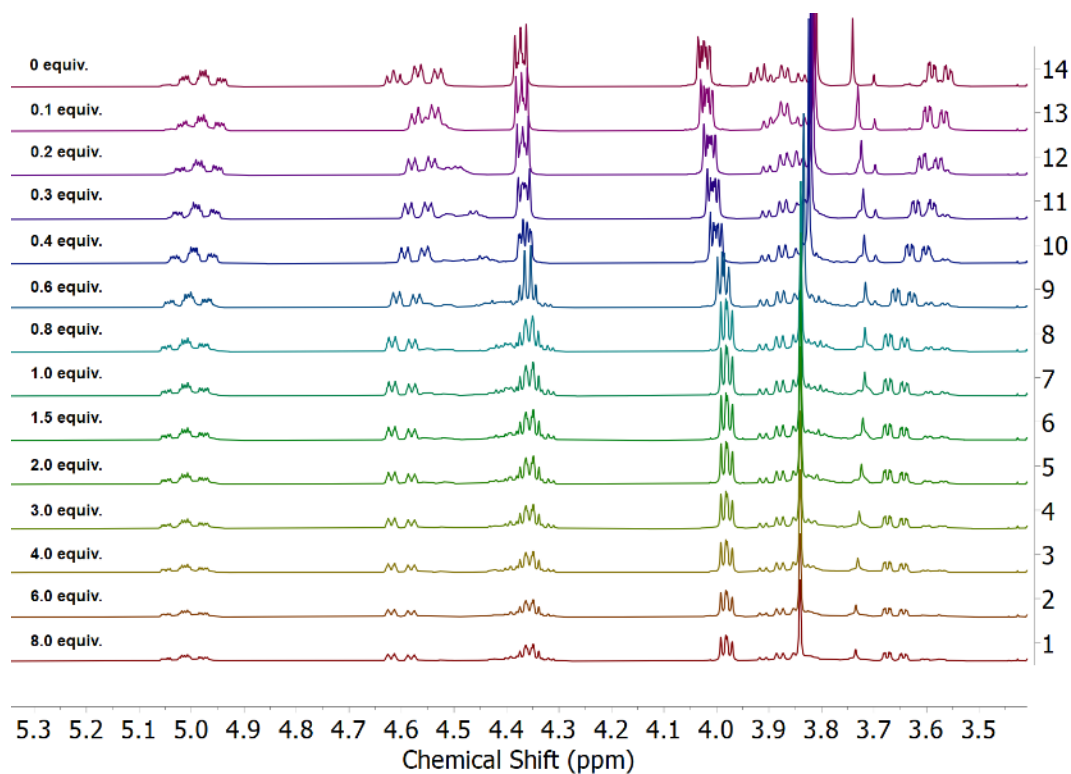


Figure S148. NMR titration experiments of L^6UO_2 with KOTf showing the aliphatic region.

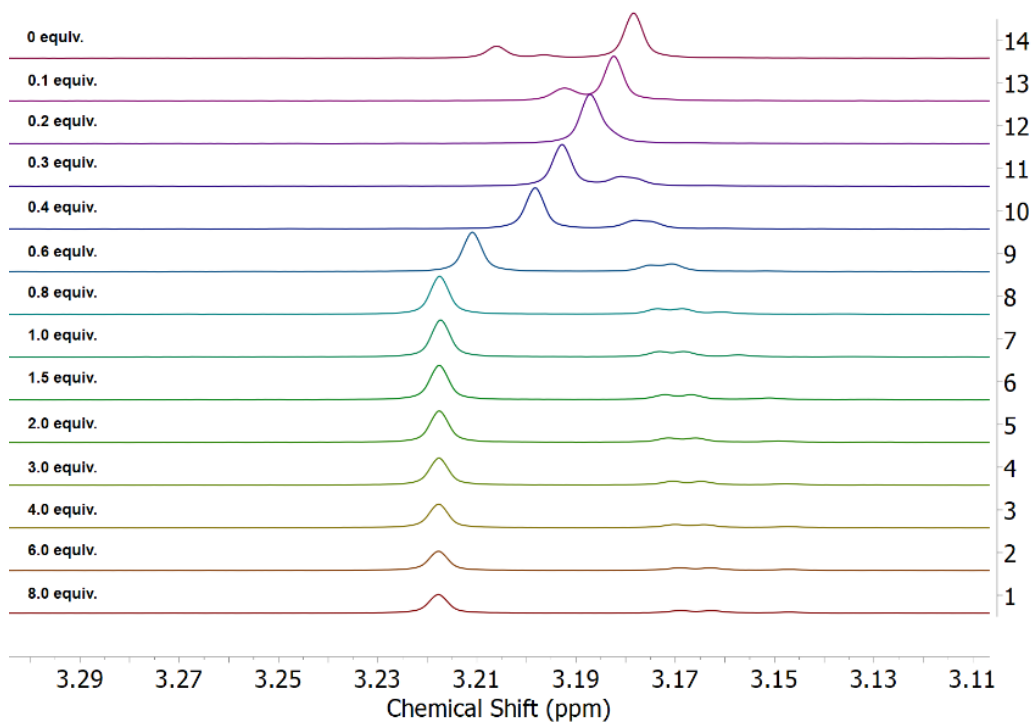


Figure S149. NMR titration experiments of L^6UO_2 with KOTf showing the peak corresponding to the $-N-CH_3$ group used to make binding curves.

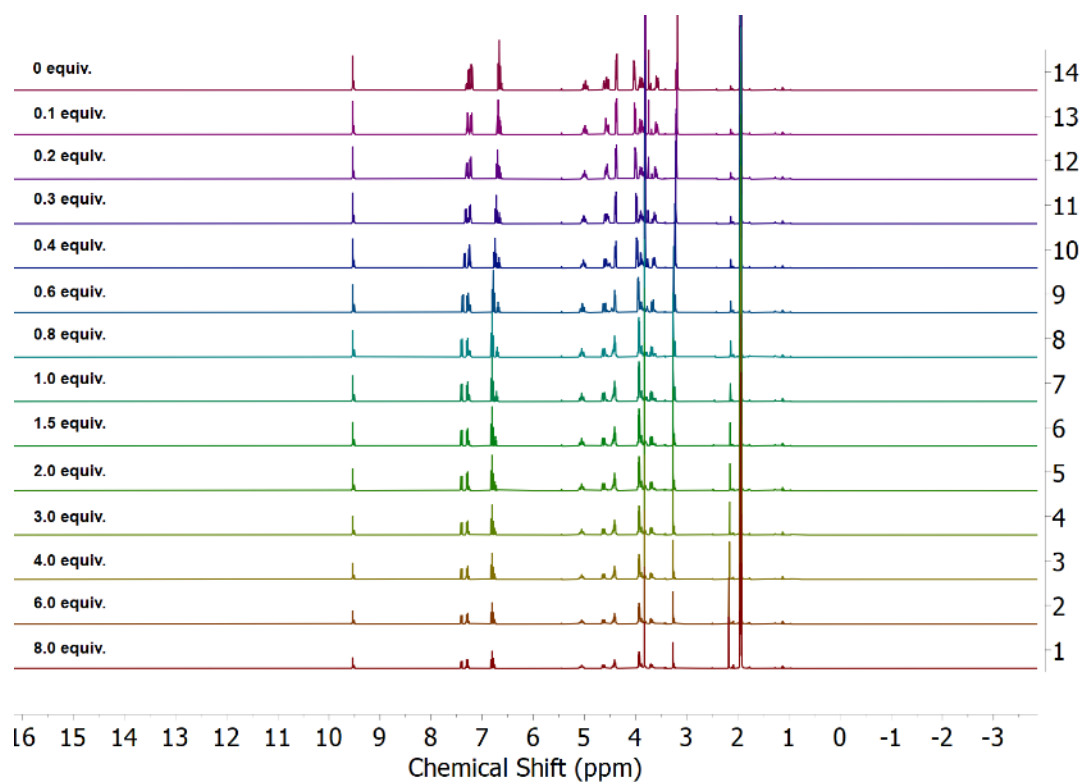


Figure S150. NMR titration experiments of L^6UO_2 with NaOTf showing the full region.

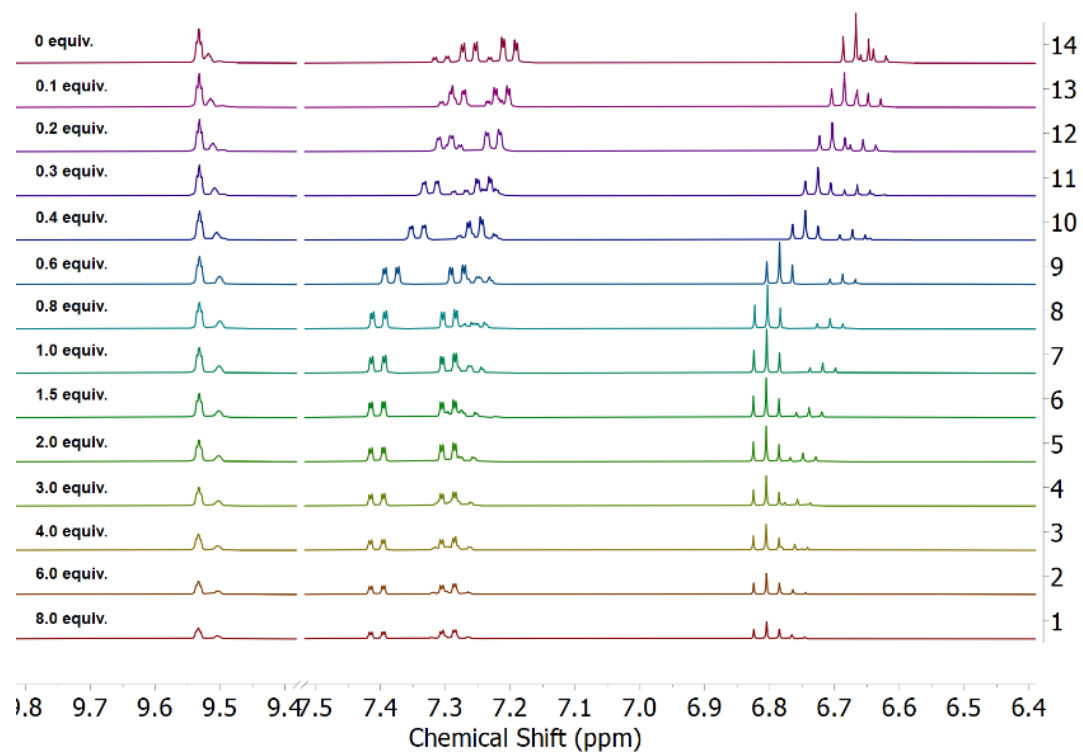


Figure S151. NMR titration experiments of L^6UO_2 with NaOTf showing the imine and aromatic region.

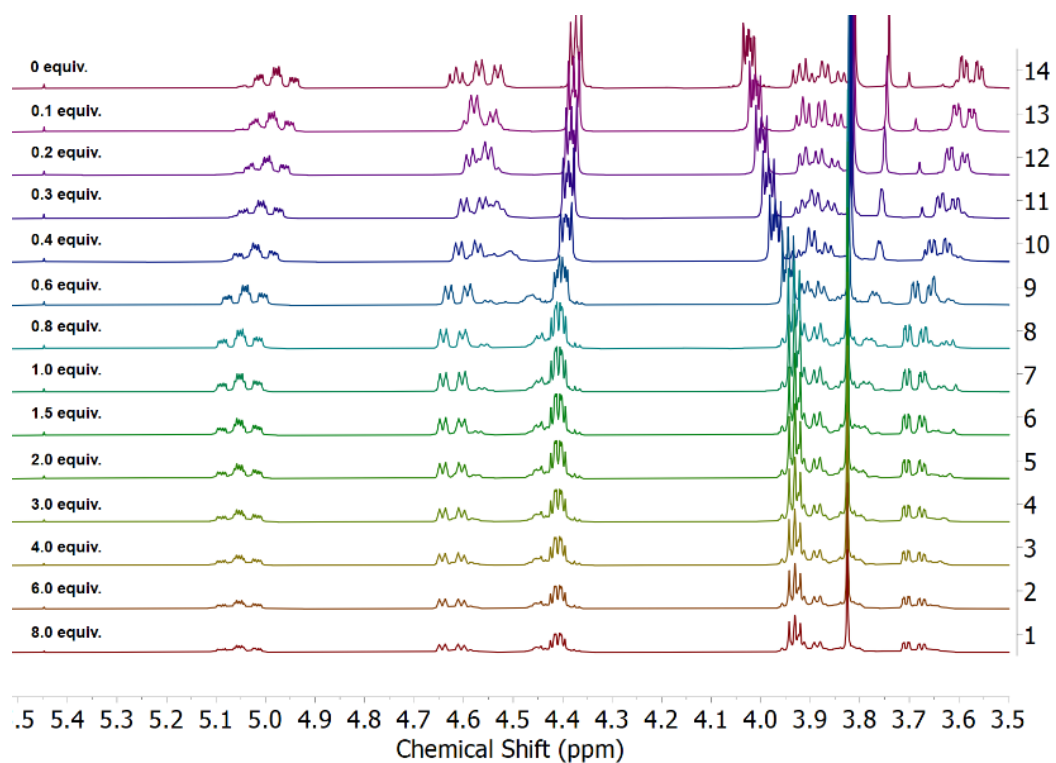


Figure S152. NMR titration experiments of L^6UO_2 with NaOTf showing the aliphatic region.

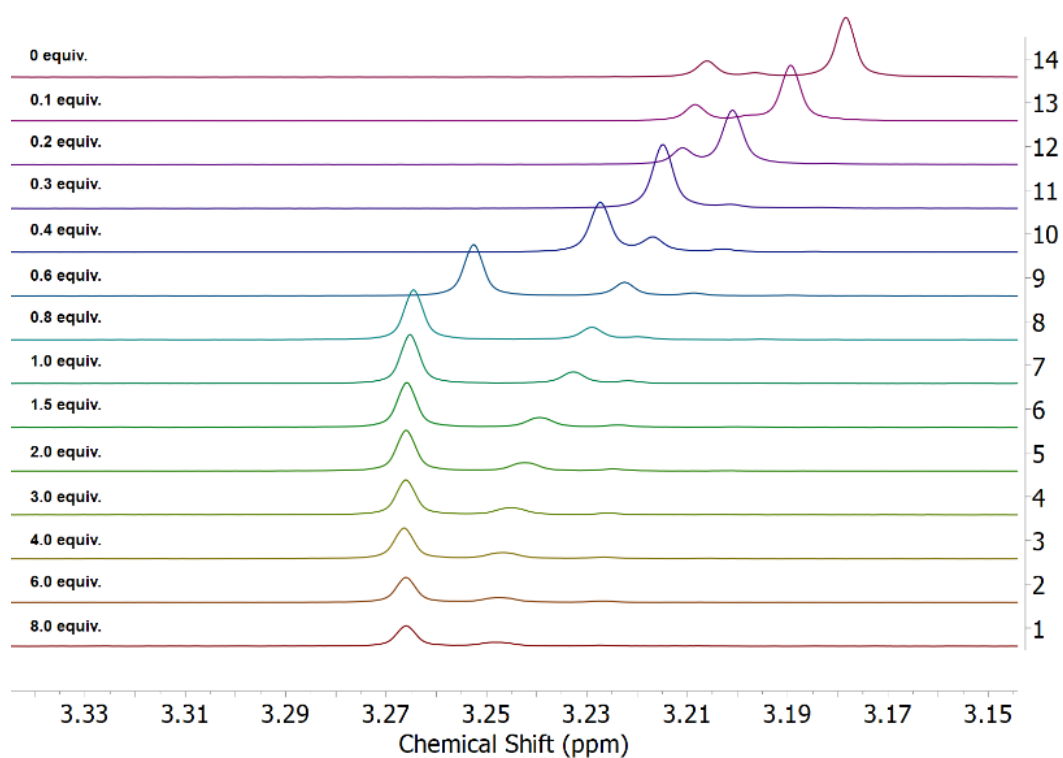


Figure S153. NMR titration experiments of L^6UO_2 with NaOTf showing the peak corresponding to the $-N-CH_3$ group used to make binding curves.

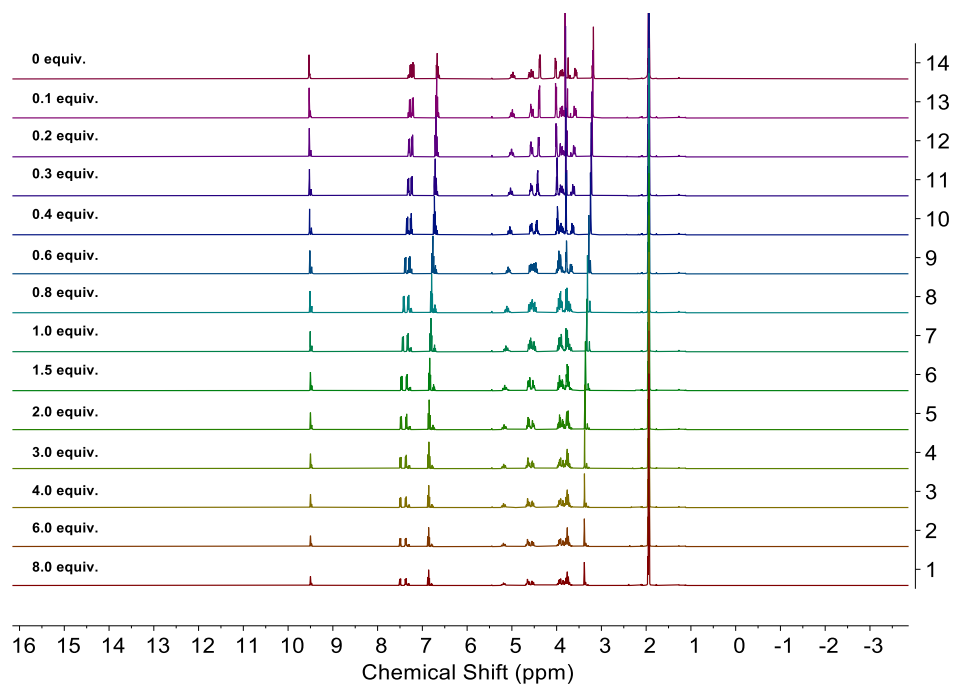


Figure S154. NMR titration experiments of L^6UO_2 with LiOTf showing the full spectra.

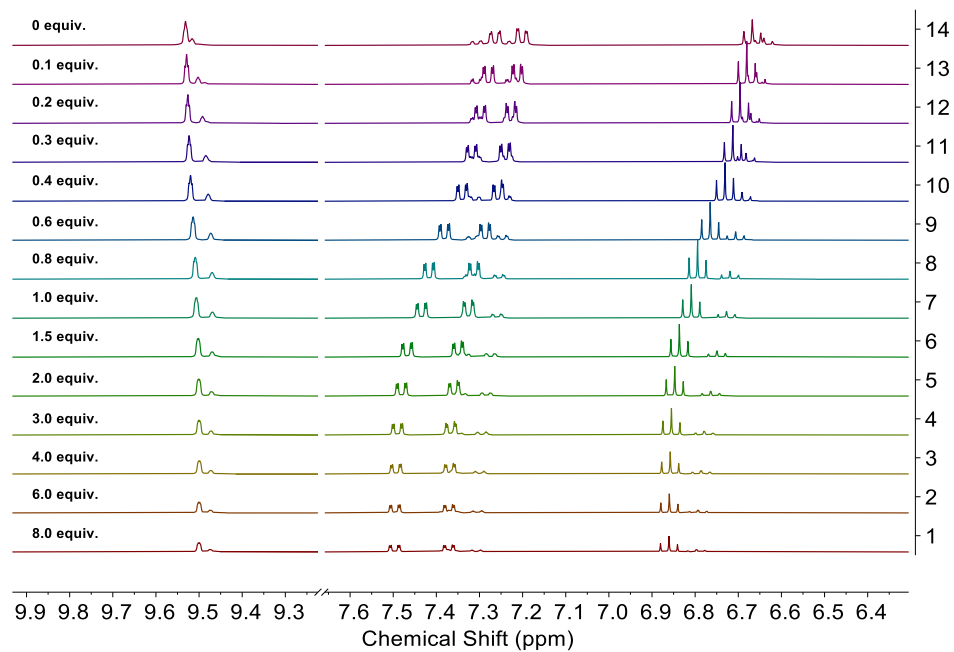


Figure S155. NMR titration experiments of L^6UO_2 with LiOTf showing the imine and aromatic region.

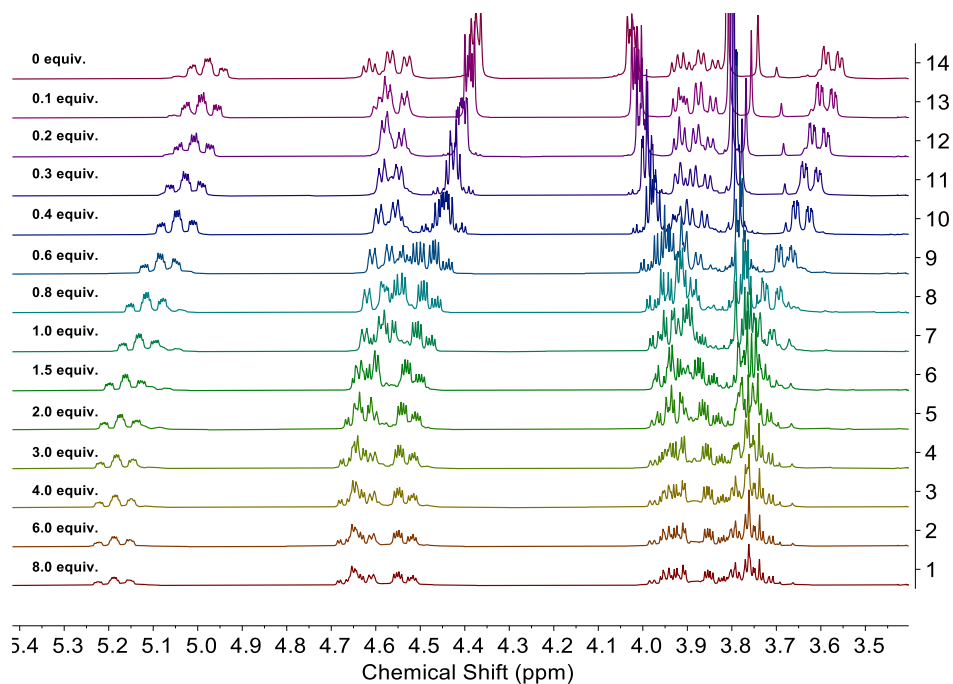


Figure S156. NMR titration experiments of L^6UO_2 with LiOTf showing the aliphatic region.

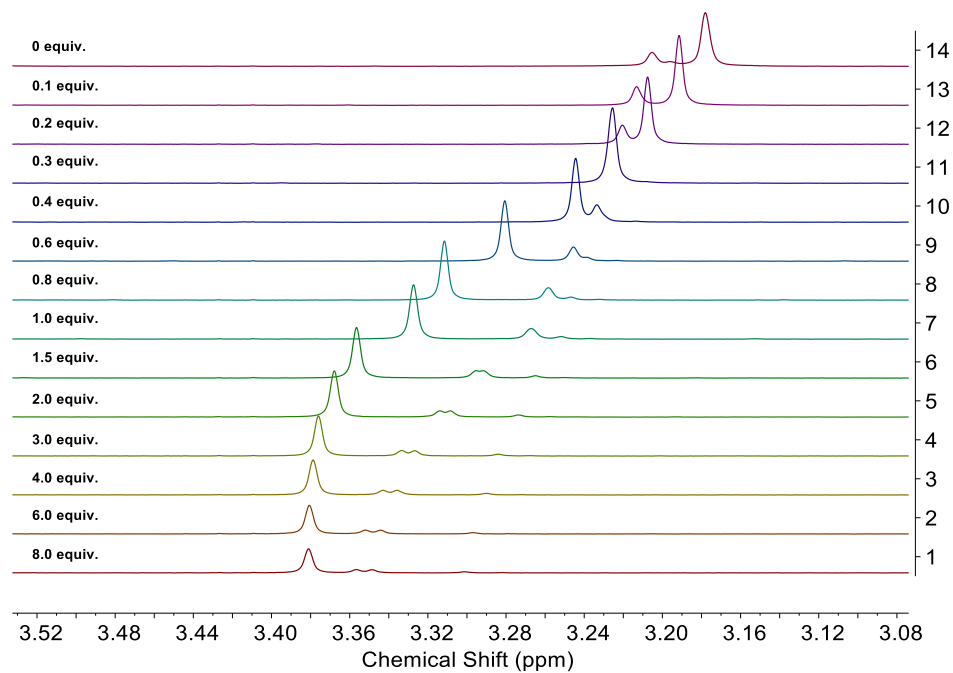


Figure S157. NMR titration experiments of L^6UO_2 with LiOTf showing the peak corresponding to the $-N-CH_3$ group used to make binding curves.

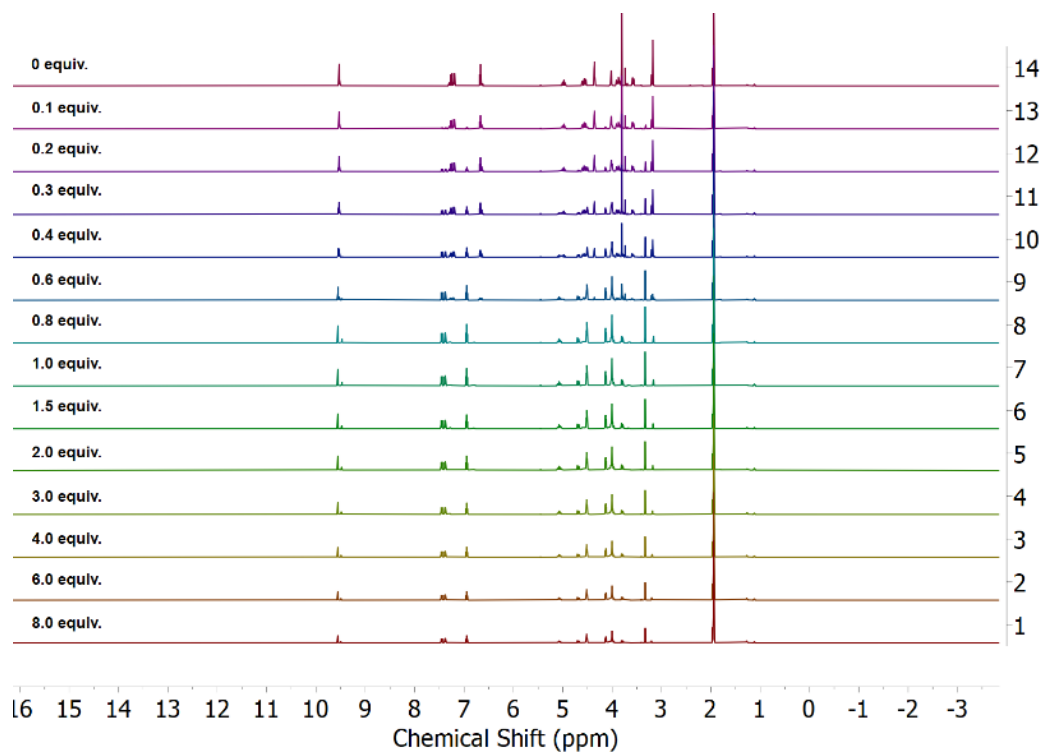


Figure S158. NMR titration experiments of L^6UO_2 with $Ca(OTf)_2$ showing the full region.

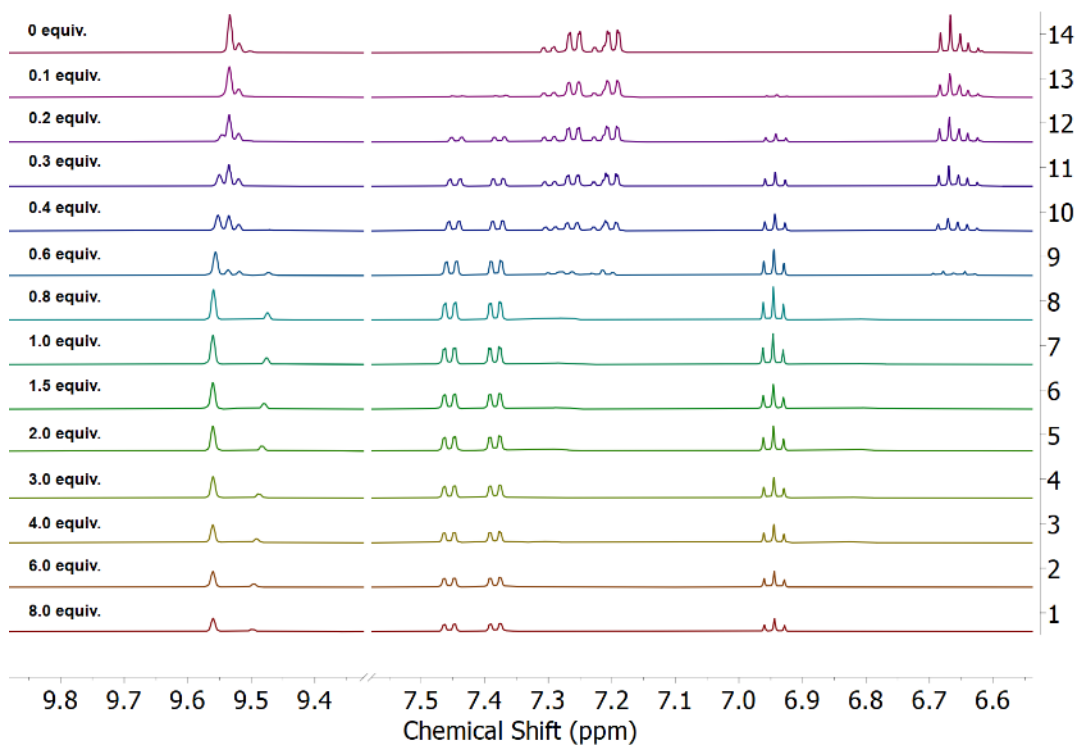


Figure S159. NMR titration experiments of L^6UO_2 with $Ca(OTf)_2$ showing the imine and aromatic region.

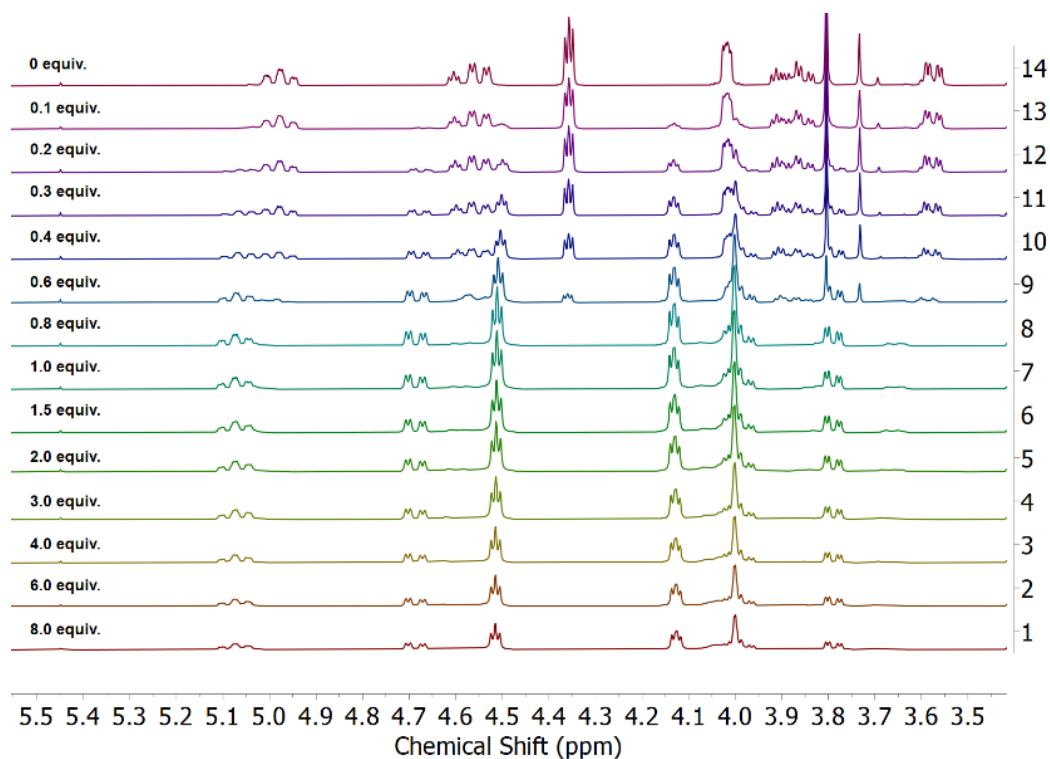


Figure S160. NMR titration experiments of L^6UO_2 with $Ca(OTf)_2$ showing the aliphatic region.

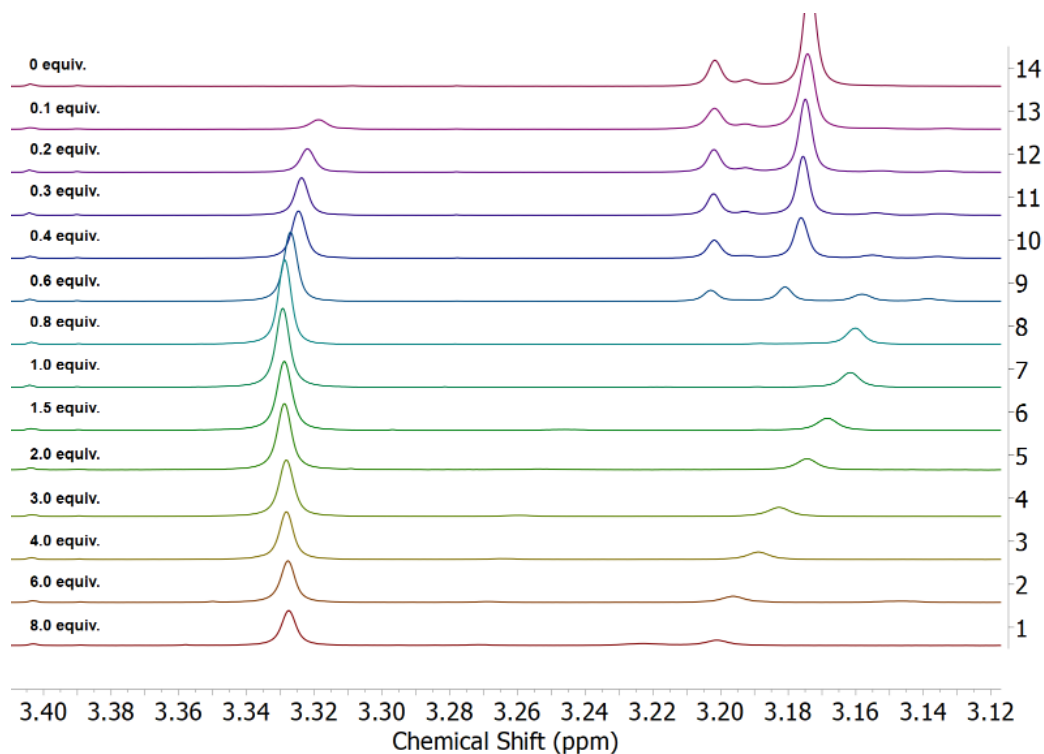


Figure S161. NMR titration experiments of L^6UO_2 with $Ca(OTf)_2$ showing the peak corresponding to the $-N-CH_3$ group used to make binding curves.

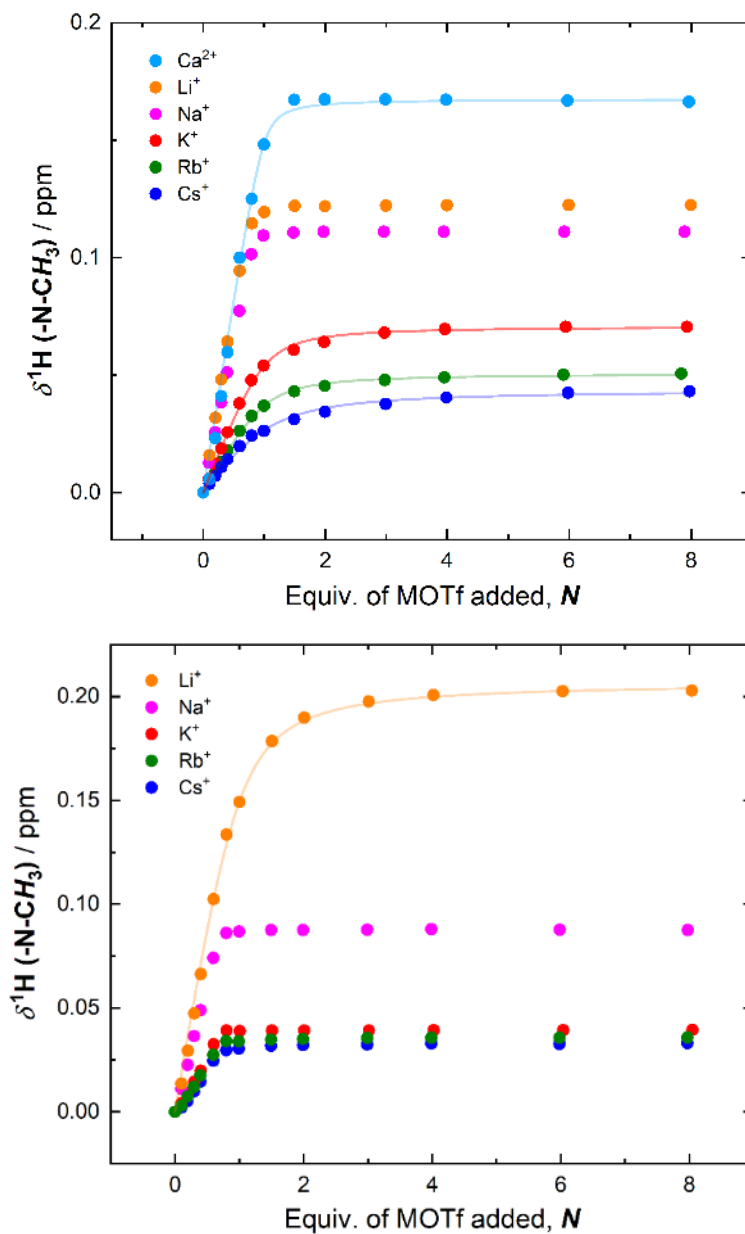


Figure S162. Titration studies showing 1:1 binding of monovalent metal ions with L^5UO_2 (top) and L^6UO_2 (bottom). Solvent: d_3 -MeCN. The initial concentrations of the monometallic uranium complexes used for these experiments were 7.2 mM for L^5UO_2 and 6.9 mM for L^6UO_2 .

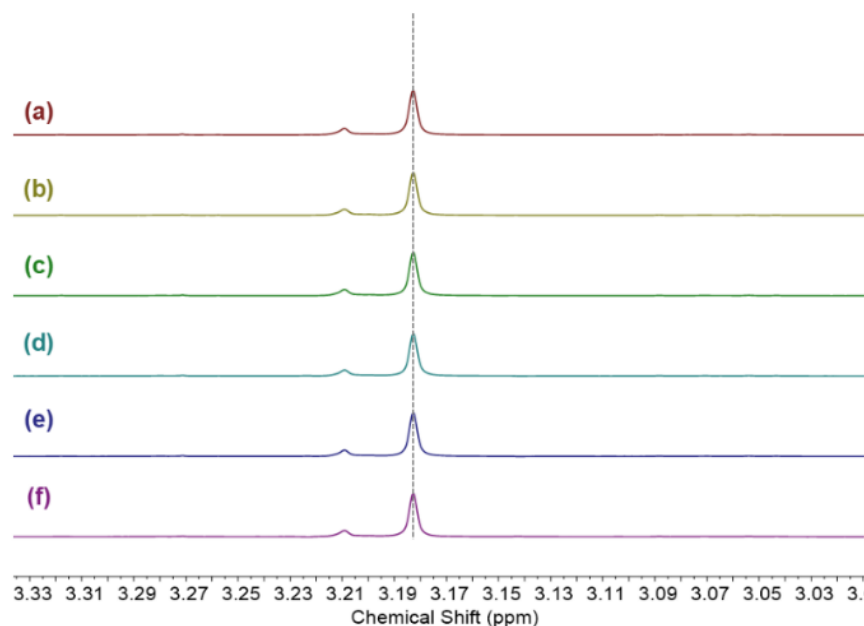


Figure S163. ^1H NMR spectra (500 MHz, CD_3CN) for a single sample of L^6UO_2 recorded over five hours. Spectra are referenced relative to solvent residual signal of CD_3CN .

Table S11. ^1H NMR chemical shifts (δ) of the peak corresponding to the $-\text{N}-\text{CH}_3$ protons from replicate measurements of a single sample of L^6UO_2 recorded over five hours.

Measured Spectrum Index	Time (h)	$\delta(^1\text{H})$ of $-\text{N}-\text{CH}_3$ (ppm)	Linewidth (Hz) ^a	Linewidth (ppm) ^b
a	0	3.183	1.56	0.00312
b	1	3.183	1.55	0.00310
c	2	3.183	1.66	0.00332
d	3	3.183	1.66	0.00332
e	4	3.183	1.55	0.00310
f	5	3.183	1.55	0.00310
<i>Averages</i>		3.183^d		± 0.003^c

^a Raw linewidth values (in Hz) were measured in each of the replicate ^1H NMR spectra of L^6UO_2 (see Figure S163 for spectral data).

^b Conversion of the linewidths to chemical shift in ppm was accomplished by dividing the values in Hz by the spectrometer frequency (in this case, 500 MHz).

^c Uncertainty in $\delta(^1\text{H})$ in ppm is given as $\pm 1\sigma$ and was calculated as the arithmetic mean of the individual measured linewidth values.

^d Possible sources of error on determination of $\delta(^1\text{H})$ include spectral variations induced by electronic factors, quality of sample shimming, magnetic field inhomogeneity, and sample concentration uncertainty.

Evaluation of the heterogeneous electron transfer rate, k^0

We have used the Randles-Ševčík equation to determine the diffusion coefficient D , of the oxidized species at different scan rates.^{5,6}

$$i_p = 0.4463 * nFAc \sqrt{\left(\frac{nFvD}{RT}\right)}$$

where i_p is the maximum peak current in amps, n is the number of electrons transferred, F is Faraday constant in $C \text{ mol}^{-1}$, A is electrode area in cm^2 , C is concentration in mol/cm^3 , v is scan rate in V/s , R is gas constant in $\text{J K}^{-1} \text{ mol}^{-1}$, and T is temperature (298K).

For determining the charge transfer coefficient α , the following equation was used.⁷

$$E_{p/2} - E_p = 1.857 \frac{RT}{\alpha F}$$

Where E_p and $E_{p/2}$ are peak potential and half-peak potential respectively.

The heterogeneous electron transfer rate, k^0 can be calculated from the equation developed by Nicholson⁸ and elaborated by Bard & Faulkner.⁹

$$\psi = \frac{\left(\frac{D_{ox}}{D_{red}}\right)^{\alpha/2} k^0}{\sqrt{D_o \pi v (nF/RT)}}$$

Here, ψ is the dimensionless parameter that can be calculated from known values of the peak-to-peak separations, ΔE_p calculated from the CV data, where α is the charge transfer coefficient, D_{ox} and D_{red} are the diffusion coefficients of the oxidized and the reduced forms in cm^2/s , n is the number of electrons transferred, F is the Faraday constant in $C \text{ mol}^{-1}$, R is the gas constant in $\text{J K}^{-1} \text{ mol}^{-1}$, and T is temperature (298 K).

X-Ray Crystallographic Information

Refinement Details

Crystals for all ten compounds were mounted on a goniometer head using Paratone oil with MiTeGen MicroMounts and placed in a cold nitrogen stream. Complete sets of low-temperature diffraction data frames were collected for crystals of all ten compounds using either 0.5° or 1.0°-wide ω - and/or ϕ -scans.

X-rays for six (**BaPenta**, **L⁵UO₂**, **L⁵UO₂Na**, **L⁵UO₂Na'**, **L⁵UO₂Na-DCE**, **L⁵UO₂Na-MeCN**) of the ten total datasets were provided by a Bruker MicroStar microfocus rotating anode generator running at 45 mA and 60 kV (Cu K α = 1.54178 Å). Data for **BaPenta** (q55j), **L⁵UO₂** (q70k), **L⁵UO₂Na** (q50k), **L⁵UO₂Na-DCE** (q49k), **L⁵UO₂Na-MeCN** (q56k) were collected with a Bruker APEX II CCD detector positioned at 50.0 mm and equipped with Helios multilayer mirror optics; data for **L⁵UO₂Na'** (v16f) were collected with a Bruker Platinum 135 CCD detector positioned at 80.0 mm and equipped with Helios high-brilliance multilayer mirror optics.

X-rays for **L⁵UO₂Li**, **L⁵UO₂Ca** and **L⁵UO₂Ca'** were provided by a fine-focus sealed tube (Mo K α = 0.71073 Å). X-rays for **L⁶UO₂Li** were provided by Incoatec micro-focus sealed tube (Cu K α = 1.54178 Å). Data for **L⁵UO₂Li** (ak2133c) were collected with a Bruker APEX-II detector equipped with Bruker TRIUMPH curved-graphite optics; data for **L⁵UO₂Ca** (ak2153g) and **L⁵UO₂Ca'** (ak2153n-No33) were collected with a Bruker PHOTON-II detector equipped with Bruker TRIUMPH curved-graphite optics; data for **L⁶UO₂Li** (ak2133c) were collected with a Bruker PHOTON-II detector equipped with MONTEL multilayer optics.

All diffractometer manipulations, including data collection, integration and scaling were carried out using the Bruker APEX2 or APEX3 software packages.^{10,11} The data for **BaPenta** was corrected empirically for variable absorption effects with SADABS^{12,13} using equivalent reflections. A numerical face-indexed absorption correction was used for datasets of all the other eight structures. Probable space groups were determined on the basis of systematic absences and intensity statistics and the structures were solved by direct methods using SIR2004¹⁴ or XS¹⁵ (incorporated into SHELXTL) and refined to convergence by weighted full-matrix least-squares on F_o² using the with SHELXL^{15,16} in SHELXle¹⁷ and/or in the Olex2 software package.¹⁸

Unless otherwise stated in the special refinement section for each structure, the final structural model for each compound incorporated anisotropic thermal parameters for all non-hydrogen atoms and isotropic thermal parameters for all included hydrogen atoms. Non-methyl hydrogen atoms bonded to carbon in each complex were fixed at idealized riding model sp²- or sp³-hybridized positions with C–H bond lengths of 0.95 - 0.99 Å. Methyl groups were incorporated into the structural models either as sp³-hybridized riding model groups with idealized “staggered” geometry and a C–H bond length of 0.98 Å or as idealized riding model rigid rotors (with a C–H bond length of 0.98 Å) that were allowed to rotate freely about their C–C bonds in least-squares refinement cycles. The isotropic thermal parameters of idealized hydrogen atoms in all nine structures were fixed at values 1.2 (non-methyl) or 1.5 (methyl or

hydroxyl) times the equivalent isotropic thermal parameter of the carbon or oxygen atom to which they are covalently bonded.

The relevant crystallographic and structure refinement data for all ten compounds are given in Tables S18, S19, S20, S21, and S22.

CCDC entries 2344717-2344726 contain the supplementary crystallographic data for this paper. These data can be obtained free of charge from the Cambridge Crystallographic Data Centre.

Special Refinement Details for BaPenta (q55j)

Two outer-sphere diethyl ether solvent molecules were found. One (associated with O2S/O2S') is 51/49(1) disordered with two orientations of all atoms. The other (associated with O1S) is 69/31(2) disordered with two orientations of just one terminal methyl group. Near idealized geometries were imposed for all the orientations of the disordered diethylether molecules by restraining the bond lengths and interatomic separations defining bond angles to be appropriate multiples of the C(sp³)–C(sp³) bond length that was included as a free variable that refined to a final value of 1.434(3) Å. This is quite reasonable when compared to the expected value of 1.513 Å.¹⁹

Hydrogen atoms bonded to N1A, N2A, N1B and N2B that are involved in intramolecular N–H•••O hydrogen-bonds were located from a difference Fourier and included as independent isotropic atoms whose parameters were allowed to vary in least-squares refinement cycles. The freely refined hydrogen atoms behaved well, giving reasonable bond lengths and angles in the final model that are consistent with the anticipated H-bonding pattern. The observation that these protons could be freely refined is an indication of high-quality diffraction data; the data can also be concluded to be of high quality based on the values of R_{int} (3.95%) and R₁ (4.38%; for reflections with I > 2σ(I)). The ratio of restraints to parameters is also quite reasonable for the final model (53/834), underscoring the quality of the structural data.

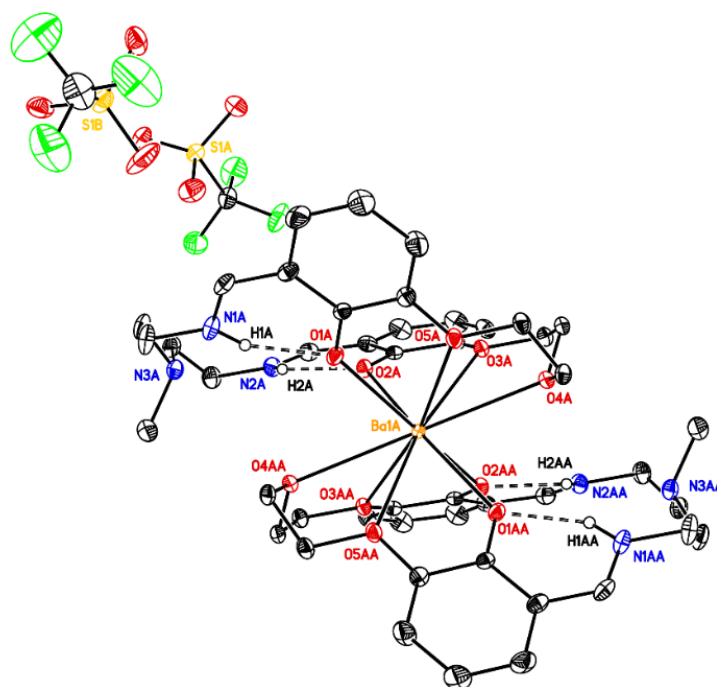


Figure S164. Solid-state structure from XRD of the first dimeric unit (A) of **BaPenta** with two nearby triflate (S1A and S1B) counteranions. H-atoms, except those covalently bonded to N1A, N2A, N1AA, N2AA and involved in intramolecular N–H•••O hydrogen-bonds, and co-crystallized solvent molecules of diethyl ether are omitted for clarity. Displacement ellipsoids are shown at the 20% probability level. H-bonding interactions are shown with hollow dashed lines.

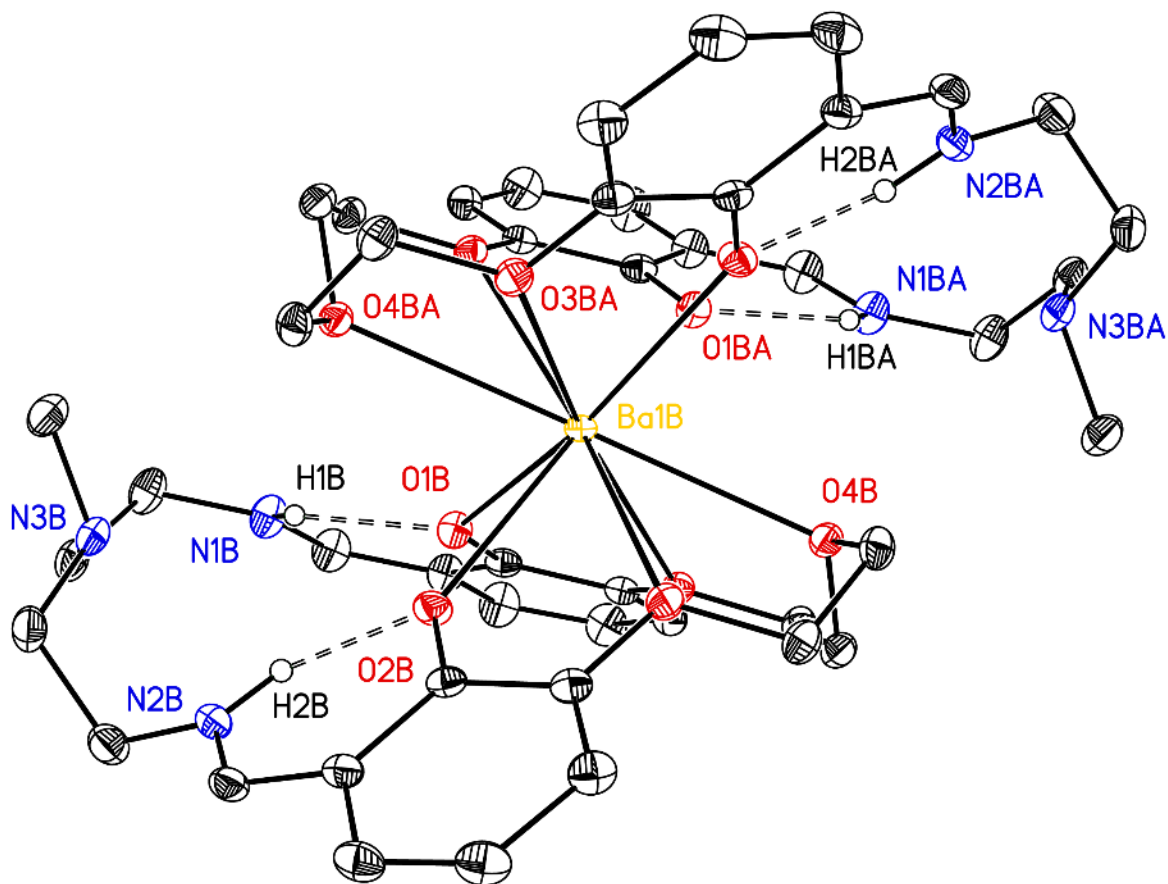


Figure S165. Solid-state structure from XRD of the second dimeric unit (B) of **BaPenta**. H-atoms, except those covalently bonded to N1B, N2B, N1BA, N2BA and involved in intramolecular N–H•••O hydrogen-bonds, triflate counteranions, and co-crystallized solvent molecules of diethyl ether are omitted for clarity. Displacement ellipsoids are shown at the 20% probability level. H-bonding interactions are shown with hollow dashed lines.

Full Solid-state Asymmetric Unit of BaPenta (q55j)

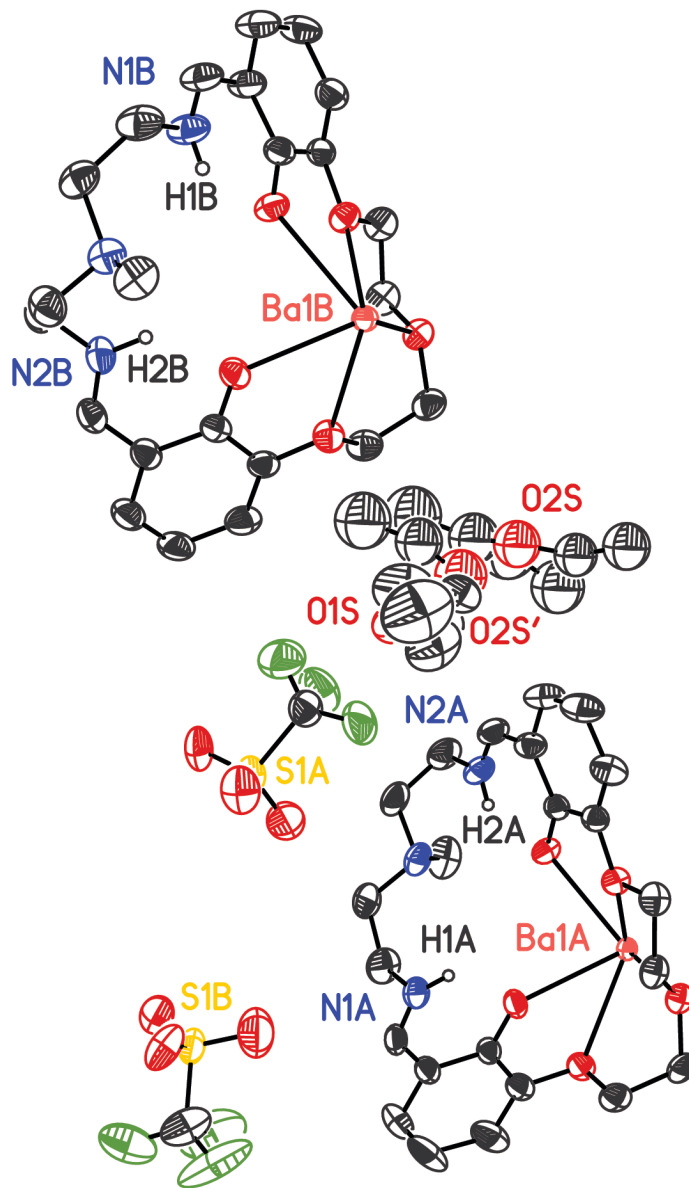


Figure S166. Full solid-state asymmetric unit for **BaPenta** showing 69/31(2) disorder of one equivalent of outer-sphere diethyl ether (associated with O1S) with two orientations of just one terminal methyl group and 51/49(1) disorder for the second equivalent of outer sphere diethyl ether (associated with O2S/O2S'). H-atoms, except those covalently bonded to N1A, N2A, N1B, N2B and involved in intramolecular N–H•••O hydrogen-bonds, are omitted for clarity. Displacement ellipsoids are shown at the 50% probability level.

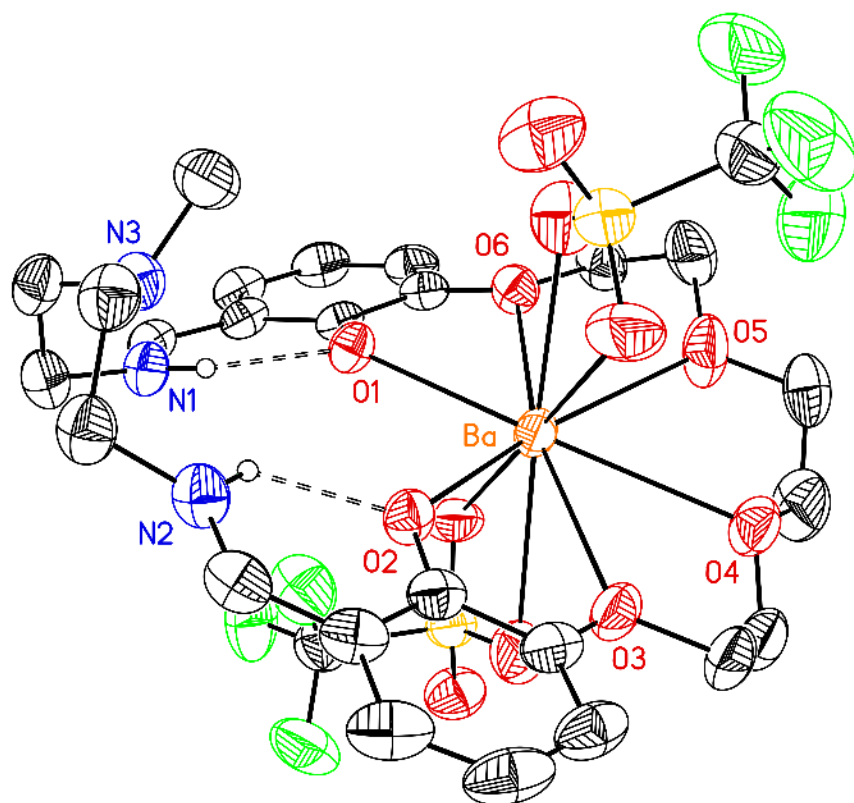


Figure S167. Solid-state structure from XRD of **BaHexa**.⁴ H atoms, except those that are hydrogen-bonded to O1 and O2, are omitted for clarity. Displacement ellipsoids are shown at the 50% probability level.

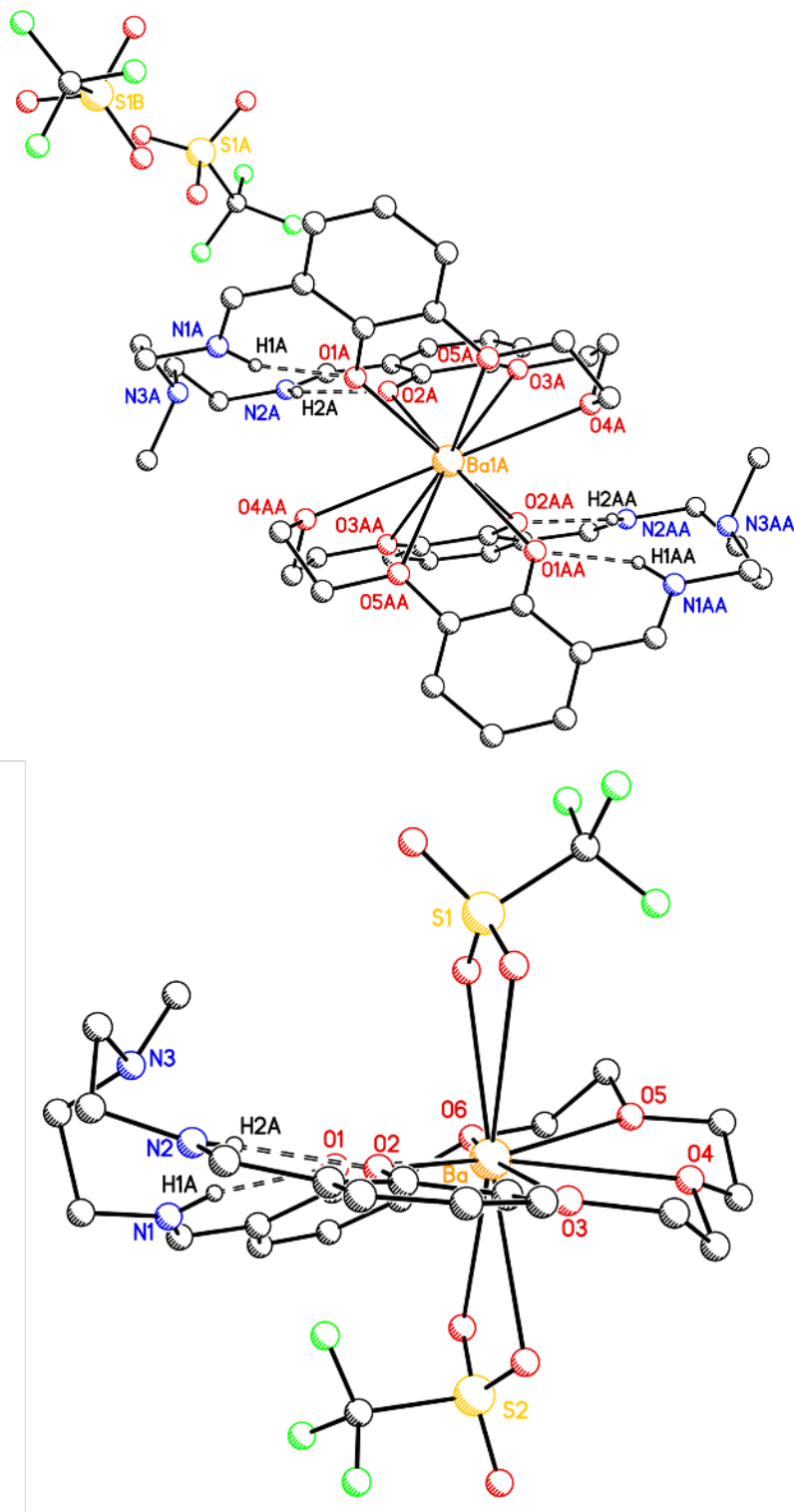


Figure S168. The structures of **BaPenta** (upper structure; dimeric unit A from q55j) and **BaHexa** (lower structure; from reference 4). The Ba^{2+} ion is significantly displaced above the plane of the crown ether site in the case of **BaPenta**, while it nestles comfortably into the site in the case of **BaHexa**.

Table S12. Comparison of coordination numbers and selected bond lengths, interatomic distances, root mean square deviations (ω), and displacement of Ba atoms from a plane (ψ).

Compound	BaPenta		BaHexa ^a
	Molecule A	Molecule B	
C.N. of Ba	10	10	10
O1...O2 (Å)	3.425(4)	3.230(4)	3.641(3)
Ba–O1_{phenoxide} (Å)	2.698(2)	2.732(3)	2.696(2)
Ba–O2_{phenoxide} (Å)	2.741(2)	2.691(3)	2.693(3)
Ba–O_{phenoxide} (avg) (Å)	2.720(2)	2.711(3)	2.695(3)
$\omega_{\text{crown}}^{\text{b}}$	0.262	0.246	0.233
$\omega_{\text{salben}}^{\text{c}}$	0.180	0.388	0.607
$\psi_{\text{Ba}} (\text{Å})^{\text{d}}$	1.563	1.577	0.048

(a) Structural data taken from references 4 and 20 (CCDC 1960625). (b) Defined for **BaPenta** as the root mean square deviation (r.m.s.d.) of O1, O2, O3, O4, and O5 from the mean plane of their positions. O6 was also included in the calculation for **BaHexa**. (c) r.m.s.d. of O1, O2, N1, N2, and N3. (d) Defined for **BaPenta** as the distance between Ba atom and the centroid of the plane defined by O1, O2, O3, O4, and O5. O6 was also included in the plane for **BaHexa**. Atom labels are consistent with those given in the raw crystallographic data (see Supporting Information).

Special Refinement Details for L⁵UO₂ (q75k).

The structure of q75k appears to reveal 78/22(1) disorder of the atoms to bonded to N3. In actuality, this represents two distinct isomers of the complex that have co-crystallized in the same volume of the unit cell. Simple rotation about any of the N3 bonds would not invert N3; a bond would have to be broken to interconvert the isomers. The bond lengths and angles for atoms modeling the two co-crystallized isomers were restrained to have nearly idealized geometry by requiring them to be appropriate multiples of the C(sp³)–C(sp³) bond length. This length was included in the refinement as a free variable that refined to a final value of 1.519(4) Å. This is quite reasonable when compared to the expected C(sp³)–C(sp³) bond length of 1.513 Å.¹⁹ All minor orientation atoms were incorporated into the molecular model with isotropic thermal parameters that were allowed to vary in refinement cycles.

The structure also contains one molecule of co-crystallized acetonitrile that is located near the crown-ether-like site. Initial solution and refinement enabled the three atoms of this solvent molecule to be located from a difference Fourier and to be successfully refined as independent anisotropic atoms (see Figure S171, part a) with the expected bond lengths and C–C–N angle. The anisotropic displacement parameters (ADPs) indicated that the CH₃CN probably had slightly different orientations/positions in various asymmetric units but that the methyl was engaged in intrinsically weak C–H•••O hydrogen bonds to phenoxy and/or ether oxygens of the two disordered and co-crystallized metal complex isomers. This initial structure with a single full-occupancy CH₃CN refined to $R_1 = 3.64\%$ with no restraints on the CH₃CN.

In the course of peer review, one reviewer deemed this structure, and by extension the entire study presented here, unpublishable due to the unconventionally (but quite understandably) large ADPs for the CH₃CN atoms and insisted that, in order to move this structure and the broader study toward publication, that the CH₃CN positional disorder should be “resolved” or the CH₃CN be removed from the model with a solvent mask (e.g., SQUEEZE). This positional disorder effort was therefore taken up and significant time invested in preparing a new model that ultimately refined to $R_1 = 3.62\%$ but with 59 more parameters (variables) and 128 more restraints for the CH₃CN. These details are described here as they pertain to a case, often encountered in crystallography, in which alternative models differ significantly in their implementation.

In the final structure preferred by the noted peer reviewer, the co-crystallized CH₃CN molecule was found to be disordered across three orientations in the ratio 41:27:32(3). These three orientations represent three unique but very closely separated CH₃CN molecules in which the individual carbon atoms are associated with 2.46, 1.62 and 1.92 electrons, respectively. We note that these atomic positions are being modeled in the presence of a fully ordered uranium atom with 92 electrons. The individual atoms for the CH₃CN moieties could not be refined independently, a sensible finding as they are not only extremely close to one another (see Figure S172) but they also represent a low (relative) electron count. For example, the C2SA•••C2SB distance is 0.398 Å, C2SA•••C2SC is 0.383 Å, and C2SB•••C2SC is 0.524 Å; the C1SA•••C1SB distance is 0.589 Å, C1SA•••C1SC is 0.908 Å, and C1SB•••C1SC is 0.364 Å; the N1SA•••N1SB distance is 0.934 Å, N1SA•••N1SC is 1.850 Å, and N1SB•••N1SC is 0.923 Å. These metrics underscore that there are especially short pairings

between the modeled atoms of the “central” CH₃CN moiety and the “outer” ones, as one would expect in a situation of this type.

Therefore, in order to achieve a satisfactory refinement, the parameters for the CH₃CN moieties had to be heavily restrained. The bond lengths for each of the independent orientations were restrained to have nearly idealized geometry by requiring them to be appropriate multiples of the N(sp)–C(sp) bond length. This length was included in the refinement as a free variable that refined to a final value of 1.142(6) Å. This is quite reasonable when compared to the expected N(sp)–C(sp) bond length of 1.136 Å.¹⁹ The atoms associated with the three independent orientations of the co-crystallized molecule of CH₃CN were also restrained in the final model with mild isotropic and similarity restraints. As a result, nearly every structural feature for the three independent CH₃CN solvent moieties had to be imposed (rather than independently found and refined) for a satisfactory refinement.

If details for these refined CH₃CN moieties are taken as acceptable, the observation of three independent orientations of the co-crystallized acetonitrile molecule is possibly attributable to unique patterns of intrinsically weak C–H•••O hydrogen bonds in each case. In Orientation A [41(3)% occupancy], C2SA appears to be engaged in two weak electrostatic H-bonds, as it is located 3.27(3) Å from O1 and 3.39(3) Å from O2. In Orientation B [27(3)% occupancy], C2SB appears to be engaged in two (different) weak electrostatic H-bonds, as it is located 3.32(4) Å from O5 and 3.35(3) Å from O2. And, in Orientation C [32(3)% occupancy], C2SC appears to be engaged in single but more moderate electrostatic H-bond, as it is located 3.14(3) Å from O2.²¹

Although we find these observations regarding weak H-bonding superficially satisfying, we caution that the standard uncertainties for the pairs of C•••O separations render them essentially equivalent. Considering this, it may be that the original model with large ADPs for the co-crystallized CH₃CN represents a more believable (realistic) structure in which the individual atomic positions for the CH₃CN atoms were refined based on the available data instead of being restrained. It may also not be unreasonable to consider the CH₃CN disorder as associated with the co-crystallization of two isomers of the desired L⁵UO₂ complex with essentially the same (although actually different but unresolved) positions for O1, O2 and O5 in the various asymmetric units. From this perspective, the methyl group of the CH₃CN methyl could/would engage in weak H-bonds to these O-atoms with unique patterns in each asymmetric unit, but essentially in an unresolved manner that is in accord with the unresolved positions of O1, O2, and O5 for the co-crystallized isomers of the metal complex. These H-bonds would, however, effectively tie down C2S and allow slightly different positions (and larger ADPs) for C1S and N1S. Considering this, our initial refined structure with a single CH₃CN certainly represents an average structure and the reviewer-preferred model with three CH₃CN positions represents a “snapshot” of three possible structures, albeit associated with the inevitable uncertainty that results from the use of significant restraints.

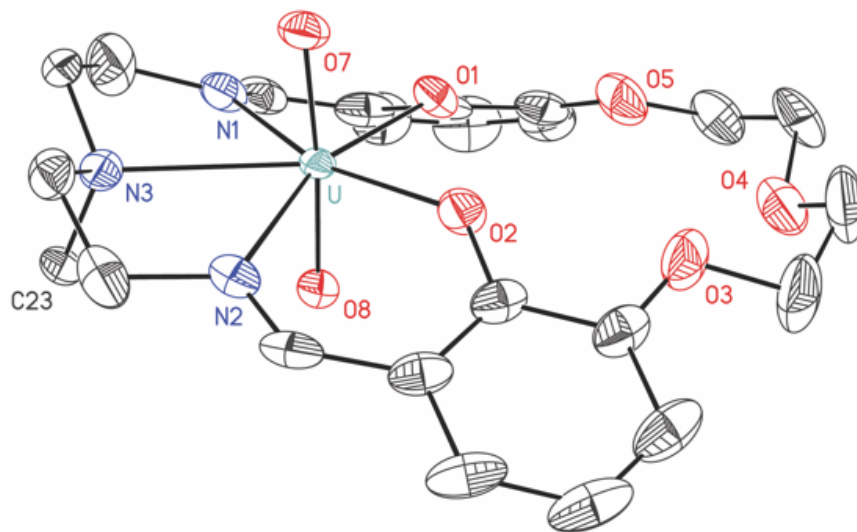


Figure S169. Solid-state structure from XRD of L^5UO_2 showing the major co-crystallized isomer. All H-atoms, the outer sphere acetonitrile molecule, and atoms associated with minor components of apparent disorder are omitted for clarity. Displacement ellipsoids are shown at the 50% probability level.

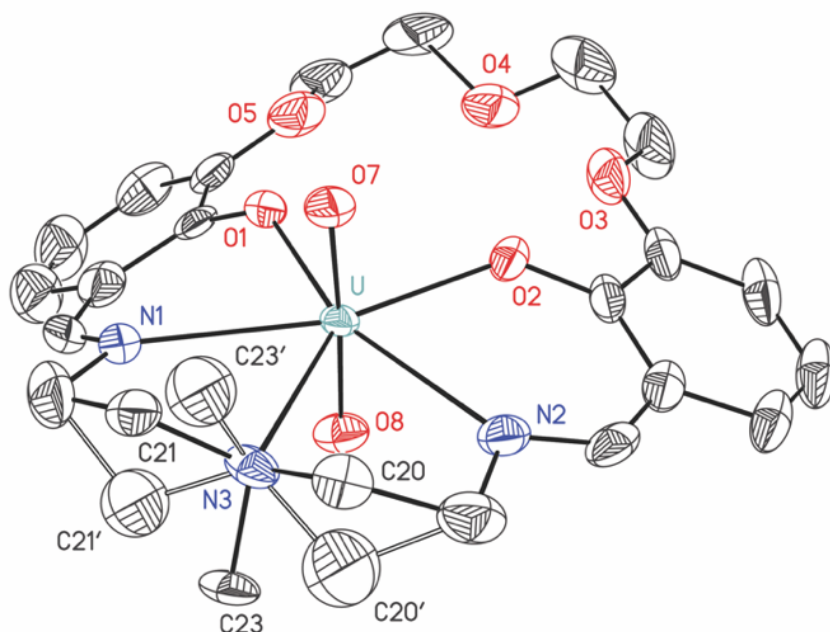


Figure S170. Solid-state structure from XRD of the two co-crystallized isomers of L^5UO_2 . The presence of the two co-crystallized isomers of the macrocyclic uranium complex is represented in the final refinement model as 78/22(1) disorder for the atoms bonded to the amine nitrogen. Solid bonds are used for the major (78%) isomer and hollow bonds for the minor isomer. Atoms C20, C21, and C23 are not common to the individual isomers. All H-atoms and a co-crystallized acetonitrile molecule are omitted for clarity. Displacement ellipsoids are shown at the 50% probability level.

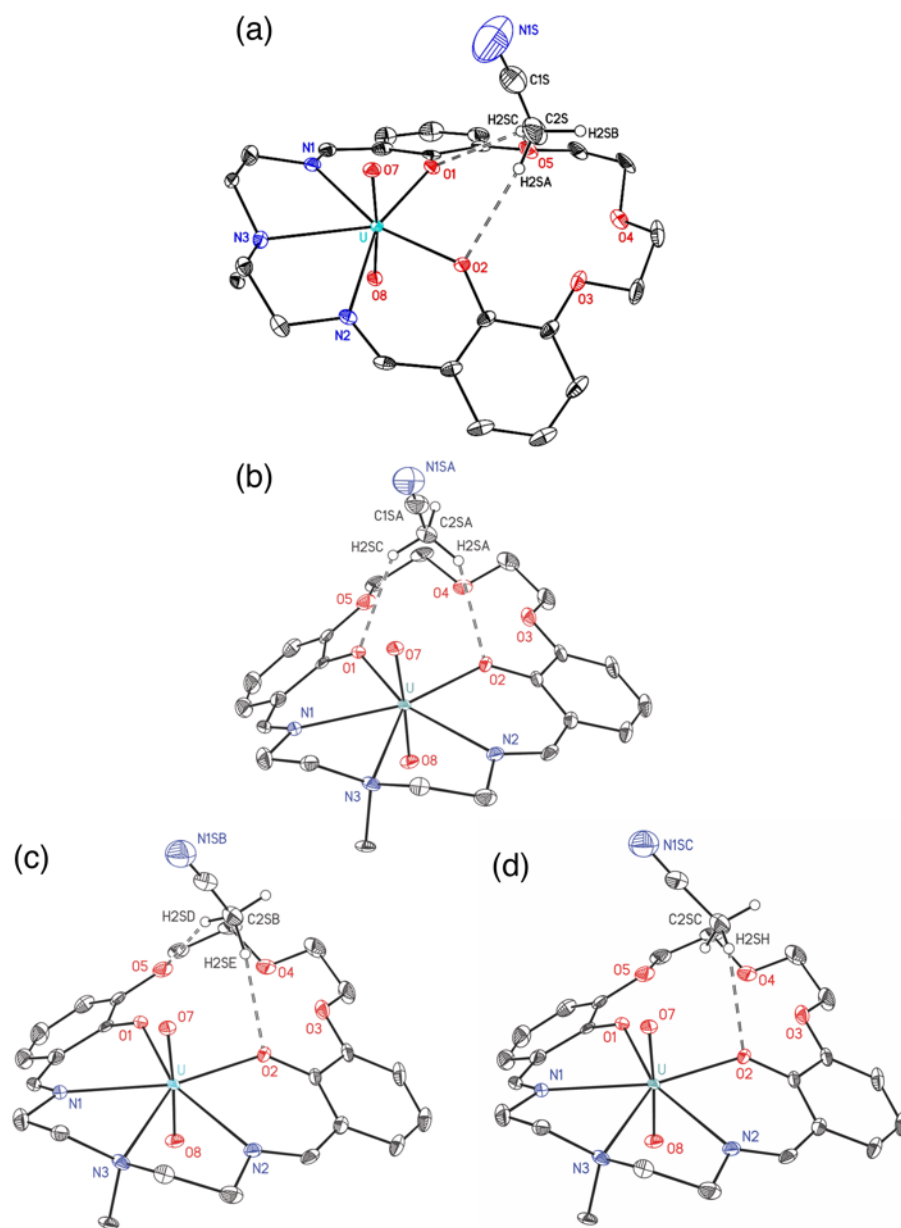


Figure S171. Views of the solid-state structure from XRD of L^5UO_2 comparing the initial and final (reviewer preferred) refinement models for the co-crystallized acetonitrile molecule. View (a) shows the structure from the initial refinement model that features a single refined CH_3CN molecule (associated with N1S, C1S, and C2S). Views (b)–(d) highlight the three apparent (restrained) orientations of the CH_3CN . All H-atoms, except those covalently bonded to the carbon atoms of the outer sphere acetonitrile molecule, and disordered atoms associated with the main uranium-containing macrocyclic species are omitted for clarity in all images. Displacement ellipsoids are shown at the 20% probability level. Values for the $C\cdots O$ distances corresponding to the apparent $C-H\cdots O$ hydrogen bonds are given on p. S150.

Full Solid-state Asymmetric Unit of L^5UO_2 (q75k)

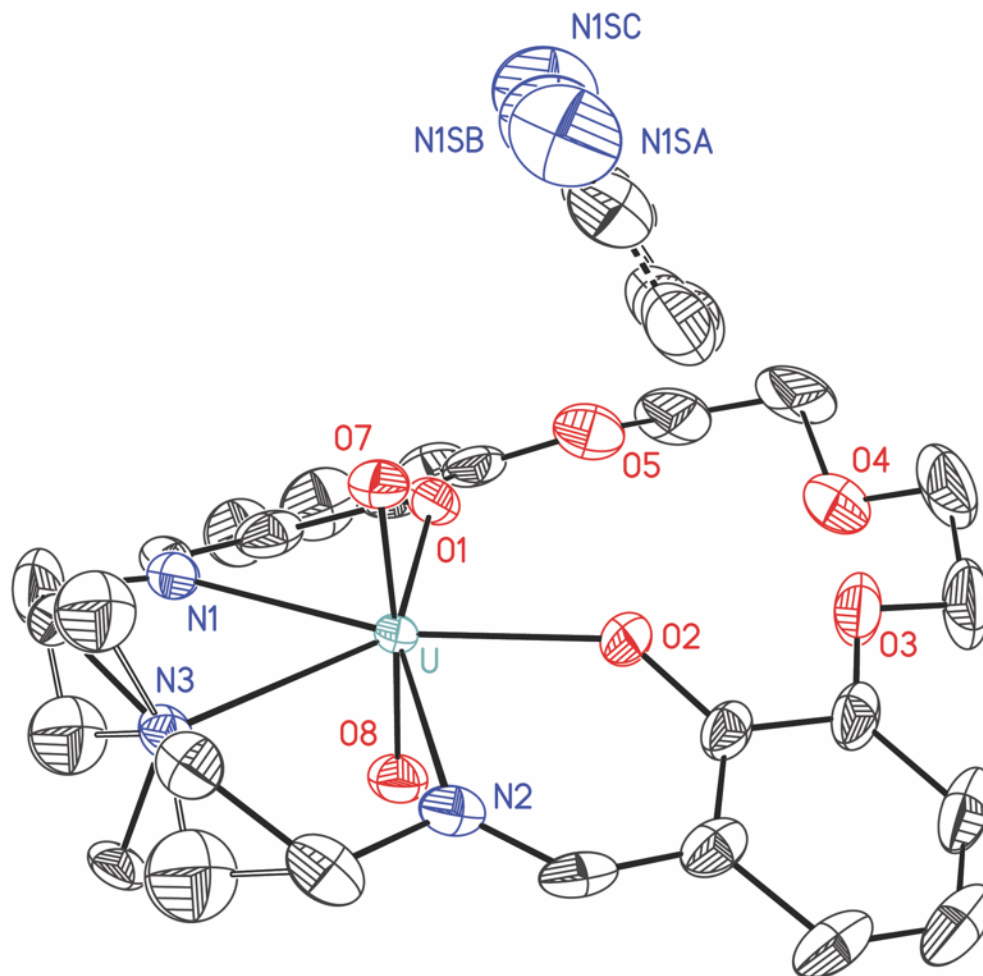


Figure S172. Full solid-state asymmetric unit for L^5UO_2 showing the apparent 78/22(1) disorder for the atoms bonded to amine nitrogen N3 in the two co-crystallized isomers of the macrocyclic uranium complex and the three individual CH_3CN moieties associated with the co-crystallized acetonitrile molecule (associated with N1SA, N1SB, and N1SC; modeled occupancies 41:27:32(3)) as described in the Special Refinement Details on pp. 149-150. Solid bonds are used for the major (78%) orientation about the U–N3 bond and hollow bonds for the minor (22%) orientation. All H-atoms are omitted for clarity. Displacement ellipsoids are shown at the 50% probability level.

Table S13. Comparison of selected bond lengths, interatomic distances, root mean square deviations (ω), and displacements of the uranium center from the plane (ψ) of L^5UO_2 with the previously published structure.

Compound	L^5UO_2	L^5UO_2 from literature ^a
O1•••O2 (Å)	3.138(5)	3.154(14)
U–O7_{oxo} (Å)	1.771(4)	1.782(11)
U–O8_{oxo} (Å)	1.781(4)	1.788(12)
U–O_{oxo} (avg) (Å) ^b	1.776(4)	1.785(12)
U–O1_{phenoxide} (Å)	2.249(4)	2.251(11)
U–O2_{phenoxide} (Å)	2.231(4)	2.258(10)
U–O_{phenoxide} (avg) (Å)	2.240(4)	2.255(11)
U–N1_{imine} (Å)	2.559(5)	2.597(13)
U–N2_{imine} (Å)	2.594(5)	2.557(14)
U–N_{imine} (avg) (Å)	2.577(5)	2.577(14)
ω_{crown} ^c	0.055	0.033
ω_{salben} ^d	0.077	0.089
ψ_U ^e	0.043	0.007

(a) Structural data taken from reference 22. (b) Average of the U–O7 and U–O8 bond distances. (c) Defined as the root mean square deviation (r.m.s.d.) of the following atoms from the mean plane of their positions: O1, O2, O3, O4, and O5. (d) Defined as the r.m.s.d. of O1, O2, N1, N2, and N3. Atom labels are consistent with those given in the raw crystallographic data. (e) Absolute value of the distance between U and the mean plane of O1, O2, N1, N2, and N3.

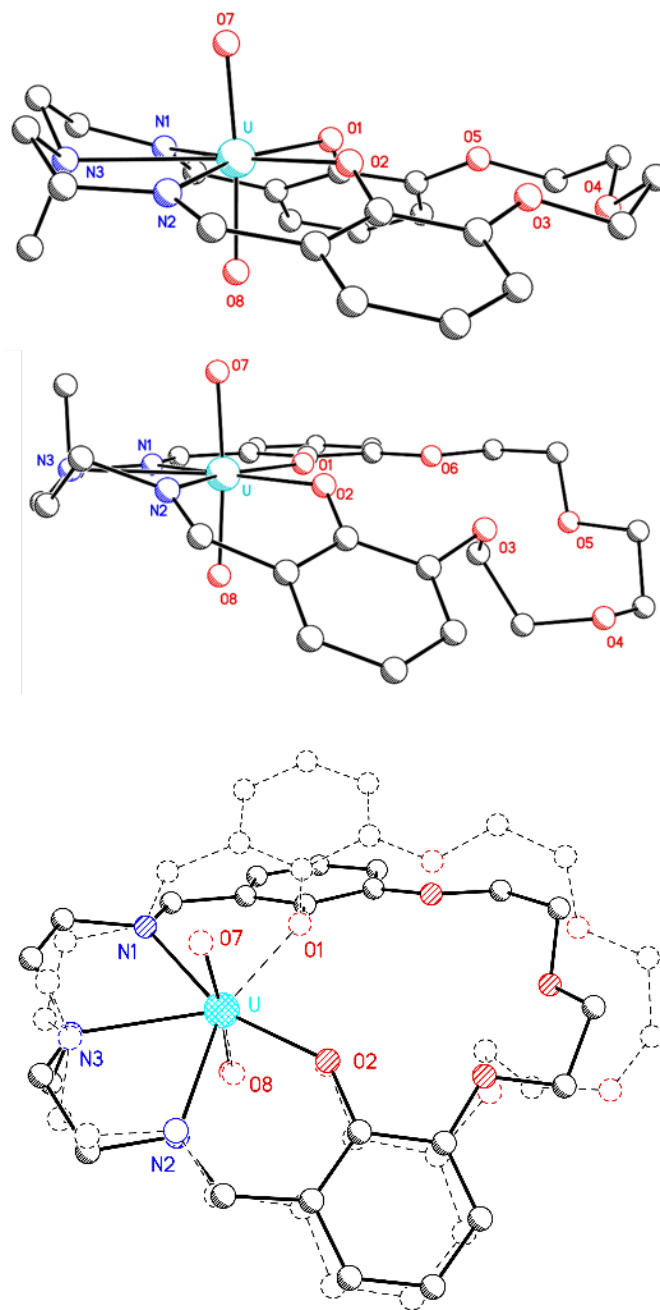


Figure S173. Images of the major crystallized isomer of L^5UO_2 (upper structure) and L^6UO_2 (middle structure), demonstrating the significantly greater co-planarity of the polyether oxygen atoms in L^5UO_2 compared to L^6UO_2 . The lower image shows a superimposed view of the solid-state structures of the major isomer of L^5UO_2 (solid bonds) and L^6UO_2 (dashed bonds). Atom positions for U, O1, O2, O7, O8, N1, N2, and N3 were fitted to prepare this image. The superposition deviation of the two U positions is 0.019 Å, of the two O1 positions is 0.043 Å, of the two O2 positions is 0.095 Å. The overall superposition deviation of the given atom list is 0.063 Å, demonstrating rather close uniformity of the first coordination spheres about the uranyl dications in these complexes.

Table S14. Comparison of selected bond lengths, interatomic distances, root mean square deviations (ω), and displacement of select metal atoms from the plane (ψ) in monometallic UO_2^{2+} complexes.

Compound	L^5UO_2	L^6UO_2 ^a
O1•••O2 (Å)	3.138(5)	3.137(10)
U–O7_{oxo} (Å)	1.771(4)	1.783(8)
U–O8_{oxo} (Å)	1.781(4)	1.792(7)
U–O_{oxo} (avg) (Å) ^b	1.776(4)	1.788(8)
U–O1_{phenoxide} (Å)	2.249(4)	2.250(7)
U–O2_{phenoxide} (Å)	2.231(4)	2.207(8)
U–O_{phenoxide} (avg) (Å)	2.240(4)	2.229(8)
U–N1_{imine} (Å)	2.559(5)	2.595(9)
U–N2_{imine} (Å)	2.594(5)	2.559(9)
U–N_{imine} (avg) (Å)	2.577(5)	2.577(9)
ω_{crown} ^c	0.055	0.358
ω_{salben} ^d	0.077	0.049
ψ_{U} ^e	0.043	0.005

(a) Structural data taken from references 4 and 23 (CCDC 1960626). (b) Average of the U–O7 and U–O8 bond distances. (c) Defined as the root mean square deviation (r.m.s.d.) of atoms O1, O2, O3, O4, and O5 from the mean plane of their positions for L^5UO_2 . O6 was included in the calculation for L^6UO_2 . (d) Defined as the r.m.s.d. of O1, O2, N1, N2, and N3. Atom labels are consistent with those given in the raw crystallographic data. (e) Absolute value of the distance between U and the mean plane of O1, O2, N1, N2, and N3.

Special Refinement Details for L^5UO_2Na (q50k).

The structure of q50k appears to reveal 60/40(1) disorder of the atoms to bonded to N3. In actuality, this represents two distinct isomers of the complex that have co-crystallized in the same volume of the unit cell. Simple rotation about any of the N3 bonds would not invert N3; a bond would have to be broken to interconvert the isomers.

Notably, structures q50k (L^5UO_2Na) and v16f (L^5UO_2Na') are nearly isomorphous (see Table S19). The structures are *only nearly* isomorphous, as they differ in terms of the ratio of the isomeric orientations about N3 (60/40 for q50k vs. 67/33 for v16f). Additionally, the triflate in structure v16f was found to be disordered across two orientations, whereas the triflate in q50k appears fully ordered.

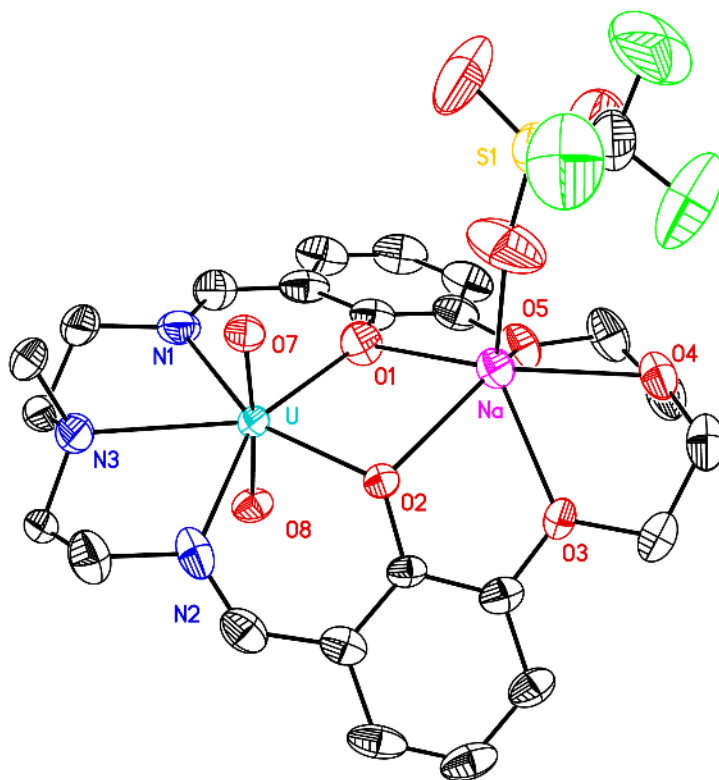


Figure S174. Solid-state structure from XRD of the major co-crystallized isomer of L^5UO_2Na . All H-atoms and the atoms associated with the minor co-crystallized isomer are omitted for clarity. Displacement ellipsoids are shown at the 50% probability level.

Full Solid-state Asymmetric Unit of L^5UO_2Na (q50k)

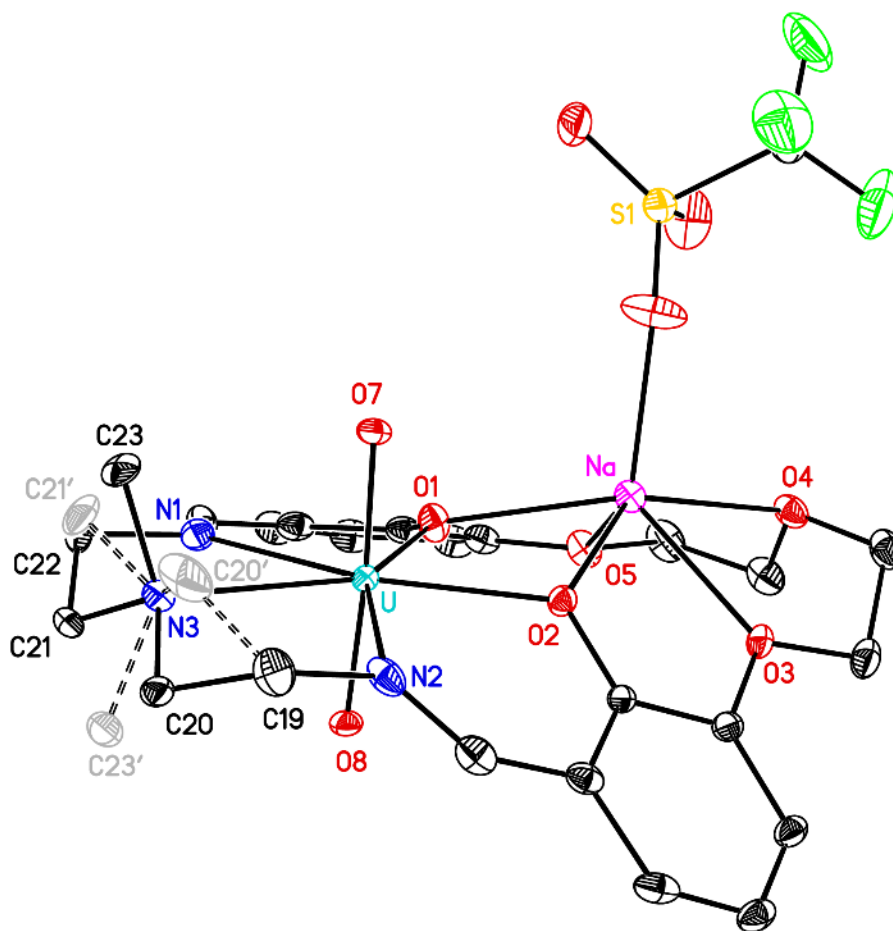


Figure S175. Full solid-state asymmetric unit for L^5UO_2Na showing 60/40 apparent disorder for the atoms bonded to amine nitrogen N3. Solid bonds are used for the major (60%) orientation about the U–N3 bond and dashed bonds for the minor (40%) orientation. All H-atoms are omitted for clarity. Displacement ellipsoids are shown at the 20% probability level.

Special Refinement Details for L^5UO_2Na' (v16f).

The structure of v16f appears to reveal 67/33(2) disorder of the atoms to bonded to N3. In actuality, this represents two distinct isomers of the complex that have co-crystallized in the same volume of the unit cell. Simple rotation about any of the N3 bonds would not invert N3; a bond would have to be broken to interconvert the isomers. Additionally, the inner-sphere triflate counteranion was found to be 87/13(1) disordered with two orientations. All minor orientation atoms were incorporated into the model with isotropic thermal parameters that were allowed to vary in refinement cycles.

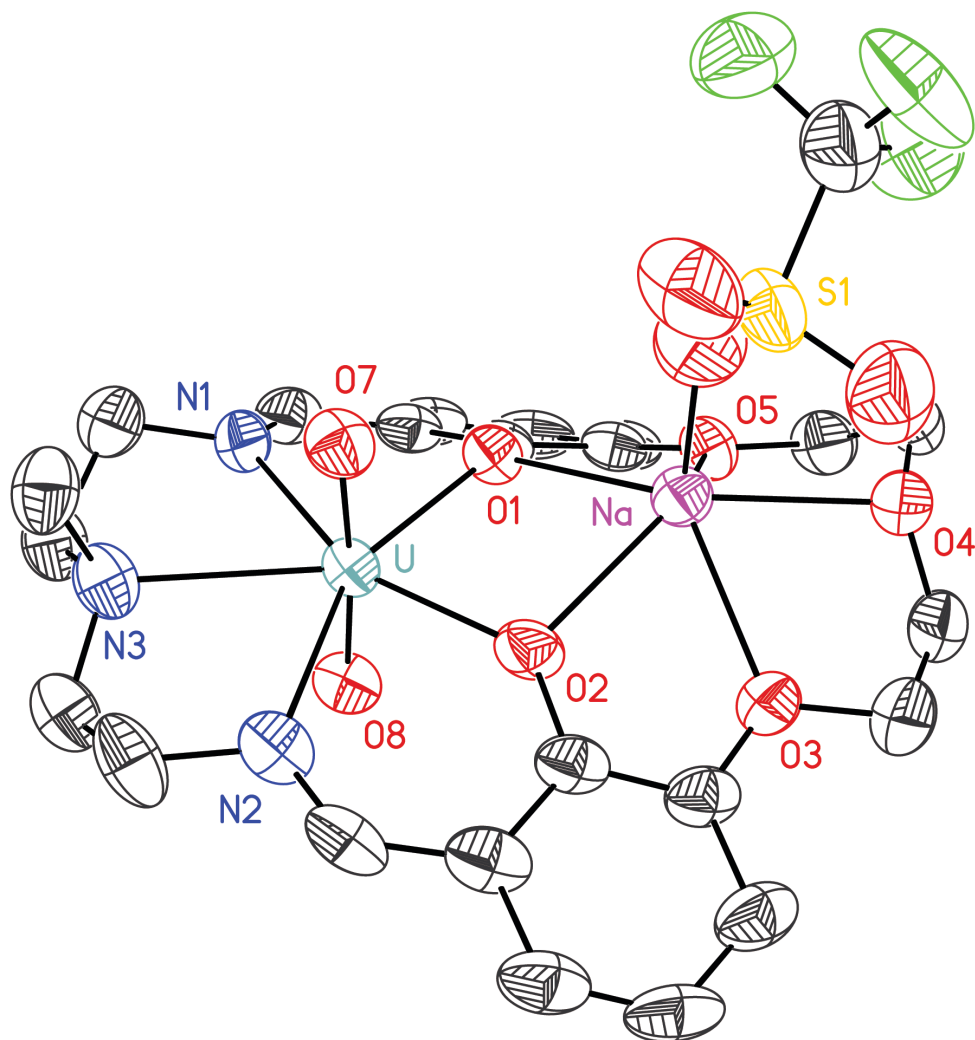


Figure S176. Solid-state structure from XRD of the major co-crystallized isomer of L^5UO_2Na' . All H-atoms and atoms unique to the minor co-crystallized isomer omitted for clarity. Displacement ellipsoids are shown at the 50% probability level.

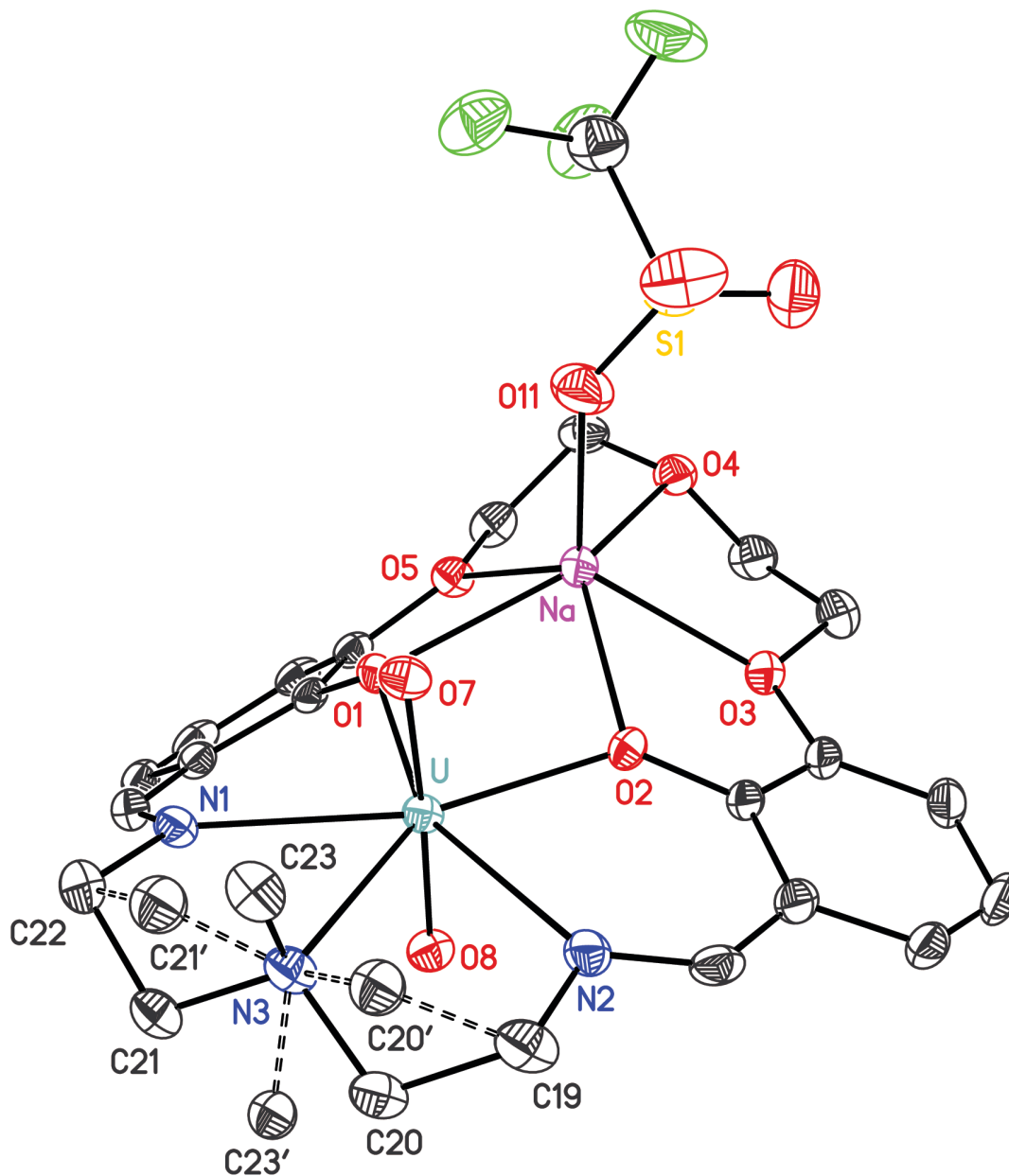


Figure S177. Solid-state structure from XRD of L^5UO_2Na' . The presence of the two co-crystallized isomers could be represented as 67/33 disorder for the atoms bonded to the amine nitrogen. Solid bonds are used for the major (67%) isomer and dashed bonds for the minor isomer. Atoms C20, C21, and C23 are not common to the individual isomers. All H-atoms and disorder associated with the inner-sphere triflate counteranion are omitted for clarity. Displacement ellipsoids are shown at the 20% probability level.

Full Solid-state Asymmetric Unit of L^5UO_2Na' (v16f)

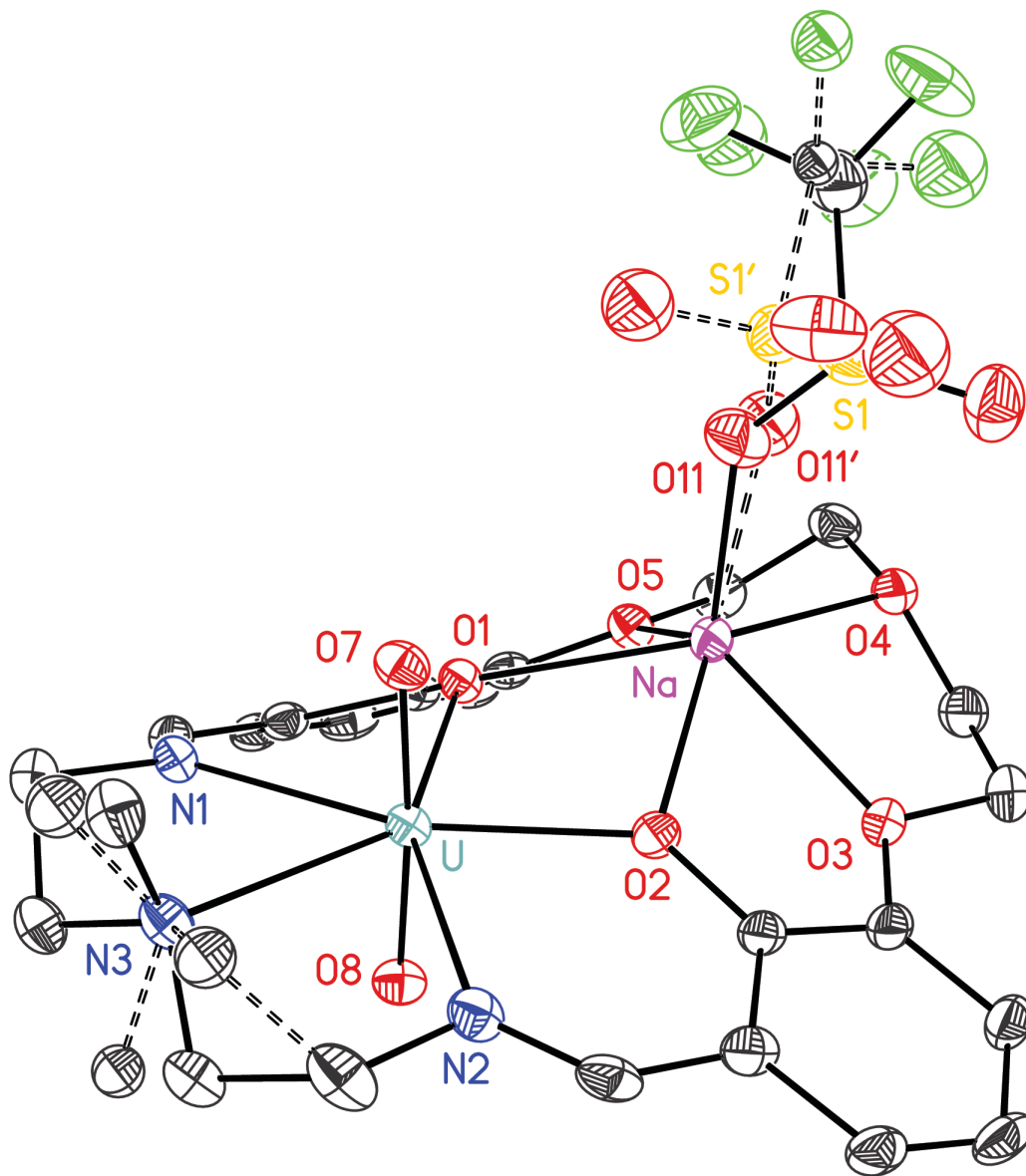


Figure S178. Full solid-state asymmetric unit for L^5UO_2Na' showing the 67/33 apparent disorder for the atoms bonded to amine nitrogen N3 and 87/13 disorder for the inner-sphere triflate counteranion. Solid bonds are shown for the major orientations and dashed hollow bonds for the minor orientations. All H-atoms are omitted for clarity. Displacement ellipsoids are shown at the 20% probability level.

Special Refinement Details for L^5UO_2Na -DCE (q49k).

One molecule of co-crystallized dichloroethane (DCE) solvent was found in a fully occupied site in the outer coordination sphere.

The structure of q49k appears to reveal 62/38(1) disorder of the atoms to bonded to N3. In actuality, this represents two distinct isomers of the complex that have co-crystallized in the same volume of the unit cell. Simple rotation about any of the N3 bonds would not invert N3; a bond would have to be broken to interconvert the isomers. The bond lengths for the apparently disordered region corresponding to the two co-crystallized isomers were restrained to have nearly idealized geometry by requiring them to be appropriate multiples of the $C(sp^3)$ – $C(sp^3)$ bond length. This length was included in the refinement as a free variable that refined to a final value of 1.513(5) Å. This is quite reasonable when compared to the expected $C(sp^3)$ – $C(sp^3)$ bond length of 1.513 Å.¹⁹

Mild isotropic restraints were applied to the anisotropic displacement parameters (ADPs) for C19, C20, C21, and C22; these atoms are associated with the major co-crystallized isomer of the heterobimetallic complex. Mild isotropic restraints were also applied to the ADPs for C20', C21', and C23'; these atoms are associated with the minor co-crystallized isomer of the heterobimetallic complex.

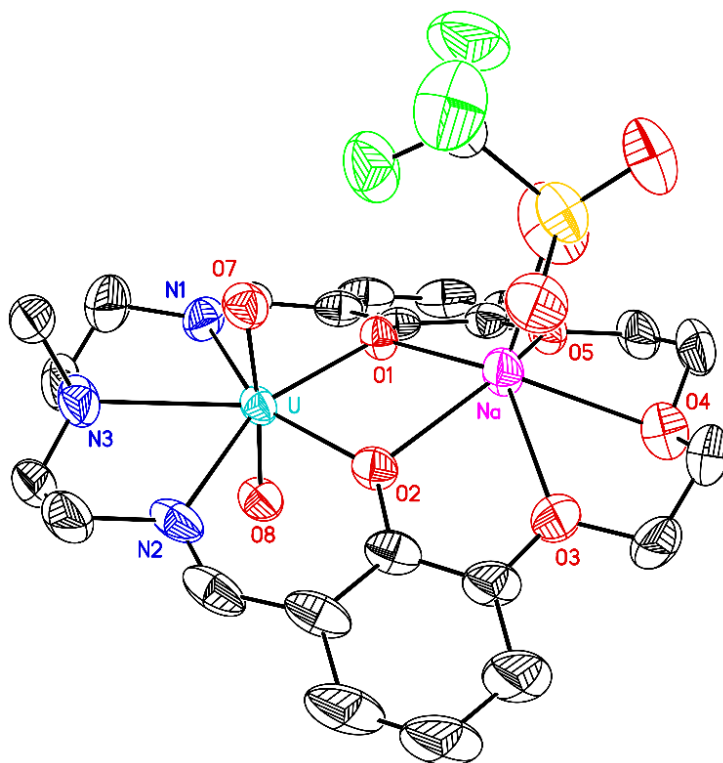


Figure S179. Solid-state structure from XRD of the major co-crystallized isomer of L^5UO_2Na -DCE. All H-atoms, a co-crystallized dichloroethane molecule, and the atoms associated with the minor co-crystallized isomer are omitted for clarity. Displacement ellipsoids are shown at the 50% probability level.

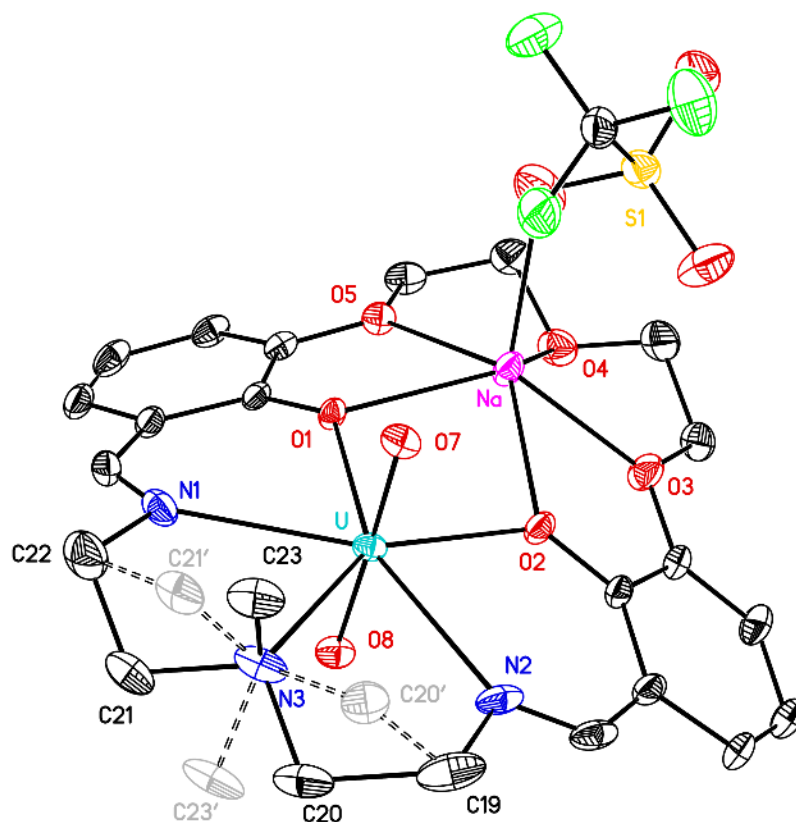


Figure S180. Solid-state structure from XRD of L^5UO_2Na -DCE showing the 62/38 apparent disorder for the atoms bonded to amine nitrogen N3. Solid bonds are used for the major (62%) isomer and dashed bonds for the minor (38%) isomer. All H-atoms and atoms associated with a co-crystallized dichloroethane molecule are omitted for clarity. Displacement ellipsoids are shown at the 20% probability level.

Full Solid-state Asymmetric Unit of L^5UO_2Na -DCE (q49k).

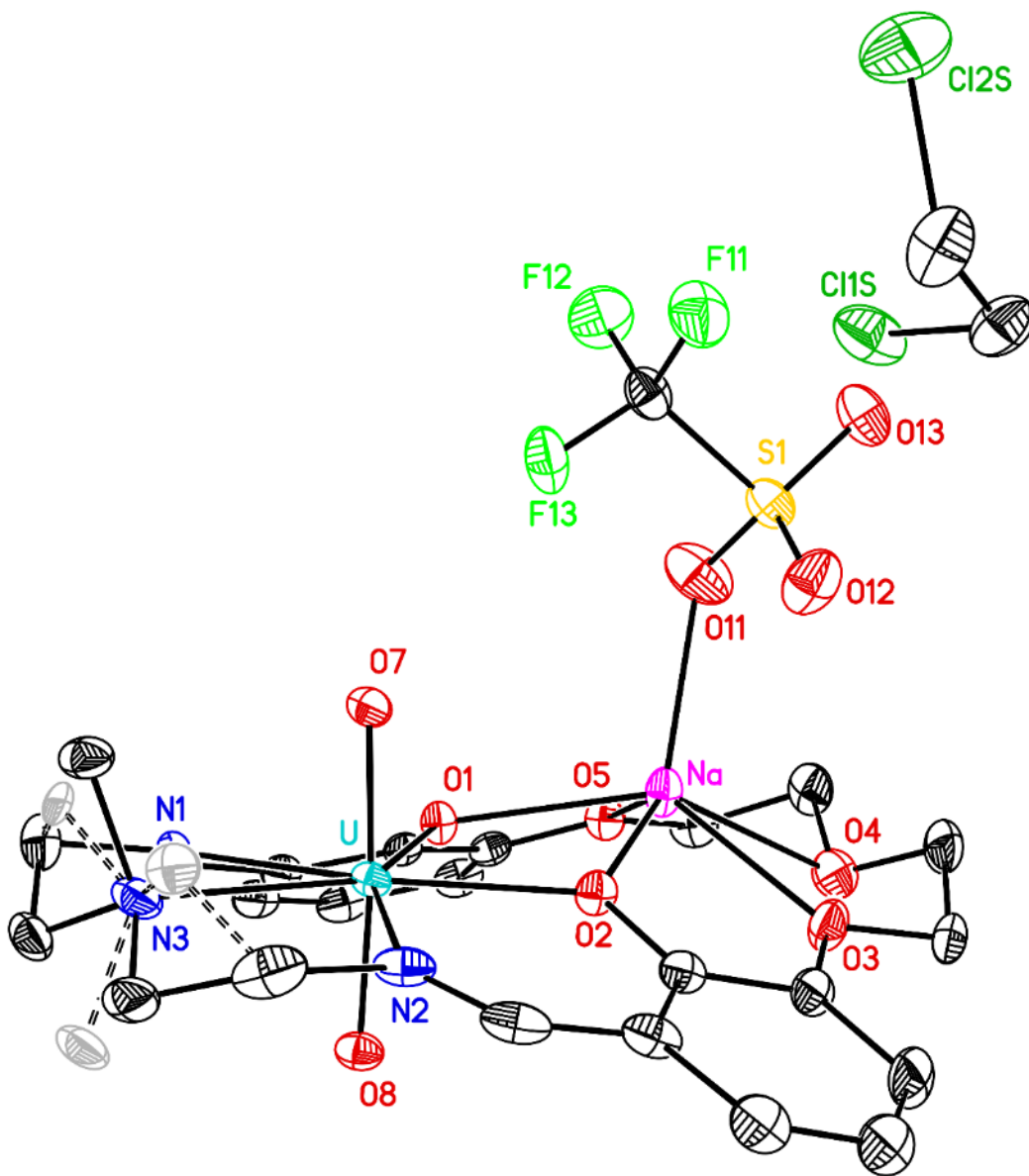


Figure S181. Full solid-state asymmetric unit for L^5UO_2Na -DCE showing 62/38 apparent disorder for the atoms bonded to amine nitrogen N3 and a co-crystallized $C_2H_4Cl_2$ (dichloroethane) molecule. Solid bonds are shown for the major (62%) co-crystallized isomer and dashed bonds for the minor (38%) co-crystallized isomer. All H-atoms are omitted for clarity. Displacement ellipsoids are shown at the 20% probability level. Atoms unique to the minor (38%) isomer are shown with a lighter shade.

Special Refinement Details for $L^5UO_2Na-MeCN$ (q56k).

The structure of q56k appears to reveal 67/33(1) disorder of the atoms to bonded to N3. In actuality, this represents two distinct isomers of the complex that have co-crystallized in the same volume of the unit cell. Simple rotation about any of the N3 bonds would not invert N3; a bond would have to be broken to interconvert the isomers. The bond lengths for the apparently disordered region corresponding to the two co-crystallized isomers were restrained to have nearly idealized geometry by requiring them to be appropriate multiples of the $C(sp^3)-C(sp^3)$ bond length. This length was included in the refinement as a free variable that refined to a final value of 1.513(5) Å. This is quite reasonable when compared to the expected $C(sp^3)-C(sp^3)$ bond length of 1.513 Å.¹⁹

The triflate counteranion is bound to the sodium cation and is 91/9(1) disordered with two different orientations in the same volume of the unit cell. The bond lengths and angles for the disordered triflate anion were restrained to have nearly idealized geometry by requiring them to be appropriate multiples of the S–O bond length. This length was included in the refinement as a free variable that refined to final value of 1.432(2) Å. This is quite reasonable when compared to the expected S–O bond length of 1.472 Å.¹⁹ In order to model the triflate disorder, stringent similarity restraints were applied to the displacement parameters of C24A and C24B, corresponding to the carbon atoms of the disordered triflate orientations. Stringent similarity restraints were also applied to F11B, F12B, and F13B.

The structures of $L^5UO_2Na-MeCN$ (q56k) L^5UO_2Li (ak2133c) are nearly isomorphous (see p. S169 for details, as well as Tables S20 and S21).

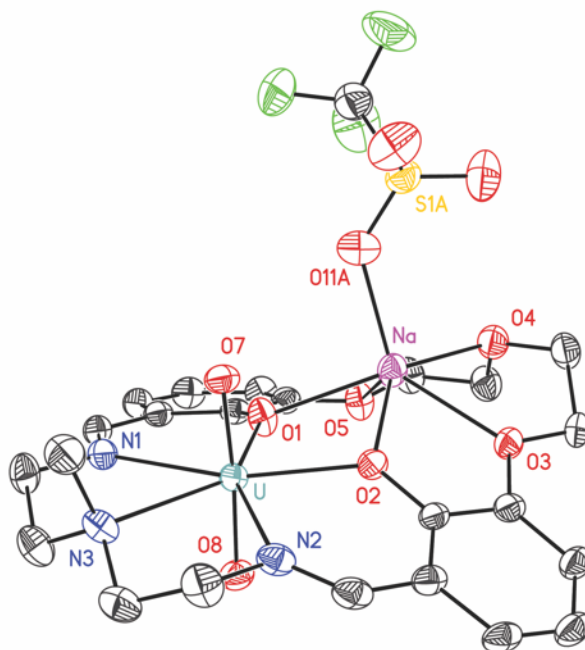


Figure S182. Solid-state structure from XRD of the major co-crystallized isomer of $L^5UO_2Na-MeCN$. All H-atoms, a co-crystallized acetonitrile molecule, and all atoms associated with minor components of apparent disorder are omitted for clarity. Displacement ellipsoids are shown at the 50% probability level.

Full Solid-state Asymmetric Unit of $L^5UO_2Na-MeCN$ (q56k)

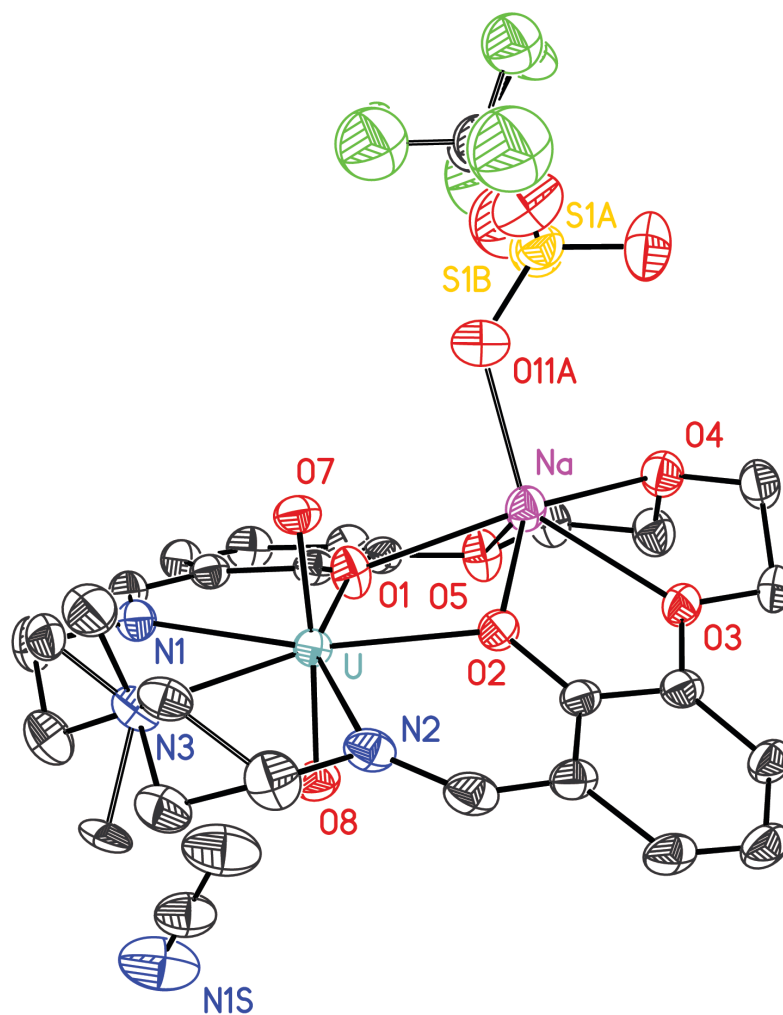


Figure S183. Full solid-state asymmetric unit for $L^5UO_2Na-MeCN$ showing 67/33(1) apparent disorder for the atoms bonded to amine nitrogen N3, 91/9(1) disorder for the triflate bound to Na, and a co-crystallized acetonitrile molecule. Solid bonds are shown for the major orientations and dashed bonds for the minor orientations in the disordered regions. All H-atoms are omitted for clarity. Displacement ellipsoids are shown at the 20% probability level. Hollow lines are shown for bonds in the minor components of (apparent) disorder. The distance from S1A to S1B is 0.887 Å.

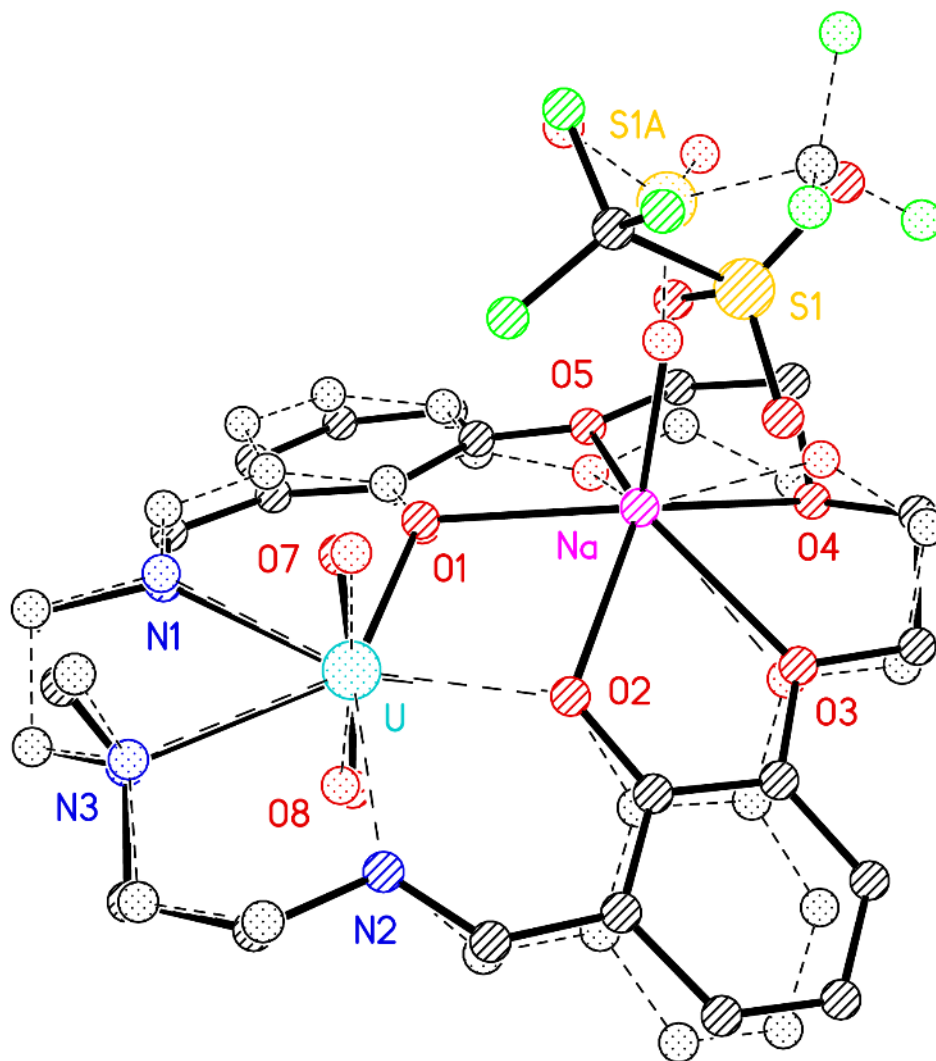


Figure S184. Superimposed view of the solid-state structures of the major co-crystallized isomers of L^5UO_2Na (solid bonds) and of $L^5UO_2Na-DCE$ (dashed bonds). Atom positions for the U, Na, O1, O2, O3, O4, O5, O7, O8, N1, N2, and N3 cores were superimposed to prepare this image. The superposition deviation of the two U atoms is 0.035 Å and of the two Na atoms is 0.050 Å, with the overall superposition deviation being 0.270 Å for the aforementioned list of superimposed atoms. The greater deviation between L^5UO_2Na and $L^5UO_2Na-DCE$ versus that for L^5UO_2Na and $L^5UO_2Na-MeCN$ on p. S167 is attributable to the deviations of atoms O3 (0.331 Å), O4, (0.610 Å), and O5 (0.562 Å). These atoms are associated with the flexible polyether linkage, and thus they can be concluded to adopt preferred positions based on the solid-state (packing) environment. This environment appears to be influenced by the identity of the co-crystallized outer-sphere dichloroethane molecule in this case, which was derived from the conditions used for crystallization.

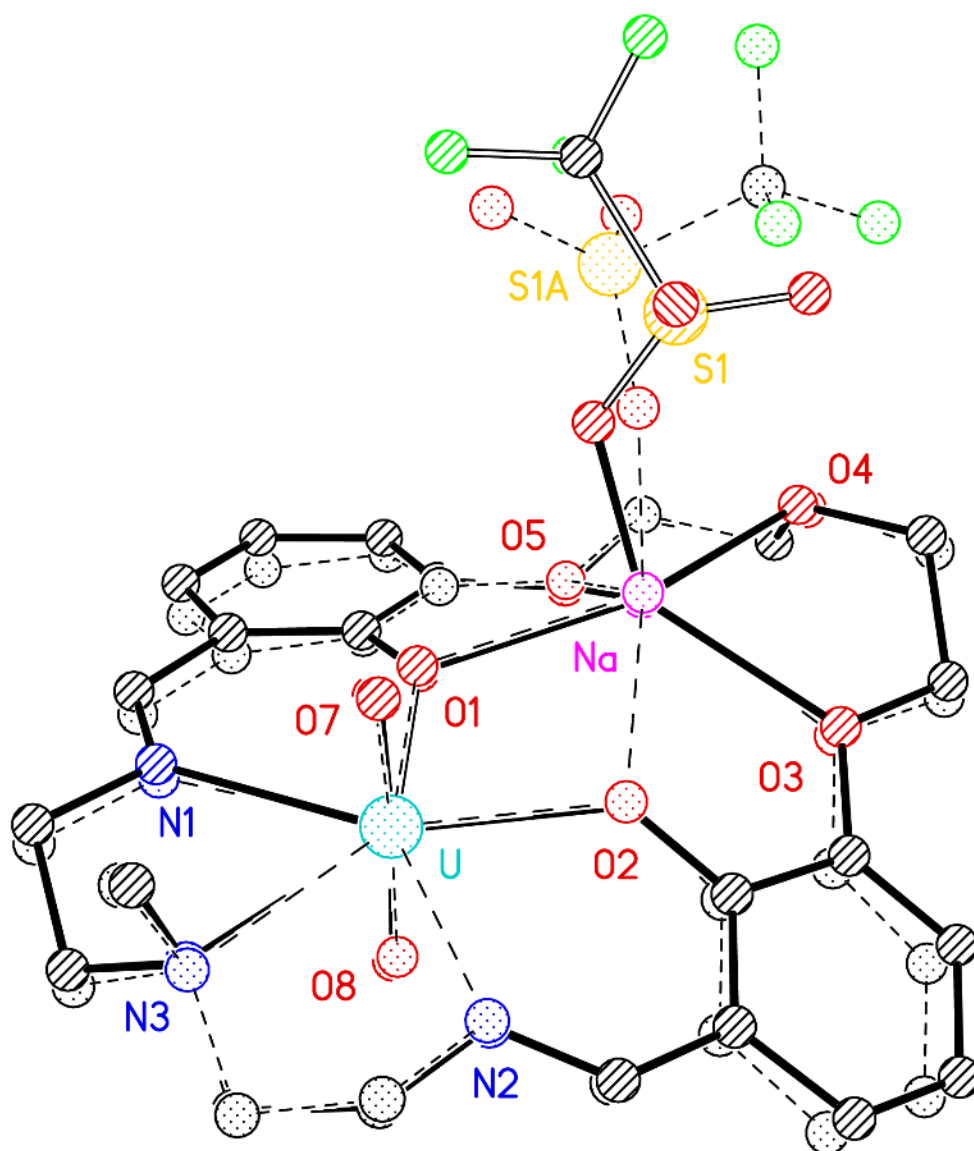


Figure S185. Superimposed view of the solid-state structures of the major co-crystallized isomers of L^5UO_2Na (solid bonds) and of $L^5UO_2Na-MeCN$ (dashed bonds). Atom positions for the U, Na, O1, O2, O3, O4, O5, O7, O8, N1, N2, and N3 cores were superimposed to prepare this image. The superposition deviation of the two U atoms is 0.032 Å and of the two Na atoms is 0.049 Å, with the overall superposition deviation being 0.0855 Å for the aforementioned list of superimposed atoms.

Table S15. Comparison of R_1 values and selected bond lengths, interatomic distances, root mean square deviations (ω), and displacements of U and Na atoms from defined planes (ψ) in the structures of the [UO₂,Na] complex of L⁵.

Compound	L ⁵ UO ₂ Na	L ⁵ UO ₂ Na'	L ⁵ UO ₂ Na-DCE	L ⁵ UO ₂ Na-MeCN
Structure Code	q50k	v16f	q49k	q56k
R_1 (%)	3.92%	3.35%	3.83%	2.27%
U•••M (Å)	3.605(2)	3.602(2)	3.584(3)	3.574(1)
O1•••O2 (Å)	2.945(6)	2.931(6)	2.992(6)	2.943(3)
U–O7_{oxo} (Å)	1.761(5)	1.789(5)	1.779(5)	1.779(3)
U–O8_{oxo} (Å)	1.770(4)	1.791(4)	1.780(5)	1.783(3)
U–O_{oxo} (avg) (Å) ^a	1.766(5)	1.790(5)	1.780(5)	1.781(3)
U–O1_{phenoxide} (Å)	2.258(5)	2.263(4)	2.281(4)	2.258(2)
U–O2_{phenoxide} (Å)	2.272(4)	2.252(5)	2.276(5)	2.268(2)
U–O_{phenoxide} (avg) (Å) ^a	2.265(5)	2.258(5)	2.279(5)	2.263(2)
U–N1_{imine} (Å)	2.543(6)	2.541(6)	2.542(6)	2.588(3)
U–N2_{imine} (Å)	2.544(6)	2.536(6)	2.545(5)	2.542(3)
U–N_{imine} (avg) (Å) ^a	2.544(6)	2.539(6)	2.544(6)	2.565(3)
Na–O1_{phenoxide} (Å)	2.403(5)	2.440(5)	2.411(5)	2.384(3)
Na–O2_{phenoxide} (Å)	2.444(4)	2.399(5)	2.411(5)	2.426(3)
Na–O_{phenoxide} (avg) (Å) ^a	2.424(5)	2.420(5)	2.411(5)	2.405(3)
ω_{crown} (Å) ^b	0.366	0.339	0.025	0.327
ω_{salben} (Å) ^c	0.112	0.106	0.100	0.106
ψ_{U} (Å) ^d	0.032	0.035	0.023	0.008
ψ_{M} (Å) ^e	0.838	0.834	0.791	0.799

(a) Defined as the average interatomic distance between the noted metal and the relevant oxygen/nitrogen atoms. Stated estimated standard deviations (e.s.d.'s) on distances were taken as the largest of the individual values in the refined data for the independent bond distance. (b) Defined as the root mean square deviation (RMSD) of the positions of crown atoms O1, O2, O3, O4, and O5 from the mean plane of their positions. (c) Defined as the root mean square deviation (RMSD) of O1, O2, N1, N2, and N3 from the mean plane of their positions. (d) Absolute value of the distance between U and the mean plane of O1, O2, N1, N2, and N3. (e) Absolute value of the distance between M and the mean plane of O1, O2, O3, O4, and O5. Atom labels are consistent with those given in the raw crystallographic data.

Special Refinement Details for L^5UO_2Li (ak2133c)

The structure of ak2133c appears to reveal 56/44(1) disorder of the atoms to bonded to N3. In actuality, this represents two distinct isomers of the complex that have co-crystallized in the same volume of the unit cell. Simple rotation about any of the N3 bonds would not invert N3; a bond would have to be broken to interconvert the isomers. The bond lengths for the two co-crystallized isomers were restrained to have nearly idealized geometry by requiring them to be appropriate multiples of the $C(sp^3)-C(sp^3)$ bond length. This length was included in the refinement as a free variable that refined to a final value of 1.535(2) Å. This is quite reasonable when compared to the expected $C(sp^3)-C(sp^3)$ bond length of 1.513 Å.¹⁹

The inner-sphere triflate counteranion is 82/18(1) is also disordered with two orientations about the Li-O11 bond. The bond lengths and angles for the disordered triflate were restrained to have nearly idealized geometry by requiring them to be appropriate multiples of the S-O bond length. This length was included in the refinement as a free variable that refined to final value of 1.433(2) Å. This is quite reasonable when compared to the expected S-O bond length of 1.472 Å.¹⁹ In order to successfully model the triflate disorder, stringent isotropic restraints were applied to the displacement parameters of O11B, O12B, O13B, F11B, F12B, and F13B, as well as F12A, F13A, and C24A. Stringent similarity restraints were also applied to O13A and O13B.

One molecule of co-crystallized acetonitrile was found in a fully occupied site in the outer coordination sphere.

The structures of L^5UO_2Li (ak2133c) and $L^5UO_2Na-MeCN$ (q56k) are nearly isomorphous (see Tables S20 and S21). The structures are *only nearly* isomorphous, as they differ in terms of both the ratio of isomeric orientations about N3 (56/44 for ak2133c vs. 67/33 for q56k) and the ratio of disordered atoms for the triflate counteranion in each structure (82/18 for ak2133c vs. 91/9 for q56k).

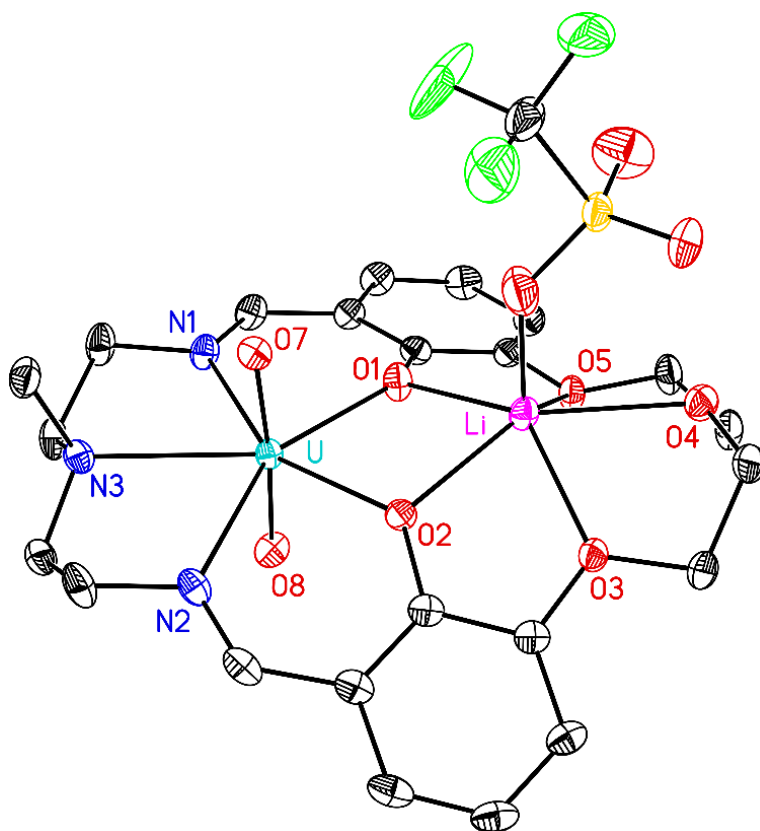


Figure S186. Solid-state structure from XRD of the major co-crystallized isomer of L^5UO_2Li . All H-atoms, atoms associated with the minor co-crystallized isomer, and a co-crystallized acetonitrile molecule are omitted for clarity. Displacement ellipsoids are shown at the 50% probability level.

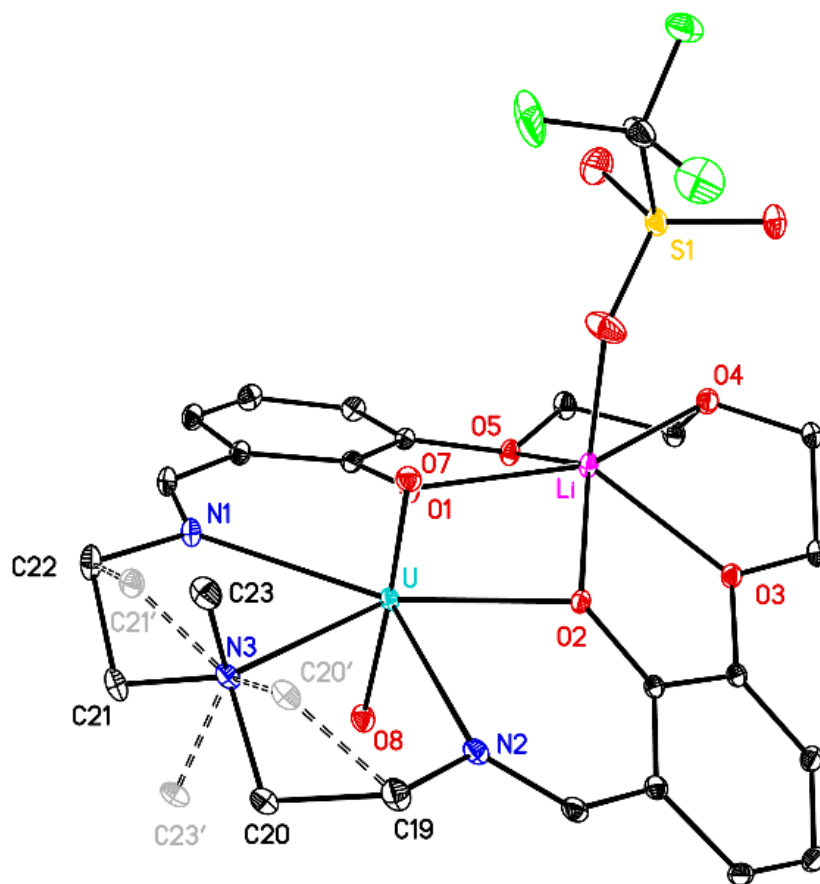


Figure S187. Solid-state structure from XRD of L^5UO_2Li . The presence of the two co-crystallized isomers could be represented as 56/44 disorder for the atoms bonded to the amine nitrogen. Solid bonds are used for the major (56%) isomer and dashed bonds for the minor isomer. Atoms C20, C21, and C23 are not common to the individual isomers. All H-atoms, a co-crystallized acetonitrile molecule, and disordered atoms associated with the triflate anion are omitted for clarity. Displacement ellipsoids are shown at the 20% probability level.

Full Solid-state Asymmetric Unit of L^5UO_2Li (ak2133c)

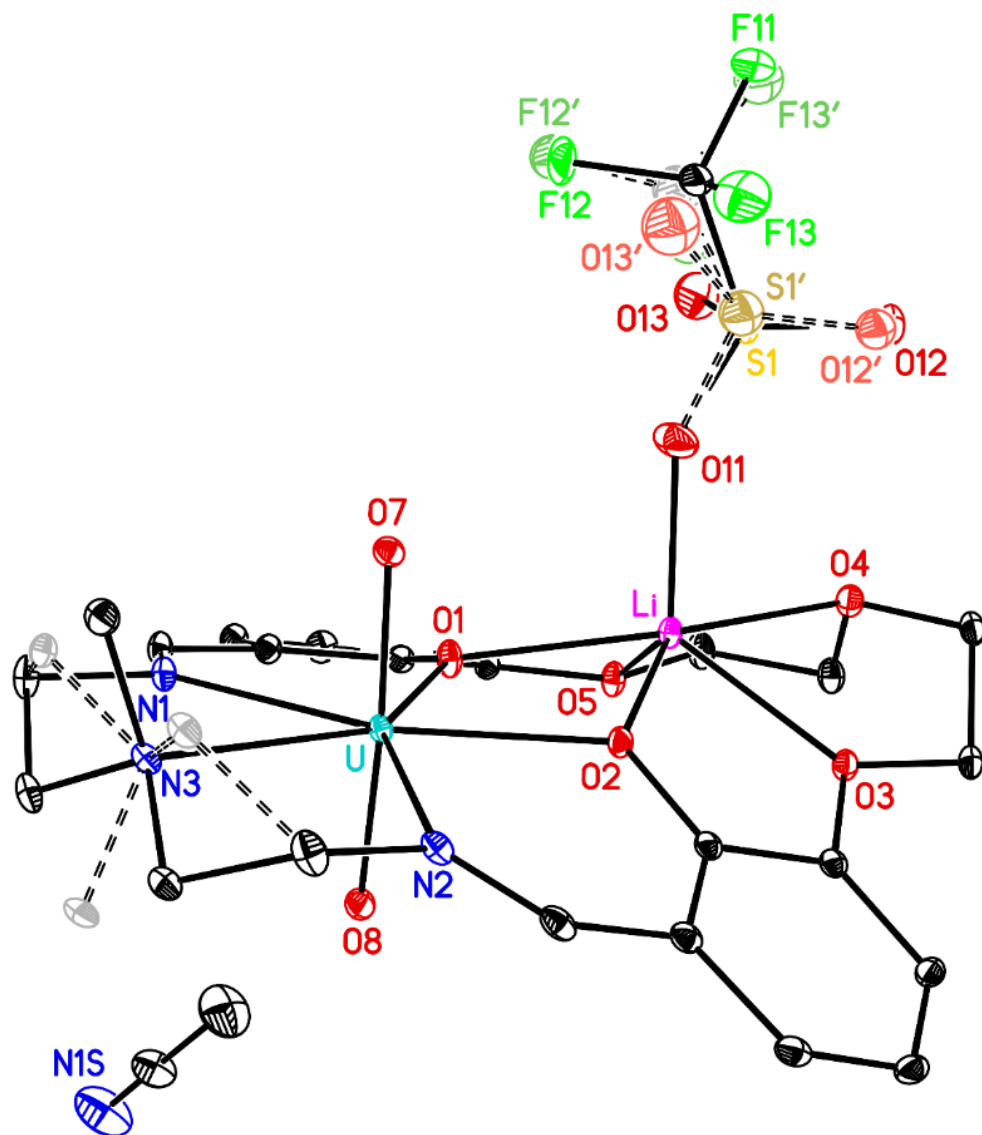


Figure S188. Full solid-state asymmetric unit for L^5UO_2Li showing the 56/44 apparent disorder for the atoms bonded to amine nitrogen N3, the 82/18 disorder for the inner-sphere triflate counteranion, and the co-crystallized outer-sphere acetonitrile molecule. Solid bonds are shown for the major isomer of the main molecule as well as the major orientation of the triflate. Dashed bonds are shown for the minor isomer of the main molecule and the minor orientation of the triflate. All H-atoms are omitted for clarity. Displacement ellipsoids are shown at the 20% probability level. The distance from S1 to S1' is 0.876 Å.

Special Refinement Details for L^6UO_2Li (ak2152c)

The solid-state structure of ak2152c appears to display 74/26(1) disorder for the atoms bonded to N3. In reality, however, the structure reveals the presence of a dimerized structure about a crystallographic inversion center composed of two individual heterobimetallic species. The aforementioned disorder ratio could represent two isomers of the dimeric (tetrametallic) species; one has both methyl groups (C24) oriented toward O7 and the other has both methyl groups oriented toward O8. Because of the ratio, if the only disorder is derived from packing effects rather than disorder about the inversion center, one might infer that these are only two possible dimers that can exist. This is notable because the isomers would presumably exist in solution and would be unique compounds. A third possible isomer would have the methyl groups pointed in the same direction, one towards O7 and one towards O8; we note however that this third species could pack like the other two isomers, and if this were the case, then the detected disorder pattern would be representative of all three isomers present in the solid state. However, the structure would no longer have rigorous inversion symmetry if that were the case.

The bond lengths for the apparently disordered atoms about N3 were restrained to have nearly idealized geometry by requiring them to be appropriate multiples of the $C(sp^3)-C(sp^3)$ bond length. This length was included in the refinement as a free variable that refined to a final value of 1.511(5) Å. This is quite reasonable when compared to the expected $C(sp^3)-C(sp^3)$ bond length of 1.513 Å.¹⁹ The carbon atoms bonded to N3 in the minor co-crystallized isomer were incorporated into the model with isotropic displacement parameters that were allowed to vary in refinement cycles.

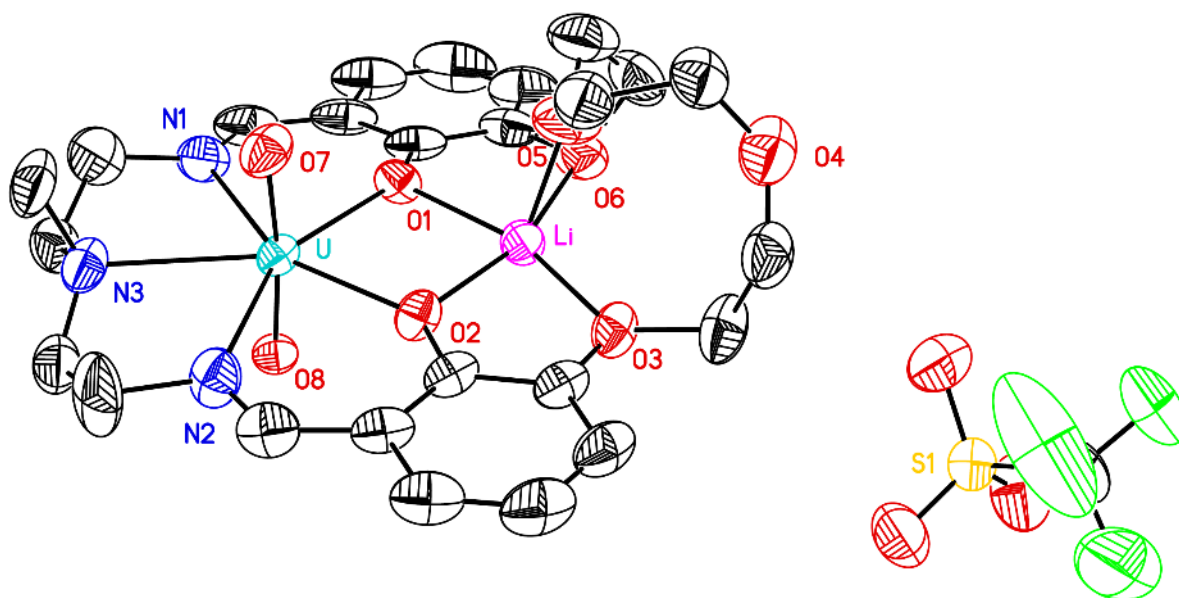


Figure S189. Solid-state structure from XRD of the major co-crystallized isomer of L^6UO_2Li . All H-atoms and atoms associated with the minor co-crystallized isomer are omitted for clarity. Displacement ellipsoids are shown at the 50% probability level.

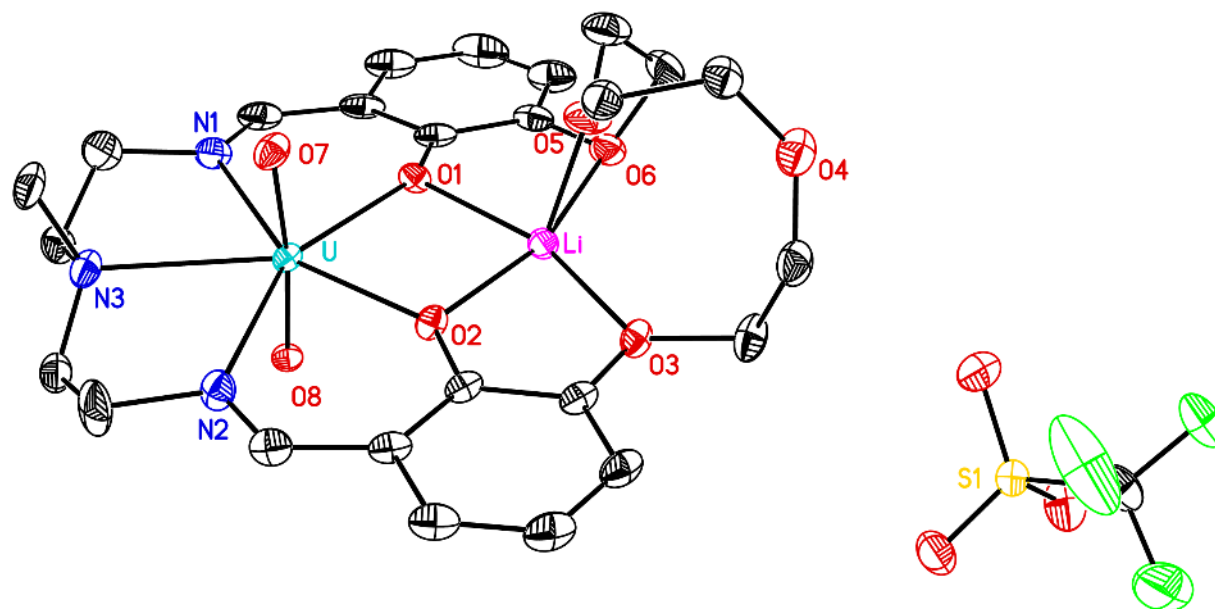


Figure S190. Solid-state structure from XRD of the major co-crystallized isomer of L^6UO_2Li . All H-atoms and atoms associated with the minor co-crystallized isomer are omitted for clarity. Displacement ellipsoids are shown at the 20% probability level.

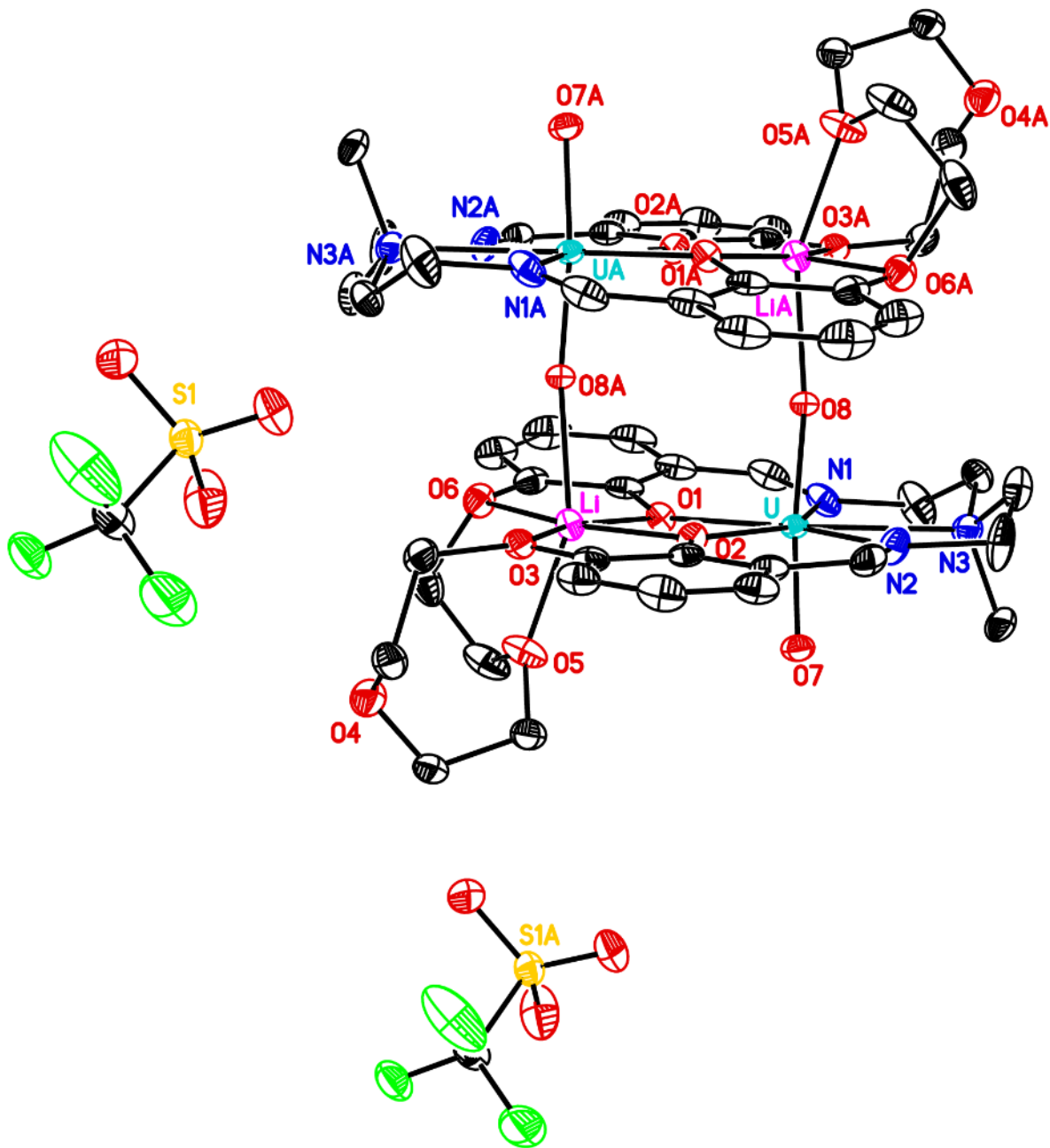


Figure S191. Image of the solid-state structure from XRD of the L^6UO_2Li dimer generated by a rigorous crystallographic inversion center as well as two nearby outer-sphere triflate counteranions. All H-atoms and atoms associated with the minor isomer(s) are omitted for clarity. Displacement ellipsoids are shown at the 20% probability level.

Full Solid-state Asymmetric Unit of L^6UO_2Li (ak2152c)

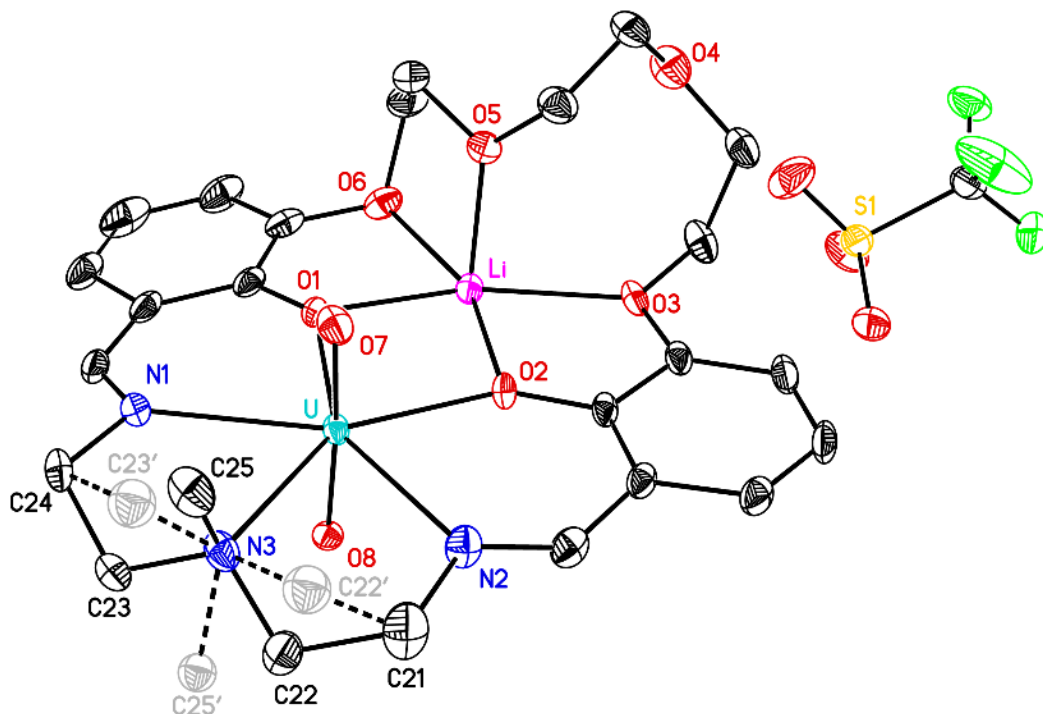


Figure S192. Full solid-state asymmetric unit for L^6UO_2Li showing 74/26 apparent disorder for the atoms bonded to amine nitrogen N3. Solid bonds are used for the atoms in the major co-crystallized isomer (74%) and dashed bonds are shown for atoms associated with only the minor co-crystallized isomer (26%). All H-atoms are omitted for clarity. Displacement ellipsoids are shown at the 20% probability level. Atoms associated with the minor isomer are shown with a lighter shade.

Special Refinement Details for L^5UO_2Ca (ak2153g)

The structure of ak2153g appears to reveal 71/29(1) disorder of the atoms to bonded to N3. In actuality, this represents two distinct isomers of the complex that have co-crystallized in the same volume of the unit cell. Simple rotation about any of the N3 bonds would not invert N3; a bond would have to be broken to interconvert the isomers. Carbon atoms bonded to N3 in the minor co-crystallized isomer were incorporated into the model with isotropic thermal parameters that were allowed to vary in refinement cycles. Additionally, select atoms in the crown ether linkage were found to be 50/50(1) disordered with two alternate orientations for atoms O3, O4, and C8 through C17. The bond lengths in the apparently disordered region of N3 and also in the disordered region of the crown ether linkage were restrained to have nearly idealized geometry by requiring them to be appropriate multiples of the $C(sp^3)-C(sp^3)$ bond length. This length was included in the refinement as a free variable that refined to a final value of 1.523(1) Å. This is quite reasonable when compared to the expected $C(sp^3)-C(sp^3)$ bond length of 1.513 Å.¹⁹

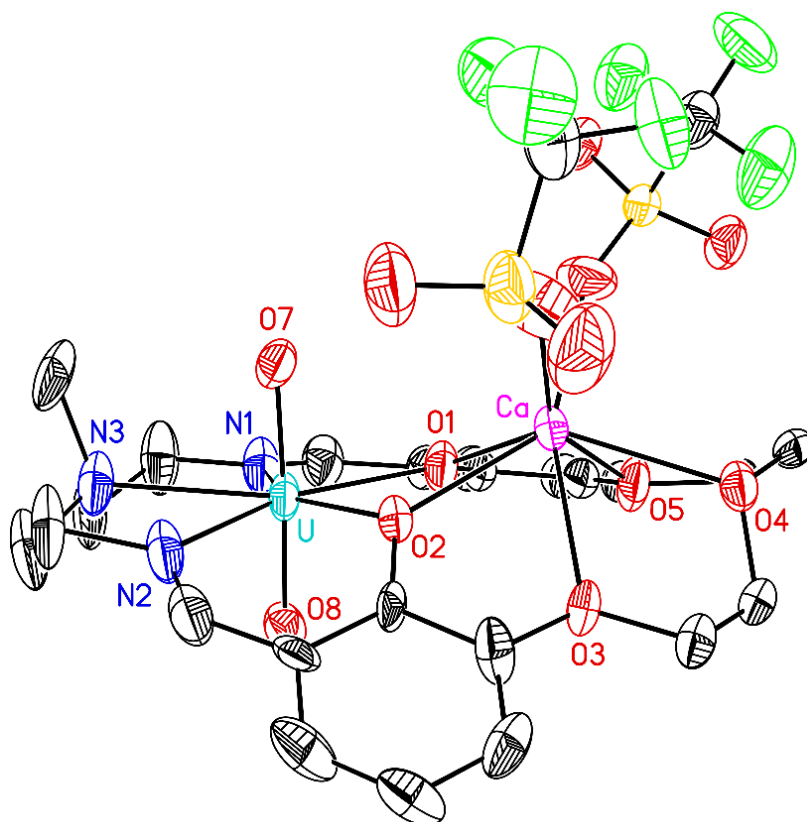


Figure S193. Solid-state structure from XRD of the major co-crystallized isomer of L^5UO_2Ca . All H-atoms and atoms associated with the minor isomer/orientation are omitted for clarity. Displacement ellipsoids are shown at the 50% probability level.

Full Solid-state Asymmetric Unit of L^6UO_2Ca (ak2153g)

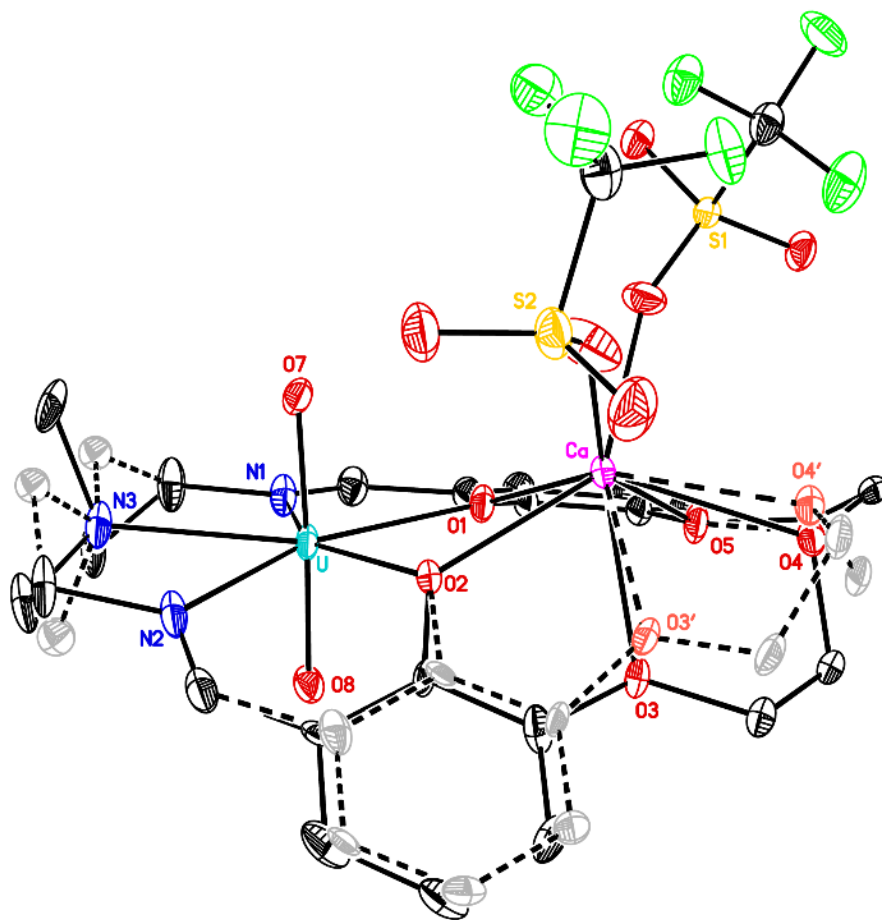


Figure S194. Full solid-state asymmetric unit for L^5UO_2Ca showing 71/29 apparent disorder for the atoms bonded to amine nitrogen N3 and 50/50 disorder for select atoms in the crown-ether-like site and one phenyl ring of the Schiff-base site. The different disorder ratios would seem to indicate that different packing considerations exist for the amine and polyether ends of the molecule and both isomers would presumably have a 50/50 preference for the placement of the polyether chain and one phenyl ring. Interestingly, this is the only complex in the series described in this report that displays the additional disorder in the polyether portion of the molecule. All H-atoms are omitted for clarity. Displacement ellipsoids are shown at the 20% probability level. Atoms shown with a lighter shade on the amine end are associated strictly with the minor isomer; other light shaded atoms are presumably associated with both isomers with respect to the 50/50 disorder in the polyether/phenyl moiety.

Special Refinement Details for L^5UO_2Ca' (ak2153n-No33).

The complex crystallizes as orange block-like crystals. There are four molecules of the mixed-metal uranium-calcium complex in the unit cell of the crystal, which can be assigned to the primitive, non-centrosymmetric, orthorhombic space group $Pna2_1$. The data crystal was found to be a racemic twin through a BASF refinement that converged to a final value of ca. 0.52(1).

The pseudo- C_s -symmetric L^5UO_2Ca' orients itself in the unit cell with eight atoms positioned near a potentially rigorous crystallographic mirror plane at $(x, 0.25, z)$. This caused an initial structure solution to be performed in the centrosymmetric space group $Pnma/Pnam$. This structure refined to a quite acceptable final R_1 value of 5.42%. The resulting structure appeared to have significant disorder across a mirror plane, suggesting that the noted crystallographic mirror plane may not have been rigorous. Structure solution was then performed in space group $Pna2_1$ (No. 33); this resulted in a nearly fully ordered structure that refined to a better R_1 value of 3.18% with the commonly observed apparent disorder only about the N3 amine nitrogen in the ligand backbone.

Similar to the other structures in this report, in actuality the apparent 61/39(1) disorder about N3 represents two distinct isomers of the complex that have co-crystallized in the same volume of the unit cell. Simple rotation about any of the N3 bonds would not invert N3; a bond would have to be broken to interconvert the isomers. In the case of ak2153n-No33, the occupancy factors of atoms in the individual isomers were found to be 61/39. The bond lengths in the apparently disordered region of N3 were restrained to have nearly idealized geometry by requiring them to be appropriate multiples of the $C(sp^3)-C(sp^3)$ bond length. This length was included in the refinement as a free variable that refined to a final value of 1.520(6) Å. This is quite reasonable when compared to the expected $C(sp^3)-C(sp^3)$ bond length of 1.513 Å.¹⁹

It is noteworthy that the atoms U1, Ca1, N3, C23, C23', O4, O6, and O7 have z -coordinates that are very near to 0.25; these atoms would essentially be located on the crystallographic mirror plane if the correct space group were the centrosymmetric $Pnma/Pnam$. However, as a result of this obvious pseudo-symmetry, high correlations exist between the parameters associated with atoms related by the pseudo-mirror. Despite this inherent feature of the structure, anisotropic displacement parameters were successfully included for all non-hydrogen atoms in the structure with moderate isotropic restraints needed for the displacement parameters of C1–C7 and C12–C18 that are related by the crystallographic pseudo-mirror plane. Moderate isotropic restraint was also applied to one oxygen atom (O23) associated with a triflate and atoms C20, C20', C21, C21', C22, C22', C23, and C23' in the apparently disordered region about N3.

The fact that this Ca^{2+} -adduct structure does not exhibit the 50/50 disorder of the polyether end of the molecule as was found for ak2153g is an indication that crystal packing due to different crystallization solvent conditions is the factor causing the 50/50 disorder in that case. The present structure of the Ca^{2+} -adduct (ak2153n-No33) thus can be concluded to not show the noted disorder pattern as a consequence of unique packing effects in the individual and unique structure.

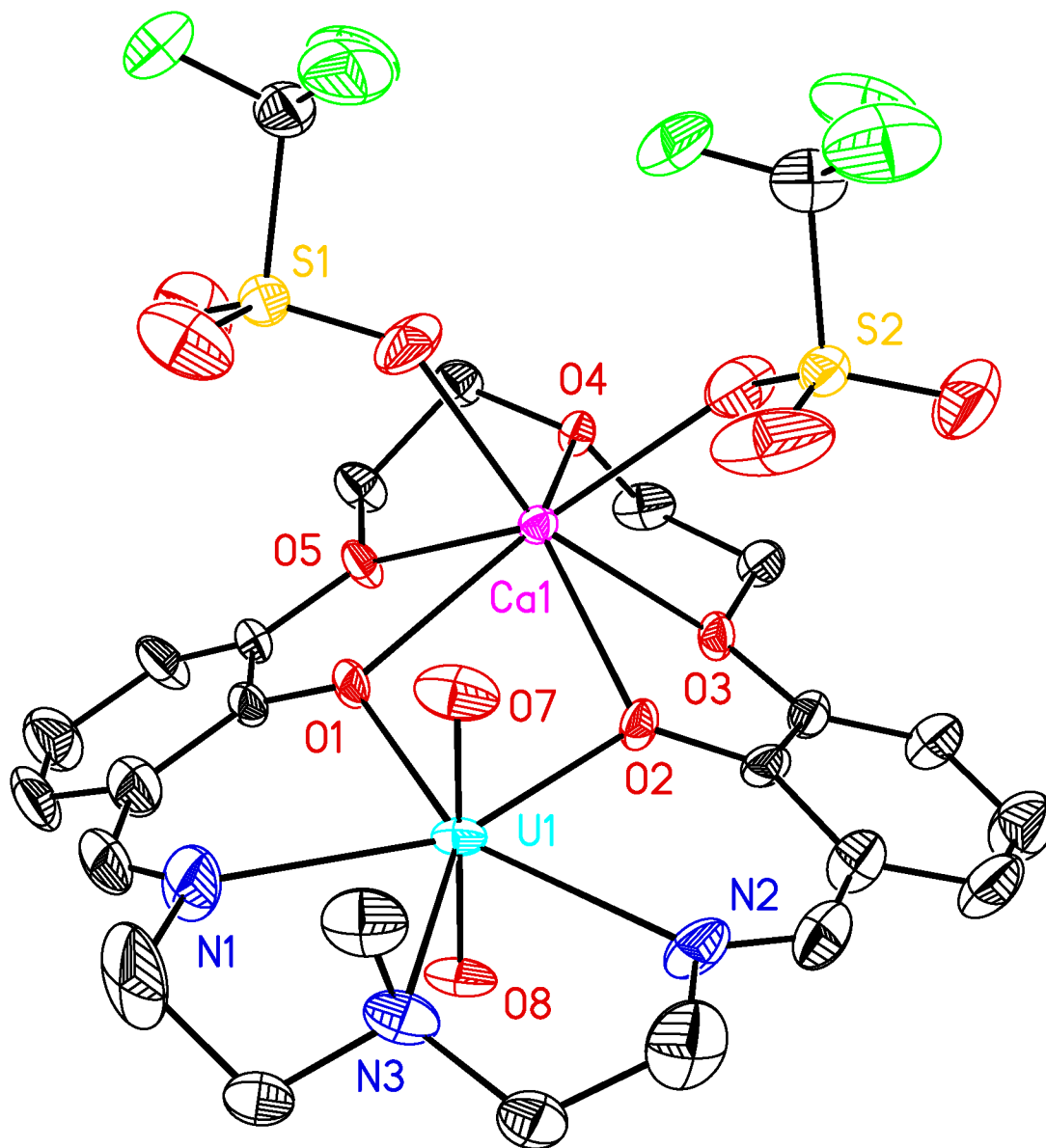


Figure S195. Solid-state structure from XRD of the major isomer of L^5UO_2Ca' . All H-atoms and atoms associated with the minor co-crystallized isomer are omitted for clarity. Displacement ellipsoids are shown at the 50% probability level.

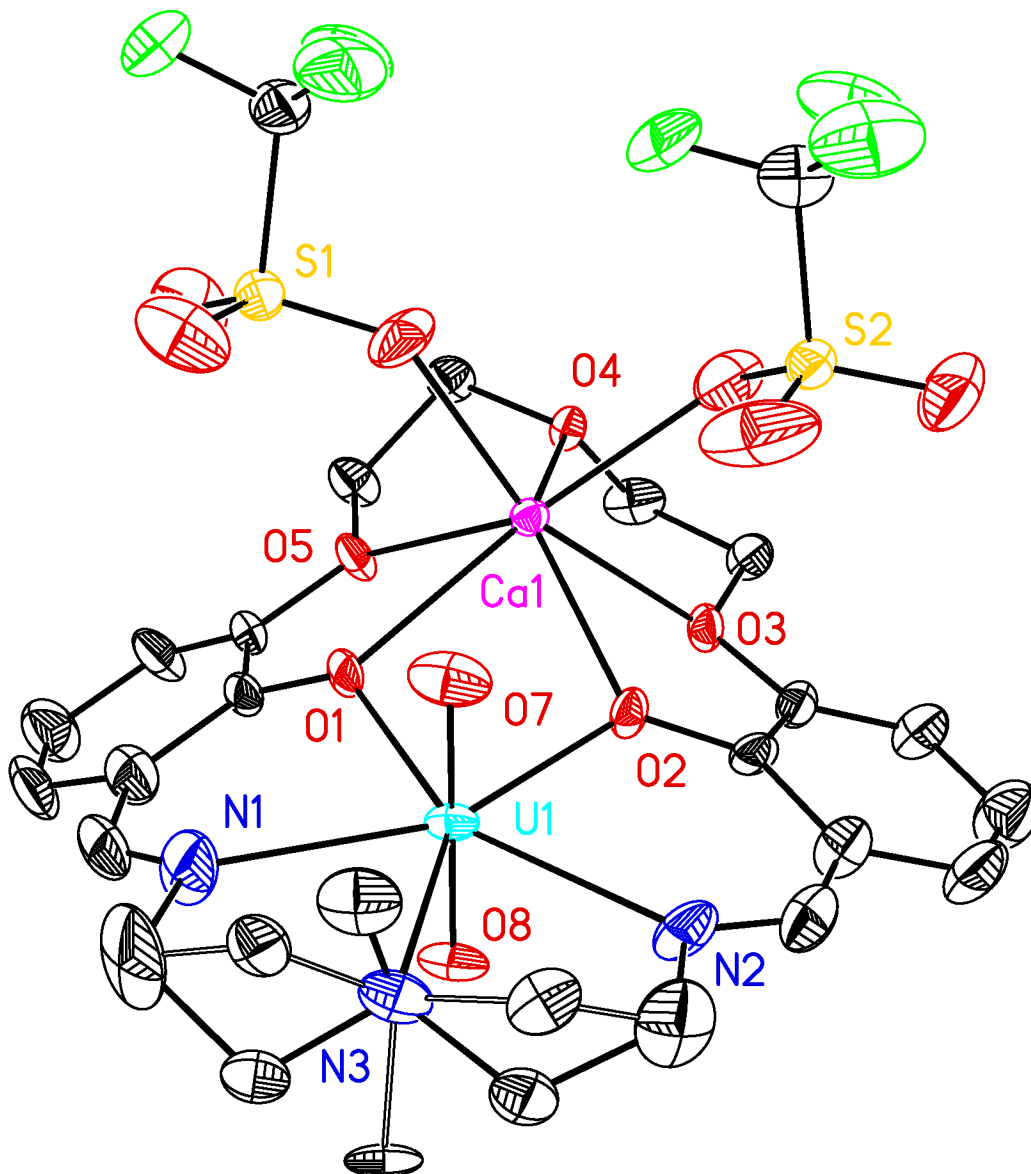


Figure S196. Full solid-state asymmetric unit of L^5UO_2Ca' . Solid bonds are shown for the major isomer and hollow bonds are shown for the atoms associated with the minor isomer. All H-atoms are omitted for clarity. Displacement ellipsoids are shown at the 50% probability level.

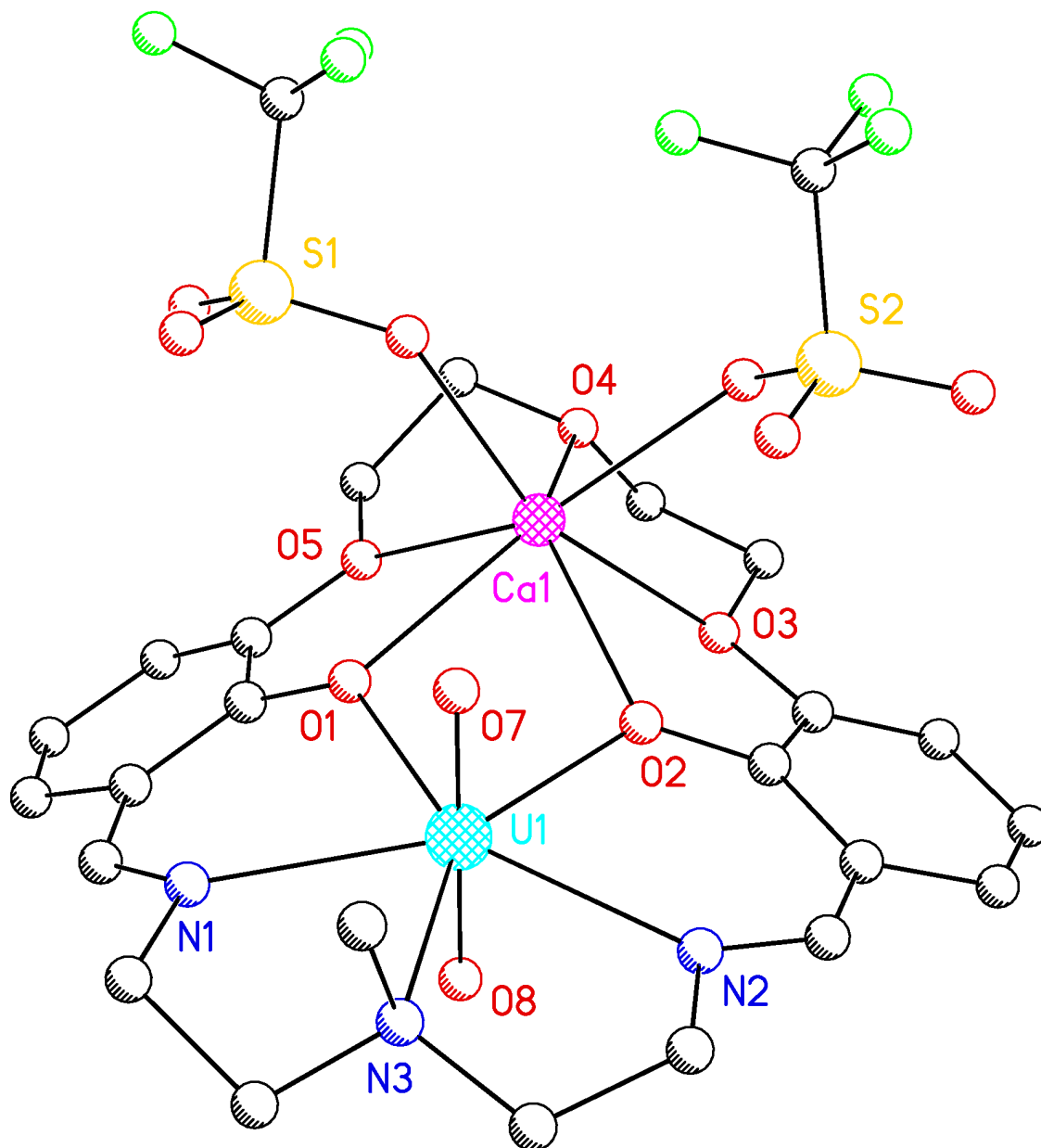


Figure S197. Ball-and-stick representation of L^5UO_2Ca' . All H-atoms and atoms associated with the minor co-crystallized isomer are omitted for clarity.

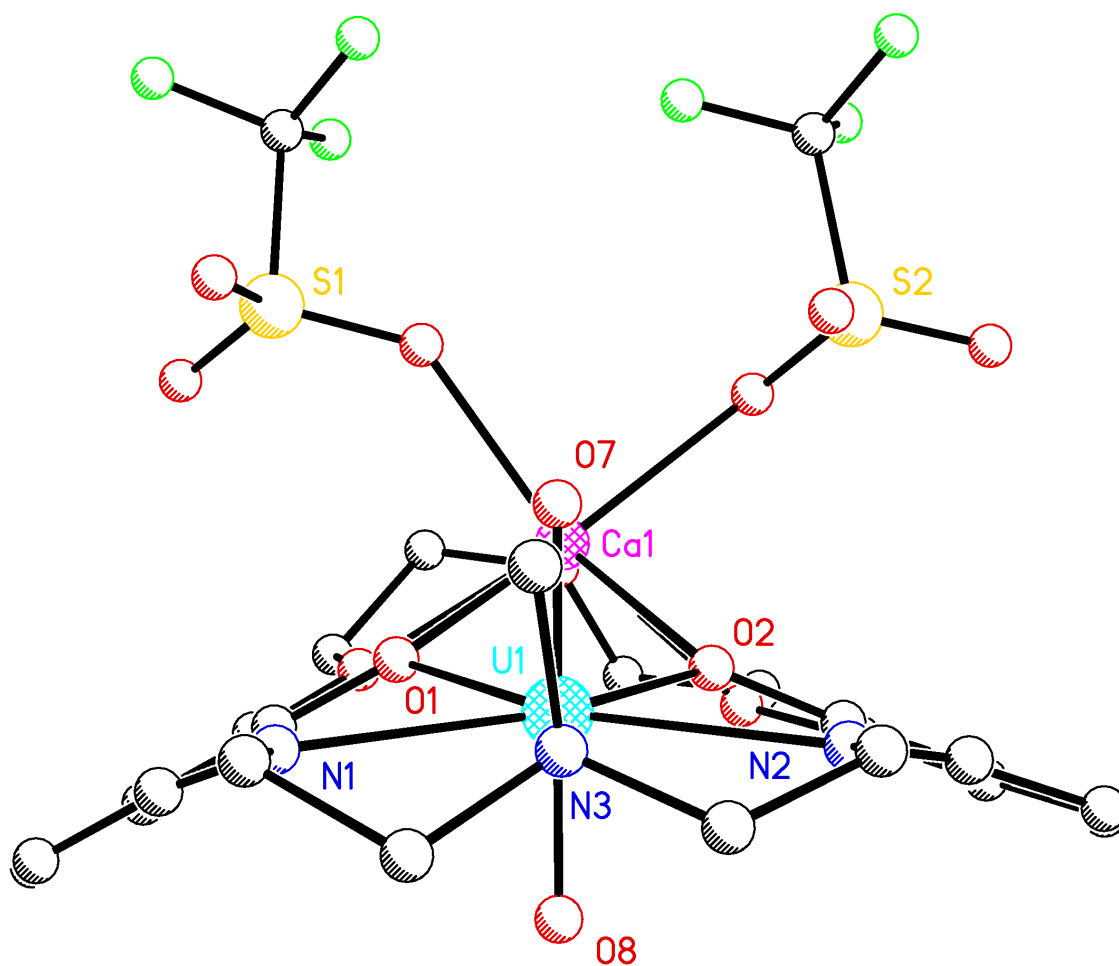


Figure S198. Solid-state structure from XRD of the major isomer of L^5UO_2Ca' showing an end-to-end view to highlight the pseudo-mirror-symmetric nature of the molecule. All H-atoms and atoms associated with the minor co-crystallized isomer are omitted for clarity. The following atoms have z -coordinates that are very near to 0.25, which would be the crystallographic mirror plane in the corresponding centrosymmetric space group: U1, Ca1, N3, C23, C23', O4, O6, and O7.

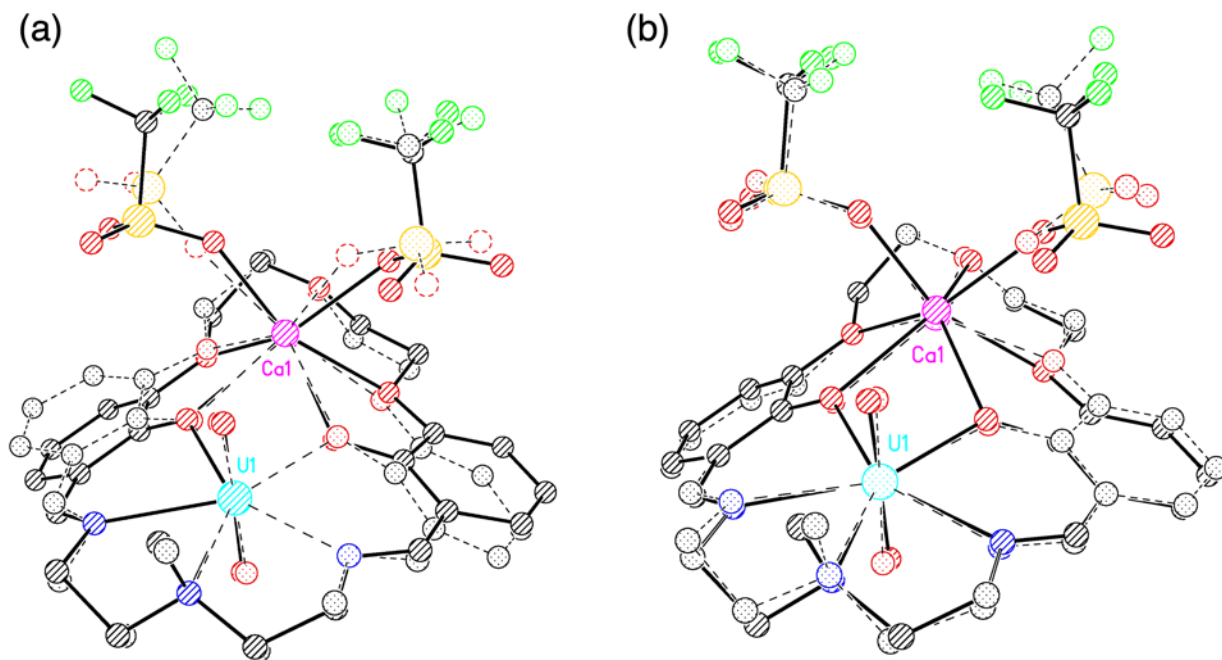


Figure S199. Superimposed views of the solid-state structures of the major isomers of L^5UO_2Ca' (ak2153n-No33; solid bonds) and L^5UO_2Ca (ak2153g; dashed bonds). Atom positions for the U, Ca, O1, O2, O3, O4, O5, O7, O8, N1, N2, and N3 coordination cores were superimposed to prepare these images. In image (a), the first orientation of the 50/50 disordered polyether moiety from ak2153g was used to prepare the figure; the deviation of the superimposed positions of the two U atoms is 0.029 Å and of the superimposed positions of the two Ca atoms is 0.088 Å, with an overall deviation of 0.111 Å for the noted list of atoms. In image (b), the second orientation of the 50/50 disordered polyether moiety from ak2153g was used to prepare the figure; the deviation of the superimposed positions of the two U atoms is 0.009 Å and of the superimposed positions of the two Ca atoms is 0.140 Å, with an overall deviation of 0.1050 Å for the noted list of atoms.

The fact that ak2153n-No33 and the second orientation of ak315g (image b) have virtually identical overlays would seem to indicate that this might be the preferred structure and that otherwise minor variations in the crystallization conditions induce the 50/50 disorder for the polyether portion of the macrocycle for both isomers of ak2153g. This 50/50 disorder is independent of packing forces which favor xx/yy crystallization of both isomers.

Table S16. Comparison of R_1 values and selected bond lengths, interatomic distances, root mean square deviations (ω), and displacements of U and Ca atoms from planes (ψ) in the structures of the [UO₂,Ca] complexes of L⁵.

Compound	L ⁵ UO ₂ Ca	L ⁵ UO ₂ Ca'
Structure Code	ak2153g	ak2153n-No33
R_1 (%)	4.81%	3.18%
U•••M (Å)	3.690(1)	3.723(1)
O1•••O2 (Å)	2.818(7)	2.810(7)
U–O _{7oxo} (Å)	1.772(5)	1.767(4)
U–O _{8oxo} (Å)	1.776(5)	1.768(4)
U–O _{oxo} (avg) (Å) ^a	1.774(5)	1.768(4)
U–O _{1phenoxide} (Å)	2.303(4)	2.301(7)
U–O _{2phenoxide} (Å)	2.289(4)	2.293(7)
U–O _{phenoxide} (avg) (Å) ^a	2.297(4)	2.297(7)
U–N _{1imine} (Å)	2.520(6)	2.495(11)
U–N _{2imine} (Å)	2.514(6)	2.550(9)
U–N _{imine} (avg) (Å) ^a	2.517(6)	2.523(10)
Ca–O _{1phenoxide} (Å)	2.398(5)	2.471(7)
Ca–O _{2phenoxide} (Å)	2.419(4)	2.377(7)
Ca–O _{phenoxide} (avg) (Å) ^a	2.409(5)	2.424(7)
ω_{crown} (Å) ^b	0.332	0.349
ω_{salben} (Å) ^c	0.116	0.114
ψ_{U} (Å) ^d	0.017	0.032
ψ_{M} (Å) ^e	1.123	1.047

(a) Defined as the average interatomic distance between the noted metal and the relevant oxygen/nitrogen atoms. Stated estimated standard deviations (e.s.d.'s) on distances were taken as the largest of the individual values in the refined data for the independent bond distance. (b) Defined as the root mean square deviation (RMSD) of the positions of crown atoms O1, O2, O3, O4, and O5 from the mean plane of their positions. (c) Defined as the root mean square deviation (RMSD) of O1, O2, N1, N2, and N3 from the mean plane of their positions. (d) Absolute value of the distance between U and the mean plane of O1, O2, N1, N2, and N3. (e) Absolute value of the distance between M and the mean plane of O1, O2, O3, O4, and O5. Atom labels are consistent with those given in the raw crystallographic data for L⁵UO₂Ca.

Table S17. Comparison of U–O_{oxo} bond lengths across the series of UO₂²⁺ complexes.

Complex	U–O7	U–O8	U–O_{oxo} (avg., Å)^b
L⁵UO₂	1.772(4)	1.781(4)	1.777(4)
L⁶UO₂^a	1.783(8)	1.792(7)	1.788(8)
L⁵UO₂Na	1.761(5)	1.770(4)	1.766(5)
L⁵UO₂Na'	1.789(5)	1.791(5)	1.790(5)
L⁵UO₂Na-DCE	1.779(5)	1.780(5)	1.780(5)
L⁵UO₂Na-MeCN	1.779(3)	1.783(3)	1.781(3)
L⁶UO₂Na^a	1.782(5)	1.780(5)	1.781(5)
L⁵UO₂Li	1.778(1)	1.784(2)	1.781(2)
L⁶UO₂Li	1.782(4)	1.786(4)	1.784(4)
L⁵UO₂Ca	1.772(5)	1.776(5)	1.774(5)
L⁵UO₂Ca'	1.767(4)	1.768(4)	1.768(4)
L⁶UO₂Ca^a	1.795(4)	1.783(4)	1.789(4)

(a) Structural data taken from references 24 (CCDC 1960628), 25 (CCDC 1960628), 26 (CCDC 1960629), and 27 (CCDC 1960630). (b) Average of the U–O7 and U–O8 bond distances.

Table S18. Crystal and Refinement Data for **BaPenta** and **L⁵UO₂**.

	BaPenta (q55j)	L⁵UO₂ (q75k)
CCDC accession code	2344717	2344718
Empirical formula	C ₂₈ H ₃₉ N ₃ O ₉ F ₃ SBa _{0.5}	C ₂₅ H ₃₀ N ₄ O ₇ U
Formula weight	719.35	736.56
Temperature	200(2) K	200(2) K
Wavelength	1.54178	1.54178
Crystal system	Orthorhombic	Monoclinic
Space group	Pccn (No. 56)	P2 ₁ /c (No. 14)
<i>a</i>	20.6676(3) Å	10.3526(3) Å
<i>b</i>	23.1000(4) Å	13.0258(3) Å
<i>c</i>	27.4588(4) Å	19.7606(5) Å
<i>α</i>	90°	90°
<i>β</i>	90°	100.3600(10)°
<i>γ</i>	90°	90°
Volume	13109.4(4) Å ³	2621.29(12) Å ³
Z	16	4
Density (calculated)	1.458 g cm ⁻³	1.866 g cm ⁻³
Absorption coefficient	6.073 mm ⁻¹	17.867 mm ⁻¹
F(000)	5936.0	1424.0
Crystal size	0.19 × 0.06 × 0.05 mm ³	0.089 × 0.067 × 0.036 mm ³
Theta range	2.869 to 70.352°	4.085 to 70.183°
Index ranges	-25 ≤ h ≤ 24, -27 ≤ k ≤ 26, -33 ≤ l ≤ 23	-11 ≤ h ≤ 12, -15 ≤ k ≤ 15, -21 ≤ l ≤ 23
Reflections collected	84666	16635
Independent reflections	12311 [R _{int} = 0.0395, R _{sigma} = 0.0250]	4798 [R _{int} = 0.0510, R _{sigma} = 0.0489]
Completeness/θ_{max}	99.9%/66.000°	99.6%/66.000°
Absorption correction	Multi-scan	Multi-scan
Max./Min. Transmission	1.000 and 0.525	1.000 and 0.723
Refinement method	Full-matrix least-squares on F ²	Full-matrix least-squares on F ²
Data/restraints/parameters	12311/53/834	4798/128/409
Goodness-of-fit on F²	1.036	1.095
Final R indices [I > 2σ(I)]	R ₁ = 0.0438, wR ₂ = 0.1252	R ₁ = 0.0362, wR ₂ = 0.0887
R indices (all data)	R ₁ = 0.0544, wR ₂ = 0.1360	R ₁ = 0.0394, wR ₂ = 0.0917
Largest diff. peak & hole	1.11 and -0.71 e.Å ⁻³	2.13 and -2.32 e.Å ⁻³

Table S19. Crystal and Refinement Data for L⁵UO₂Na and L⁵UO₂Na'.

	L ⁵ UO ₂ Na (q50k)	L ⁵ UO ₂ Na' (v16f)
CCDC accession code	2344720	2344719
Empirical formula	C ₂₄ H ₂₇ F ₃ N ₃ O ₁₀ SNaU	C ₂₄ H ₂₇ F ₃ N ₃ O ₁₀ SNaU
Formula weight	867.56	867.56
Temperature	200(2) K	200(2) K
Wavelength	1.54178	1.54178
Crystal system	Monoclinic	Monoclinic
Space group	P2 ₁ /c (No. 14)	P2 ₁ /c (No. 14)
<i>a</i>	12.1266(4) Å	12.1206(4) Å
<i>b</i>	12.9389(4) Å	12.9470(4) Å
<i>c</i>	19.1605(6) Å	19.1487(6) Å
<i>α</i>	90°	90°
<i>β</i>	104.0830(10)°	104.1704(11)°
<i>γ</i>	90°	90°
Volume	2916.02(16) Å ³	2913.48(16) Å ³
Z	4	4
Density (calculated)	1.976 g cm ⁻³	1.978 g cm ⁻³
Absorption coefficient	17.193 mm ⁻¹	17.208 mm ⁻¹
F(000)	1672.0	1672.0
Crystal size	0.158 × 0.033 × 0.028 mm ³	0.025 × 0.080 × 0.085 mm ³
Theta range	3.758 to 70.180°	4.165 to 68.335°
Index ranges	-12 ≤ h ≤ 14, -12 ≤ k ≤ 14, -23 ≤ l ≤ 22	-14 ≤ h ≤ 14, -15 ≤ k ≤ 11, -20 ≤ l ≤ 22
Reflections collected	18416	16811
Independent reflections	5266 [R _{int} = 0.0598, R _{sigma} = 0.0582]	5185 [R _{int} = 0.0429, R _{sigma} = 0.0428]
Completeness/θ_{max}	97.7%/70.180°	99.0%/66.000°
Absorption correction	Numerical	Numerical
Max./Min. Transmission	1.000 and 0.368	1.000 and 0.279
Refinement method	Full-matrix least-squares on F ²	Full-matrix least-squares on F ²
Data/restraints/parameters	5266/0/418	5185/31/436
Goodness-of-fit on F²	1.048	1.042
Final R indices [I > 2σ(I)]	R ₁ = 0.0392, wR ₂ = 0.0981	R ₁ = 0.0335, wR ₂ = 0.0845
R indices (all data)	R ₁ = 0.0432, wR ₂ = 0.1019	R ₁ = 0.0382, wR ₂ = 0.0876
Largest diff. peak & hole	3.04 and -2.02 e.Å ⁻³	2.53 and -1.98 e.Å ⁻³

Table S20. Crystal and Refinement Data for L⁵UO₂Na-DCE and L⁵UO₂Na-MeCN.

	L ⁵ UO ₂ Na-DCE (q49k)	L ⁵ UO ₂ Na-MeCN (q56k)
CCDC accession code	2344721	2344722
Empirical formula	C ₂₆ H ₃₁ N ₃ O ₁₀ F ₃ SCl ₂ NaU	C ₂₆ H ₃₀ N ₄ O ₁₀ F ₃ SNaU
Formula weight	966.52	908.62
Temperature	200(2) K	200(2) K
Wavelength	1.54178	1.54178
Crystal system	Triclinic	Triclinic
Space group	P $\bar{1}$ (No. 2)	P $\bar{1}$ (No. 2)
<i>a</i>	10.2238(3) Å	9.7725(3) Å
<i>b</i>	12.1909(4) Å	12.1131(4) Å
<i>c</i>	13.9815(5) Å	14.1658(5) Å
<i>α</i>	99.7935(14)°	75.1951(11)°
<i>β</i>	98.0293(15)°	80.6655(12)°
<i>γ</i>	103.3418(13)°	73.5073(10)°
Volume	1641.52(9) Å ³	1547.22(9) Å ³
Z	2	2
Density (calculated)	1.955 g cm ⁻³	1.950 g cm ⁻³
Absorption coefficient	16.814 mm ⁻¹	16.248 mm ⁻¹
F(000)	936.0	880.0
Crystal size	0.146 × 0.04 × 0.025 mm ³	0.099 × 0.074 × 0.024 mm ³
Theta range	3.811 to 70.574°	3.242 to 70.062°
Index ranges	-11 ≤ h ≤ 12, -14 ≤ k ≤ 14, -14 ≤ l ≤ 16	-11 ≤ h ≤ 11, -14 ≤ k ≤ 14, -14 ≤ l ≤ 16
Reflections collected	20295	18109
Independent reflections	5758 [R _{int} = 0.0497, R _{sigma} = 0.0453]	5409 [R _{int} = 0.0296, R _{sigma} = 0.0283]
Completeness/θ_{max}	96.0%/66.000°	96.1%/66.000°
Absorption correction	Numerical	Numerical
Max./Min. Transmission	1.000 and 0.099	1.000 and 0.315
Refinement method	Full-matrix least-squares on F ²	Full-matrix least-squares on F ²
Data/restraints/parameters	5758/52/455	5409/44/472
Goodness-of-fit on F²	1.047	1.080
Final R indices [I > 2σ(I)]	R ₁ = 0.0371, wR ₂ = 0.0960	R ₁ = 0.0227, wR ₂ = 0.0564
R indices (all data)	R ₁ = 0.0388, wR ₂ = 0.0980	R ₁ = 0.0232, wR ₂ = 0.0568
Largest diff. peak & hole	1.86 and -1.87 e.Å ⁻³	1.83 and -1.51 e.Å ⁻³

Table S21. Crystal and Refinement Data for L⁵UO₂Li and L⁶UO₂Li.

	L ⁵ UO ₂ Li (ak2133c)	L ⁶ UO ₂ Li (ak2152c)
CCDC accession code	2344723	2344724
Empirical formula	C ₂₆ H ₃₀ F ₃ LiN ₄ O ₁₀ SU	C ₂₆ H ₃₁ F ₃ LiN ₃ O ₁₁ SU
Formula weight	892.57	895.57
Temperature	120(2) K	120(2) K
Wavelength	0.71073	1.54178
Crystal system	Triclinic	Monoclinic
Space group	P $\bar{1}$ (No. 2)	P2 ₁ /c (No. 14)
<i>a</i>	9.8299(11) Å	12.7315(5) Å
<i>b</i>	12.1237(14) Å	10.6287(4) Å
<i>c</i>	13.9454(16) Å	22.1874(10) Å
<i>α</i>	75.861(2)°	90°
<i>β</i>	78.916(2)°	98.1210(10)°
<i>γ</i>	70.940(2)°	90°
Volume	1511.7(3) Å ³	2972.3(2) Å ³
Z	2	4
Density (calculated)	1.961 g cm ⁻³	2.001 g cm ⁻³
Absorption coefficient	5.518 mm ⁻¹	16.780 mm ⁻¹
F(000)	864.0	1736.0
Crystal size	0.272 × 0.149 × 0.053 mm ³	0.234 × 0.098 × 0.041 mm ³
Theta range	1.517 to 28.313°	3.507 to 69.872°
Index ranges	-13 ≤ h ≤ 13, -16 ≤ k ≤ 16, -18 ≤ l ≤ 18	-15 ≤ h ≤ 15, -12 ≤ k ≤ 12, -26 ≤ l ≤ 26
Reflections collected	35001	88628
Independent reflections	7504 [R _{int} = 0.0223, R _{sigma} = 0.0177]	5581 [R _{int} = 0.0520, R _{sigma} = 0.0205]
Completeness/θ_{max}	100.0%/28.313°	100.0%/69.872°
Absorption correction	Numerical	Numerical
Max./Min. Transmission	1.000 and 0.442	1.000 and 0.420
Refinement method	Full-matrix least-squares on F ²	Full-matrix least-squares on F ²
Data/restraints/parameters	7504/66/486	5581/22/431
Goodness-of-fit on F²	1.075	1.048
Final R indices [I > 2σ(I)]	R ₁ = 0.0172, wR ₂ = 0.0395	R ₁ = 0.0347, wR ₂ = 0.0904
R indices (all data)	R ₁ = 0.0195, wR ₂ = 0.0402	R ₁ = 0.0362, wR ₂ = 0.0917
Largest diff. peak & hole	1.35 and -0.8 e.Å ⁻³	4.03 and -1.03 e.Å ⁻³

Table S22. Crystal and Refinement Data for L⁵UO₂Ca and L⁵UO₂Ca'.

	L ⁵ UO ₂ Ca (ak2153g)	L ⁵ UO ₂ Ca' (ak2153n-No33)
CCDC accession code	2344725	2344726
Empirical formula	C ₂₅ H ₂₇ N ₃ O ₁₃ F ₆ S ₂ CaU	C ₂₅ H ₂₇ N ₃ O ₁₃ F ₆ S ₂ CaU
Formula weight	1033.72	1033.72
Temperature	120(2) K	120(2) K
Wavelength	0.71073	0.71073
Crystal system	Monoclinic	Orthorhombic
Space group	P2 ₁ /c (No. 14)	Pna2 ₁ (No. 33)
<i>a</i>	12.2866(8) Å	15.7347(10) Å
<i>b</i>	18.0256(12) Å	10.8087(7) Å
<i>c</i>	15.5245(10) Å	19.3100(12) Å
<i>α</i>	90°	90°
<i>β</i>	106.773(2)°	90°
<i>γ</i>	90°	90°
Volume	3292.0(4) Å ³	3284.1(4) Å ³
Z	4	4
Density (calculated)	2.086 g cm ⁻³	2.091 g cm ⁻³
Absorption coefficient	5.316 mm ⁻¹	5.329 mm ⁻¹
F(000)	2000.0	2000.0
Crystal size	0.21 × 0.151 × 0.12 mm ³	0.164 × 0.128 × 0.074 mm ³
Theta range	1.730 to 28.325°	2.159 to 28.314°
Index ranges	-16 ≤ h ≤ 16, -24 ≤ k ≤ 21, -20 ≤ l ≤ 20	-20 ≤ h ≤ 20, -14 ≤ k ≤ 14, -25 ≤ l ≤ 25
Reflections collected	85825	87657
Independent reflections	8210 [R _{int} = 0.0581, R _{sigma} = 0.0315]	8182 [R _{int} = 0.0449, R _{sigma} = 0.0222]
Completeness/θ_{max}	100.0%/25.242°	99.9%/28.314°
Absorption correction	Numerical	Multi-scan
Max./Min. Transmission	1.000 and 0.638	1.000 and 0.865
Refinement method	Full-matrix least-squares on F ²	Full-matrix least-squares on F ²
Data/restraints/parameters	8210/78/561	8182/149/492
Goodness-of-fit on F²	1.077	1.094
Final R indices [I > 2σ(I)]	R ₁ = 0.0481, wR ₂ = 0.1042	R ₁ = 0.0318, wR ₂ = 0.0659
R indices (all data)	R ₁ = 0.0652, wR ₂ = 0.1115	R ₁ = 0.0361, wR ₂ = 0.0675
Largest diff. peak & hole	3.74 and -1.68 e.Å ⁻³	2.51 and -1.56 e.Å ⁻³

References

- (1) Fulmer, G. R.; Miller, A. J. M.; Sherden, N. H.; Gottlieb, H. E.; Nudelman, A.; Stoltz, B. M.; Bercaw, J. E.; Goldberg, K. I. NMR Chemical Shifts of Trace Impurities: Common Laboratory Solvents, Organics, and Gases in Deuterated Solvents Relevant to the Organometallic Chemist. *Organometallics* **2010**, *29*, 2176-2179.
- (2) Harris, R.K.; Becker, E.D.; Cabral de Menezes, S.M.; Goodfellow, R.; Granger, P. NMR nomenclature. Nuclear spin properties and conventions for chemical shifts (IUPAC Recommendations 2001). *Pure Appl. Chem.* **2001**, *73*, 1795-1818.
- (3) Harris, R.K.; Becker, E.D.; Cabral de Menezes, S.M.; Granger, P.; Hoffman, R.E.; Zilm, K.W. Further conventions for NMR shielding and chemical shifts (IUPAC Recommendations 2008). *Pure Appl. Chem.* **2008**, *80*, 59-84.
- (4) Kumar, A.; Lionetti, D.; Day, V. W.; Blakemore, J. D. Redox-inactive metal cations modulate the reduction potential of the uranyl ion in macrocyclic complexes. *J. Am. Chem. Soc.* **2020**, *142*, 3032-3041.
- (5) Randles, J. E. B. Cathode-ray polarograph. II. Current-voltage curves. *Trans. Faraday Soc.* **1948**, *44*, 327-338.
- (6) Ševčík, A. Oscillographic polarography with periodical triangular voltage. *Collect. Czech. Chem. Commun.* **1948**, *13*, 349-377.
- (7) Savéant, J. M.; Costentin, C. *Elements of Molecular and Biomolecular Electrochemistry, An Electrochemical Approach to Electron Transfer Chemistry*, Wiley, Hoboken, NJ, **2019**.
- (8) Nicholson, R. S. Theory and application of cyclic voltammetry for measurement of electrode reaction kinetics. *Anal. Chem.* **1965**, *37*, 1351-1355.
- (9) Bard, A. J.; Faulkner, L. R. *Electrochemical Methods: Fundamentals and Applications*. 2nd ed.; Wiley: Hoboken, NJ, 2001.
- (10) *APEX2, Version 2 User Manual, M86-E01078*. Bruker Analytical X-ray Systems: Madison, WI, June 2006.
- (11) *SAINTE. Ver. 8.34A*. Bruker Analytical X-ray Systems: Madison, WI, June 2014.
- (12) G. M. Sheldrick, SADABS (version 2008/1): Program for Absorption Correction for Data from Area Detector Frames, University of Göttingen, 2008.
- (13) Krause, L.; Herbst-Irmer, R.; Sheldrick, G. M.; Stalke, D. Comparison of silver and molybdenum microfocus X-ray sources for single-crystal structure determination. *J. Appl. Cryst.* **2015**, *48*, 3-10.
- (14) Sheldrick, G. M. SHELXT - Integrated space-group and crystal-structure determination. *Acta Cryst. A* **2015**, *71*, 3-8
- (15) Sheldrick, G. Crystal structure refinement with SHELXL. *Acta Cryst. C* **2015**, *71*, 3-8.
- (16) Sheldrick, G. M. A short history of SHELX. *Acta Cryst. A*, **2008**, *64*, 112-122.
- (17) Hübschle, C. B.; Sheldrick, G. M.; Dittrich, B. ShelXle: a Qt Graphical User Interface for SHELXL. *J. Appl. Cryst.*, **2011**, *44*, 1281-1284.

- (18) Dolomanov, O. V.; Bourhis, L. J.; Gildea, R. J.; Howard, J. A. K.; Puschmann, H., OLEX2: a complete structure solution, refinement and analysis program. *J. Appl. Crystallogr.* **2009**, *42*, 339-341.
- (19) Allen, F. H.; Watson, D. G.; Brammer, L.; Orpen, A. G.; Taylor, R. In *International Tables for Crystallography*; Vol. C, pp. 790-811.
- (20) Kumar, A.; Lionetti, D.; Day, V. W.; Blakemore, J. D. CCDC 1960625: Experimental Crystal Structure Determination, **2020**, DOI: 10.5517/ccdc.csd.cc23t5z3.
- (21) Jeffrey, G. A., *An Introduction to Hydrogen Bonding*. Oxford University Press: New York, NY, 1997, p. 12.
- (22) (a) Casellato, U.; Tamburini, S.; Tomasin, P.; Vigato, P. Uranyl (VI) complexes with [1+1] asymmetric compartmental ligands containing a Schiff base and a crown ether-like chamber. *Inorg. Chim. Acta* **2002**, *341*, 118-126. (b) Casellato, U.; Tamburini, S.; Tomasin, P.; Vigato, P. A. CCDC 203852: Experimental Crystal Structure Determination, 2003, DOI: 10.5517/cc6v3w0
- (23) Kumar, A.; Lionetti, D.; Day, V. W.; Blakemore, J. D. CCDC 1960626: Experimental Crystal Structure Determination, **2020**, DOI: 10.5517/ccdc.csd.cc23t605
- (24) Kumar, A.; Lionetti, D.; Day, V. W.; Blakemore, J. D. CCDC 1960626: Experimental Crystal Structure Determination, 2020, DOI: 10.5517/ccdc.csd.cc23t605
- (25) Kumar, A.; Lionetti, D.; Day, V. W.; Blakemore, J. D. CCDC 1960628: Experimental Crystal Structure Determination, 2020, DOI: 10.5517/ccdc.csd.cc23t627
- (26) Kumar, A.; Lionetti, D.; Day, V. W.; Blakemore, J. D. CCDC 1960629: Experimental Crystal Structure Determination, 2020, DOI: 10.5517/ccdc.csd.cc23t638
- (27) Kumar, A.; Lionetti, D.; Day, V. W.; Blakemore, J. D. CCDC 1960630: Experimental Crystal Structure Determination, 2020, DOI: 10.5517/ccdc.csd.cc23t649